THE UNIVERSITY OF CHICAGO

LIFE, DEATH, AND PROPAGATION OF TURBULENCE

A DISSERTATION SUBMITTED TO
THE FACULTY OF THE DIVISION OF THE PHYSICAL SCIENCES
IN CANDIDACY FOR THE DEGREE OF
DOCTOR OF PHILOSOPHY

DEPARTMENT OF PHYSICS

BY
TAKUMI MATSUZAWA

CHICAGO, ILLINOIS
AUGUST 2023

Dedicated to my mother

The scientist does not study nature because it is useful to do so. He studies it because he takes pleasure in it, and he takes pleasure in it because it is beautiful. If nature were not beautiful it would not be worth knowing, and life would not be worth living.

- Henri Poincaré

TABLE OF CONTENTS

LIST OF FIGURES

LIST OF TABLES

ACKNOWLEDGMENTS

The year of writing this section marks the 140th year since Osborne Reynolds performed his iconic experiment on the laminar-turbulent transition, investigating different flow rates of water by injecting a jet of dyed water into the stream of water passing through a large glass pipe. It is my sincere hope that my work on isolated turbulence contributes to the collective endeavor to understand and ultimately harness it. However, no work is completed by a single individual. Here, I would like to acknowledge the names behind the scenes, whose contributions have been invaluable to this endeavor.

I am very grateful for having the chance to interact with faculty who are endlessly curious about science and life. I would first like to thank my research advisor, William Irvine. William is a scientific visionary and an incredible communicator. His attitude to foster creativity and technical rigor in science has greatly inspired me, and I feel very fortunate to have had his guidance and support. I would next like to thank my committee members: Sidney Nagel, Fausto Cattaneo, and Stephanie Palmer, for their valuable inputs on my research and thesis. Like many, I have admired Sid's personality and his approach toward science. I will always take his words to heart: "The commonplace is extraordinary. Examine the world around you, and many things that you take for granted are astonishing." I would also like to thank my collaborators: Nigel Goldenfeld and his student, Minhui Zhu. Working with them showed me how outstanding theorists think, and helped me truly realize that scientific progress is made when experiments and theories work together. At the James Franck Institute, I have had precious opportunities to expand my scientific horizon and witness numerous scientific accomplishments unfold. I treasure my interactions with Tom Witten and have admired his endless curiosity in everything. Heinrich Jaeger, Vincenzo Vitelli, and Arvind Murugan also helped shape my scientific mind. I would also like to thank John Phillips, Bentley Wall, Justin Jureller, Luigi Mazzenga, and Brenda Thomas for keeping everything running.

I have also learned a lot from my friends at graduate school. Vishal Soni, Noah Mitchell, Robert (Bob) Morton, Ephraim Bililign, Yehuda Ganan, Severine Atis, Stéphane Perrard, Sofia Magikiriadou, Martin Falk, Jiayi Wu, Hridesh Kedia, Thomas Videbaek, Mengfei He, Nidhi Pashine, Kieran Murphy, Endao Han, Alexander Bogatskiy, Jelani Hannah, Melody Lim, Savannah Gowen, Zhaoning Liu, Chloe Lindeman, Samar Alqatari, Matteo Sabato, Yaocheng Li, Ankur Agrawal, Bipul Pandey, Brendan Saxberg, Jackson O'Brien, Mark Di-Tusa, Ti-Lin Chou, John Devany, Cheyne Weiss, Peter Fields, Brady Wu, Samantha Livermore, Seth Musser, Sattvic Ray, Jessica Metzger, Bennet Sessa, Catherine No, and Glasha Osipycheva. Thank you for the years of support and friendship. The ways you thought, wrote, questioned, and interacted with me and others helped me become a better scientist but also a friend. I would like to thank especially Noah, Bob, Ephraim, Yehuda, and Matteo for being in the trenches with me.

I am deeply indebted to my mother, Mutsumi, and brother, Yoshiaki. My mother's unwavering resilience and steadfast spirit have been a profound influence on me, and her approach to the unseen events in life has been an invaluable guiding light in today's complex world. Coming from a small family, my brother's presence has been immense in my life. Together, we have shared our childhood, experiencing both numerous setbacks and a few triumphant moments. I wholeheartedly wish him a wonderful life ahead, filled with happiness, alongside his wife, Kozue, and their recently born daughter, Riho.

Finally, I would like to acknowledge friends at different stages of my life. Every single one of them offered a unique learning experience and friendship that I treasure. My first special thanks extend to Michiko Lee, who is a talented musician and a friend who encouraged me to pursue a liberal arts education in the United States. Without her beautiful voice, my interdisciplinary curiosity would have never flourished. I deeply thank Carolyn Topper for our long-lasting friendship. Her endless creativity is a pure delight to watch. My special thanks extend to Jinghui Liu. From the very beginning, my exchanges with her have been a

constant source of inspiration and joy. When I was (over)working in the lab, she helped me establish a healthy sleeping schedule. I am truly blessed for our encounter at the Flatiron Institute in 2019.

To anyone reading this not named here: please accept my apologies. You should be here.

ABSTRACT

Turbulence is hard to control. A plethora of experimental methods have been developed to generate this elusive state of matter, leading to fundamental insights into its statistical and structural features as well as its onset. In all cases, however, the material boundaries of the experimental apparatus pose a challenge for understanding what the turbulence has been fed, and how it would freely evolve.

Here, we build and control a confined state of turbulence using elemental building blocks – vortex rings. We create a stationary and isolated blob of turbulence in a quiescent environment, initiated and sustained solely by vortex rings. We assemble a full picture of its three-dimensional structure, onset, energy budget and tunability. The incoming vortex rings can be endowed with conserved quantities, such as helicity, which can then be controllably transferred to the turbulent state.

When the injection of vortex rings stops, a spherical front that separates the turbulent region from the quiescent surroundings propagates in the chamber, and the turbulence decays. By using a simple low-order closure model, we construct a spatially-extended description of the turbulence propagation, and compare its predictions of energy profile and non-diffusive dynamics with data.

The turbulent blob, which can be measured in its entirety and is free to evolve in isolation, offers a playground for fundamental studies on inhomogeneous turbulence, response of turbulence to a periodic drive, and the role of conserved quantities in turbulence decay and cascading process.

CHAPTER 1

INTRODUCTION: A VOYAGE THROUGH TURBULENCE

Active control of turbulence has long been sought for decades. A plethora of methods have been developed to constantly stir fluids in containers, such as boxes and pipes; however, a little is known about how to manipulate this ephemeral phase of flow using flow alone. Can turbulence be confined and held in place as an isolated cloud in a tank? Being able to create such a state, far from boundaries, would enable us to 'play' with turbulence in a controlled manner and to tackle questions about the nature of turbulence as a material phase that have been difficult to address using traditional experimental methods: what happens at the interface between turbulent and non-turbulent regions?; how are the inviscid conserved quantities (energy, impulse, angular impulse and helicity [117]) transported across the turbulent/non-turbulent interface, and what are their global budgets?; how does a cloud of turbulence expand and decay without the walls?

Manipulating this out-of-equilibrium state of matter is not as simple as with conventional states of matter. To fill in the gap, this thesis addresses an approach to position, localize, and tailor its properties. Moreover, the resulting confined turbulence provides a unique playground to study its intrinsic properties of turbulence such as how turbulence fills a quiescent space. With the recent experimental, theoretical, and numerical advances, it is a ripe time to revisit turbulence from fresh angles and with modern apparatuses.

1.1 A very brief history of turbulence and a modern outlook

In this section we introduce a brief history of turbulence research. As one of the oldest and considerably most important open problems in physics and mathematics, the literature on this topic is vast [9, 10, 55, 140, 121, 164, 163, 97]. It is not the scope of this thesis to cover the historical endeavor of the field; however, tracing it will clarify what this thesis aims to

achieve.

[32] offers a view that turbulence research has had three movements: statistical, structural, and deterministic. In all movements, a common starting ground is a continuum description of a fluid with its governing equation known as the Navier-Stokes equation

$$\rho \left[\partial_t u_i + u_j \partial_j u_i\right] = -\partial_i p + \nu \partial_j \partial_j u_i + f_i \tag{1.1}$$

where u_i is a velocity field, p is pressure, ρ is mass density, ν is kinematic viscosity, and f_i is a body force. While the NS equation was already accepted as the correct formulation of turbulent flow in late 19th Century, it did not take long for scientists to realize that direct analysis of the NS equation would not result in understanding of turbulence. The nonlinear advective term gives rise to motions across scales by coupling different spatial modes. To fully capture this nonlinear transfer, one needs infinitely many recursion relations to close the dynamics, known as the closure problem or the problem of the hierarchy. This intrinsic difficulty geared the pioneers, such as L.F. Richardson, G.I. Taylor, G.K. Batchelor, and A. Kolmogorov, to formulate a statistical theory of turbulence. The central idea is the energy cascade, meaning that large eddies break down into smaller ones as famously summarized in L.F. Richardson's verse:

> Big whorls have little whorls
> Which feed on their velocity,
> And little whorls have lesser whorls
> And so on to viscosity in the molecular sense.

It was later argued that this cascade process results in homogeneous, isotropic statistics of small-scale motions with a universal form, leading to Kolmogorov's 1941 paper [84]. The implication in their theory is that this energy cascade is a Hamiltonian process. In other words, there exists a regime where energy is transferred from one scale to the other without friction. In this 'inertial' subrange, the dimensional analysis and the above hypotheses result

in the so-called five-third law of the energy spectral function $E(\kappa)$:

$$E(\kappa) = C\epsilon^{2/3}\kappa^{-5/3} \tag{1.2}$$

where ϵ is the average dissipation rate per unit mass, κ is a wavenumber, and C is the Kolmogorov constant, approximately to 1.5[a][166]. This celebrated result is a hallmark prediction of turbulence which has stood the test of numerous experiments and simulations. However, their hypotheses were found inaccurate especially at a high Reynolds number due to the incomplete similarity at the large scales. This led to Kolmogorov's refined similarity hypothesis, resulting in the inclusion of the intermittency exponent β to the energy spectrum function:

$$E(\kappa) = C'\epsilon^{2/3}\kappa^{-5/3}(\kappa L)^{-\beta} \tag{1.3}$$

where L is the integral scale of the turbulent motions. The intermittency exponent β is, however, relatively small ($O(10^{-3})$ [135]) so the K41 result still remains consistent with numerous experimental and numerical tests [142].

The structural movement is motivated by the observations that relatively stable structures, commonly called "coherent structures" exist at the onset or in fully developed turbulence. The speculation that there is a specific path ways that lead to turbulence has possibly started in the identification of Tollmien–Schlicting waves in 1948 [154, 32]. This movement still persists today [3], and gave a birth to a trend of identifying coherent structures using principal orthogonal decomposition (POD) [68, 138] and other machine-learning-based techniques [25]. However, there are gaps in understanding how these coherent structures give rise to turbulent motions. The authors of [135] conclude that the statistical movements

a. Historically, we refer the coefficient of the 1D energy spectrum as the Kolmogrov constant. i.e. $E_{11} = C_1\epsilon^{2/3}\kappa^{-5/3}$. With the assumption of isotropy, $C = (55/18)C_1$.

produced "structureless theory having little power of conceptulization" while the structural movements produced "structures without theory."

The deterministic movement highlights the work of Lorentz on deterministic chaos [105], and may go back to Poincore's work on nonlinear differential equations [132]. The traditional deterministic approach such as the bifurcation theory, however, has given only superficial answers about how turbulence arises from the NS equation. An exciting advancement in recent years is the successful application of statistical mechanics to demonstrate that the onset of turbulence, in case of a Taylor-Couette flow and a pipe flow, belongs to the direct percolation universality class [157, 99, 133, 160].

In reality, research contains aspects from more than one movement listed above. For example, the direct numerical simulations (DNS) or large eddy simulations (LES) contains aspects of both deterministic and statistical movements, and a computational approach became a pillar of turbulence research to probe the intermittency and ever high Reynolds number flows that is not accessible to experiments. Conversely, available experimental methods and a computational capability strongly influence the formulation of the movements. A modern fluid mechanics research involves an array of techniques to measure quantities such as density, velocity, and pressure both locally and globally. For Osborne Reynolds, dye visualization revealed intermittent formation of puffs and slugs in a pipe flow at the onset of turbulence. The hot-wire anemometry enabled quantitative measurement of turbulent fluctuations for at a high precision, providing a means to test the statistical theory of turbulence. The acoustic Doppler velocimetry paved a non-intrusive method to measure a 3D vector at the point of interest. Starting in 90s, particle image velocimetry (PIV) and their cousins (stereo-PIV, tomo-PIV, micro-PIV, etc.) have become a dominant approach in experimental fluid mechanics [186] mostly because it is non-intrusive, and provides an instantaneous velocity field in a full view. In the last decade, the PIV technique has made a significant progress toward volumetric and high-speed measurements. Significant development of soft-

ware and hardware underwent in parallel to measure all three components of velocity fields using multiple high-speed cameras. In the year of this thesis is being written (2023), there exists much know-how to perform PIV on various flows [136]. Together with Particle Tracking Velocimetry (PTV), a technique that tracks individual particles instead of using image correlation like PIV, we have reached a stage where we can acquire a wealth of high-fidelity data of complex flows with a faster turnaround [22].

1.2 Scope of this thesis

Chapter 2 provides a comprehensive overview of the experimental system and techniques employed throughout this study. The author was responsible for the design, installation, and maintenance of the high-fidelity 2D/3D velocimetry station. In Chapter 3, we delve into the methodology for generating self-confining turbulence using vortex rings as the fundamental building blocks. Vortex rings can be endowed with conserved quantities such as energy and helicity that characterizes knottedness of a vortical structure. We show how vortex rings controls the properties of the resulting turbulence from length scales of motions and turbulent intenstiy. We assemble a full picture by examining of three-dimensional structure, onset, energy budget, and tunability.

Chapter 4 is divided into two sections that investigate the decay of turbulence, and propagation of the isolated spherical turbulent burst in a quiescent fluid. In the first section, we explore the decay of the isolated turbulence blob as the injection of vortex rings is ceased. By employing a novel experimental technique that allows us to capture the complete decay process, we demonstrate that the flow remains turbulent despite a significant decay in its kinetic energy, spanning five orders of magnitude. Furthermore, we observe two distinct decay regimes characterized by different power laws. To provide further context, we examine alternative methods for generating turbulence that decays with a single power law, and offer insights into the relationship between these findings and the growth of the integral length

scale.

In the second section, we study the enhanced diffusive properties of turbulence by examining how the isolated turbulent burst spread in the flow chamber. Through our analysis, we reveal that that the region of turbulence spreads out self-similarly. We compare the measured shape of the front with measurements in quantum turbulence [161], and investigate its dependence on Reynolds number. We demonstrate that the observed dynamics of decay and propagation can be effectively captured by a simple reaction-diffusion equation incorporating eddy diffusivity.

CHAPTER 2

APPARATUS AND METHODS

In this section we describe the experimental flow chamber geometry, the flow actuation and our imaging methods.

2.1 Flow chambers

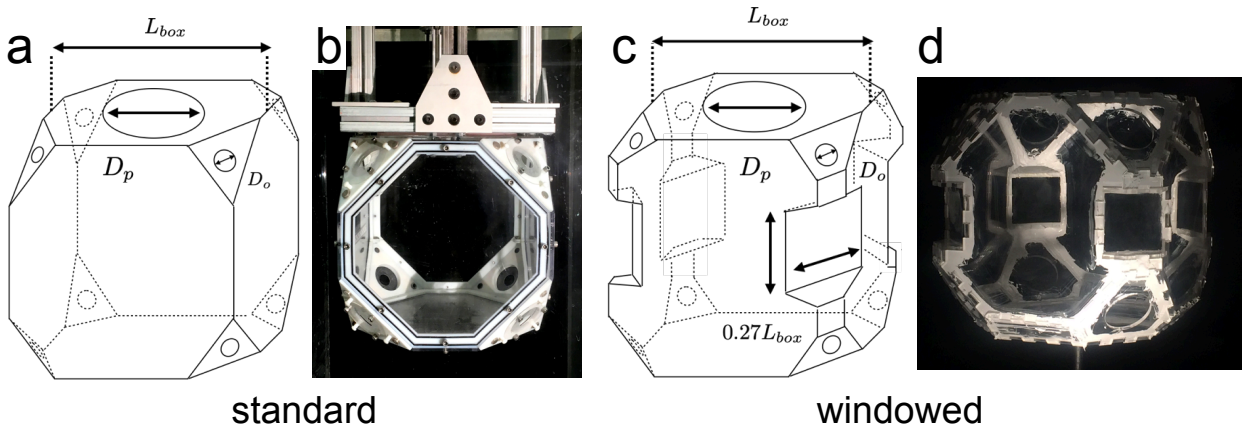

Figure 2.1: **Geometry of the flow chambers.** (a-b) The "standard chamber" consists of a 3D-printed frame and acrylic faces. (c-d) The "windowed chamber", made of acrylics, has four additional windows to measure vortex ring properties by particle image velocimetry.

Our experiments were performed in either of the two flow chambers depicted in Figure 2.1. Both chambers have the geometry of a cube with corners truncated by triangular plates, each containing an orifice through which vortex rings are generated. The linear dimension of the cube is $L = 351$mm in both cases. The chambers differ in their method of construction and their optical accessibility.

The chamber hereby referred to as the 'standard chamber' consists of a 3D-printed frame onto which acrylic sheets are bolted, whereas the 'windowed chamber' was assembled by gluing acrylic sheets together and features four windows inserted long the vertical edges of the cube. These windows allow 'edge-on' visualization of the flow, typically by laser sheet in a diagonal plane which contains the axis along which the vortex rings travel.

For both chambers, the top plate of the chamber contains a circular hole with diameter of $200mm$. An additional acrylic sheet with a hole of diameter D_p is bolted on top face of the chamber, through which a piston is inserted. This allows forcing with different size of the piston. The piston is an acrylic cylinder with diameter D_p, and is attached to the actuator by stainless steel threads. Additionally, we attach a silicone rubber on the top face to reduce any excess flow dragged by the motion of the piston. At each truncated triangular plate, we magnetically attach a holster bolted with a 1/16in acrylic sheet with a hole of diameter D_o, through which a vortex ring is generated. In this study, we use two primary settings of D_p and D_o as summarized in Table 2.1.

Unlike the standard chamber, the windowed chamber is fully made of acrylic and calking materials. The other difference is that it does not have holsters at the triangular plates, instead a circular acrylic piece with a hole of diameter D_p is bolted to the plate directly.

2.2 Actuation

The flow is set up by translating a piston by a linear motor (STA2510S, Copley Controls Corp).. When the piston is actuated impulsively in the vertical direction, it pulls a slug of fluid through each orifice into the flow chamber. This creates a vortex ring at each orifice.

The actuation velocity is programmable, and controlled by a National Instrumental instrument DAQ board. A typical signal is shown in Figure 2.3(b) as a dotted line. As the piston lifts up every cycle, some volume of fluid is drawn into the chamber through the orifices at the triangular plates, creating a set of vortex rings. The properties of the rings are described in Section 3.6. For periodic forcing, we program the motor to slowly move the piston back to its starting position.

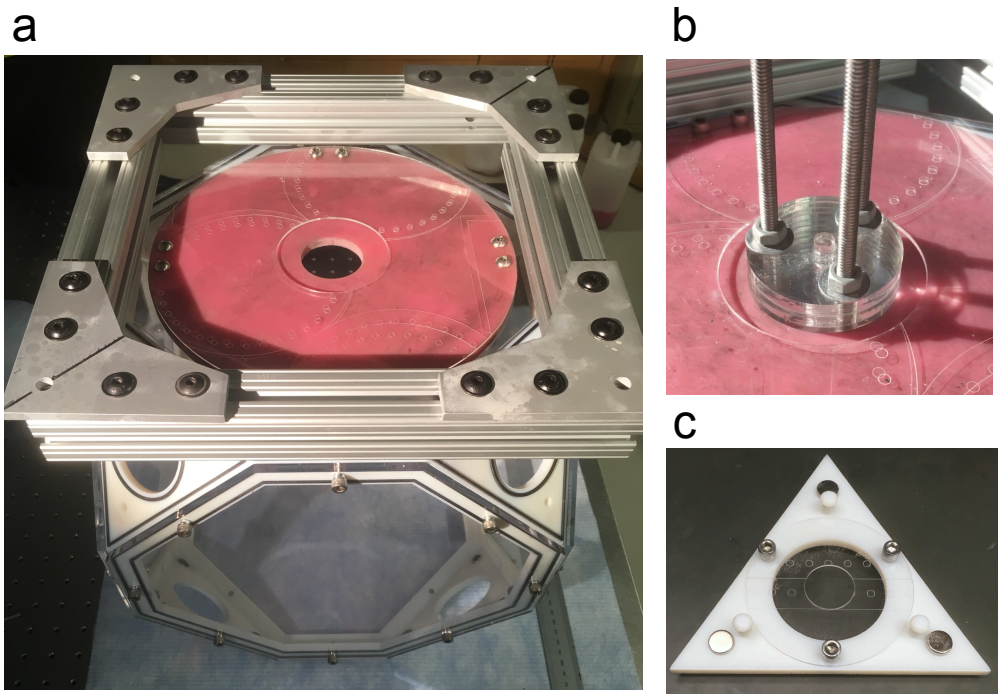

Figure 2.2: **Components of the experimental chamber.** (a) A silicone rubber ("flap") with a hole of diameter D_p is attached on the top face to minimize excess flow into/out of the chamber. (b)An acrylic, cylindrical piston is inserted through the hole. (c) A 3D-printed "holster" is magnetically attached to each truncated surface of the chamber. An acrylic sheet with an orifice or a 3D-printed helical mask is bolted to the holster.

2.3 PIV experiments

We suspend fluorescent particles (fluorescent red, $d = 100\mu m, \rho = 0.995 g/\text{cm}^3$, Cospheric LLC) in water. To prepare the solution, we add 0.7g of sodium dodecyl sulfate (Sigma-Aldrich) to 500mL of DI water. We then add 4g of fluorescent red particles while the solution is stirred. The solution is then injected into the chamber. We create a laser sheet with either a CW (DPSS laser (λ =532nm, $\leq$ 500mW), Beijing Viasho Technology Co., Ltd)., or an Nd:YLF pulsed laser (λ = 526.5nm, Photonics Industries International, Inc). and a cylindrical lens to fluoresce the particles at the peak emission wavelength of 630nm. We image the particles using a high-speed camera (Phantom v2512, VEO640L, or VEO4k 990L Vision Research) at adequate frame rate, ranging from 250 to 2000Hz. To suppress the

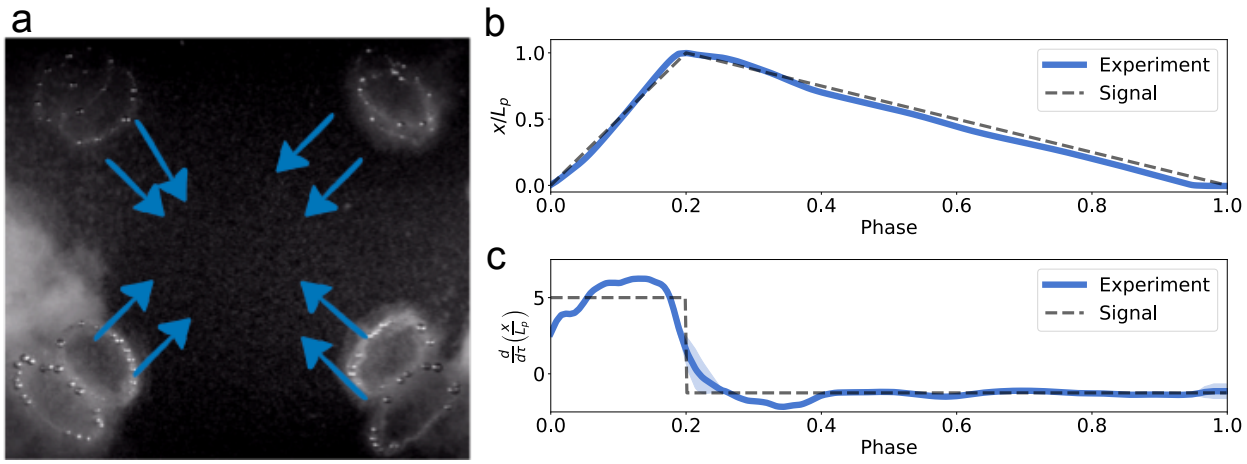

Figure 2.3: **Controlled generation of vortex rings** (a) Generated vortex rings are visualized by bubbles. (b) An actuating signal (gray) and realized motion of the piston are plotted against the phase. The curve is obtained by averaging the encoder output in a phase-locked manner. L_p is the commanded stroke length. (c) Commanded (gray) and realized (blue) velocity profiles are plotted against the phase. The shade represents the standard deviation of the collected velocity profiles ($n = 8$).

background originated from the laser sheet, we use a high-pass filter to eliminate the light below $\lambda = 540$nm. The frame rate and the interrogation window size are chosen so that a "quarter rule" is always satisfied for the fastest motion. The general rule of thumb is to use the frame rate such that the majority of particles move about 1-5 pixels per frame [136].

We conduct PIV experiments with both chambers (standard and windowed). The standard chamber is primarily used to investigate the turbulent nature of the flow (Figure 2.4). The windowed chamber is used to study the properties of vortex rings, and the view is provided by the rectangular windows.

We extract velocity fields using either the LaVision "DaVis" PIV software package or the PIVLab [171] package on MATLAB. Both packages are based on a standard cross-correlation algorithm with window deformation (WIDIM) [148]. In addition, DaVis offers a multi-frame pyramid algorithm [155] that we use for turbulent flows. The performance of these two algorithms is discussed in Sect.3.10.

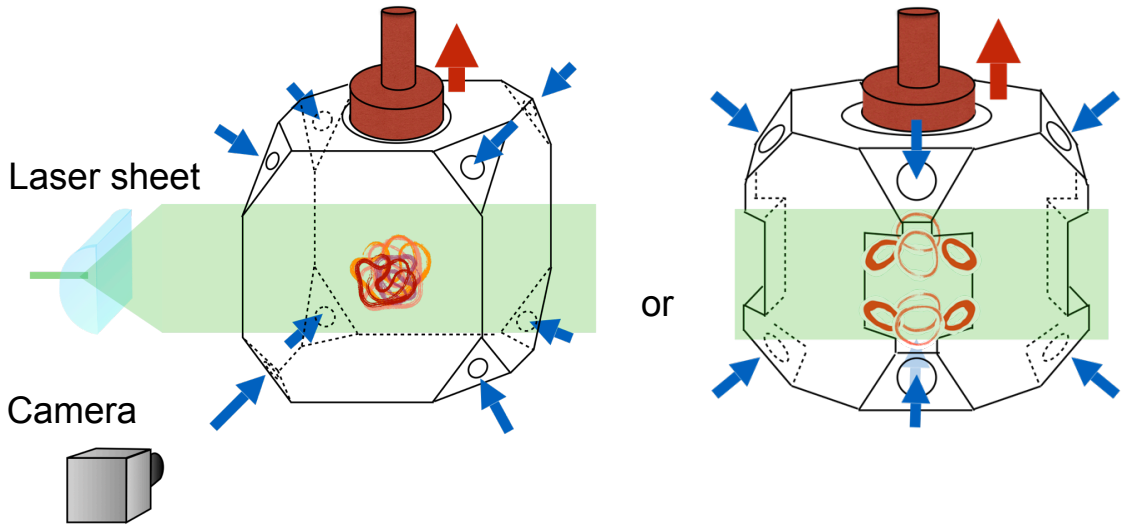

Figure 2.4: **A schematic of the PIV experiments using the standard chamber and the windowed chamber.** The standard chamber is primarily used to characterize a blob of turbulence, whereas, the windowed chamber is used to characterize the incoming vortex rings.

2.4 3D PTV experiments

We perform 3D PTV with three or four high-speed cameras (Phantom VEO640L, Vision Research) in the setup depicted in Figure 2.5). Each camera is equipped with a Scheimpflug adaptor to correct the focus as the lens is tilted with respect to the imaging plane. The same band-pass filter as described in the PIV section is used to eliminate the background illumination. Two cylindrical lenses are used to expand the beam from an Nd:YLF pulsed laser ($\lambda = 526.5$nm) to create an illuminated *volume* as opposed to a plane. We use the same fluorescent particles as described above.

We extract velocity fields using the LaVision "Shake-the-box" package [150]. The 3D PTV experiments include a two-step calibration procedure. The first step uses a static target to create mapping functions between the each camera view and the real 3D space. The second step self-consistently refines the mapping functions using particle images. Details of the method can be found in [150]. The maximum volume for the measurement is approximately 200mm x 120mm x 100mm (width x height x depth). In this volume, $O(10^5)$ particles are

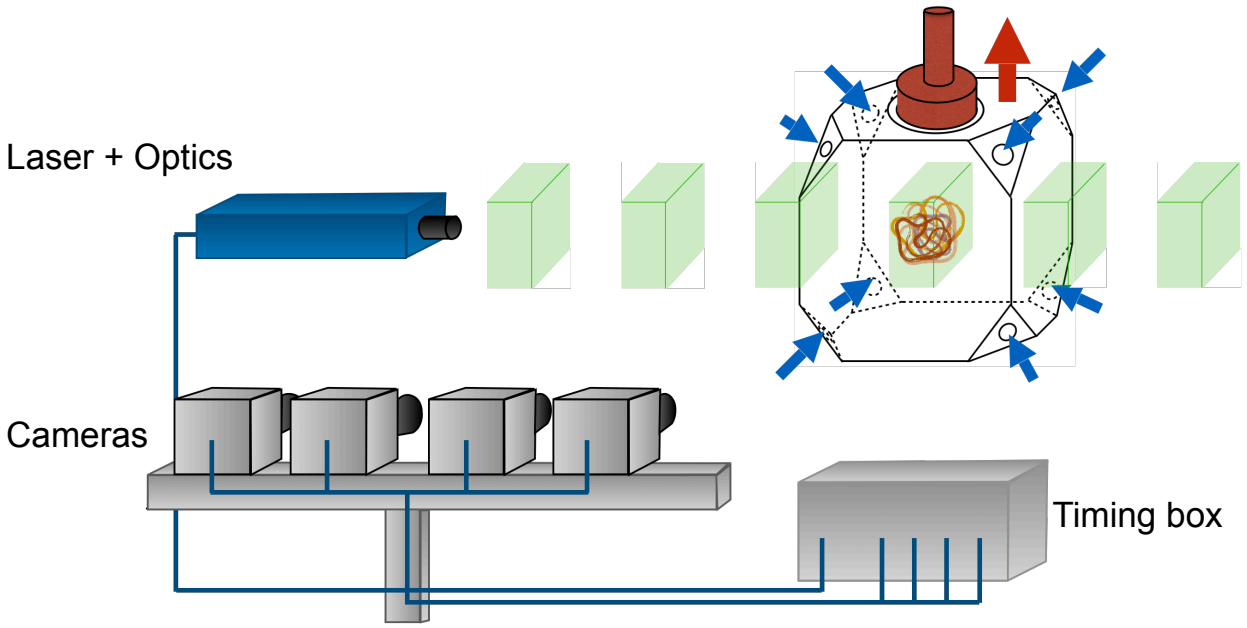

Figure 2.5: **A schematic of the 3D PTV experiments.** A Nd:YDF, pulsed laser and two cylindrical lenses are used to create an illuminated region in the chamber. Four cameras track the $O(10^5)$ particles every frame that are used to reconstruct an Eulerian velocity field.

Name	L_{box} (mm)	D_p (mm)	D_o (mm)	Box Type
Setting 1	351.0	160.0	25.6	Standard chamber
Setting 2	351.0	57.0	12.8	Standard chamber
Setting 3	351.0	160.0	25.6	Windowed chamber

Table 2.1: **Dimensions of the chamber used in this paper**

registered after successful calibrations, and $50 - 80\%$ are recognized as tracks.

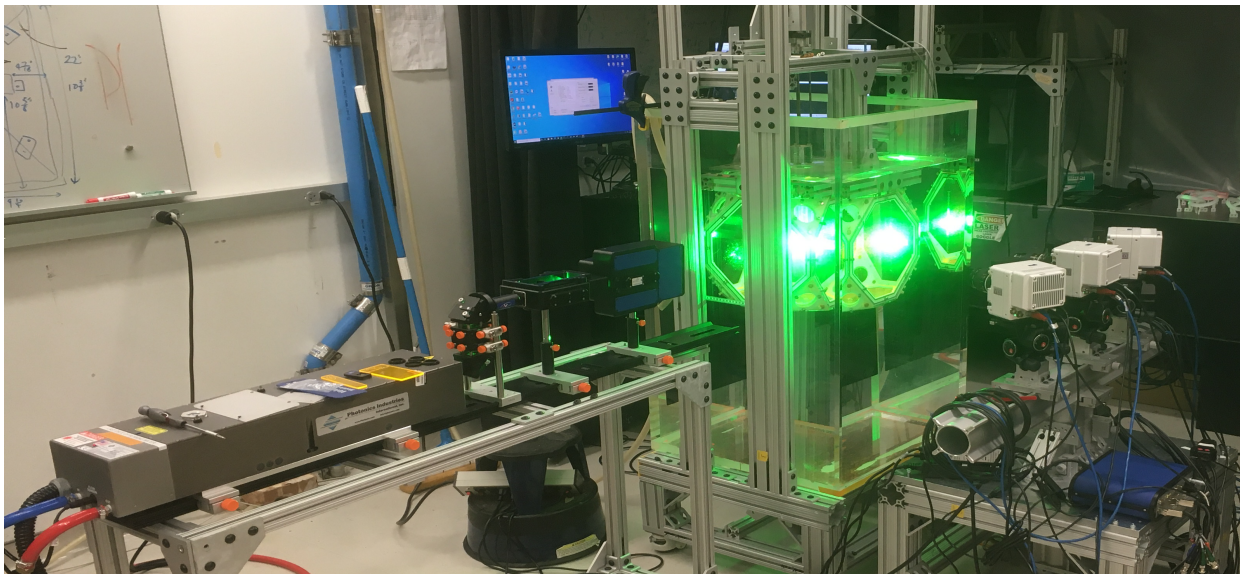

Figure 2.6: **The 3D PTV setup** (left) A Nd:YDF, pulsed laser and two cylindrical lenses are used to create an illuminated region in the chamber. (Middle) The 3D-printed, standard chamber is fixed in a water tank. (Right) Multiple (up to four) high-speed cameras are mounted on the mobile cart.

CHAPTER 3

CREATION OF AN ISOLATED BLOB OF TURBULENCE

Turbulence is hard to control. Many experimental methods have been developed to generate this elusive state of matter, leading to fundamental insights into its statistical and structural features as well as its onset. In all cases, however, the material boundaries of the experimental apparatus pose a challenge for understanding what the turbulence has been fed, and how it would freely evolve. Here, we build and control a confined state of turbulence using elemental building blocks – vortex rings. We create a stationary and isolated blob of turbulence in a quiescent environment, initiated and sustained solely by vortex rings. We assemble a full picture of its three-dimensional structure, onset, energy budget and tunability. The incoming vortex rings can be endowed with conserved quantities, such as helicity, which can then be controllably transferred to the turbulent state. This 'one eddy at a time' approach paves the way for sculpting turbulent flows much as a state of matter, 'printing' it at a targeted position, localizing it, and ultimately harnessing it.

3.1 What is turbulence made of?

Vorticity, which measures the local rotation rate of a fluid, is the building block of flow. In its absence, any fine structure in an incompressible flow decays rapidly with distance from material boundaries. Conversely, injection of vorticity can power complex bulk flows [175, 184], the quintessential example being the iconic multi-scale liveliness of turbulence. Canonical methods of generating turbulence rely on the spontaneous shedding of vorticity from boundaries [163, 3, 38, 195, 1, 2, 142, 170], be it of pipes [139, 123, 54, 70], grids [72, 82, 40, 21], or spinning plates [50, 181, 94]. This makes it hard to control, or have detailed knowledge of, the fabric of the injected vorticity. It also often couples the turbulence to boundaries, posing a challenge to study its unconstrained evolution. Yet, our most basic models of turbulence

are cast in terms of vorticity alone, with no reference to walls.

Knowing the structure of the vorticity that feeds turbulence is fundamental to a full understanding of turbulence because it determines the inviscid invariants including the amount of energy, helicity, linear impulse, and angular impulse that are injected into the turbulence. The balance of the latter two invariants, for example, might lead to different types of turbulence in the large scales [89], and have been proposed to rule the decay of turbulence [48, 47, 144, 96]. To make it possible to address these fundamental questions, we set out to build and sustain an isolated region of turbulence far away from boundaries, while controlling the injection of inviscid conserved quantities and fully observing its free evolution.

Vortex loops are a natural candidate to this end. A vortex ring is readily generated by impulsively drawing water through an orifice in a tank (Figure 3.1b). Seeding the water with bubbles reveals the coherent motion of the ring as it travels across the tank carrying its 'atmosphere' as it propagates (Figure 3.1c). Such a ring can, in an ideal fluid, travel infinitely far away from the boundaries. In real fluids, vortex rings eventually decay via viscous processes, or break down due to instabilities [42, 174, 98]. Nonetheless, they coherently carry their vorticity, and associated inviscid invariants, far from the boundaries that gave rise to them.

We set out to combine vortex loops like LEGO blocks, firing them together to 'print' a stationary region of turbulence in the center of our tank (Figure 3.1a). As demonstrated in iconic vortex collision experiments [126, 102, 113], recently revisited as a minimal means to understand the inertial cascade in real space [24, 112, 113, 128], two vortex rings fired together can multiply into a series of smaller rings, giving rise to turbulence. Figure 3.1e shows a version of this experiment using a pair of vortices created by drawing fluid into our tank through opposing orifices (Figure 3.1d). The rings, visualized using bubbles, approach each other, stretch and recombine into smaller, outwardly propagating rings. While this example demonstrates the tendency of colliding rings to produce turbulence, it also highlights the

tendency of colliding vortices to divide and redirect, escaping confinement. The situation is unchanged in the case of four vortices (Figure 3.1f) or eight (Figure 3.2a-d). This generic behavior of vortices colliding, reconnecting, and escaping challenges the idea that a blob of turbulence can be printed and confined at a target position.

3.2 Self-confining turbulence

In a naïve attempt to hold the escaping vorticity in place, we fired subsequent sets of eight vortex rings at repeating intervals so that the outgoing vortices would interact with the in-going vortices. To image the flow we use a combination of Particle Imaging Velocimetry (PIV), seeded bubble tracking, and 3D Particle Tracking Velocimetry (PTV). At a low frequency ($f = 0.2$Hz), we observe a simple repetition of the single-shot reconnection dynamics (Figure 3.2a-d); coherent vorticity comes in and leaves. However, when the frequency is sufficiently high to enable the outgoing vortex rings to interact with the incoming rings, a novel state with a remarkably different vorticity distribution emerges (Figure 3.2e-g, $f = 4$Hz).

In this new state, vorticity is confined, and is evenly distributed within an approximately spherical region. The flow inside the blob is in stark contrast to its surroundings which remain relatively quiescent. The blob is sustained as long as the vortex rings are injected. Both energy and enstrophy averaged over the measured plane indicate the comparative steadiness of the state (Figure 3.2h) with weak dependence on the periodic forcing.

In Figure 3.3a we show a Reynolds decomposition of this complex flow into mean and fluctuating components: $U_i = \langle U_i \rangle + u_i$. The blue cloud represents the average energy associated with the fluctuations and occupies the central region alone, whereas the yellow clouds represent the mean flow energy, associated with the paths along which the vortex rings are fed. We find that the flow inside the blob is dominated by fluctuations ($\langle u^2 \rangle / \langle U \rangle^2 \approx 10^{1.5} - 10^3$) whereas the flow outside the blob is dominated by coherent flow. Furthermore, the velocity fluctuations inside the blob are only weakly dependent of the forcing phase,

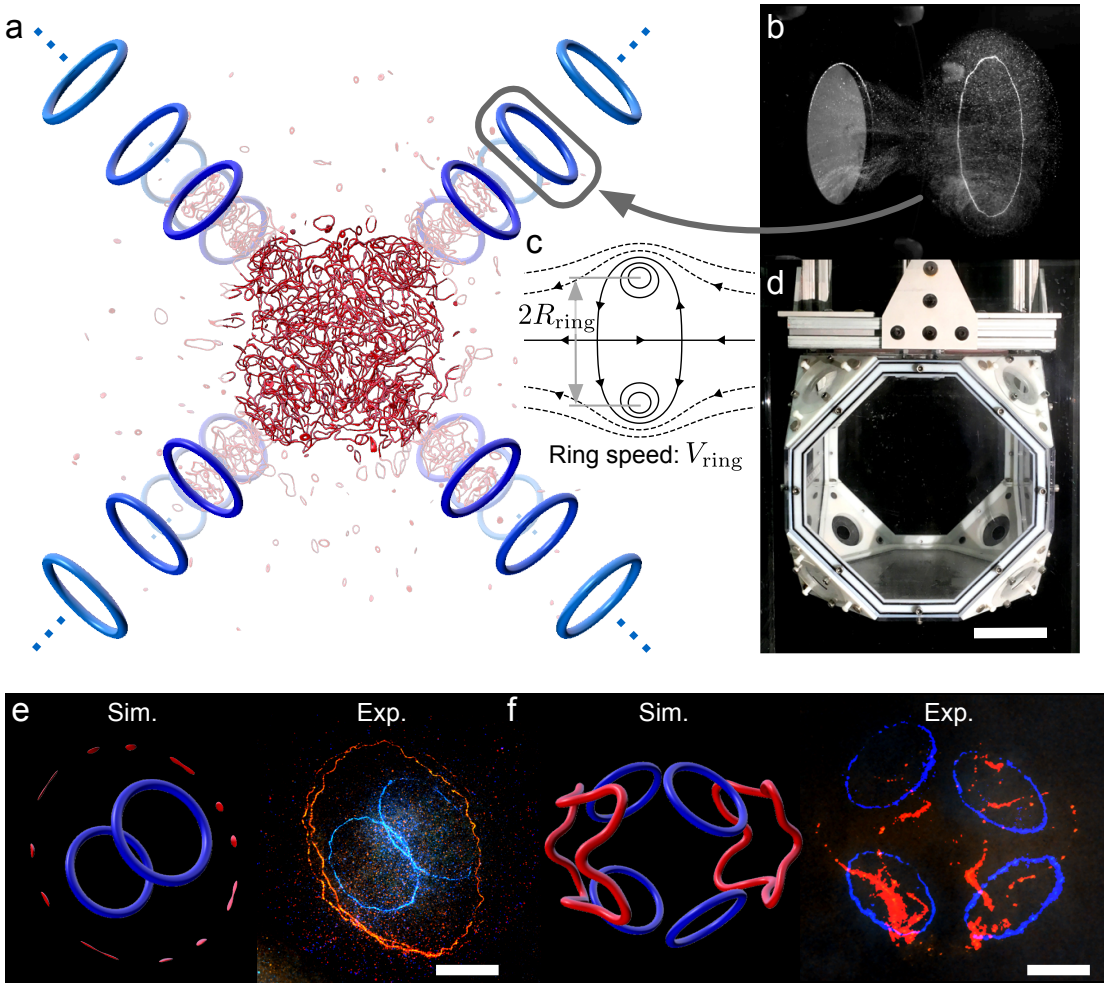

Figure 3.1: **Generation of turbulence using vortex rings and their resistance to confinement.** (**a**) We envisage colliding vortex rings creates turbulence at a target location far from boundaries with a controlled injection rate of energy. (**b**) A vortex ring and its atmosphere is visualized by bubbles. (**c**) Streamlines of a vortex ring in the co-moving frame. (**d**) A photograph of the experimental chamber. The scale bar represents 100mm. (**e-f**) Voriticty resists confinement. (**e**) A head-on collision of two identical vortex rings (blue) generates numerous secondary rings after reconnections occur (red). The left panel shows the result of a Gross-Pitaevskii simulation, whereas the right panel shows the experiment, visualized by bubbles. The scale bar represents 30mm along the semi-major axis of the red ellipse. The red ellipse is a projection of a circle. (**f**) A collision of four identical vortex rings results in two vortex loops after reconnections (red). The scale bar is the same as (e).

whereas the coherent flow outside the blob is phase-dependent, reflecting the laminar motion of the vortex rings. The temporally-and-radially averaged profiles of both fluctuating energy and enstrophy are approximately constant up to a radius R_{blob}, and decay rapidly for $r > R_{\text{blob}}$ approximately as r^{-4}. The local dissipation rate $\epsilon_{s_{ij}}(r) = 2\nu\langle s_{ij}s_{ij}\rangle$ also possesses the same radial profile as energy and enstrophy (Figure 3.3b) where $s_{ij} = (\partial_j u_i + \partial_i u_j)/2$.

To investigate the character of the flow inside the blob, we compute the fluctuating energy spectrum and the second-order structure function. PIV measurements are inherently limited at small scales by image resolution and at large scales by the finite field of view. To span the full range of scales in our turbulent flow, we performed 2D PIV measurements at three levels of magnification (Figure 3.3d, spatial resolutions: $\Delta_x = 0.5, 1.3, 2.4$ mm$\approx 2.4\eta, 6.2\eta, 11.4\eta$) and stitched the results together by taking into account the spectral leakage and low-pass filtering effects of PIV. With 3D PTV, we measure a one-dimensional energy spectrum on the slice that cuts the middle of the turbulent blob with a spatial resolution of $\Delta_x = 3.0$ mm $= 14.4\eta$. In addition, the resulting 4D velocity field offers a direct computation of a three-dimensional energy spectrum without the assumption of isotropy (See Sect. 3.9.2). The resulting one-dimensional energy spectrum $E_{11}(\kappa_1)$ and the second-order structure function D_{LL} of the fluctuating component of the flow are shown in Figure 3.3e-f. Our measurements at the three levels of magnification agree where their ranges of validity overlap. The rescaled spectrum is in agreement with the universal curve obtained by grid turbulence and turbulent boundary layer experiments [142]. Similarly, the second-order longitudinal structure function when rescaled by the 2/3 power law in the inertial sub-range is consistent with that of homogeneous isotropic turbulence.

Our spectra and structure function support the notion that the flow inside the blob is turbulent and therefore that its statistical properties can be captured by a dissipation rate ϵ_0 and an integral scale $\mathcal{L}$ [84, 85], together with the fluid viscosity ν. The value of ϵ_0 is notoriously challenging to measure [49, 193]. It can be inferred from the local strain rate

measurements, from fitting the measured spectrum to the universal curve, or by fitting the peak value in the scaled second order structure function [49]. As discussed in Sect. 3.11.2, we find all three methods are in agreement when computed on our median-filtered, spatio-temporally resolved velocity fields. The corresponding value of the Kolmogorov length $\eta = (\nu^3/\epsilon_0)^{1/4}$ is shown in Figure 3.3e. A measurement of the turbulent r.m.s. velocity $u' = \sqrt{\langle u_i u_i \rangle/3}$ in turn provides the estimate of the integral length scale $\mathcal{L} = u'^3/\epsilon_0$.

3.3 Turbulent length scales within a blob

How are the properties of this turbulent blob controlled by the incoming vortex rings? As shown in Figure 3.3e, we find the value of the integral length-scale to be close to that of the blob diameter $2R_{\text{blob}}$, suggesting both blob radius and integral length-scales are determined by the largest scale in the incoming vortex rings. This observation is supported by repetitions of our experiment in which we varied frequency of injection of the incoming vortex rings and found no change in either $\mathcal{L}$ or R_{blob}. A repetition of our experiment in which the incoming vortex ring radius was halved, resulted instead in a halving of both $\mathcal{L}$ or R_{blob} (See Sect. 3.14.1).

The smallest (Kolmogorov) length-scale of the turbulent blob η (Figure 3.3e) has by contrast little relation to the vortex ring radius, and is instead strongly affected by the incoming vortex ring energy and frequency of injection. This is consistent with the notion that at the smallest length-scales turbulence 'forgets' about the large-scale forcing that gave rise to it and the velocity field depends only on energy flux ϵ_0 and viscosity ν. We thus turn our attention to the balance of energy in our system.

Because the flow is at dynamical equilibrium, the dissipated power must match the power injected by the vortex rings. If we neglect any residual dissipation due to the mean flow, the

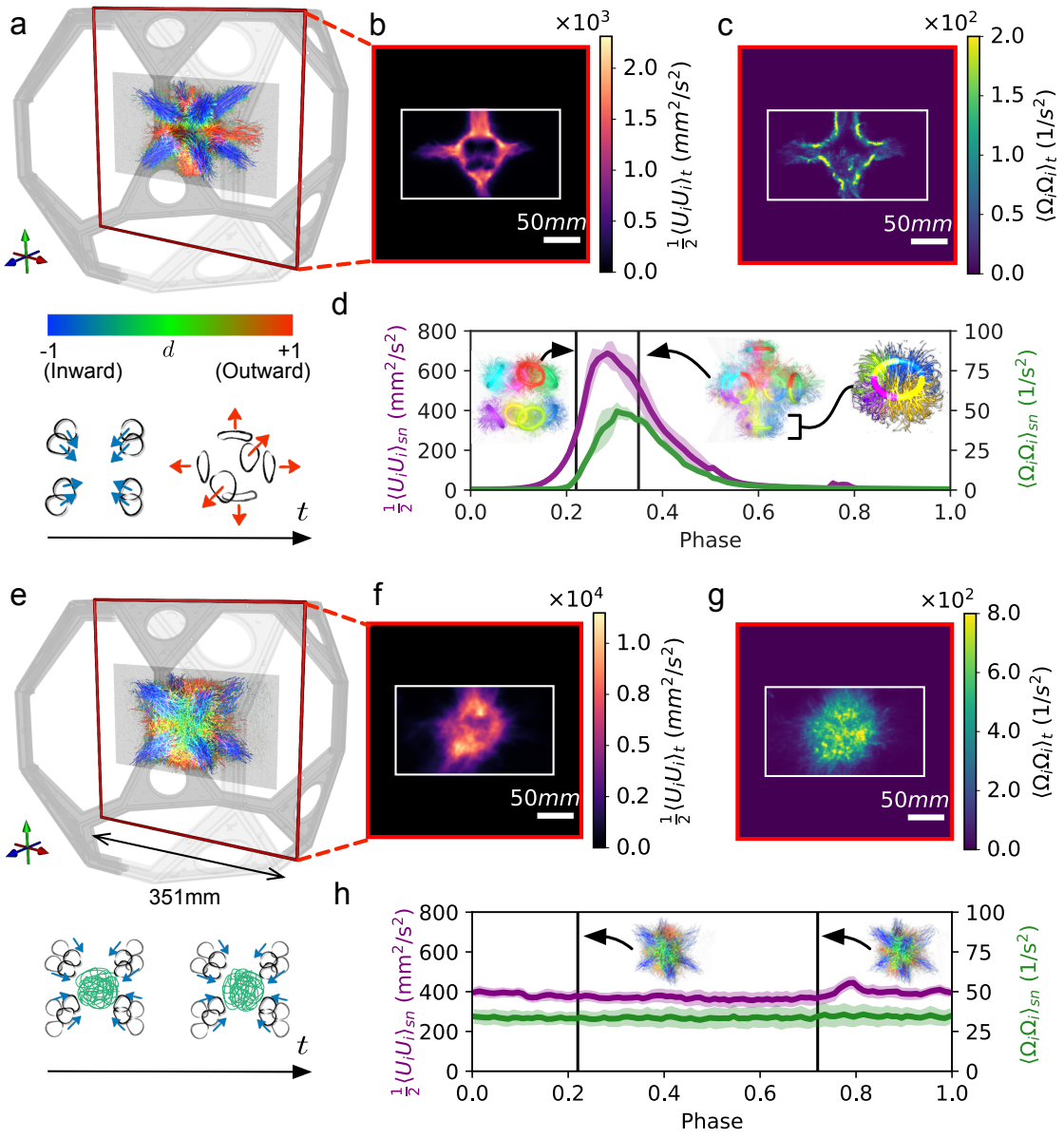

Figure 3.2: **Two phases emerge as eight vortex rings repeatedly collide: coherent reconnections and a confined state of turbulence.** (**a**) Coherent vortex reconnections of eight vortex rings (blue) result in six secondary rings (red), visualzied by 3D Lagrangian trajectories. The color represents the radial component of instantaneous Lagrangian speed, $d = (\vec{U}_{\text{Lag}} \cdot \hat{r})/|\vec{U}_{\text{Lag}}|$. $(V_{\text{ring}}/R_{\text{ring}}, f) = (20\text{Hz}, 0.2\text{Hz})$. (**b-c**) Time-averaged energy/enstrophy on the central slice shows the passage of vortex rings as they enter, reconnect and leave the central region. (**d**) Spatially-averaged energy and enstrophy on the central plane. The inset figures show the 3D Lagrangian trajectories before and after the reconnections. (**e**) Lagrangian trajectories around a turbulent blob display uniform, nearly isotropic outflow from the core. $(V_{\text{ring}}/R_{\text{ring}}, f) = (20\text{Hz}, 5\text{Hz})$ (**f-g**) Time-averaged energy/enstrophy shows an isolated region with high energy/enstrophy. (**h**) Spatially-averaged energy and enstrophy shows the state to be steady. The error bands in (d) and (h) represent SEM (n=5 and 25cycles respectively).

energy balance is

$$4\pi\rho \int \epsilon(r) r^2 dr \approx 8 K_{\text{ring}} f, \tag{3.1}$$

where $\epsilon(r) = \epsilon_0$ if $r \leq R_{\text{blob}}$, $\epsilon_0 (R_{\text{blob}}/r)^4$ otherwise. K_{ring} is the kinetic energy inside the vortex atmosphere of any one of the incoming vortices.

When integrated over all space, the L.H.S. evaluates to $16/3\pi\epsilon_0 R_{\text{blob}}^3 = 4/3\pi\epsilon_0 R_{\text{eff}}^3$, whereas if integrated up to R_{blob} we have $4/3\pi\epsilon_0 R_{\text{blob}}^3$. The R.H.S. requires knowledge of K_{ring}. When there is a vortex ring in a flow, the energy over all space K is generally the sum of the energy inside the vortex atmosphere K_{ring} and the energy of the added mass associated with the potential flow that surrounds the atmosphere K_{added}. K_{ring} can be further decomposed into the translational kinetic energy of the vortex atmosphere $K_{\text{rect}} = 4/3\pi R_{\text{atmosphere}}^3 V_{\text{ring}}^2$, and the energy associated with the rotational motion within the vortex atmosphere K_{int}. While the exact partitioning varies by the vortex model, the variation for K_{ring} is small (<3.3%) for realistic vortex ring models. We directly measured the energy of our vortex rings, and found $K_{\text{ring}} = (2.0 \pm 0.4) K_{\text{rect}}$ similar to $23/14 K_{\text{rect}} \approx 1.6 K_{\text{rect}}$ of Hill's spherical vortex (see Sect. 3.6.3).

In Figure 3.3c we compare the measured dissipated vs injected power for a collection of blobs that are created by altering ring size, speed, and frequency of injection. The dissipated power scales linearly with the injected power, with a slope of approximately 1. A more granular accounting, e.g. including only the energy contained within the vortex ring atmosphere and computing ϵ_0 only within R_{blob}, yields a linear relationship with lower proportionality constants: 1 (total energy, total turbulent dissipation), 0.68 (energy within the incoming vortex ring atmospheres, turbulent dissipation within a sphere of radius R_{eff},) and 0.33 (energy within the incoming vortex ring atmospheres, turbulent dissipation within a sphere of radius R_{blob}).

Crucially, increasing the velocity or frequency of injection increases the rate of energy

dissipation while keeping the integral length-scale fixed, thereby increasing the separation of scales $\mathcal{L}/\eta$. Thus ring radius and energy injection provide independent control knobs for producing turbulence of a desired intensity localized to a given region.

The picture is in stark contrast to the single-collision experiment (Figure 3.2a) in which vortices come in, reconnect, and go out. At these low forcing frequencies the conversion from coherent vortex motion to turbulence is far less efficient. Even though in practice reconnections trigger energy loss within the outgoing vortices, in the limit of a single coherent collision with large separation of scales, the fraction of advected energy can be in principle 100%.

3.4 Transition from coherent reconnections to turbulence

What governs the transition to a blob state? The most basic criterion is suggested by geometry: the outgoing rings will collide with the incoming rings for $f \gtrsim V_{\text{ring}}/R_{\text{ring}}$. A visualization of coherent vorticity in our flow using the Q criterion supports this hypothesis. A completely different conceptual approach is to seek to 'match' the incoming vortex 'eddies' to the turbulent state. A central idea in a turbulent cascade is that energy from each scale ℓ is transported to the next in a time $\tau_\ell \sim (\ell^2/\epsilon_0)^{1/3}$. If we demand that the time between incoming vortices $1/f$ match the timescale for the largest eddy to transfer energy down the cascade we have $1/f > \tau_{\mathcal{L}}$. For our fully developed turbulent blob we have $\mathcal{L} \propto R_{\text{ring}}$ (Figure 3.4a, $\alpha_0 = 2.17 \pm 0.13$) and $\epsilon_0 \propto V_{\text{ring}}^2 f$ (Figure 3.4b, $\alpha_1 = 0.35 \pm 0.02$) with proportionality constants determined in experiment. We then obtain a criterion for transition: $f_c = (\alpha_1/\alpha_0)V_{\text{ring}}/R_{\text{ring}}$ with the proportionality constant determined by the independent measurements of $\mathcal{L}(R_{\text{ring}})$ and $\epsilon_0(V_{\text{ring}})$ in the fully developed turbulent state.

Figure 3.4e shows the time-averaged enstrophy field for experiments in which we varied both f and $V_{\text{ring}}/R_{\text{ring}}$. The transitional range predicted by matching vortex arrival intervals with the largest eddy turnover time is shown by the blue band for comparison. The

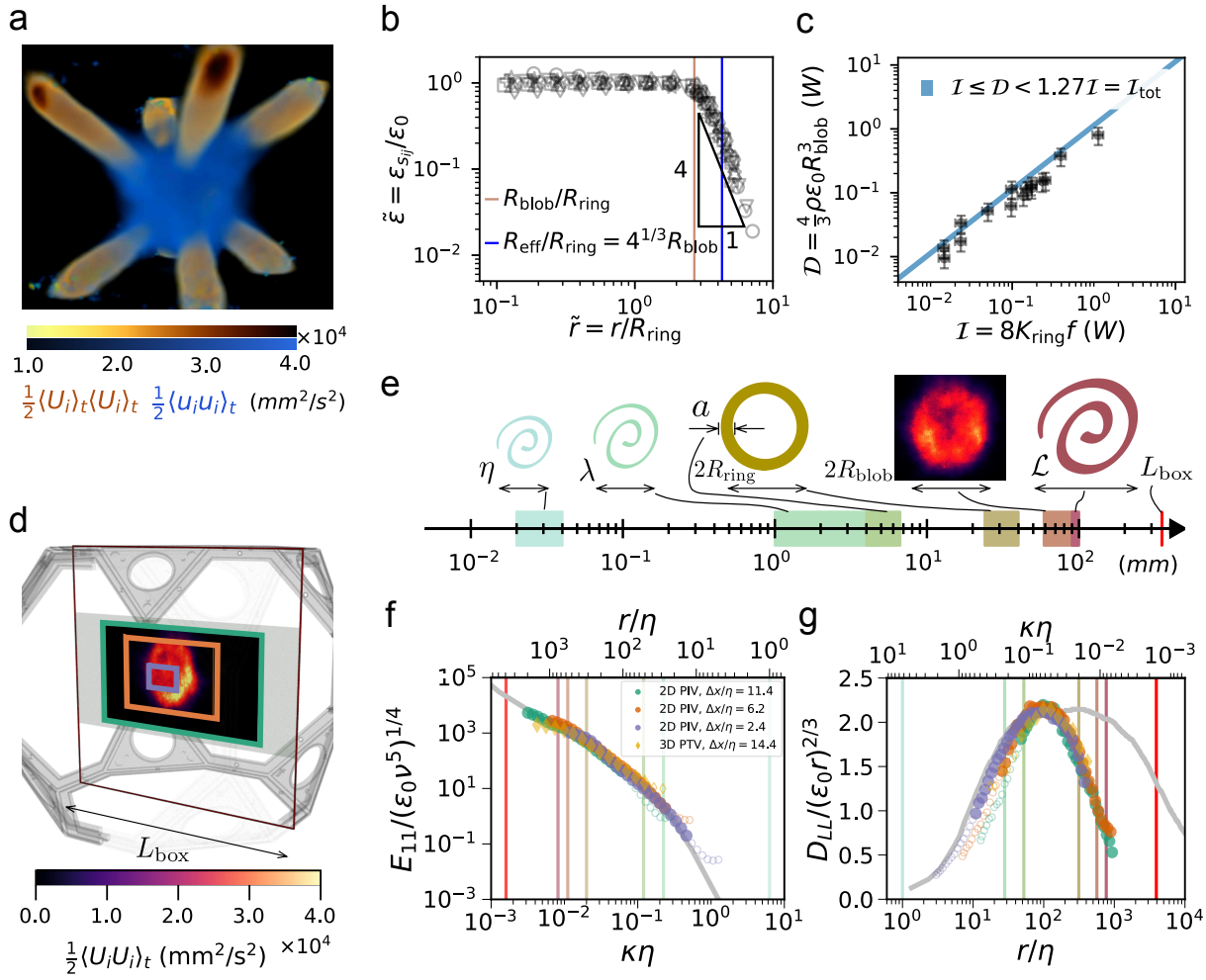

Figure 3.3: **Turbulent flow statistics and energy balance in a turbulent blob.** (**a**) Yellow: the mean flow energy $\langle U_i\rangle_t\langle U_i\rangle_t/2$. Blue: the mean turbulent energy $\langle u_iu_i\rangle_t/2$. (**b**) Radial profile of the dissipation rate on the central plane reveals an homogeneous region up to $R = R_{\text{blob}} \approx \sqrt{6}R_{\text{ring}}$, and a tail that decays with $\sim r^{-4}$. The profile collapses for rings with different radii. (Piston stroke ratio, piston effective stroke velocity, frequency)=($L/D, v_{eff}$ in mm/s, f in Hz)- circle (1.5, 196, 5), up-pointing triangle (2.0, 418, 5), down-pointing triangle (3.0, 443, 5), square (3.0, 443, 7), diamond (3.5, 318, 5), plus (3.5, 594, 5), diagonal cross (3.5, 594, 7), star (3.5, 594, 8). (**c**) Dissipated power in the sphere of radius R_{blob} linearly scales with the power injected into the blob by vortex rings. Data are presented as mean +/-SEM (n=12). (**d**) Planes display the measurement regions of 2D PIV ($i = 1, 2$) performed at three levels of magnification. (**e**) Turbulence lengthscales with respect to the relevant geometries (blob radius R_{blob}, ring radius R_{ring}, and core diameter a). (**f**) Rescaled one-dimensional spectra are computed in the homogeneous region ($r \leq R_{\text{blob}}$). ($\epsilon_0 = 6.0 \times 10^4$ mm^2/s^3, $\nu = 1.004$mm^2/s, $Re_\lambda = 200$). The gray master curve is taken from [142] ($Re_\lambda \approx 600$) as a reference. The attenuated signal due to PIV is addressed by hollow data points. (**g**) Rescaled second-order structure functions of the same data as (**f**) are shown with a reference curve from [142] ($Re_\lambda \approx 600$).

relationship between f_c and $V_{\text{ring}}/R_{\text{ring}}$, consistent with predictions, is qualitatively visible from the change in shape as frequency is increased. A second criterion to classify whether a given flow is in a blob state is to compute the enstrophy flux through a sphere that encloses the blob (Figure 3.4c). For the barotropic, incompressible fluids the integrated enstrophy flux is given by

$$\Phi_Z(t) = \int_{\partial \mathcal{V}} \Omega^2 U_i n_i dS, \tag{3.2}$$

where $\Omega_i = \epsilon_{ijk}\partial_j U_k$ is vorticity. The phase-averaged (integrated) flux $\langle \Phi_Z \rangle_n$ is shown in Figure 3.4c for an experiment with $f < f_c$ (red) and one with $f > f_c$ (blue). The red curve shows a trough (influx > outflux), followed by a crest (influx < outflux) as the secondary rings transport enstrophy away from the considered volume. The blue curve, by contrast, shows little to no outflux. As f is increased for a given $V_{\text{ring}}/R_{\text{ring}}$, the escaping enstrophy per cycle (shaded green region in Figure 3.4c) smoothly decreases as the frequency is increased (Figure 3.4d.). This corresponds to the suppression of coherent reconnections and development of turbulence. Placing a threshold (<5% relative to the values at $f = 1$Hz) on the escaping enstrophy reveals that the transitional frequency depends on $V_{\text{ring}}/R_{\text{ring}}$ in a linear fashion (Figure 3.4e, orange band). The upper limit of the orange band in Figure 3.4e lies within 10-20% of the predicted transition frequency.

For $f > f_c$, the energy and enstrophy are completely transferred to the blob, in sharp contrast to the single shot experiment ($f \ll f_c$) in which neither are left behind nor in fact penetrate the central region. By contrast, the mass associated with the vortex atmospheres must flow in and out in equal amounts and cannot be left behind. We find it interesting that the blob state can occur in the first place given this fact. Our work raises the question of whether vortex ring trains are in some sense optimally suited to confining and 'feeding' turbulence. What types of flow 'input' lead to a maximally localized blob states vs delocalized states in which the necessary outward advection destabilizes confinement?

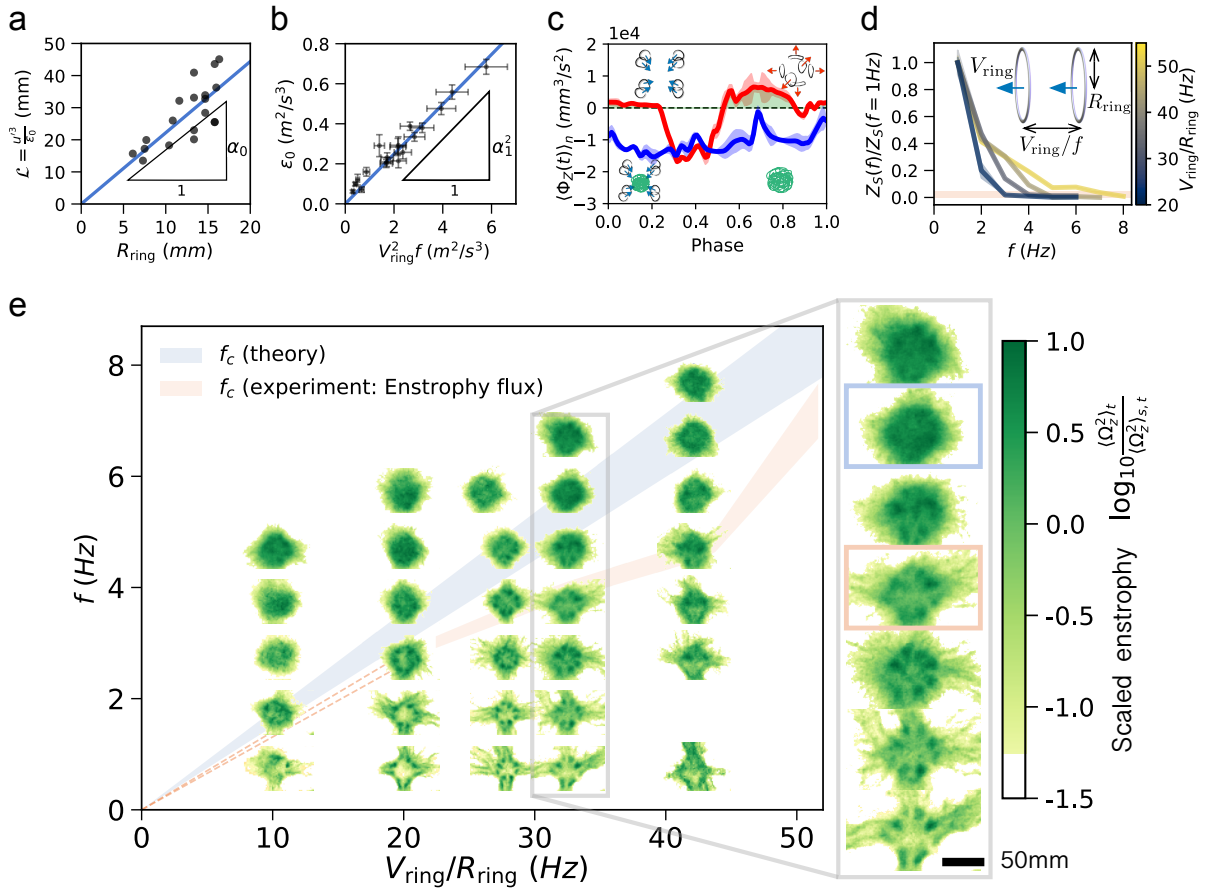

Figure 3.4: **$\mathbf{V}_{\text{ring}}/(\mathbf{R}_{\text{ring}}\mathbf{f})$ governs the transition from coherent reconnections to turbulence.** (**a**) The integral length scale $\mathcal{L}$ is proportional to the radius of the injected vortex ring R_{ring}. (**b**) Dissipation rate ϵ_0 inside the turbulent core is proportional to the power injected by vortex ring $\propto V_{\text{ring}}^2 f$. The x-error bar represents SEM(n=5), and the y-error bar represents SD of a time series of dissipation rate (n=500).(**c**) Phase-averaged enstrophy flux through a sphere with radius of $1.9R_{\text{blob}}$ captures outgoing enstrophy below the transition (red, $f = 1$Hz), and its absence above the transition (blue, $f = 6$ Hz) for rings with $V_{\text{ring}}/R_{\text{ring}} = 20$Hz. The data are presented as phase-locked average +/- SEM (red: n=2, blue: n=10). (**d**) The scaled escaping enstrophy per cycle decreases as the injection frequency increases, indicating a transition to a blob. The orange band corresponds to <5%. (**e**) Formation of a turbulent blob depends on $V_{\text{ring}}/R_{\text{ring}}$. Scaled time-averaged enstrophy fields show agreements with the transition frequencies expected from our theory and measurements on the enstrophy flux. The orange band represents the frequencies that the escaping enstrophy becomes 0-5% of the values at $f = 1$Hz. The data are presented as mean +/- SEM (n=3).

3.5 Controlled injection of inviscid invariants

Finally, we explore the tunability of our turbulent blob through control of the vortex rings. The ring radius R_{ring} tunes the integral scale $\mathcal{L}$ and the blob radius R_{blob}. Meanwhile, the energy balance sets the smallest scale of turbulence (Kolmogorov scale η) as it leads to $\epsilon_0 = \alpha_1^2 V_{\text{ring}}^2 f \sim \Gamma_{\text{ring}}^2 f / R_{\text{ring}}^2$. Hence, the separation of scales is given by $\mathcal{L}/\eta \sim (\Gamma_{\text{ring}}/\nu)^{3/4}(R_{\text{ring}} f / V_{\text{ring}})^{1/4}$, consistent with the usual relation $\mathcal{L}/\eta \sim Re_{\mathcal{L}}^{3/4} \sim (u'\mathcal{L}/\nu)^{3/4}$ for general turbulence [134]. Notice that it is expressed solely by the variables of the injecting vortex rings and thus can be completely controlled by tuning their properties.

Can our approach to building a turbulent blob be harnessed to endow the turbulence with additional properties? Beyond energy, natural candidates include the inviscid invariants of impulse, angular impulse and helicity. To test this possibility we replaced the circular orifices in the corners of our tank with 3D-printed masks with helical rims. As discussed in Sect. 3.6.3, we found this method produces helical vortex rings that carry both angular impulse and helicity. Colliding these helical rings can in turn produce blobs with finite helicity (Sect 3.14.2). In Figure 3.5 we show measurements of the total helicity in a blob created by colliding helical vortex loops in combinations that inject a total helicity of $+8\mathcal{H}_{\text{ring}}$, $-8\mathcal{H}_{\text{ring}}$ and $0\mathcal{H}_{\text{ring}}$, while injecting zero angular impulse and zero linear impulse. Although the vorticity field is not completely resolved (See Sect. 3.6.3), clearly the answer is affirmative.

3.6 Vortex rings

In this section, we dissect vortex rings generated in our experimental chamber in a following order. First, we review general properties of vortex rings, referring to their canonical theories. Then, we consider the experimental conditions to generate a vortex ring in our chamber that gives a rise to the accessible parameter space. Finally, we present our measurements using 2D PIV and 3D PTV, comparing to the theories and the results obtained by different

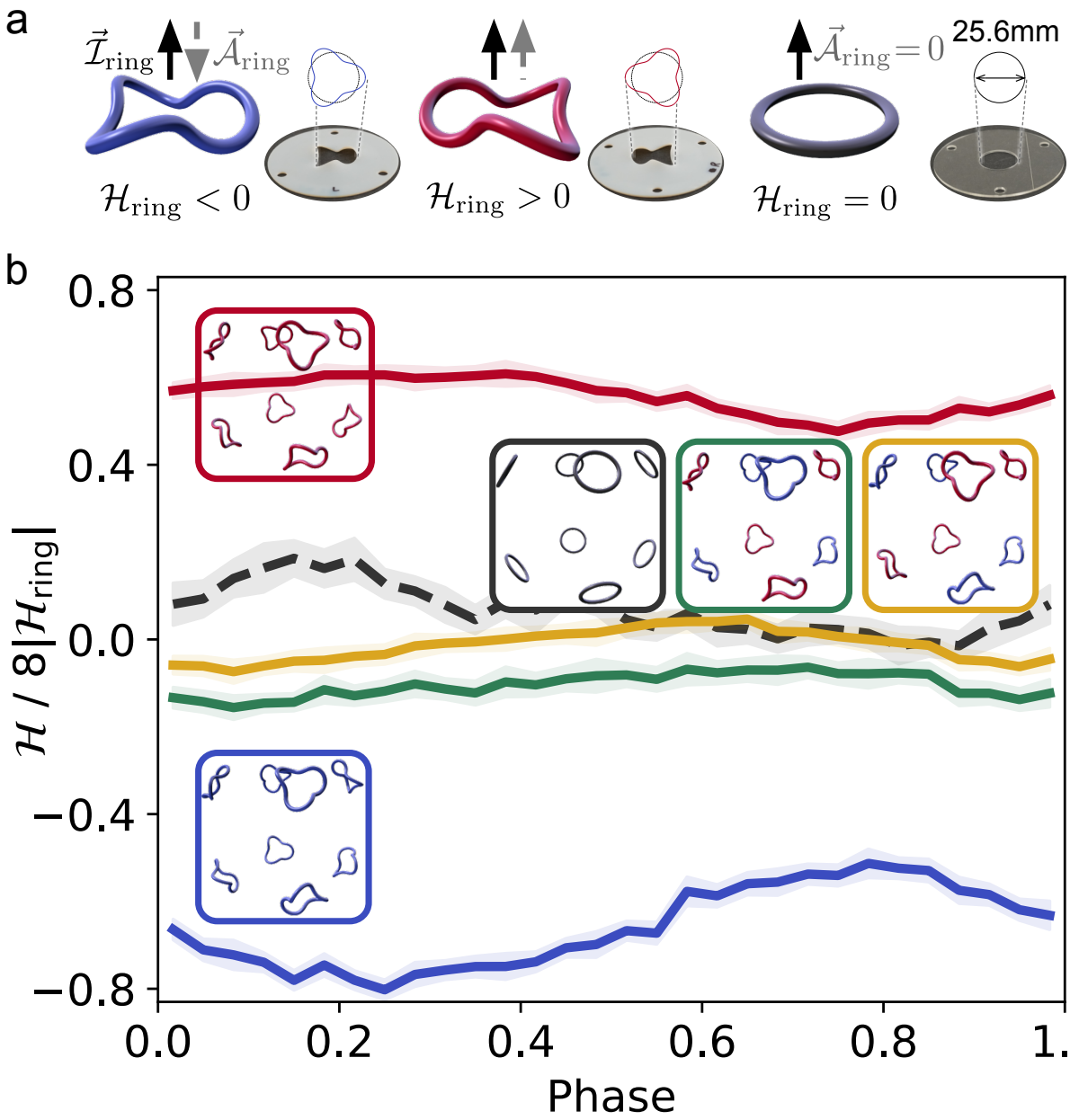

Figure 3.5: **Repeated collision of helical rings transfers helicity to turbulence in a controlled fashion.** (a) Helical masks generate helical rings. Handedness is defined by the relative orientation of linear impulse $\vec{\mathcal{I}}_{\rm ring}$ to angular impulse $\vec{\mathcal{A}}_{\rm ring}$, and is tuned from antiparallel (blue) to parallel (red). (b) Helicity is transferred from helical rings to a blob of turbulence. Different configurations allow injection of helicity with different handedness. The five configurations of the measurements are illustrated in the insets. (Net heliciy per cycle, net angular impulse per cycle) = $(8\mathcal{H}_{\rm ring}, 0)$ [Red: 8 Right], $(0, 0)$ [Green: 4 Right + 4 Left], $(0, 0)$ [Yellow: 4 Right + 4 Left], $(0, 0)$ [Black: 8 Planar], $(-8\mathcal{H}_{\rm ring}, 0)$ [Blue: 8 Left]. A vortex ring of $(V_{\rm ring}/R_{\rm ring}, f) = (40\text{Hz}, 5\text{Hz})$) was used, and the graph shows the helicity integrated over a sphere of radius 60 mm$\approx R_{\rm blob}$. The shade represents the standard error of the mean.

experimental systems.

3.6.1 Anatomy of injected vortex loops

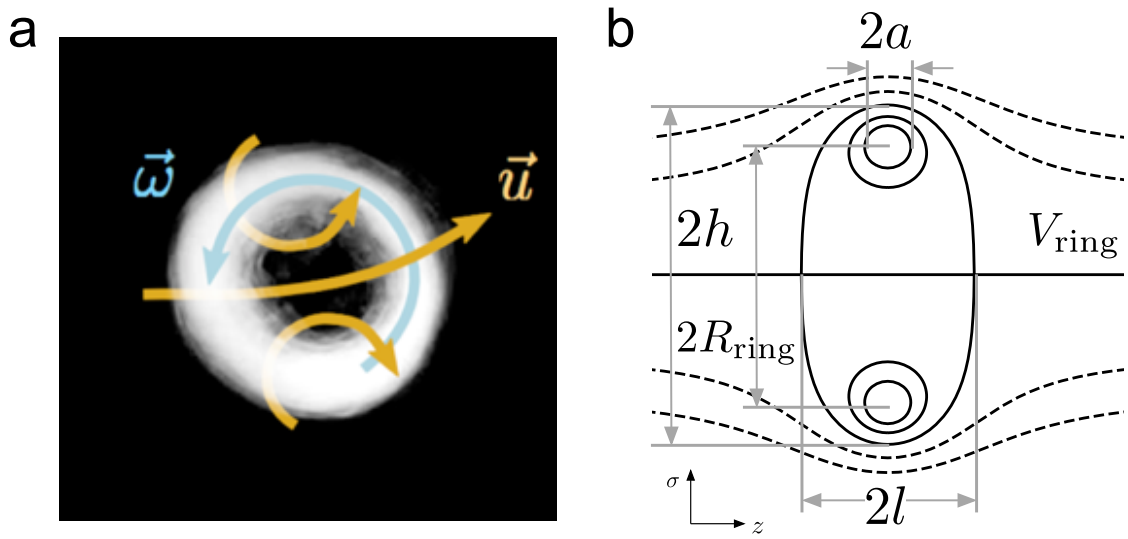

Figure 3.6: (a) A vortex ring (b) Streamline pattern of a vortex ring in the comoving frame

The vortex loops we generate in our experiment all share a similar anatomy to the ring depicted in Figure 3.6. The vorticity is concentrated in a finite region with the topology of a torus and a geometry somewhere between a thin ring and a sphere. The precise distribution of vorticity varies as a function of time under the action of advection and viscous diffusion. At each moment in time the vortex loop propagates under its self-induced velocity field, which can be obtained from the vorticity field by Biot-Savart inversion.

The resulting flow is naturally sub-divided into an advected 'atmosphere' and a surrounding potential flow that is matched to the atmosphere at its surface. The latter is most easily identified by plotting the flow streamlines in the co-moving frame of reference (Figure 3.6b).

While the vorticity distribution provides a complete specification of a vortex loop, much additional insight can be gained by comparing its instantaneous structure to canonical analytic stationary solutions for vortex loops in inviscid fluids, computing their inviscid invariants (Impulse I, Angular Impulse A, Helicity H, Energy E, and circulation Γ (see Box 1),

and rationalizing their values in terms of the 'atmospheric' flow structure.

Several analytical models have been developed for vortex loops [95, 77, 124]. Canonical examples include vortex loops on the thin toroidal ring end of the geometric spectrum and Hill's spherical vortex on the more spherical end. A single-parameter family of solution due to Norbury conveniently interpolates between the two [124]. See Box 2 for a comparison of the corresponding integral invariants.

Box 1: Inviscid invariants

The inviscid invariants are important to characterize a vortex ring besides its velocity field [145, 5]. We may interpret that a vortex ring houses these invariants except energy inside its atmosphere. For what fraction of energy is housed inside the atomopshere, see Box 3.

$$\text{Circulation} : \Gamma = \int_{\Sigma} \omega(z,\sigma) d\sigma dz \tag{3.3}$$

$$\text{Linear Impulse} : \vec{I} = \frac{1}{2}\rho \int_{\Omega} \vec{x} \times \vec{\omega} dV \tag{3.4}$$

$$= \rho \int_{\Omega} \vec{u} dV + \frac{1}{2}\rho \int_{\Sigma} \vec{x} \times (\hat{n} \times \vec{u}) dA \tag{3.5}$$

$$= \pi\rho \int_{\Sigma} \omega \sigma^2 d\sigma dz \text{ (axisymmetric)} \tag{3.6}$$

$$\text{Energy} : K = \frac{1}{2}\rho \int \vec{u} \cdot \vec{u} dV \tag{3.7}$$

$$= \pi\rho \int_{\Sigma} \psi \omega d\sigma dz \text{ (axisymmetric)} \tag{3.8}$$

$$\text{Angular impulse} : \vec{A} = \frac{1}{3}\rho \int_{\Omega} \vec{x} \times (\vec{x} \times \vec{\omega}) dV \tag{3.9}$$

$$= \rho \int_{\Omega} \vec{x} \times \vec{u} dV + \int_{\Sigma} \left[\frac{1}{2} r^2 (\hat{n} \times \vec{u}) - \frac{1}{6} r^2 \vec{x} (\vec{\omega} \cdot \hat{n}) \right] dS \tag{3.10}$$

$$\text{Helicity} : H = \int_{\Omega} \vec{u} \cdot \vec{\omega} dV \tag{3.11}$$

Here Ω and Σ refer to the volume and cross-sectional area of the vortex atmosphere. ψ is a corresponding streamfunction.

While planar (axisymmetric) vortex loops carry non-zero impulse, energy and circulation, non-planar (azimuthally varying) geometries are required to carry, in addition, angular impulse and helicity. Canonical models of nonplanar rings include thin cored helical vortex rings [151] and the generalization of Hill's spherical vortex to include swirl [117, 116] each of which carries finite angular impulse and helicity. Box 2 includes a computation of the inviscid invariants for these canonical flows.

Physical intuition for the values of the inviscid invariants of vortex loops can be readily obtained by examining their co-moving atmosphere. Circulation is given by integrating the velocity along any loop that passes along the axis of symmetry and otherwise is exterior to the vortex atmosphere. It represents the topological charge or 'strength' of the loop. The impulse I (Box 1,2) is given by the product of translational velocity of the atmosphere V_{ring}, multiplied by the sum of the mass enclosed in the atmosphere $m = \rho\Omega_{\text{atmosphere}}$ and the added mass m' of the potential flow past the atmosphere ($m/2$ for a spherical atmosphere): $I = (m + m')V_{\text{ring}}$. The energy E is similarly given by the kinetic energy of the potential flow past the atmosphere $\frac{1}{2}m'V_{\text{ring}}^2$, the kinetic energy associated with the translation of the atmosphere $\frac{1}{2}mV_{\text{ring}}^2$ and an additional contribution from the rotational energy within the atmosphere, which is vortex model dependent, but nonetheless proportional to V_{ring}^2. Similar arguments can be constructed for the angular impulse.

Helicity by contrast, is most intuitively understood in terms of the topology and geometry of the vorticity field. The value of helicity is given by the average circulation weighted linking number between vortex tube pairs [117]. In practice, for thin cored helical rings, the effects of viscosity drive the value towards the $\Gamma^2 Wr$, where Wr is the writhe of the vortex loop center line.

Box 2: Canonical vortex ring models and their properties

Below we summarize the properties of two canonical axisymmetric vortex rings with a finite cross-section: the thin-cored model and Hill's spherical vortex. In general, incompressibility and the axisymmetry reduce the problem of identifying steadily translating solutions to solving a Poisson equation for the stream function $\psi(z,\sigma)$, $\nabla^2\psi = -\omega$. The result is

$$\psi(z,\sigma) = \frac{1}{2\pi}\int_\Sigma \sigma^{\frac{1}{2}}\left[\left(\frac{2}{q}-k\right)K_1(q) - \frac{2}{q}K_2(q)\right]\omega(z',\sigma')dz'd\sigma', \tag{3.12}$$

where $q = \left[4r\sigma/\left((z-z')^2+(\sigma-\sigma')^2\right)\right]$, and Σ is the cross-section of the ring. $K_1(q)$ and $K_2(q)$ are the first and the second kind of the elliptic integrals [95, 5]. The thin-cored model [95] assumes ω = const. inside the core with radius $a \ll R_{\text{ring}}$. The nature of the core such as the medium can be specified by additional coefficients α and β [95, 61, 168, 4]. As for Hill's vortex ring with its speed V_{ring}, it assumes $\omega(z,\sigma) = -15V_{\text{ring}}/(2A_{\text{sph}}^2)\sigma$ within its vortex atmosphere with radius A_{sph}. To make a meaningful comparison with the thin-cored model, we choose $R_{\text{ring}} = \int_\Sigma \omega\sigma dS/\int_\Sigma \omega dS$ as the radius of the vortex instead of A_{sph}[a]. Table 3.1 summarizes the assumptions of the models, and their integral properties.

a. This choice of R_{ring} is arbitrary but the other candidates are sufficiently close to the first moment of vorticity $0.75A_{\text{sph}}$. In the comoving frame, the velocity becomes zero at $1/\sqrt{2}A_{\text{sph}} \approx 0.71A_{\text{sph}}$ away from the center. The square-root of the second moment is equal to $\sqrt{3/5}A_{\text{sph}} \approx 0.77A_{\text{sph}}$.

Box 2 (Cont'd): Canonical vortex ring models and their properties

Table 3.1: **Summary of the canonical vortex models: thin-cored model and Hill's spherical vortex**

Quantity	Thin-cored model	Hill's spherical vortex
$\omega(z,\sigma)$	$\begin{cases} \text{const.}, & \lVert\sigma - R_{\text{ring}}\rVert \le a \\ 0 & \text{otherwise} \end{cases}$	$\begin{cases} 15V_{\text{ring}}/(2A_{\text{sph}}^2)\sigma, & \sigma \le A_{\text{sph}} \\ 0 & \text{otherwise} \end{cases}$
R_{ring}	R_{ring}	$\frac{3}{4}A_{\text{sph}}$
Γ_{ring}	$\pi\omega a^2$	$5A_{\text{sph}}V_{\text{ring}} = \frac{20}{3}R_{\text{ring}}V_{\text{ring}}$
I_{ring}	$\approx \pi\rho\Gamma_{\text{ring}}R_{\text{ring}}^2$	$\frac{2\pi}{5}\rho\Gamma_{\text{ring}}A_{\text{sph}}^2 = \frac{32\pi}{45}\rho\Gamma_{\text{ring}}R_{\text{ring}}^2$
K_{ring}	$\frac{1}{2}\rho\Gamma_{\text{ring}}^2 R_{\text{ring}}\left[\ln\frac{8R_{\text{ring}}}{a} - \alpha\right]$	$\frac{2\pi}{35}\rho\Gamma_{\text{ring}}^2 A_{\text{sph}} = \frac{8\pi}{105}\rho\Gamma_{\text{ring}}^2 R_{\text{ring}}$
$A_{\text{sph}}, H_{\text{ring}}$	0	0
V_{ring}	$\frac{\Gamma_{\text{ring}}}{4\pi R_{\text{ring}}}\left[\ln\frac{8R_{\text{ring}}}{a} - \beta\right]$	$\frac{\Gamma_{\text{ring}}}{5A_{\text{sph}}} = \frac{3}{20}\frac{\Gamma_{\text{ring}}}{R_{\text{ring}}}$

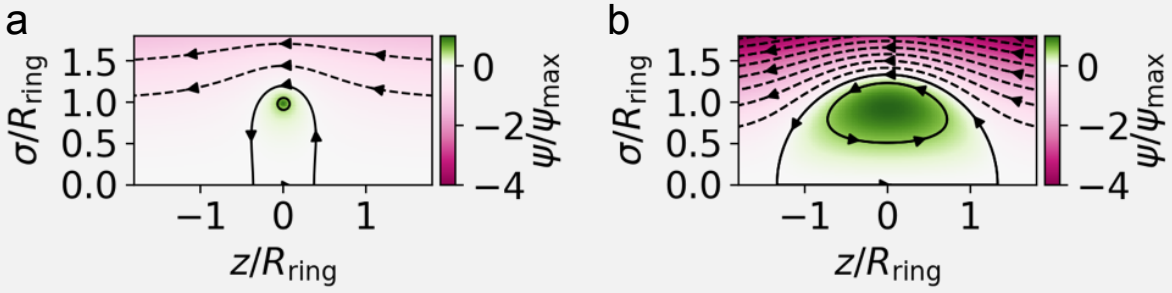

Figure 3.7: **Streamlines of the two canonical models of a vortex ring in the co-moving frame.** (a) Thin-cored model ($R_{\text{ring}}/a = 60$) (b)Hill's spherical vortex. The color indicates the value of a streamfunction, and the isocontours at every $\Delta\psi/\psi_{\max} = 0.5$ are shown. (a) and (b) have the same circulation.

Box 3: Energy distributions from the atmospheric point of view

The energy of a vortex ring may significantly vary depending on the distribution of vorticity within the vortex atmosphere. The atmospheric view provides a simplified view on the inviscid invariants. For example, the impulse of a vortex ring can be readily shown as the sum of the momentum of a fluid within the vortex atmosphere and its added mass in inviscid, incompressible flows [4]: $I_{\text{ring}} = (m + m')V_{\text{ring}}$. How is the energy partitioned from the atmospheric point of view?

As a subject of the study, we consider a family of vortex rings that satisfy $\omega \propto \sigma$. It can be parameterized by $\alpha_{\text{Norbury}} = \Sigma/(\pi R_{\text{ring}}^2)$ where Σ is the cross-sectional area of the ring [124] and $\alpha_{\text{Norbury}} \in (0, \sqrt{2}]$. This family smoothly interpolates from a vortex loop with zero cross-sectional area to Hill's spherical vortex. See their vortex atmospheres in Figure 3.8c.

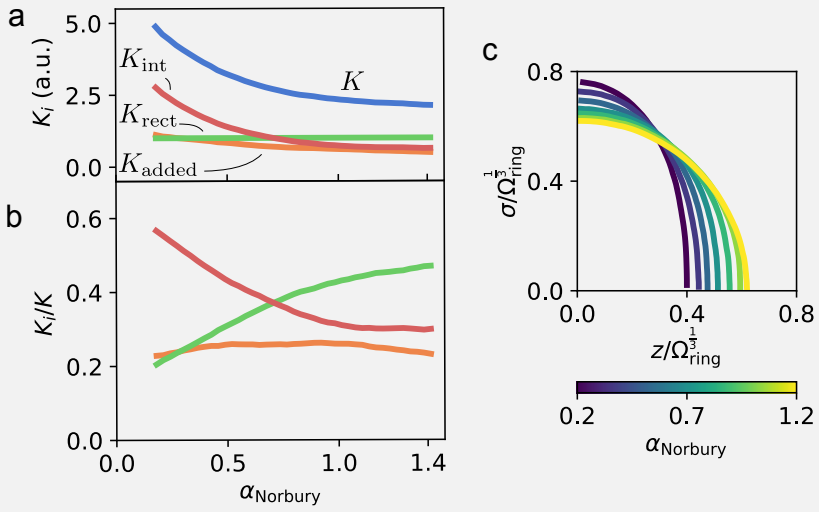

Figure 3.8: **Energy partition of Norbury's vortex rings** ($\omega(\sigma) \propto \sigma$) [124]. (a) Shape of vortex atmosphere with Norbury's shape parameter $\alpha_{\text{Norbury}} \in (0, \sqrt{2}]$. Ω_{ring} is the volume of each vortex ring. (b) Relative contribution of energy outside the vortex atmosphere K_{added}, energy of the rectilinear motion of the fluids inside the vortex atmosphere K_{rect}, and energy of the internal motion K_{int} are plotted against Norbury's shape parameter α_{Norbury}.

Box 3 (Cont'd): Energy distributions from the atmospheric point of view

In general, the energy of a vortex ring can be partitioned as

$$K = \underbrace{K_{\text{added}}}_{\text{Motion outside VA}} + \underbrace{K_{\text{rect}}}_{\text{Rectilinear motion of VA}} + \underbrace{K_{\text{int}}}_{\text{Internal motion inside VA}} \tag{3.13}$$

$$= K_{\text{added}} + K_{\text{ring}}. \tag{3.14}$$

The energy outside the atmosphere is given by $K_{\text{added}} = \frac{1}{2} M_{ij} U_i U_j$ where M_{ij} is the added mass tensor of the fluid with the same boundary as the vortex atmosphere. This is because the flow outside the vortex atmosphere in the co-moving frame is identical to the flow of a rigid body in a stream U_i in the absolute frame. Hence, we conclude that the vortex atmosphere encloses $1 - K_{\text{added}}/K$ of the energy of the entire flow. Inside the atmosphere, the motion consists of the rectilinear motion and the swirling motion. The exact partition among these modes vary, depending on the vorticity distribution as shown in Figure 3.8b. Noticeably, the energy inside the atmosphere remains nearly the same for vortex rings with $\alpha_{\text{Norbuary}} > 0.2$ that resemble the rings generated in our experiments($\alpha_{\text{Norbury}} = 0.8 - 1.0$).
For a spherical vortex, $K_{\text{added}} = \frac{1}{4} M_{\text{sph}} V_{\text{sph}}^2$ and $K_{\text{sph}} = \frac{15}{14} M_{\text{sph}} V_{\text{sph}}^2$ where the mass of the vortex atmosphere is equal to $M_{\text{sph}} = \frac{4}{3} \pi \rho A_{\text{sph}}^3$. We find
$K_{\text{added}} : K_{\text{rect}} : K_{\text{int}} = 7 : 14 : 9$, meaning that $76.\overline{6}\%$ of the entire energy is enclosed inside the vortex atmosphere.

3.6.2 Production of vortex rings

We generate vortex rings by impulsively drawing fluid through an orifice. This is a common approach in both natural settings (e.g. dolphin rings, volcanic eruption vortex rings) as well as laboratory settings where it has been studied extensively [61, 46, 4]. Sketched in Figure 3.9,

the injection of a 'slug' of fluid into otherwise quiescent fluid, is followed by the conversion of this slug into a vortex ring that propagates away from the orifice. This conversion comes about through a subtle combination of inertial and viscous dynamics, including boundary layer separation, vortex sheet roll-up and viscous entrainment [61, 46, 4].

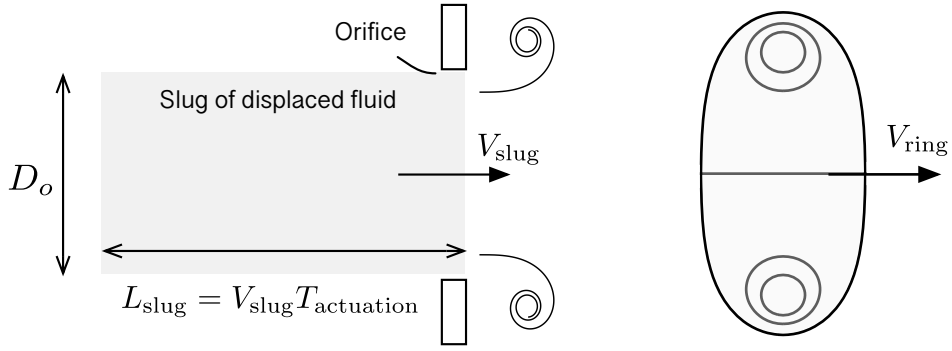

Figure 3.9: **Production of a vortex ring.** A slug of fluid is extruded through an orifice. The boundary layer at the edge of the orifice separates, and rolls up to form a vortex ring.

A natural starting point to characterize the injection process, is to consider a cylinder of fluid with velocity V_{slug}, diameter of an orifice D_o, and length $L_{\text{slug}} = V_{\text{slug}} T_{\text{actuation}}$ where $T_{\text{actuation}}$ is the time during which the fluid is actuated. In addition we have the fluid density ρ, and kinematic viscosity ν. From these we end up with dimensionless parameters:

$$L_* = \frac{V_{\text{slug}} T_{\text{actuation}}}{D_o} \quad , \quad \text{Re}_{\text{slug}} = \frac{V_{\text{slug}} D_o}{\nu}, \tag{3.15}$$

$L_* = L_{\text{slug}}/D_{\text{slug}}$ is known as the 'formation number' of a vortex ring [61, 62, 168] and is known to be a critical parameter that separates regimes in which coherent vortex rings are ejected and a regime in which a ring with a trailing jet is instead produced. Additional parameters such as the opening angle of the orifice and a velocity program factor $P = \langle V_p^2 \rangle / \langle V_p \rangle^2$ that captures the temporal dependence of the fluid injection, can also play a significant role.

In our setup, in which we draw fluid at the top of the setup which in turn draws fluid through N (typically 8) orifices at the corners of our cubic flow chamber, the length of the

cylindrical slugs and their velocity program factor must be derived from the diameter, stroke length and velocity program of the piston at the top of the chamber.

Relationship between L_* and piston control parameters

If divided evenly between the slugs emerging from the N (typically 8) orifices, the volume of fluid drawn by the piston $\pi \left(\frac{D_{\text{piston}}}{2}\right)^2 L_{\text{piston}}$ and its flux give:

$$V_{\text{slug}} = \frac{1}{N}\left(\frac{D_p}{D_o}\right)^2 V_p \quad , \quad L_* \equiv \frac{L}{D} = \frac{1}{N}\left(\frac{D_p}{D_o}\right)^2 \frac{L_p}{D_o}$$

There is however an asymmetry between top and bottom orifices in our tank due to the fact that the piston draws in fluid at the top of the tank. This results in $V_{\text{slug}}^{\text{top}} = V_{\text{slug}}(1-\delta)$ and $V_{\text{slug}}^{\text{bottom}} = V_{\text{slug}}(1+\delta)$, with δ, which can be tuned by a combination of L_* and v, in the range of $\sim$0-0.3 in our experiments.

Impulse of a slug with a velocity program

The injection of a slug of fluid will, in general, occur at velocity $V_{\text{slug}}(t)$ that varies during the slug injection process. This can occur either because of experimental limitations on acceleration, or by design, in an attempt to optimally transfer impulse and energy from the slug to a vortex ring. For example, Glezer [62] showed that different temporal signals with the same $L_* = L/D$ generate vortex rings with different properties.

To account for this time variation, it is useful to consider the impulse I_{slug} that represents the momentum or impulse of an isolated slug of fluid, decoupled from the surrounding fluid[a].

a. In general the injection of a slug into a surrounding fluid will result in an impulse that includes contributions from the pressure at the walls exterior to the orifice as well as the added mass. Nonetheless I_{slug} represents a useful characterization of the injection process.

The integrated momentum flux gives:

$$I_{\text{slug}} = \int_0^T V_{\text{slug}} \left(\rho\pi \left(\frac{D_{\text{slug}}}{2} \right)^2 V_{\text{slug}}(t) \right) \, dt = \rho\pi \left(\frac{D_{\text{slug}}}{2} \right)^2 \langle V_{\text{slug}}^2 \rangle_t T \tag{3.16}$$

$$= \frac{\pi}{4} \rho D_{\text{slug}}^2 L_{\text{slug}} P \langle V_{\text{slug}} \rangle_t = \frac{\pi}{4} N L_* \cdot \rho D_{\text{slug}}^3 v_{\text{eff}}. \tag{3.17}$$

where $P = \langle V_p^2 \rangle_t / \langle V_p \rangle_t^2 \geq 1$ and $v_{\text{eff}} \equiv P \langle V_p \rangle_t$. Figure 3.10 shows some examples of velocity programs and their associated program factor P.

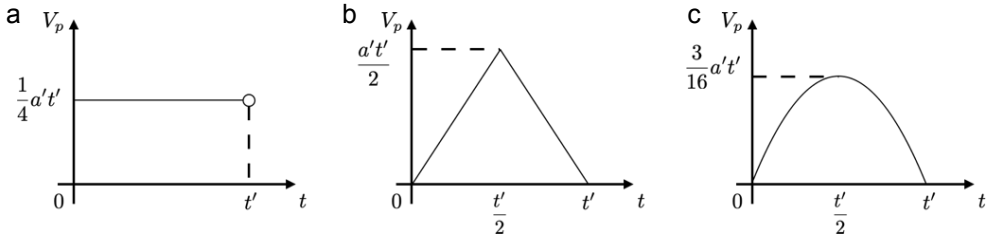

Figure 3.10: **A velocity program factor $P = \langle V_p^2 \rangle / \langle V_p \rangle^2$ characterizes a temporal profile of piston velocity V_p.** a' is equal to $4\langle V_p \rangle / t'$. Here are the values of the velocity program factor of simple signals with the same stroke length. (a) A step function: $P = 1$ (b) A triangular function: $P = 4/3$ (c) A parabolic function: $P = 6/5$.

Accessible slug parameter space

Figure 3.11 illustrates the accessible/useful slug parameter space.

An empirical bound on ring formation (gray shaded areas at low and high $\frac{L}{D}$) is given by $0.5 \lesssim \frac{L}{D} \lesssim 4.0$. On the lower end, no ring formation is observed, on the upper end a jet trails the vortex ring. These empirical bounds are close to those found in [168, 61].

v_{eff} is limited, on the upper end by the maximum acceleration a_{max} that the piston can attain (upper curved boundary). This follows $v_{\text{eff}} \leq \frac{P}{2} (a_{max} D)^{\frac{1}{2}} \left(\frac{L}{D} \right)^{\frac{1}{2}}$.

On the lower end, v_{eff} is limited by the requirement that the stroke time must be less than a forcing period (white, frequency dependent, lines): $v_{\text{eff}} \geq (PfD) \frac{L}{D}$.

To characterize the generated vortex rings under different experimental conditions $(L/D, v_{\text{eff}})$,

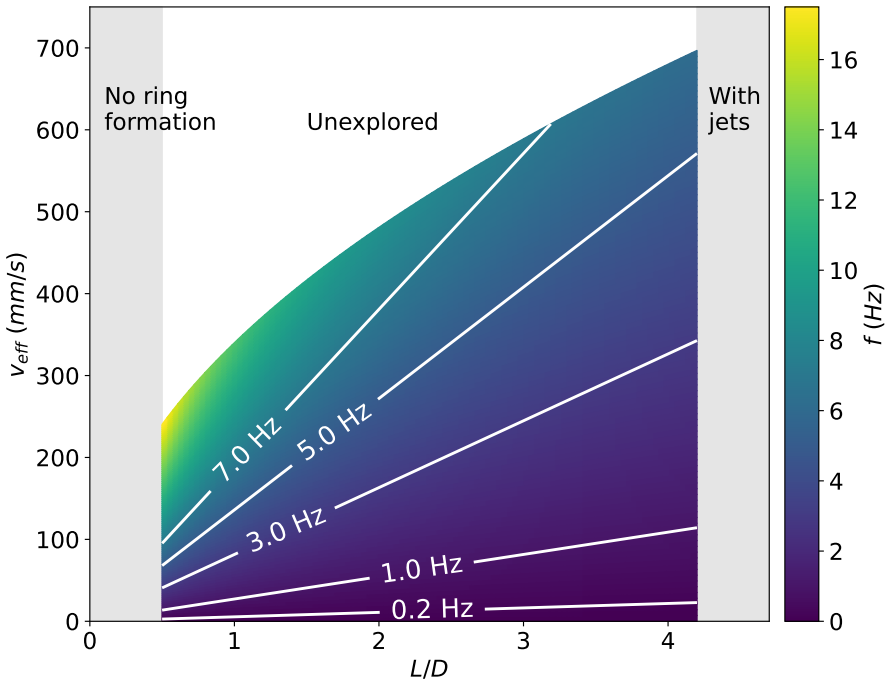

Figure 3.11: **Accessible slug parameter space is spanned by the non-dimensional stroke length and the effective stroke velocity.** The upper bound of the accessible space is set by maximum acceleration of the piston, and the curve for $(a_{max}, D_o, P) = (1.6 \times 10^4 mm/s^2, 25.6mm, 1.0)$ is shown. The lower bound (white lines) depends on the frequency of the oscillatory motion. The heat map represents the maximum frequency that a vortex ring can be generated in our experiment.

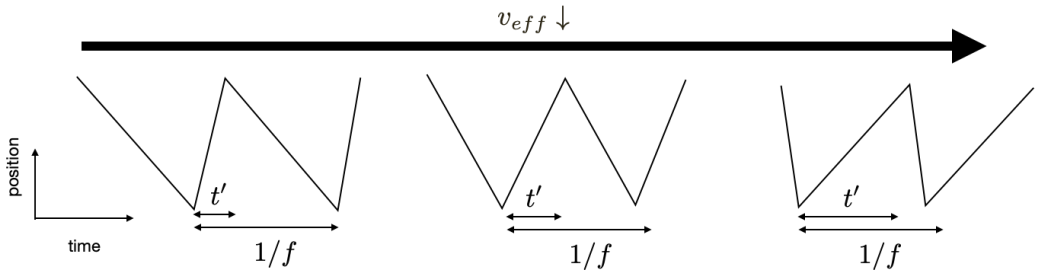

Figure 3.12: **Experimental constraint on the phase space:** The piston must move by a stroke length L faster than the forcing period $1/f$, limiting the accessible phase space: $v_{\text{eff}} \geq (PfD)\frac{L}{D}$.

we use $f = 0.2$Hz or 1Hz. We hereby assume that the same rings are generated at a higher frequency.

3.6.3 Characterization of vortex rings and data collapse

The vortex rings we produce are the fundamental building block of the turbulence we create. We take a three-pronged approach to characterize their properties:

1. We perform PIV measurements in a custom tank with side-windows (CW laser sheet, PIV Lab) to efficiently span the accessible phase space

2. We performed PIV measurements of single vortices created in a custom tank with side-windows by leaving only one orifice open (CW laser sheet, LaVision - DaVis)

3. We performed 3D PTV measurements (Pulsed laser, STB) of the 3D dynamics and structure of individual vortex rings created in the 3D-printed, standard chamber leaving only one orifice open.

Parameter space

To assemble a basic characterization of the sets of vortex rings produced when the we actuate the piston in our tank, we create sets of 8 vortex rings with varying $L_{\text{piston}}/D_{\text{piston}}$ in the box with small windows illustrated in Figure2.1c-d. We illuminate a plane on which half of the vortex rings travel towards the center of the chamber, and track them until they collide. We performed PIV measurements on the emerging vortices using a CW laser and processed the images with PIV Lab (Figure 3.13a). A typical snapshot is shown in Figure 3.13b. Four vortex dipoles can be clearly seen, corresponding to cross sections of four of the eight vortex rings.

The core position at an instant of time is then determined by taking a center of the vorticity field over a region that includes the core. Repeating this process for all the cores

until the vortex rings collide, we extracted their trajectories (Figure 3.13c). The vortex ring radius and the translational speed is measured by tracking the core positions. The circulation of each ring is then computed from the extracted velocity field via $\Gamma = \int_C \vec{u} \cdot d\vec{l}$ (Figure 3.13d). A sample integration contour is used in Figure 3.13c. By dividing the distance between the core positions at distant frames by the time it took, we obtain the instantaneous velocity of each core (Figure 3.13e). We extracted the radius by computing the distance between the instantaneous core locations (Figure 3.13f).

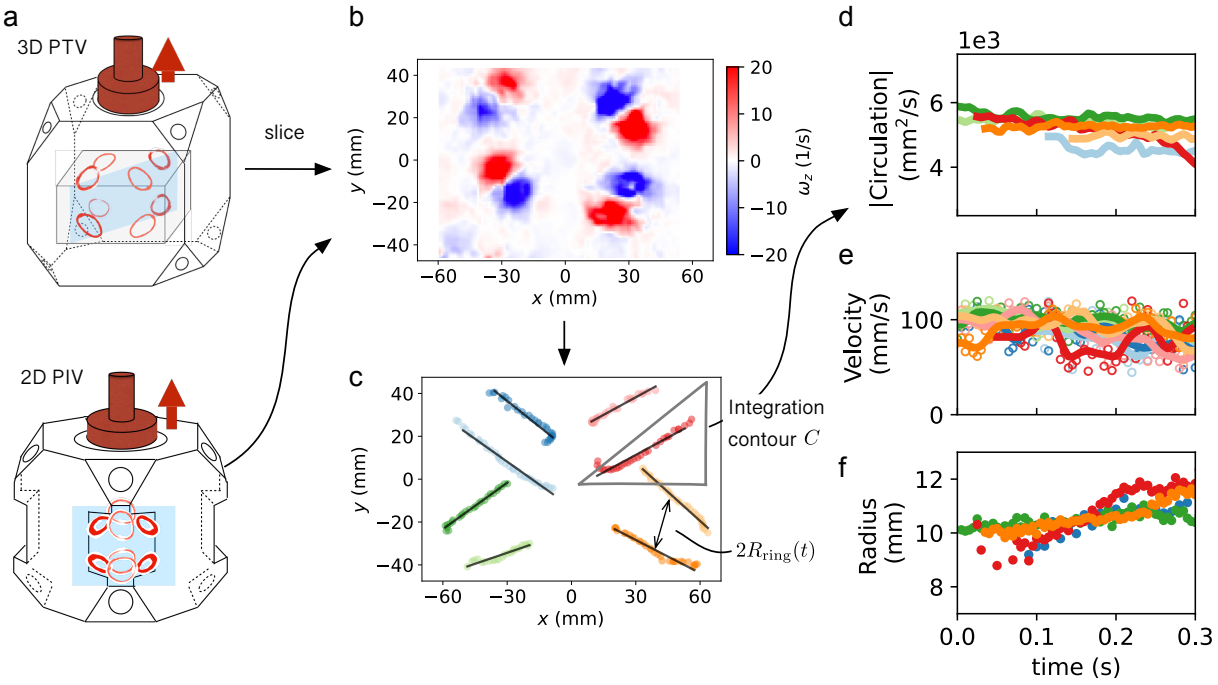

Figure 3.13: **PIV/PTV measurements on vortex ring properties.** (a) We conducted 3D PTV with the standard chamber and 2D PIV with the windowed chamber. For the former, we obtained a flow field on the plane of interest by interpolation. (b) We then compute the vorticity field by $\nabla \times \vec{u}$. (c) Taking a center of voriticity identified each core position at instant of time. (d) By computing $\int_C \vec{u} \cdot d\ell$, we measure circulation. (e-f) We measure the instantaneous velocity and radius based on the extracted trajectories in (c).

Figure 3.14 shows circulation, translational velocity, and diameter of vortices produced from the top (a-c) and bottom (d-f) orifices, and their differences (g-i). Vortex rings are successfully generated when $L/D > 0.5$, and remain isolated structures for $L/D \lesssim 4$. We

observe that rings are accompanied by a trailing jet when $L/D > 4$ as reported by several authors [61].

The asymmetry of forcing can cause the rings from the top orifices to have different properties then the ones emerging from the bottom orifices. We find asymmetries of at most $\sim$17% $\sim$30%, and $\sim$10% in Γ, V, and D respectively. The information in Figure 3.14 enabled choices of actuation parameters that kept asymmetries below $\sim$ 5% for experimental runs presented in the main text. In particular cases, by further detailed characterization, this can be reduced to $\sim$ 0% as in the case of the data presented in Figure 2 of the main text. In the parameter space, this data set corresponds to $(L/D, v_{\text{eff}}) = (2.0, 200\text{mm/s})$.

Non-dimensionalization and relation to literature

To compare our vortex production with the literature on vortex production by slug injection, we extracted non-dimensionalized relationships between R_{ring}, Γ_{ring}, V_{ring} and $L/D(= L_*)$ from [168, 61, 4] and compared them to our measured values.

[4] adopts the following list of variables to characterize vortices produced by an orifice of a tube:

$$R_{\text{ring}}, a, h, l, \Omega_{\text{atmosphere}}, V_{\text{ring}}, \Gamma_{\text{ring}}, \Gamma_c, I_{\text{ring}} \tag{3.18}$$

where R_{ring} is the radius of the vortex ring, a the radius of the vortex core, h, l the lengths of the semi-axes of the vortex atmosphere, V_{ring} the self-induced velocity of the vortex ring, Γ_{ring} the total circulation, Γ_c the circulation around the vortex core, $\Omega_{\text{atmosphere}}$ the volume of the vortex atmosphere and I_{ring} the impulse of the vortex ring. They are non-

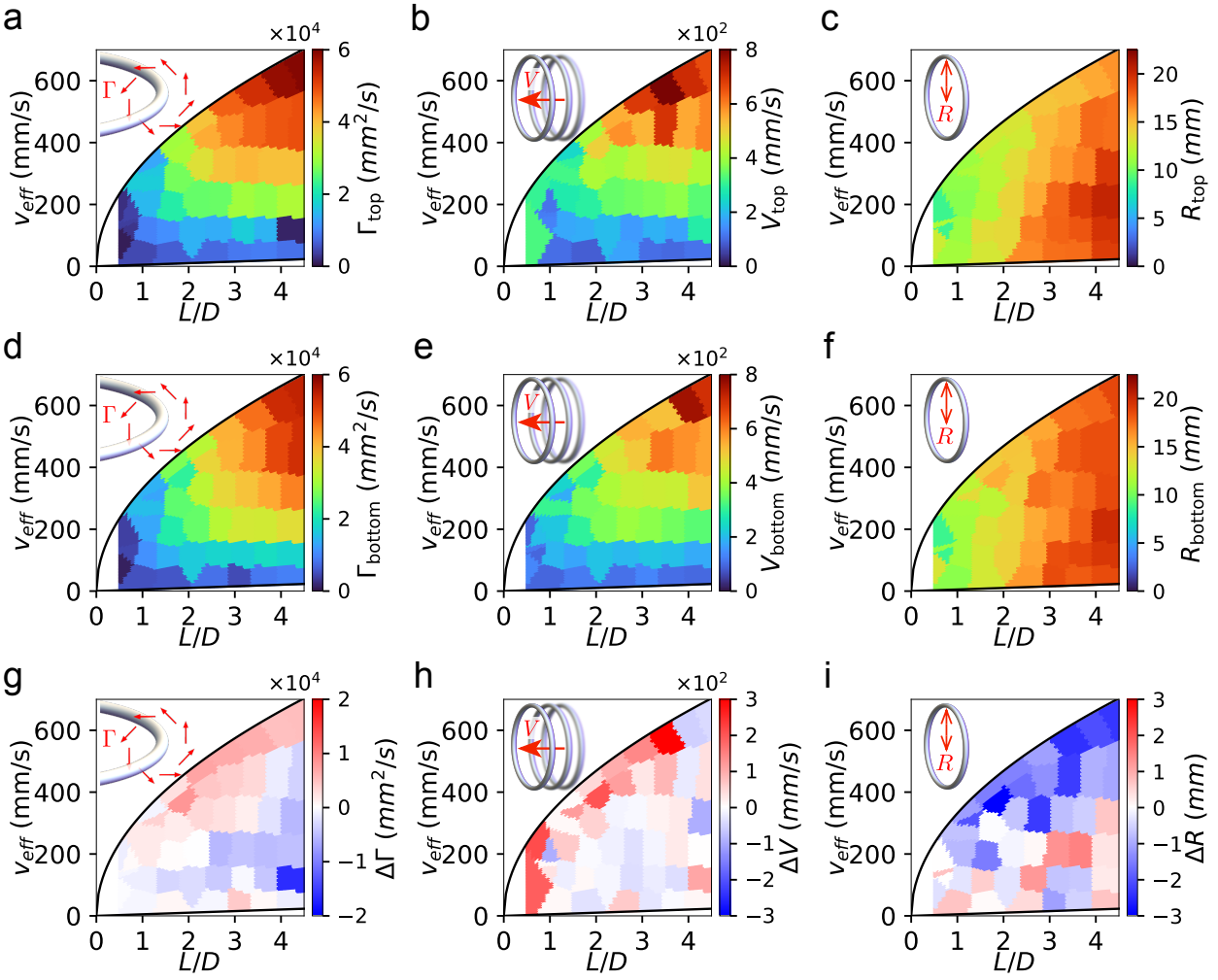

Figure 3.14: **Measured circulation Γ, translational velocity V, and radius R of the generated vortex rings are plotted in the phase space spanned by formation number L/D and effective piston velocity v_{eff}.** (a-c) Γ, V, and R of vortex rings generated at the top orifices are shown. (d-f) Γ, V, and R of vortex rings generated at the bottom orifices are shown. (g-i) Difference of each quantity between the top and the bottom orifices are shown. The solid black lines define the experimentally accessible phase space ($f = 0.2$Hz).

dimensionalized as:

$$R_* = \frac{R_{\text{ring}}}{D_o}, a_* = \frac{a}{D_o}, h_* = \frac{h}{D_o}, l_* = \frac{l}{D_o}, \Omega_* = \frac{\Omega_{\text{ring}}}{D_o^3}, \tag{3.19}$$

$$\Gamma_* = \frac{\Gamma_{\text{ring}}}{D_o V_{\text{slug}}}, \Gamma_{c*} = \frac{\Gamma_c}{D_o V_{\text{slug}}}, V_* = \frac{V_{\text{ring}}}{V_{\text{slug}}}, I_* = \frac{I_{\text{ring}}}{\rho D_o^3 V_{\text{slug}}}. \tag{3.20}$$

Figure 3.15a-c displays the non-dimensionalized radius R_*, velocity V_*, and circulation Γ_* against the formation number L_* along with literature values from [61, 168, 4]. The non-dimensionalization of our data-points assumes zero top-bottom asymmetry and we included our program factor for the slug velocity. Our re-scaled radii, velocities and circulations for both top and bottom sets of vortex rings, are consistent with literature values obtained ejecting individual slugs from tubular vortex ring generators. This supports our experimental strategy of using a single piston to actuate slugs through N orifices.

We note that our agreement with literature values is within the range of agreement between different published experiments. These relatively small variations emerge naturally from differences in the location of the measurement (distance from the orifice), the orifice geometry and actuation program which result in vortices with slightly different atmosphere shape as well as varying levels of entrainment. For example, the vortices studied in Sullivan et al. [168] are more ellipsoidal than [4] and our measurements (an eccentricity of 0.60 compared to our 0.15-0.40) and travel somewhat faster.

In addition to the comparison with literature values, also shown in Figure 3.15a-c are gray lines that represent the scalings predicted by different matching criteria between slug and ring properties. In the case of the vortex radius (Figure 3.15a), matching the mass of the slug and the mass of the vortex atmosphere predicts $R_* \propto L^{1/3}$ In the case of $V_*(L_*)$ and $\Gamma_*(L_*)$ we show three different possible scalings, each of which may be dominant in different ranges of L_*: (i) matching the circulation of a vortex with the circulation of an isolated slug gives ($\Gamma_* \propto L_*$, $V_* \propto L_*^{2/3}$). (ii) matching the impulse of the slug with the impulse of a

thin-cored vortex ring gives ($\Gamma_* \propto L_*^{1/3} V_* \propto \ln L_*$)), $V_* \propto L_*^{2/3}$) (iii) matching the impulse of the slug with the impulse of Hill's spherical vortex model gives ($\Gamma_* \propto L_*^{1/3}, V_* \propto$ const.)

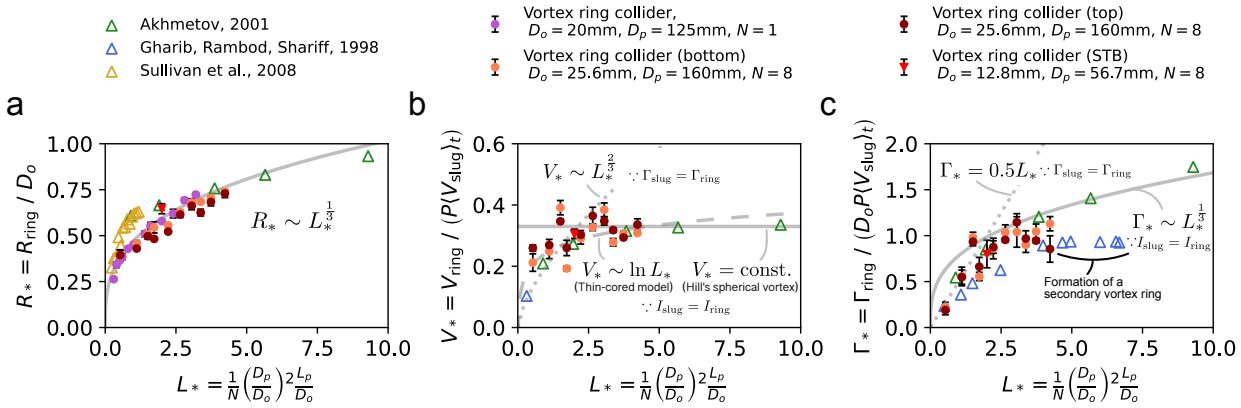

Figure 3.15: **Scaling laws of vortex ring radius R_{ring}, velocity V_{ring}, and circulation Γ_{ring} on the formation number L_*** The values of the vortex rings generated by submerging jets through a nozzle are shown as a reference, and are consistent with the measurements of the vortex ring collider. (a) Non-dimensionalized radius shows $R_* \sim L_*^{1/3}$, reflecting the conservation of mass. (b) Non-dimensionalized velocity of a vortex ring monotoniously increases with L_*, and plateaus out above $L_* = 3$. (c)Non-dimensionalized circulation agrees with the slug model (circulation matching) $\Gamma_* = 0.5 L_*$ below $L_* = 2$ but agrees better with $\Gamma_* \propto L_*^{1/3}$ at high L_*. The error bars in (a-c) represent SEM (n=12 for (a) and n=5 for (b-c)).

Individual vortex ring structure and properties - 2D

As discussed in Box 3 above, an accurate measurement of the vortex energy requires precise knowledge of the vorticity distribution within the vortex atmosphere. To characterize the detailed structure of our vortices, we covered seven out of the eight orifices and performed PIV measurements on single vortex rings as they traversed the experimental chamber.

An instantaneous vorticity field can be obtained by the direct differentiation of the velocity field. Noise in a velocity field becomes amplified by differentiation. Thus we averaged the vorticity field over neighboring frames assuming that the field was steady during the recording. For incompressible, axisymemtric flows, the streamline function can be computed

by $\psi(\sigma, z) = \int_A^B \sigma(u_z d\sigma - u_\sigma dz)$ in cylindrical coordinates. Choosing the reference point A at a different location only shifts the stream function by some constant.

The vorticity distribution of a typical vortex ring generated in the windowed chamber is shown in Figure3.16 (d). It is in good agreement with a a Gaussian distribution, as well as with the empirical formula found by Akhmetov [5] for the traditional vortex ring generator (vortex ring gun):

$$\omega(z_*, \sigma_*) = \frac{\omega_{\max}\sigma_*}{\cosh\left[c_1\left(z_*^2 + (\sigma_* - 1)^2\right)^{\frac{1}{2}}\right]};\ z_* = \frac{z}{R_{\text{ring}}},\ \sigma_* = \frac{\sigma}{R_{\text{ring}}} \tag{3.21}$$

where $c_1 = 11.7$ for a vortex ring gun [5].

When compared to the canonical Lamb-Oseen and Hill vortices, the distribution of vorticity can be clearly seen to be much closer to a diffuse spherical vortex than a concentrated Lamb-Oseen vortex.

For a planar vortex ring, such 2D PIV measurements are sufficient to further compute its inviscid invariants listed in Eq. 3.18. The important quantities are radius R_{ring}, velocity V_{ring}, circulation Γ_{ring}, vorticity distribution $\omega(z, \sigma)$, impulse $\vec{I}_{\text{ring}}$, and energy inside the vortex atmosphere K_{ring}. For example, in the case of a vortex ring in Figure 3.16, we find $|\vec{I}_{\text{ring}}| = 3.7 \times 10^{-3}$kg·m/s compared to $|I_{\text{Kelvin}}| = 5.0 \times 10^{-3}$kg·m/s=1.3$|\vec{I}_{\text{ring}}|$, and $|\vec{I}_{\text{sph}}| = 3.5 \times 10^{-3}$kg·m/s=0.95$|\vec{I}_{\text{ring}}|$. For energy, we find $K_{\text{ring}} = 0.42$mJ compared to $K_{\text{ring,Kelvin}} = 1.0\text{mJ} = 2.4K_{\text{ring}}$ and $K_{\text{ring,sph}} = 0.34\text{mJ} = 0.83K_{\text{ring}}$. Figure 3.17 compares K_{ring} between our measurements and the predictions ($K_{\text{ring,Kelvin}}$ and $K_{\text{ring,sph}}$) for various vortex rings generated by different experimental protocols. For the predicted values, we used the measured radius R_{ring}, circulation Γ_{ring}, and the ratio $K_{\text{ring}}/K = 0.77$ (see Box 3) for the expressions in Box 2. The result shows that Hill's spherical vortex model underestimates the energy by $< 30\%$ and the thin-cored model frequently overestimates the value over 50% in the range of vortex rings we used to create a turbulent state. This intermediate behavior

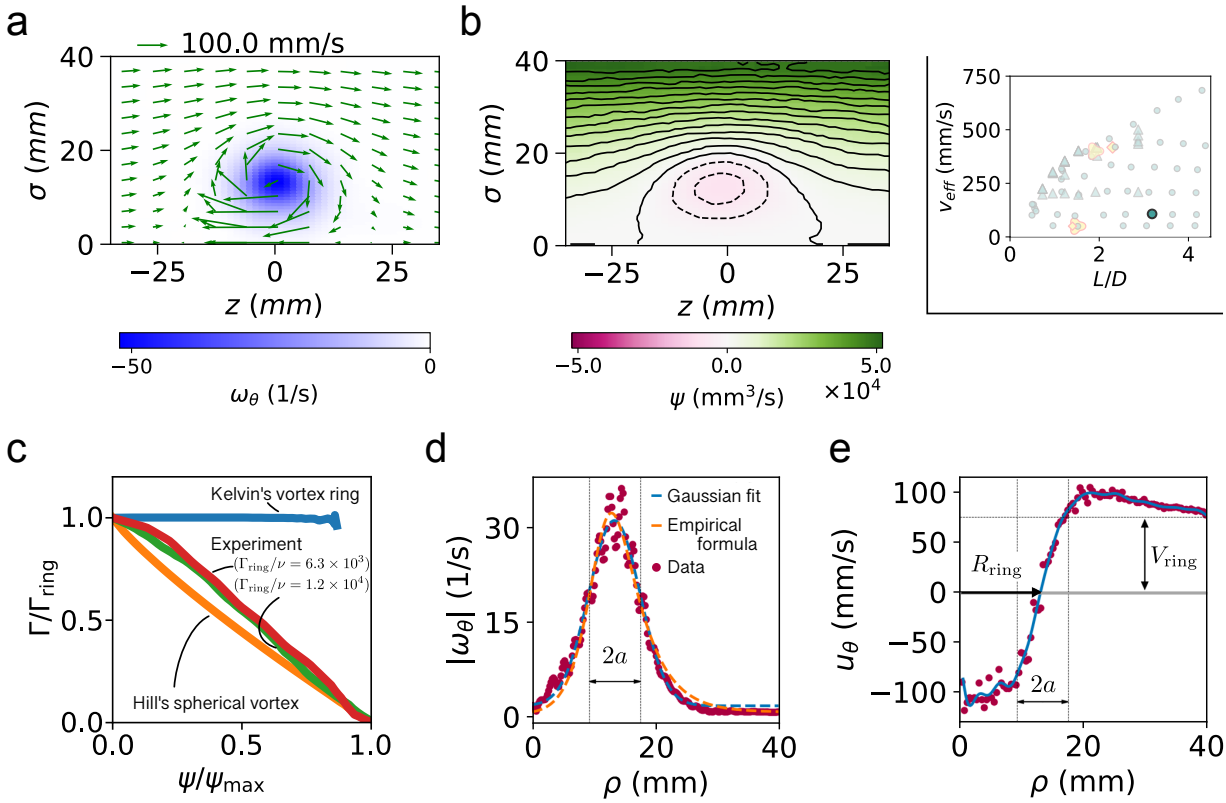

Figure 3.16: **Characterization of a vortex ring in the experiments reveals its similarity to Hill's spherical vortex.**(a) A velocity and vorticity field of a typical vortex ring in the comoving frame, obtained by PIV (b) Streamfunction and isocontours ($\Delta\psi = 5 \times 10^3 \text{mm}^3/\text{s}$) (c) Normalized circulation along the closed streamlines in the vortex atmosphere is plotted against the normalized streamfunction. (d) Voticity distribution at z=0 (e) Axial velocity profile in the plane z=0. The top right plot indicates the location of the measurement in the phase space.

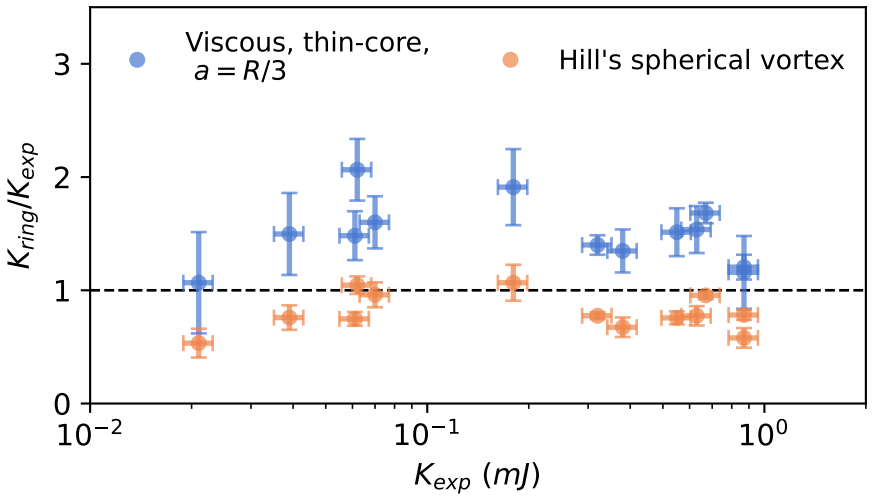

Figure 3.17: **Kinetic energy enclosed in the vortex atmosphere is consistent with the formula of Hill's spherical vortex.** The kinetic energies inside vortex atmosphere, predicted by the thin-cored and Hill's spherical vortex models(Box 3.6.1) with measured radius and circulation, quantitatively agree with the measurements by 2D PIV. We compute $K_{\text{ring}} = cK(\Gamma_{\text{ring}}, R_{\text{ring}})$ with $R_{\text{ring}}/a = 3, \alpha = 2.04$ for the thin-cored model and $A_{\text{sph}} = 4/3R_{\text{ring}}$ for Hill's spherical vortex model (see Box 2). For both models, $c = K_{\text{ring}}/K = 0.77$ is used. The error bars represent SEM (n=12).

is consistent with our measurement on the vorticity distribution in Figure 3.16c.

Three dimensional structure and properties of circular and helical vortex rings

Axisymmetric vortex rings carry energy, linear impulse, and circulation. For a vortex loop to also carry angular impulse and helicity, a departure from axisymmetry and mirror symmetry is required. A particularly simple vortex geometry that breaks both these symmetries is that of vortex loops with helical cores. Readily tunable by tuning the pitch and amplitude of the helical core, helical vortices provide an ideal vehicle for transmitting all of the inviscid invariants.

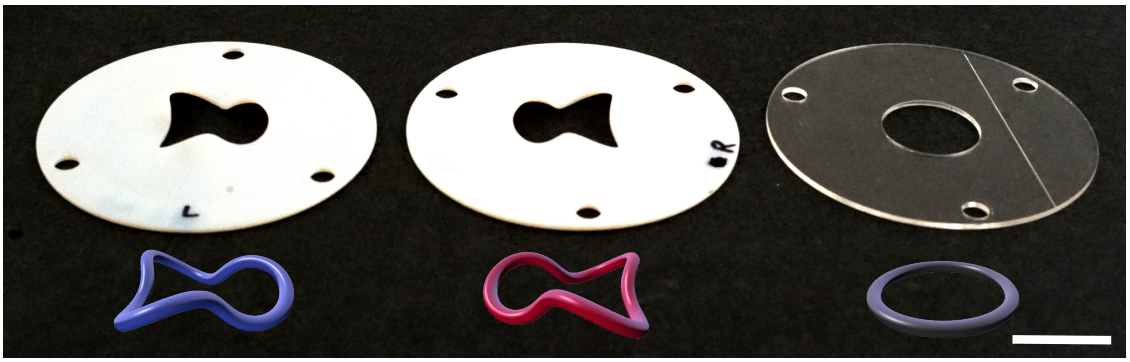

Figure 3.18: **Helical masks generate vortex rings with nonzero helicity.** (Left) A left-handed mask (Middle) A right-handed mask (Right) A planar mask as a reference. The cartoons illustrate the height profiles of the orifices. Scale bar: 25.6mm.

To create helical vortex loops in our setup, we designed and 3D-printed nozzles whose boundary is helical, as shown in Figure 3.18 and replaced the circular orifices of our tank with these. The helical apertures were designed to have the same mean radius as the planar circular apertures they replaced, and the same stroke length and velocity profile ($L/D = 1.5, v_{\text{eff}} = 50\text{mm/s}$) was used for the impulsive actuation. We found that helical vortex rings were readily produced at the orifices.

To study the properties of the vortex rings produced through these nozzles, which to the best of our knowledge is a novel approach, we then blocked seven out of the eight orifices in our setup and generated individual helical vortices. We then measured the resulting flow using 3D PTV (LaVision, Shake-the-box) in the central region of the tank as illustrated in

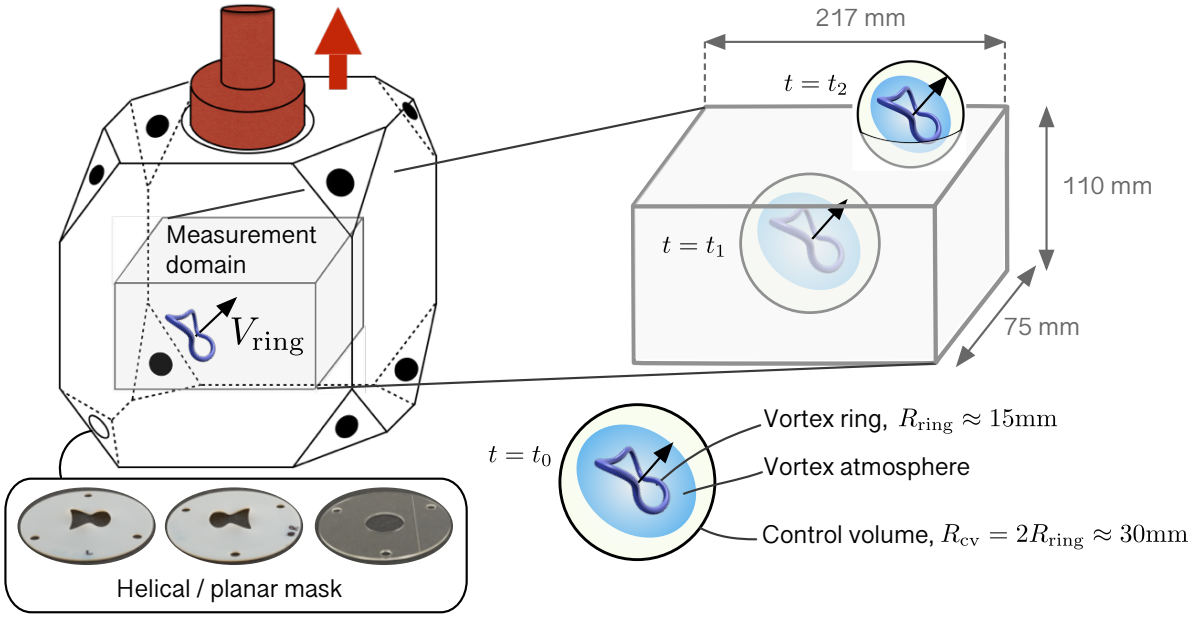

Figure 3.19: **The experimental setup and computational scheme to measure the inviscid invariants carried by a planar/vortex ring are shown.** A planar or helical vortex is generated in the chamber by lifting the piston with one orifice open while the remaining is closed. The inviscid invariants in Box 3.6.1 are computed over a moving control volume that encloses vortex atmosphere. Any contribution to the integral from the region outside the measurement domain is considered zero.

Figure 3.19.

We performed three sets of experiments: the first in which we produced circular vortex rings, and the second and third in which we produced left and right handed helices. The handedness is determined by the respective orientation of the angular impulse to the linear impulse: it is right-handed if they point in the same direction, and is left-handed if they point to the opposite directions.

Figure 3.20 shows a typical measured vorticity field on three cross-sections (the field is median filtered with a kernel size of 3×3 px^2). Despite the limited spatial resolution, the measurement captures the essential features of the vortex structure within the vortex atmosphere. Given these 3D velocity and 3D vorticity fields, all inviscid invariants are accessible by direct numerical computation. Figure 3.20(b) shows, for example, the helicity density $\vec{u} \cdot \vec{\omega}$ on the same cross-sections.

To extract the total value of each inviscid invariant (listed in 3.6.1) from our volumetric flow data, we track the position of the vortices by computing the center of mass of the energy. We then define a control volume that co-moves with the vortex and has a radius approximately twice the ring radius. Finally, we compute the inviscid invariants (listed in 3.6.1) within the control volume. Figure 3.21 summarizes this computation scheme and the results are shown in the right column of Figure 3.21.

The restriction of the computation to the control volume is adopted to eliminate contributions of spurious vorticity outside the vortex bubble. These fluctuations can significantly skew the values of the invariants because they contribute in proportion to their distance. For example, consider the linear impulse $\vec{I} = 1/2 \cdot \rho \int_{\mathcal{V}} \vec{x} \times \vec{\omega} dV$. Given the sparse and uneven distribution of spurious vorticity fluctuations, their effect does not average to zero even if the integral is performed over the entire measurement domain in our experiment. We note that the chosen radius of the control volume ($\approx 2R_{\text{ring}}$) encloses the vortex bubble in its entirety and was verified to coincide with the local convergence of the computed values of

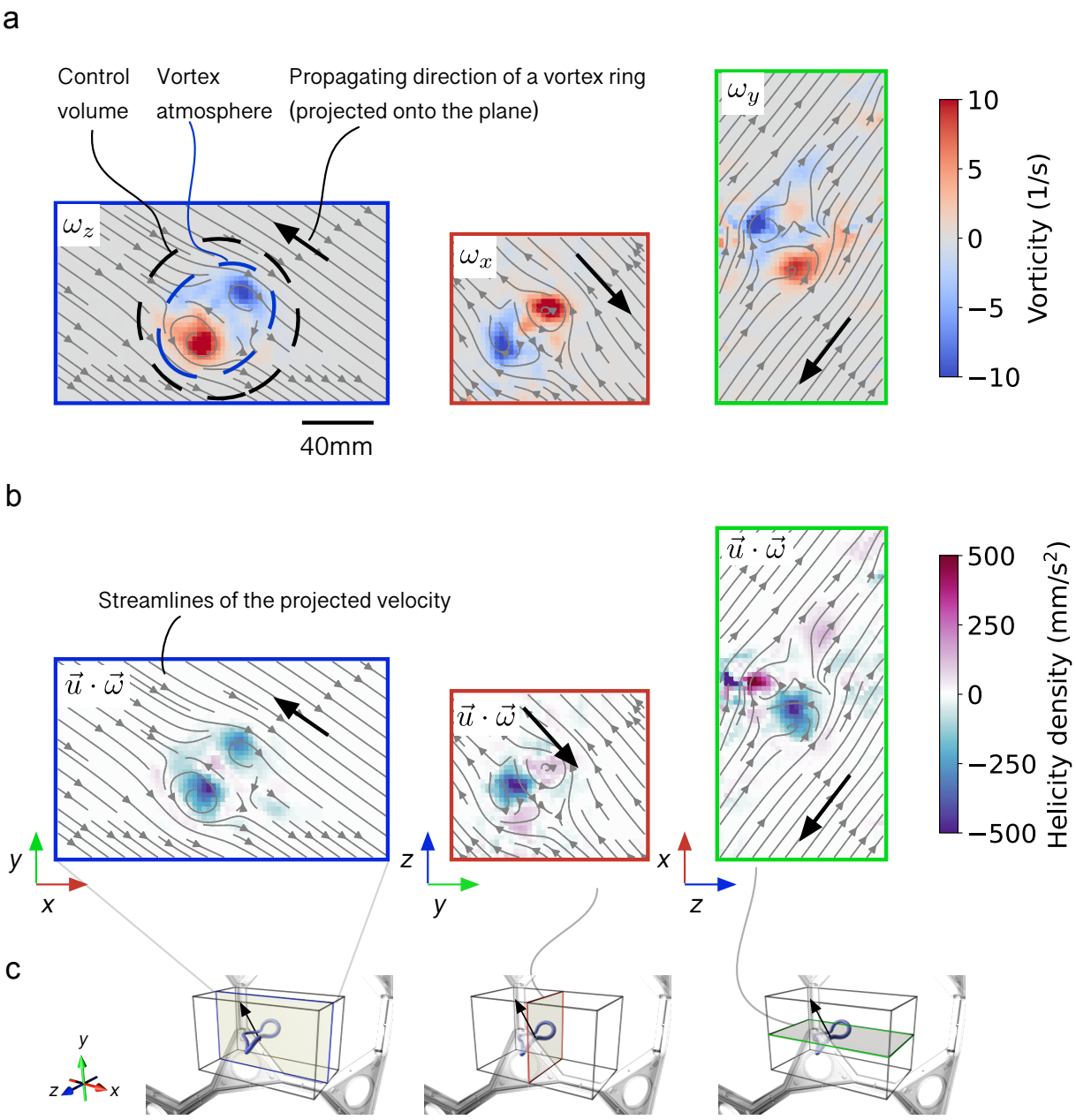

Figure 3.20: **Extracted 3D velocity and vorticity fields are used to compute inviscid invariants such as helicity.** (a) A (left-handed) helical vortex ring propagates in the measurement domain. The color maps represent the one-component vorticity (ω_z, ω_x, and ω_y) fields on the three cross-sections in the measurement domain. Streamlines of the projected velocity field in the co-moving frame reveal the vortex atmosphere. (b) Helicity density $\vec{u}\cdot\vec{\omega}$ illustrates the negative helicity concentrated along the vortex tubes. Integrating this field over the co-moving control volume yields the helicity of the helcial vortex ring. (c) The orientations of the three cross-sections with respect to the measured domain are shown.

the inviscid invariants.

In addition to the inviscid invariants listed in Box 3.6.1, we also present linear momentum $\vec{P} = \rho \int_{\mathcal{V}} \vec{u} dV$ and angular momentum $\vec{L} = \rho \int_{\mathcal{V}} \vec{x} \times \vec{u} dV$ (where $\mathcal{V}$ denotes the co-moving control volume) as a supplement. Note that linear momentum is not a well-defined quantity in this context because the surface integral in Eq. 3.5 depends on the shape of the surface. Similarly, the angular momentum is not well-defined because it is generally a divergent integral in unbounded flow. The difference between these momenta and the corresponding impulses are the surface terms in Eq. 3.5 and 3.10. These are not obvious a priori, and depend on the shape of the surface.

The inviscid vortex solution known as 'Hill's spherical vortex with swirl' [117] provides a basis for comparison with vortex models. This flow is a solution of the incompressible Navier-Stokes equation with nonzero angular momentum and helicity due to the swirling motion inside the vortex atmosphere.

The velocity field is given by

$$\vec{u} = (u_r, u_\theta, u_\phi) = \left(\frac{1}{r^2 \sin\theta} \partial_\theta \psi, -\frac{1}{r \sin\theta} \partial_r \psi, \frac{k\Xi}{r \sin\theta} \right)$$

where the (Stokes) stream function ψ is identical to Hill's spherical vortex

$$\psi = \begin{cases} -\frac{3}{4} V_{\text{ring}} r^2 \left(1 - \frac{r^2}{A_{\text{sph}}^2} \right) \sin^2\theta, & r \le A_{\text{sph}} \\ \frac{1}{2} V_{\text{ring}} r^2 \left(1 - \frac{A_{\text{sph}}^3}{r^3} \right) \sin^2\theta, & r > A_{\text{sph}} \end{cases}$$

and

$$\Xi = \begin{cases} -\frac{3}{2} V_{\text{ring}} \frac{J_{3/2}(kA_{\text{sph}})}{J_{5/2}(kA_{\text{sph}})} \left[\left(\frac{A_{\text{sph}}}{r} \right)^{\frac{3}{2}} \frac{J_{5/2}(kA_{\text{sph}})}{J_{3/2}(kA_{\text{sph}})} - 1 \right] r^2 \sin^2\theta, & r \le A_{\text{sph}} \\ \frac{1}{2} V_{\text{ring}} \left(1 - \frac{A_{\text{sph}}^3}{r^3} \right) r^2 \sin^2\theta, & r > A_{\text{sph}} \end{cases}$$

encodes for the azimuthal motion with a real parameter k. Here, $J_{3/2}$ and $J_{5/2}$ are the

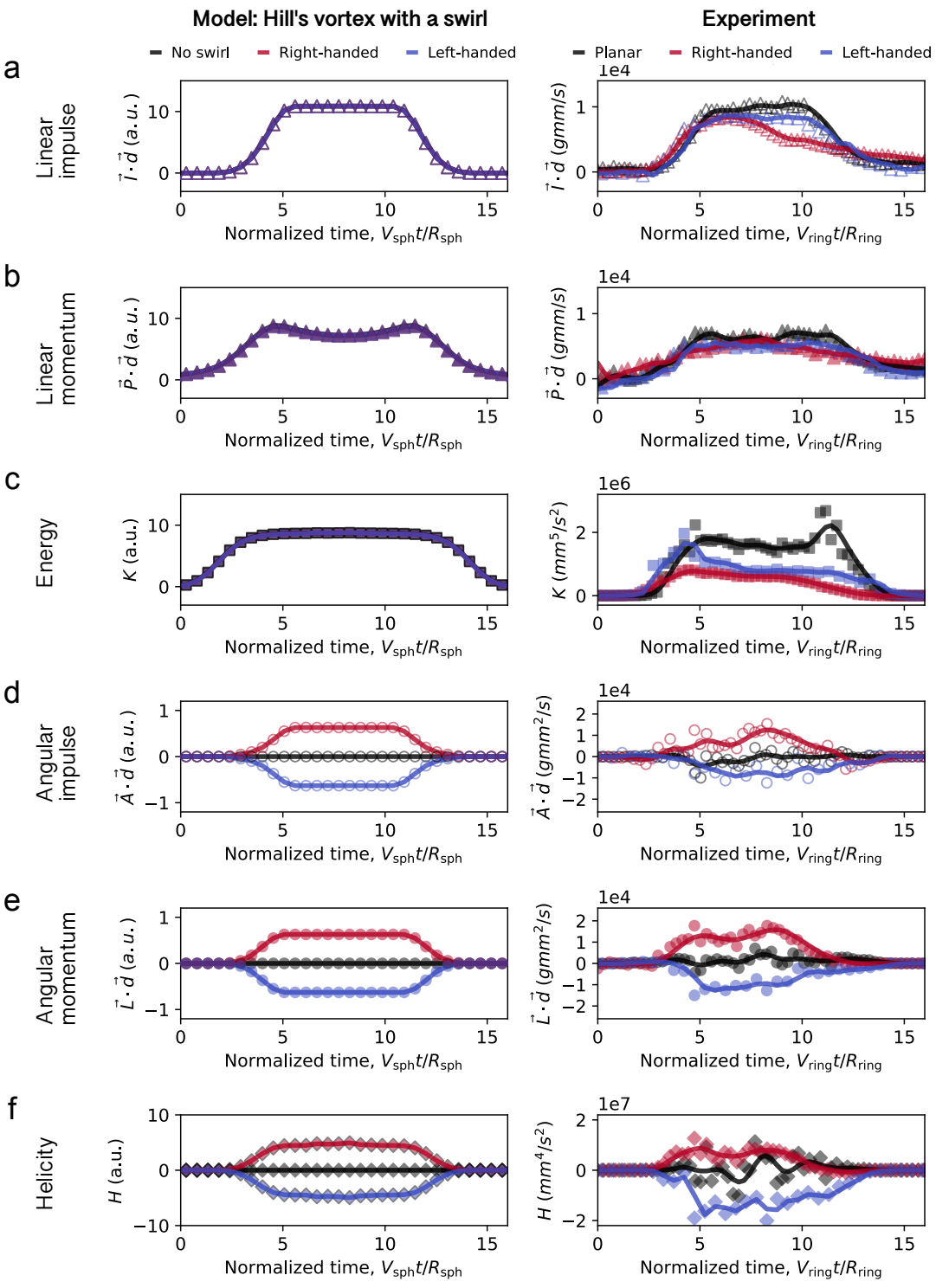

Figure 3.21: **Measured inviscid invariants of a planar, and helical vortex rings qualitatively agree with simulations. (Left column: Hill's spherical vortex ring with a swirl. Right column: Experiment).** $\vec{d}$ is a unit vector that denotes the traveling direction of a vortex. (a) Linear impulse (b) Linear momentum (c) Energy (d) Angular impulse (e) Angular momentum (f) Helicity.

Bessel function of the first kind.

The left column of Figure 3.19 shows the result of computing what we would have measured if such a vortex had swept through our measurement volume, i.e.

1. We define a synthetic measurement box with the same aspect ratio of the experimental measurement domain.

2. Synthetically place Hill's vortex with (or without) a swirl ($k = \pm 1$, or 0) at a sequence of locations as if it were propagating at V_{sph} along a simlar trajectory to the experimentally measured vortex.

3. Compute the inviscid invariants as we did for the experimental data.

Comparison of the experimental data to Hill's spherical vortex with a swirl intends to contextualize how inviscid invariants would be measured in practice, and does not provide one-to-one comparison between the experimental data and a simulation using a vortex ring with the same helical profile.

As can be seen in Figure 3.21, the experimental results compare well with the resulting trends, albeit with considerable scatter and some systematic deviations. Despite being limited by spatial resolution, our results provide a direct experimental quantification of all the inviscid invariants carried by a helical vortex ring for the first time. The non-zero angular impulse and helicity clearly demonstrate the effectiveness of our helical masks in producing vortex rings that carry helicity and angular impulse. The helical vortex loop as an isolated carrier of inviscid invariants provides a unique opportunity to control and shape turbulence with desired cocktails of inviscid invariants. In section 3.14.2 we present the result of this injection.

Estimation of the effect of coarse-graining on the measurement of helicity in isolated helical vortex rings

In Figure 5 of the main text and in and 3.21, we presented the direct measurement of helicity $\mathcal{H} = \int_{\mathcal{V}} \vec{u} \cdot \vec{\omega} dV$ over a domain that encloses a turbulent blob and a helical vortex ring. In both cases, the velocity and vorticity fields were not completely resolved, likely affecting the value of the measured helicity. In this section, we study how coarse-graining a velocity field affects the resulting helicity. We consider two test cases: models for helicity-carrying isolated vortices and DNS data for helical turbulence.

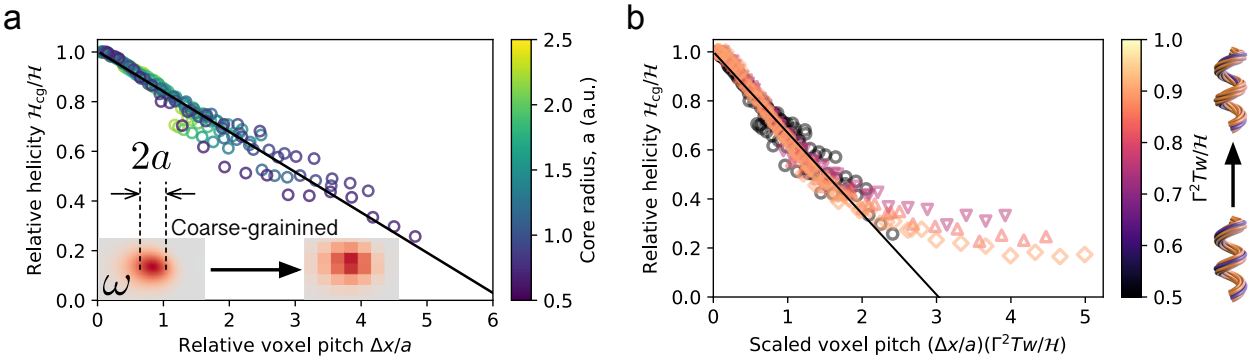

Figure 3.22: **Coarse-graining a velocity field attenuates helicity.** (a) Scaled helicity with a coarse-grained field collapses to a line. (d) Data collapse of the relative helicity when plotted against the voxel pitch scaled with a twist-to-helicity ratio and a core radius.

We generate analytical expressions for flow fields of a helical vortex tube whose vorticity field lines are organized around its center line. The implemented methodology has been developed by Hridesh Kedia, and the detailed description can be found in [151] SI, Eq.43-44. This construction enables us to tune the writhe of the center-line, the twisting of the field-lines, and the core size independently. The vorticity distribution inside the core is approximately Gaussian. The construction is based on a complex scalar potential $\psi = z_1^m / Q(z_1, z_1^*, z_2, z_2^*)$ where (z_1, z_2) are coordinates on S^3. m controls the number of windings

of the field-lines, and $Q(z_1, z_1^*, z_2, z_2^*)$ encodes the center-line. The velocity field is given by:

$$\vec{u} = \frac{a'^2}{4\pi}\left(\exp\left(-\frac{1-\chi'^2}{a'^2\chi'}\right)\nabla\eta' + \frac{1}{2i}\nabla\log\left(\frac{Q(z_1, z_1^*, z_2, z_2^*)}{Q^*(z_1, z_1^*, z_2, z_2^*)}\right)\right) \tag{3.22}$$

where $\eta' = \log(\psi/\psi^*)/(2\pi) \in [0, 2\pi)$, and a' is a clipping length scale. To mimic the three-fold helical vortex generated in the experiment, we used

$$\begin{aligned} Q(z_1, z_1^*, z_2, z_2^*) &= \frac{R_{\text{minor}}}{R_{\text{major}}} z_1^3 + z_2; \\ z_1 &= \frac{2R_{\text{major}}(x+iy)}{(R_{\text{major}}^2 + x^2 + y^2 + z^2)} \\ z_2 &= \frac{2R_{\text{major}}z + i(x^2+y^2+z^2-R_{\text{major}}^2)}{(R_{\text{major}}^2 + x^2 + y^2 + z^2)} \end{aligned}$$

where R_{major}, and R_{minor} represent the major and minor radius of the helical ring respectively. $R_{\text{major}}/R_{\text{minor}} = 4$ was chosen to be consistent with the center line of the experimental helical ring.

To mimic a flow field that is obtained by 3D PTV, we coarse-grained a spatially resolved flow field, then computed the helicity. The coarse-graining procedure is a combination of convolution with a box kernel, followed by undersampling (See insets in Figure 3.22a[b]). Coarse-graining a velocity field indeed attenuates the measured helicity as shown in Figure 3.22a for helical rings with various core size set by $\chi' \in [0.9, 0.99]$. These curves collapse onto a line when plotted against the voxel size scaled by each core size (Figure 3.22a).

We find that coarse-graining generally reduces the computed value of helicity. The reduction is greater for a helical vortex ring with a higher amount of twist within the core[c] $Tw = (\mathcal{H}/\Gamma^2 - Wr)$ where Wr is the writhe of the center-line. Unlike the writhe, twisting is

b. We coarse-grained a *velocity* field even though the inset figures show an example using a vorticity field. To compute the helicity in Figure 3.22, a vorticity was derived from the coarse-grained velocity field.

c. A more twisted helical vortex ring was generated by increasing $m \in [1, 5]$.

local winding of the vorticity field-lines; hence, it is more susceptible to the coarse-graining. We find a data collapse as we scaled the voxel pitch Δx to $(\Delta x/a)(\Gamma^2 Tw/\mathcal{H})$ (Figure 3.22b). In reality, helicity tends to writhe [151], and a case with a low twist-to-helicity ratio is more common in nature. Under moderate coarse-graining when a segment of a vortex core is represented by more than 2^3=8 voxels, the attenuation of helicity is linear in $\Delta x/a$. An equivalent amount of attenuation for data in both Figure 5 of the main text and Figure 3.21, would be approximately 10% since $(\Delta x/a)(\Gamma^2 Tw/\mathcal{H})$ is estimated to be less than $(\Delta x/a) \approx 0.3$.

Summary of experimental runs

Figure 3.23 shows the measurements performed to characterize a single vortex ring, and a helical ring.

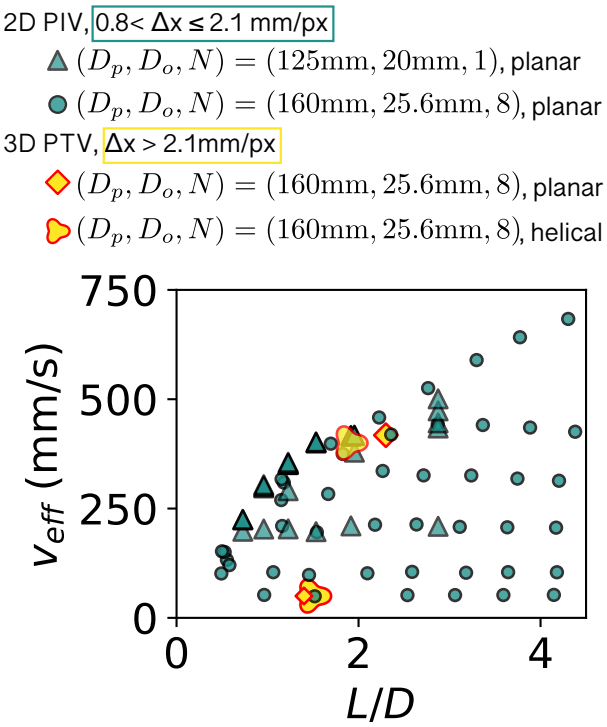

Figure 3.23: **Summary of measurements performed to characterized vortex rings in the parameter space spanned by effective piston velocity v_{eff} and formation number L/D.**

3.7 Vortex ring collisions - Summary of experimental runs

As described in the main text, firing together sets of eight vortices in our setup at repeated intervals, results, at sufficiently high frequencies, in the formation of an isolated blob of turbulence, surrounded by quiescent fluid.

To characterize the physics of the turbulent blob state, we performed a number of experiments in which we fired sets of vortex rings together while varying ring speeds, radii and the interval between sets. We then measured the ensuing dynamics using 2D PIV at different magnifications, as well as 3D PTV. Figure 3.24 summarizes the experimental runs. A version of this figure, with specific points highlighted is reproduced as an inset in SI figures to make it clear which datasets went into making each derived plot.

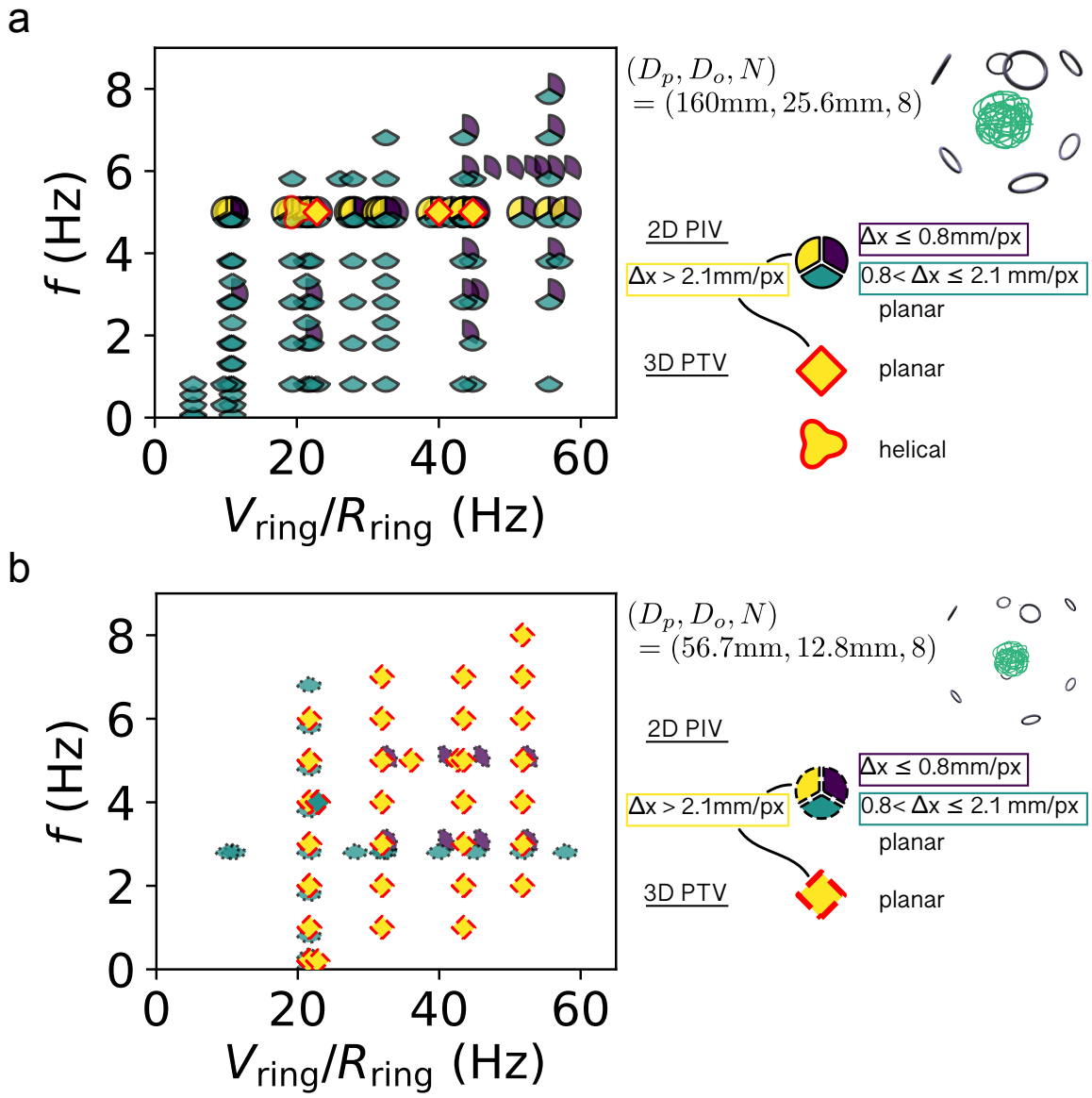

Figure 3.24: **Summary of measurements to study confined turbulence involving different techniques (2D PIV and 3D PTV) on various experimental configurations.** Altering the size of the piston diameter D_p and the orifice diameter D_o enables to vary the size of a turbulent region formed by the vortex ring collisions. Numerous PIV measurements with different resolutions allow us to investigate turbulent statistics thoroughly. (a/b) This setting enables to create a turbulent region with $R_{\text{blob}} \approx 60/30$mm. We investigate the transfer of mass, energy, and enstrophy using a small blob because it can be fully contained in the measurement volume.

3.8 Anatomy of a turbulent blob

In this section we examine the structure of a turbulent blob via Reynolds decomposition $U_i(\vec{x},t) = \langle U_i \rangle_t(\vec{x}) + u_i(\vec{x},t)$.

3.8.1 Structure of the mean flow

The (temporally averaged) mean flow reveals the strong inflow at the spots where the vortex rings arrive, and nearly uniform outflow elsewhere (Figure 3.25e-f). Such a mean flow acts to cage the injected energy and enstrophy inside the turbulent core with small ejection. This corroborates with a simple picture that energy and enstrophy are supplied by vortex rings, getting dissipated mostly inside the blob, and a small fraction of them leaves.

Inspecting two planes would be sufficient to explain the mean flow of our experiments because of the octahedral symmetry in the vorticity field. The corresponding point group is O_h in the Schönflies notation, and has two kinds of reflection operations σ_v, and σ_h. σ_v corresponds to a reflection about the plane that cuts four out of eight rings into halves (Figure 3.25a). σ_h corresponds to a reflection about the plane on which no rings are present (Figure 3.25b). There are six σ_h and three σ_v in O_h as illustrated in Figure 3.25a-b. Figure 3.25c-d show the measured, mean flow field on each plane. The σ_v plane exhibits the strong inflow in the diagonal directions due to the vortex rings, accompanied by outflow in the $\pm x'$ and $\pm y'$ directions. Meanwhile, the σ_h plane contains a source at the center.

In a simplified case, one can infer the strength of the outflow solely by the symmetry. The 6+3=9 reflection planes uniformly split the space. On the σ_v plane, there are four incoming directions (diagonal) and four outgoing directions (horizontal and vertical) (Figure 3.25g). The σ_h plane is divergent (Figure 3.25h). Because of incompresibility, the sum of the incoming and outgoing flows must be zero. There are $4 \times 6 = 24$ directions of the inflow and $4 \times 6 + 8 \times 3 = 48$ directions of the outflow. If one assumes the strength of the outflow on both planes to be the same, we expect that the outflow speed is a half of the inflow speed.

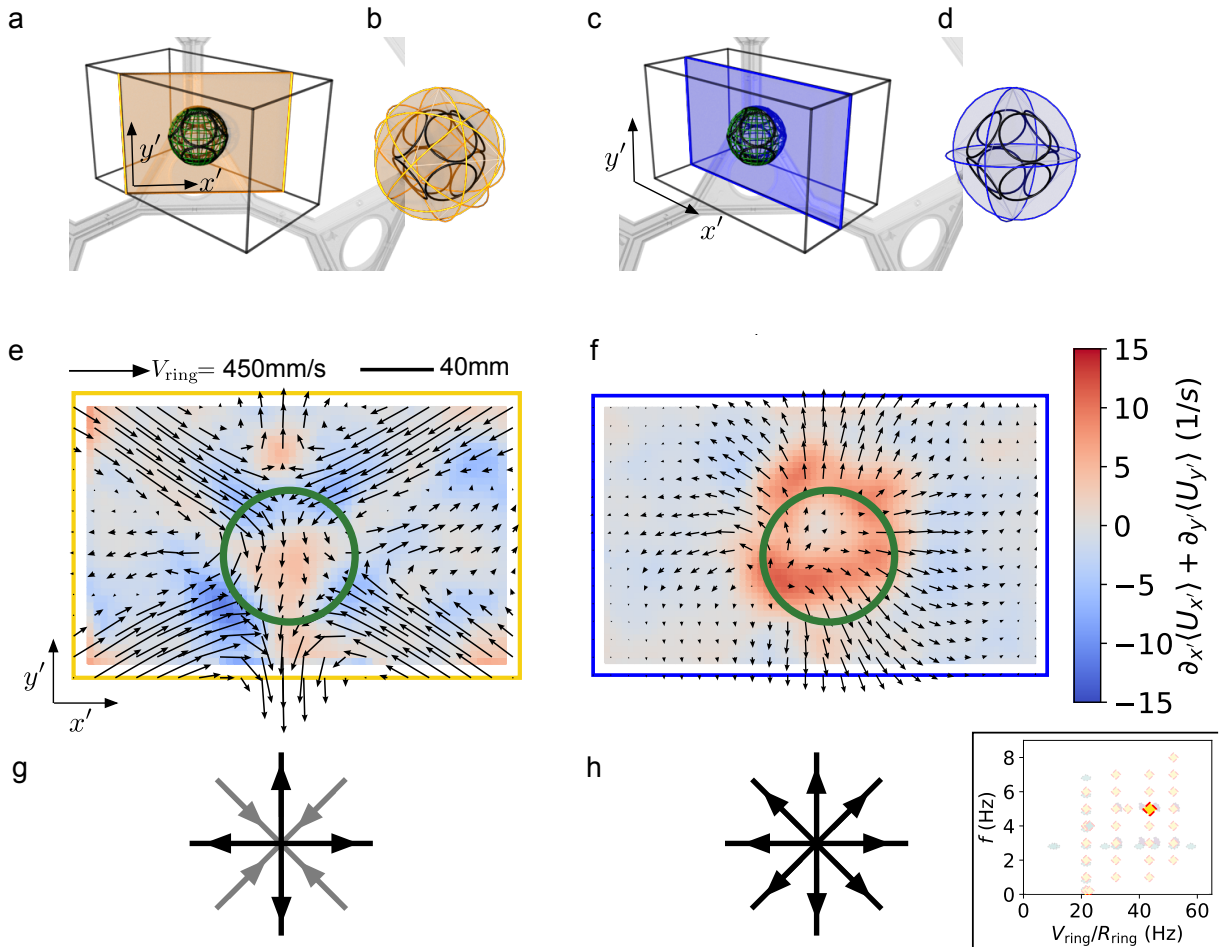

Figure 3.25: **Mean flow structure and the octahedral symmetry.** There are nine planes of reflection. (a) A diagonal plane cuts through four rings oriented on the faces of an octahedron. (b) Six diagonal planes of reflection are shown. (c) A horizontal plane is oriented between the rings. (d)Three horizontal planes of reflection are shown. (e)The mean flow on the diagonal plane shows the influx from the diagonal directions due to the vortex rings, accompanied by weak outflux in the horizontal and vertical directions. (f) The mean flow on the horizontal plane exhibits a divergent nature. (g-h) A schematic of the flow directions is shown on the diagonal/horizontal plane.

3.8.2 Fluctuating flow

We shall see that the fluctuation dominates inside the blob compared to the mean flow. The Reynolds decomposition yields

$$\frac{1}{2}\langle U_i U_i\rangle_t = \frac{1}{2}\langle U_i\rangle_t\langle U_i\rangle_t + \frac{1}{2}\langle u_i u_i\rangle_t$$

if the fluctuation has a zero mean $\langle u_i\rangle_t = 0$. We will examine this assumption in a later section. As for enstrophy, if the voriticity of the fluctuating field $\vec{\omega} = \nabla \times \vec{u}$ has zero mean, the temporally-averaged enstrophy is given by

$$\langle \Omega_i \Omega_i\rangle_t = \overline{\Omega}_i\overline{\Omega}_i + \langle \omega_i\omega_i\rangle_t; \quad \overline{\Omega}_i = \epsilon_{ijk}\partial_j\langle U_k\rangle_t.$$

Figure 3.26a-f, and h-j show the energy and enstrophy in the raw, (temporally-averaged) mean, and fluctuating velocity fields of a turbulent blob obtained by 3D PTV and 2D PIV. The fluctuating field contains the majority of both energy and enstrophy inside a turbulent blob. Averaging the energy and enstrophy density over angle yields Figure 3.26g and k respectively, revealing that the fluctuating energy is approximately 20 times greater than the mean flow energy at the center of the blob. The exact ratio may largely vary from 10 to 1000, depending on the experimental conditions (L_*, v_{eff}, f, D_p, and D_o). Outside the blob ($r > R_{\text{blob}}$), both energy and enstrophy decay as r^{-4}. The same dependency is observed for the local dissipation rate $\epsilon(r) = 2\nu\langle s_{ij}s_{ij}\rangle_{t\theta}$ (Figure 3b).

3.8.3 Breakdown of the vortex loops that feed the blob

In this section we examine the evolution of the vortex loops that feed the turbulent blob using the Q-criterion. By analyzing these structures, we gain a deeper understanding on how the incoming vortices are absorbed by the turbulent flow. The dataset corresponds to

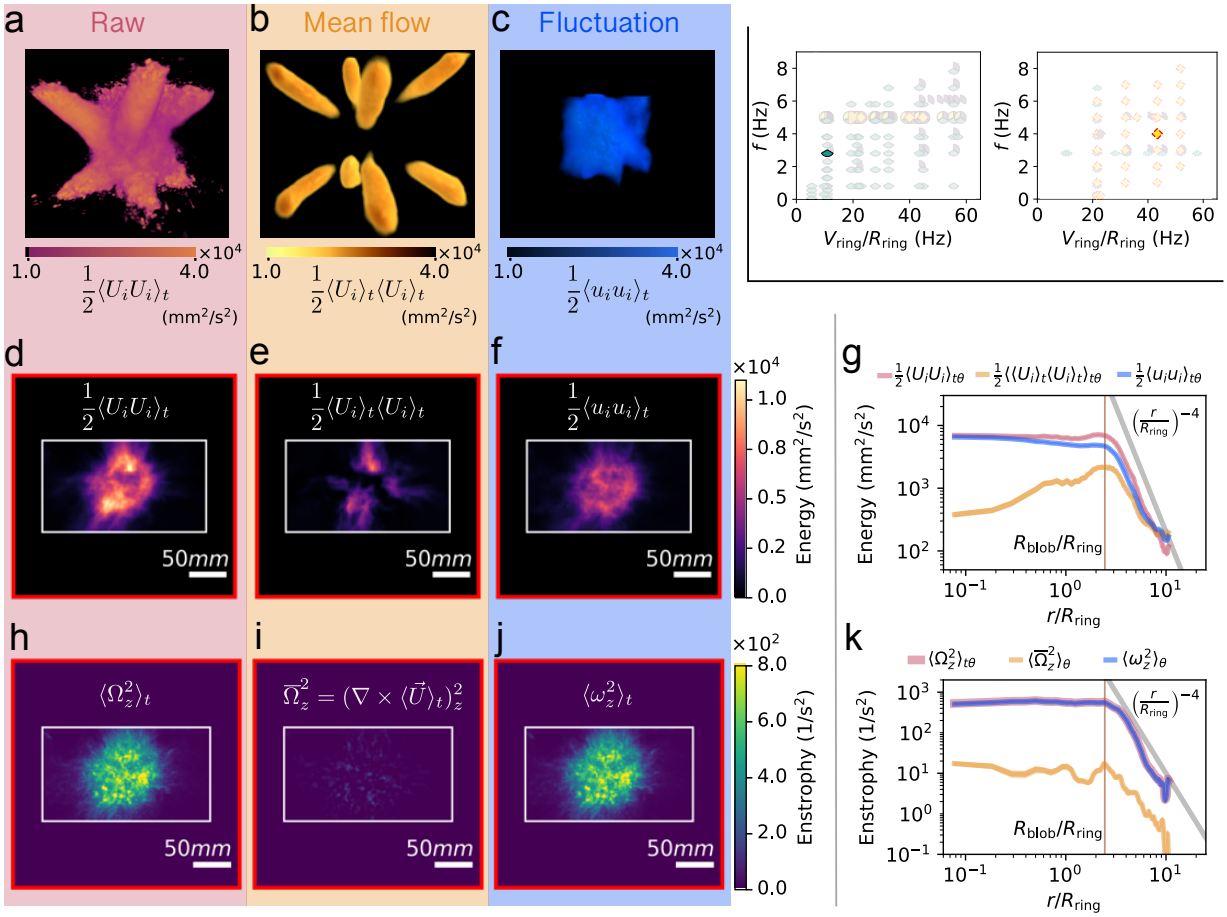

Figure 3.26: **The fluctuating velocity field contains the majority of energy and enstrophy inside a turbulent blob.**(a-c) Energy (density) fields of a 3D PTV measurement (a)Temporally-averaged energy (b)Mean flow energy (c)Temporally-averaged fluctuating energy (d-k) Energy and enstrophy fields of a 2D PIV measurement on the central slice (d)Temporally-averaged energy (e)Mean flow energy (f)Temporally-averaged fluctuating energy (g) Average energy (density) at distance r away from the center of the energy (h)Temporally-averaged enstrophy (i)Mean flow enstrophy (j)Temporally-averaged fluctuating enstrophy (k) Average enstrophy (density) at distance r away from the center of the enstrophy.

($V_{\text{ring}}/R_{\text{ring}}, f$, method) = (20Hz, 4Hz, 3D PTV) in Figure 3.24b.

The Q-value of a flow field is defined as [76]:

$$Q = \frac{1}{2}(\Omega_{Q,ij}\Omega_{Q,ji} - S_{ij}S_{ji})$$

where S_{ij} and $\Omega_{Q,ij}$ are the symmetric and anti-symmetric parts of the velocity gradient tensor $\partial_j U_i$ respectively. Note that the symbol $\Omega_{Q,ij}$ should not be confused with that used for vorticity of the total flow $\Omega_i = \epsilon_{ijk}\partial_j U_k$. The Q-criterion is used to identify coherent vortical structures in flows [52]. Connected regions with positive values of Q are interpreted as vortices while negative values are associated with shear.

We compute the Q-value by first calculating the velocity gradient tensor from the 3D PTV measurements. To eliminate spurious velocity vectors, we apply a median-filter with a kernel size of 3px $\times$ 3px. We then plot the values of $Q(\vec{x}, t)$ that are greater than 50 s^{-2} with weighted opacity. The regions with values above 600 s^{-2} are assigned with the same color and maximum opacity. This visualization - shown in Figure 3.27a-f and SI Video 12 - readily reveals the presence of coherent vortices of different strengths at every instant of time. The region outside the turbulent blob is quiescent with a low value of $|Q|$. Hence, the lower threshold. The opacity quasi-linearly scales with Q so that regions with a high value of Q are always visible.

We find that the Q-criterion highlights effectively the position and structure of the incoming vortex loops, providing valuable insight into how both the trajectories of the incoming vortex loops and the character of the collisions between them change as the number of collisions increases from the start of the experiment. As illustrated in figure 3.27a-b, the first collision is typical of a collision between coherent viscous vortices [127, 102, 113]. Canonically[79, 80, 178], when two viscous vortex tubes approach and collide, they get flattened, and form two anti-parallel vortex sheets. They form fine vortex structures called 'bridges' and 'threads' in the transverse direction. We observe the flattening behavior clearly;

however, due to the limited spatial resolution of our measurement, we see only hints of the finer structures.

As the second set arrives (Figure 3.27b) the first set can be seen to have reconnected and be on its way out of the central region. The first and second set then collide. A proliferation of small vortices can then be seen in the collision region resulting from the reconnections between incoming and outgoing vortices. After 5-9 cycles, the incoming vortices can be seen to distort and alter their trajectory on approach as a result of interaction with the fully-formed turbulent blob. The breakdown of incoming vortices is now no longer easily traceable to reconnections between incoming vortices. After 10-15 sets of rings have reached the central region, the system reaches a steady state (a turbulent blob).

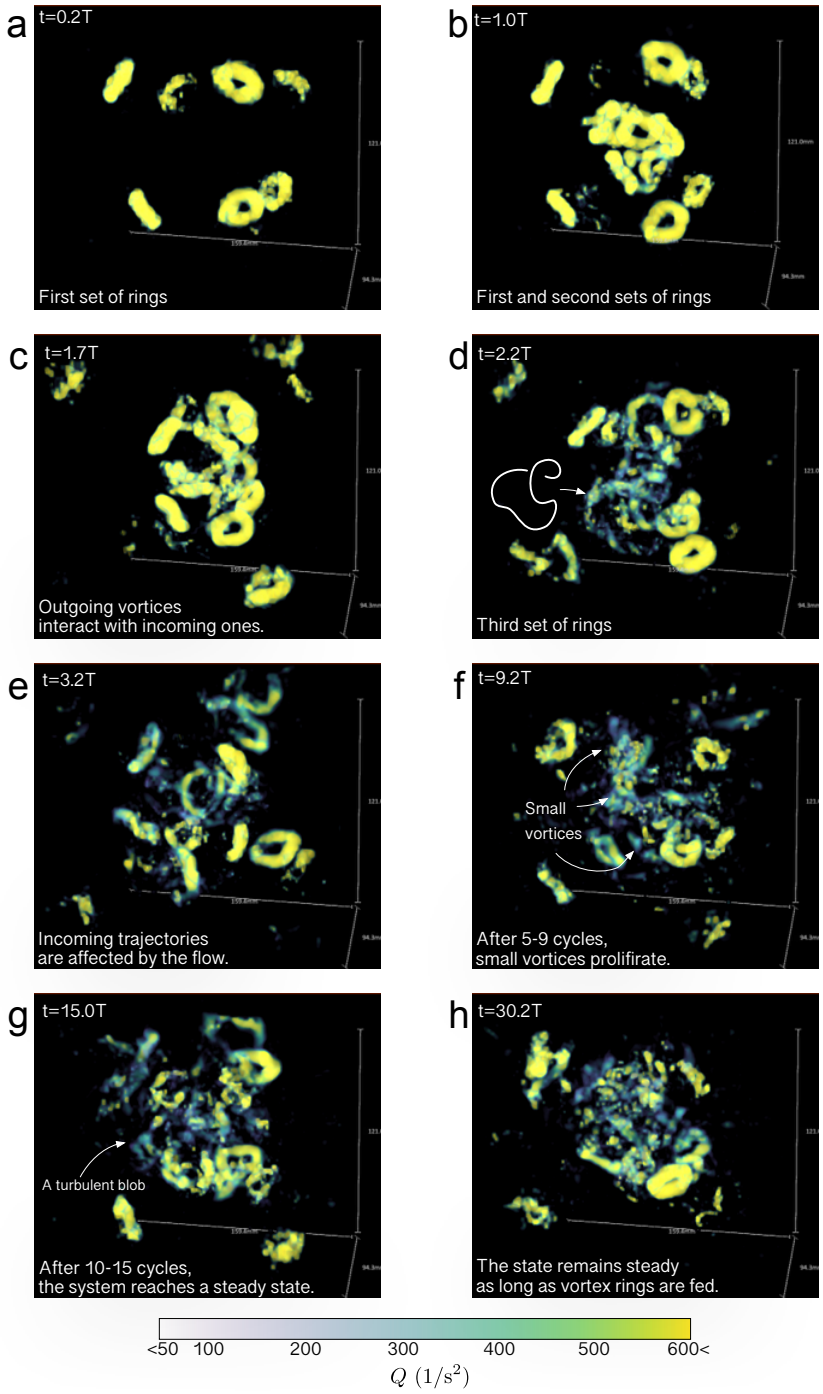

Figure 3.27: **Formation of a turbulent blob visualized via the Q-criterion.** (a) First set of vortex rings (b) First set of rings colliding with each other as the second set arrives. (c) Outgoing vortices interact with incoming ones. (d) Third set arrives. A large vortex loop spontaneously forms via vortex reconnections. (e) Incoming trajectories are affected by the induced flow. (f) Between $t = 3T - 9T$, small vortices continue to proliferate in the central region. (g) At $t \approx 15T$, the system reaches an equilibrium. (h) This vortical structure persists as long as vortex rings are fed. The average radius of the rings is 8 mm.

3.9 Turbulent statistics

In this section we discuss the velocity fluctuations in our turbulent blob. We first examine the raw fluctuating velocity spectra, addressing inhomogeneity and anisotropy of the measured fluctuating velocity field in sections 3.9.1 and 3.9.2. Section 3.10-3.10.4 discusses how we compute the spectra and the structure functions from PIV and PTV measurements. Section 3.10.7 discusses how we computed these functions using only the regions inside the blob.

The authors find it pedagogical to summarize the methods to compute 3D and 1D turbulent energy spectra and structure functions from experimental data. As PIV and PTV became an important method to study fluid mechanics, the authors hope that this section serves as a guide. The methods are standard but we explicitly discuss issues of computing the spectra from experimentally obtained 2D/3D fields without using Taylor's hypothesis. For the turbulent blob, the mean field inside the blob is substantially smaller than the fluctuating field, making Taylor's hypothesis inapplicable.

3.9.1 Definition of velocity fluctuations

There is a subtlety in defining the fluctuation of the flow because the mean flow may in principle depend on the phase with respect to the oscillatory motion. This may favor the use of a phase-averaged flow $\langle U_i \rangle_n(\vec{r}), \Theta)$ as a mean flow over a time-averaged flow $\langle U_i \rangle_t(\vec{r})$. For the definition of the phase-locked (or phase-averaged) velocity $\langle U_i \rangle_n(\vec{r}, \Theta)$, see Section A.

Consider two spherical domains with a radius $r = R_{\text{blob}}$ and $r = 3R_{\text{blob}}$ (Figure 3.28a-b). We find that both definitions of the fluctuating velocity have the same distribution inside the core, reflecting zero mean velocity throughout a cycle(Figure 3.28c). The difference of these two conventions are evident as we inspect the distribution inside the second domain that includes the ambient surrounding in addition to the turbulent core (Figure 3.28d). The overpopulation at high velocity for $U_i - \langle U_i \rangle_t$ is caused by ignoring the phase-dependence

of the vortex ring locations. In summary, the (fluctuating) velocity statistics inside the turbulent core does not depend on the phase. All turbulent analyses presented in this paper use the time-averaged flow as a mean flow.

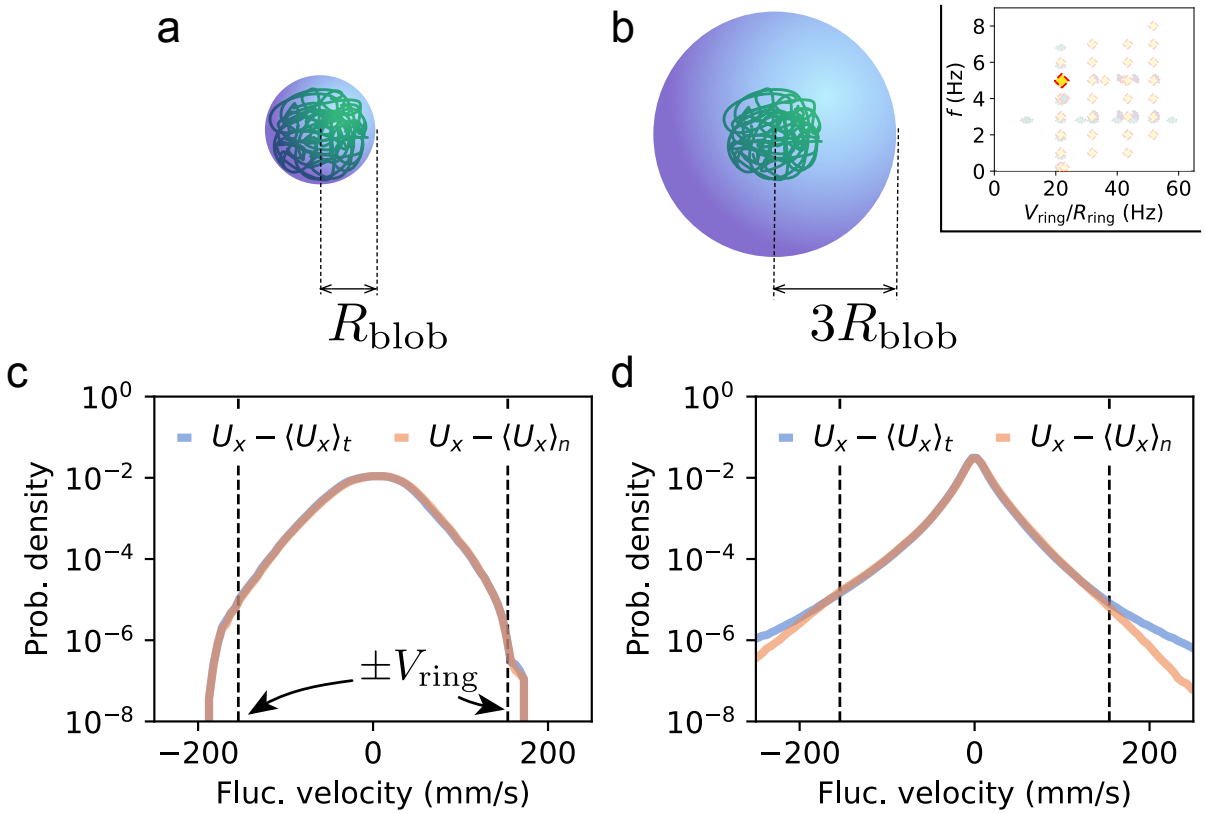

Figure 3.28: **Fluctuations inside the turbulent blob are phase-independent regardless of the choice of the mean flow between time-averaged flow and the phase-locked flow.** (a-b) Two domains are considered to examine statistics of a fluctuating velocity field: a region within a turbulent core $r < R_{\mathrm{blob}}$ and a spherical region containing the turbulent core and its ambient surroundings $r < 3R_{\mathrm{blob}}$. (c) Probability distribution functions (PDF) of the two fluctuating velocities for $(L/D, v_{\mathrm{eff}}, f)$=(2., 200mm/s, 4Hz) with R_{blob} =32mm show no difference between how the fluctuations are defined. (d) The fluctuations outside the turbulent blob depend on the phase because the vortex rings appear at specific phase in this domain $r \in (R_{\mathrm{blob}}, 3R_{\mathrm{blob}}]$, giving rise to the difference between the PDFs of the fluctuations.

3.9.2 Inhomogeneity and isotropy of the flow

The flow induced by vortex ring collision at $f > f_c$ is clearly inhomogeneous and anisotropic as it consists of a turbulent core and a mean flow structure originated from the vortex rings (Figure 3a). However, the turbulent flows inside the core $r \leq R_{\text{blob}}$ is isotropic and homogeneous. The anisotropy and inhomogeneity grows as the domain of consideration includes its surroundings. Consider two spherical domains with a radius $r = R_{\text{blob}}$ and $r = 3R_{\text{blob}}$ each (Figure 3.29a and b). Now we examine the statistics of all three components of a fluctuating velocity field of a turbulent blob, obtained by a 3D PTV experiment$(L/D, v_{\text{eff}}, f)$=(2., 200mm/s, 4Hz), R_{blob} = 32mm, recorded volume: 200mm × 108mm × 123mm, duration: 10s = 40 cycles). The probability distribution functions (PDFs) of the fluctuating velocity field inside the turbulent core (Figure 3.29c) shows almost no anisotropy. Quantitatively, the isotropy can be assessed by comparing the standard deviations for each component $\sigma_{u_i}/\sigma_{u_j}$ $(i \neq j)$. Figure 3.29e indeed shows high isotropy inside the turbulent core as well as inside the larger domain (Figure 3.29f); however, the flucutations are inhomogeneous.

The velocity PDFs over multiple spherical domains with radius r at different phases are shown in Figure 3.30. One first finds that the statistics does not depend on the phase, and the flow is nearly isotropic in all of the considered domains. The fluctuations are nearly Gaussian inside the core $r \leq R_{\text{blob}}$. The skewness is -0.1 and kurtosis is 4.0 for all velocity components within $r \leq R_{\text{blob}}$, compared to 0 and 3 if the fluctuations were Gaussian. The PDF is altered as the considered domain grows in size, including the ambient, less turbulent regions. This is reflected by a growing peak at $u_i = U_i - \langle U_i \rangle_t = 0$ in Figure 3.30 as r/R_{blob} increases.

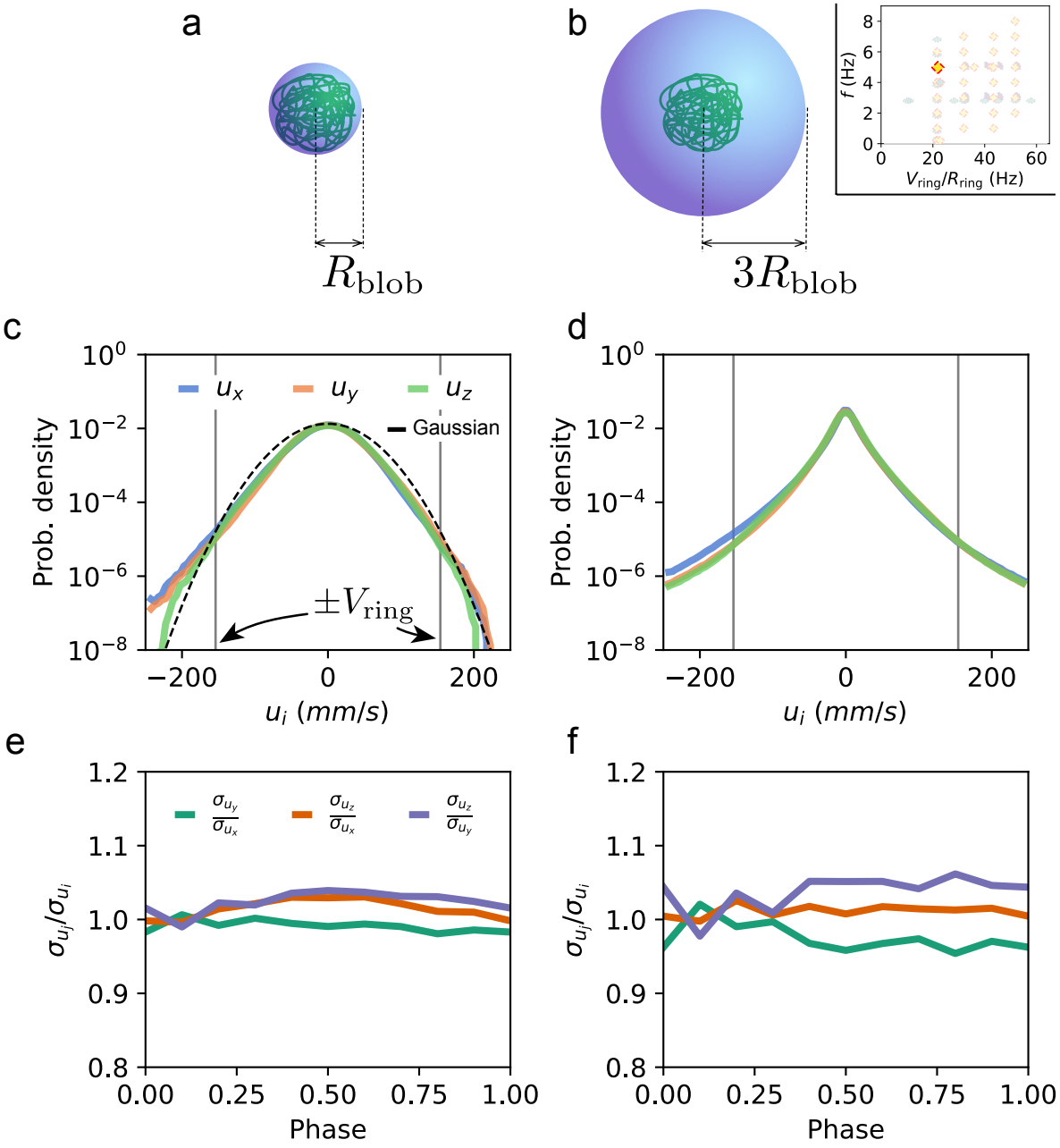

Figure 3.29: **Inhomogeneity and anisotropy of velocity fluctuations** $u_i = U_i - \langle U_i \rangle_t$ (a-b) Two domains are considered to examine statistics of a fluctuating velocity field: a region within a turbulent core $r < R_{\mathrm{blob}}$ and a spherical region containing the turbulent core and its ambient surroundings. (c-d) Probability distribution functions (PDF) of fluctuating velocities for $(L/D, v_{\mathrm{eff}}, f)$=(2.0, 200mm/s, 4Hz) with $R_{\mathrm{blob}} = 32$mm are shown for the two domains, indicating isotropy inside the core and increase of anisotropy as the region includes its surroundings. (e-f) Ratios between the two second moments of the velocity PDFs.

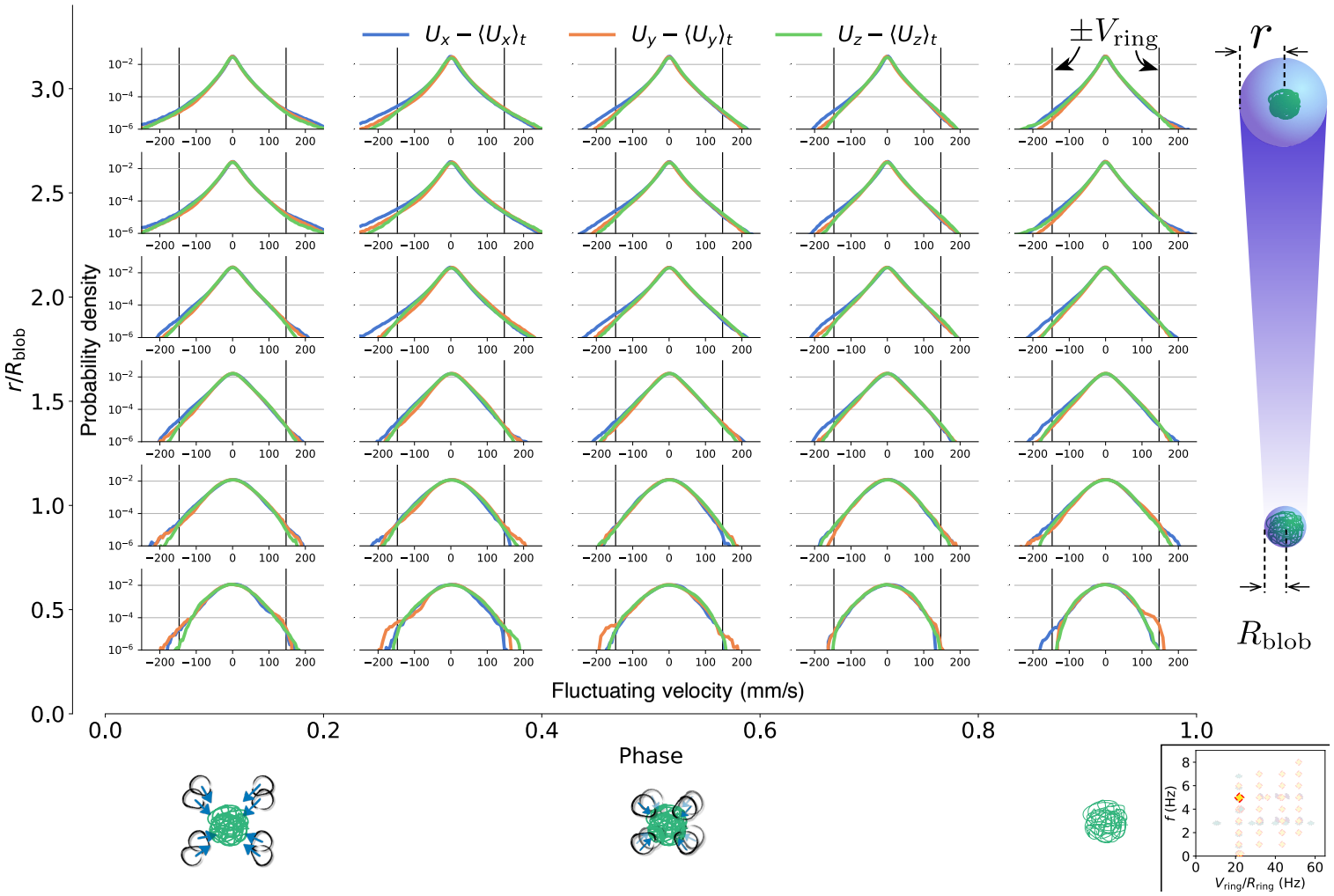

Figure 3.30: **Isotropy, homogeneity, and phase-dependence of fluctuating velocity fields** $u_i = U_i - \langle U_i \rangle_t$**.** Probability distribution functions (PDFs) of u_i over spherical domains of various radii r show high isotropy, indicated by overlap of three colors u_x, u_y, u_z. The changes in the shape of the PDFs over various r reflect the inhomogeneity of fluctuations. Small changes over the phase across different r indicates that the fluctuation is almost independent of the phase. The data is obtained by a 3D PTV experiment for $(L/D, v_{\mathrm{eff}}, f)$=(2., 200mm/s, 4Hz) with a recording time of 10s = 40 cycles. The range of the velocity vectors is roughly the propagation speed of the injected vortex ring V_{ring}.

Quantity	Setting 1	Setting 2
R_{blob}	$50-60$mm	$30-40$mm
R_{ring}	$13-18$mm	$7-9$mm
V_{ring}	$100-800$mm/s	$50-400$mm/s
Γ_{ring}	$0.1-1\times10^5$mm^2/s	$0.3-4\times10^4$mm^2/s
Γ_{ring}/ν	$1-6\times10^4$	$0.3-4\times10^4$
ϵ_0	$4\times10^5-4\times10^6$mm^2/s^3	$1\times10^4-1\times10^5$mm^2/s^3
$\eta=\left(\frac{\nu^3}{\epsilon_0}\right)^{\frac{1}{4}}$	$0.02-0.04$mm	$0.06-0.1$mm
λ	$1-5$mm	$1-5$mm
$\mathcal{L}=\frac{u'^3}{\epsilon_0}$	$100-120$mm	$60-80$mm
$Re_\lambda=\frac{u'\lambda}{\nu}$	$50-300$	$50-200$
$u'=\sqrt{\frac{1}{3}\langle u_iu_i\rangle}$	$50-250$mm/s	$25-150$mm/s

Table 3.2: **Vortex ring metrics and turbulence statistics inside the blob for the two experimental settings- Setting 1, 2:** $(D_p, D_o) = (160.0\text{mm}, 25.6\text{mm})$, $(57.0\text{mm}, 12.8\text{mm})$. The listed dissipation rates ϵ_0 are values based on the rate-of-strain tensor.

3.9.3 Turbulent statistics and vortex ring metrics

Table 3.2 summarizes the turbulent statistics and the vortex ring metrics that were measured in the two settings (See Table 2.1).

3.10 Computation of energy spectra and structure function from experimental real space velocimetry data

The fluctuating energy spectra and structure functions are an essential component of canonical characterizations of turbulent flows. For a homogeneous isotropic turbulence, the three-dimensional energy spectrum $E(\kappa)$, one-dimensional energy spectrum $E_{11}(\kappa_1)$ and the structure functions $D_{ij} = \langle \delta u_i \delta u_j \rangle$ contain equivalent information about the fluctuating velocity field. However, the computation of each is differently affected by experimental considerations such as the dimensionality of the velocity data (e.g. point measurements with anemometers or laser doppler velocimetry vs spatially resolved PIV/PTV measurements) and experimental limitation (e.g. the extent of the measurement area, resolution, noise level).

In the case of spatially resolved velocimetry, a natural approach to measuring the fluctuation energy spectrum is Fourier analysis; however, aperiodicity, discreteness, and finiteness of experimental data can give rise to artifacts. In this context, the real-space velocity (difference) correlation function D_{ij} is sometimes preferred as a measure of turbulent fluctuations because it is less susceptible to measurement artifacts as illustrated later in this section.

We begin this section by reviewing the definitions of each fluctuation-characterizing function, before studying the effects of experimental noise, finite window size and finite resolution on each measurement.

3.10.1 Definitions and relations of energy spectra

Consider the fluctuating component of a turbulent velocity field $u_i(\boldsymbol{x})$ in a domain V. The velocity two-point correlation tensor R_{ij} is defined as:

$$R_{ij}(\boldsymbol{r}) = \langle u_i(\boldsymbol{x} + \boldsymbol{r}) u_j(\boldsymbol{x}) \rangle. \tag{3.23}$$

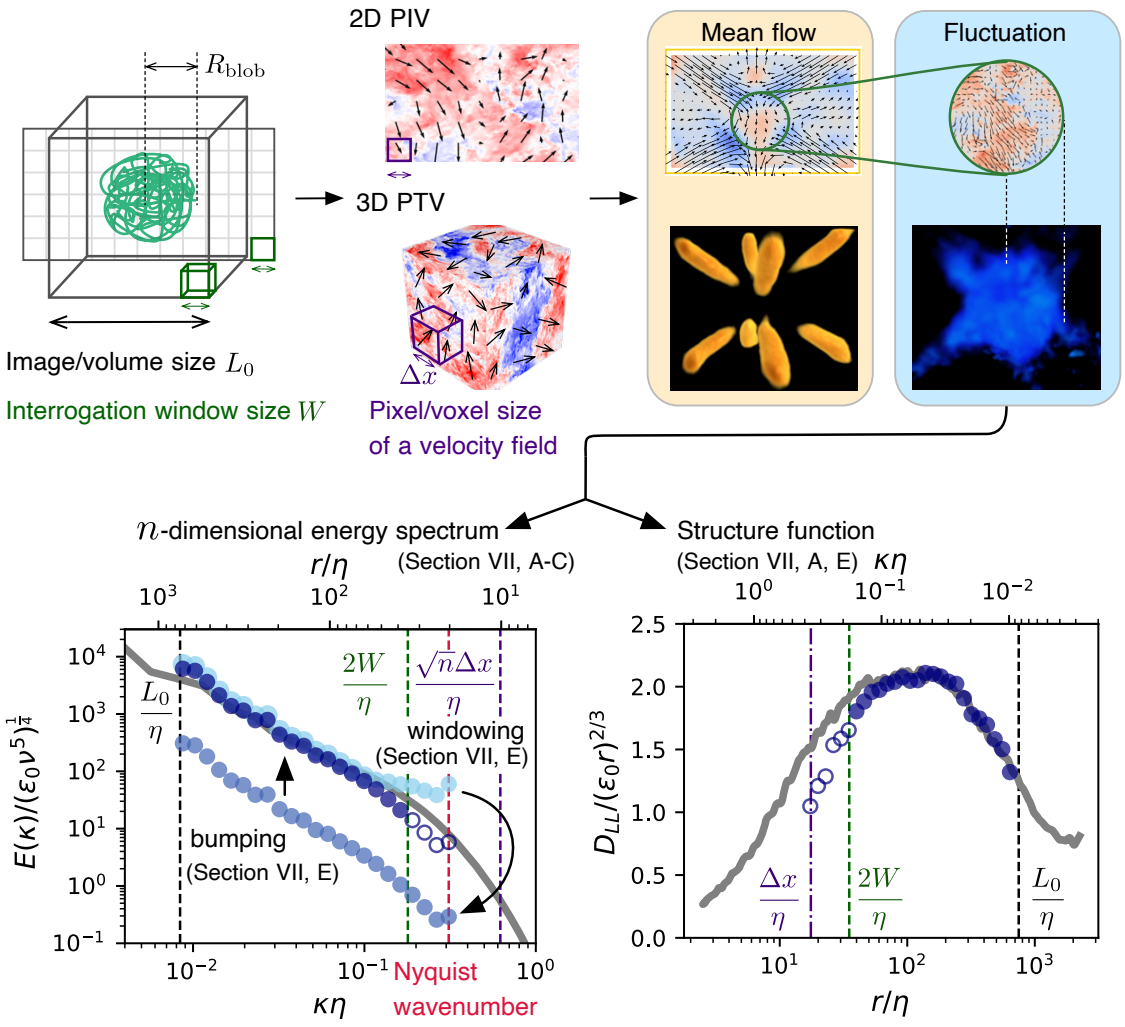

Figure 3.31: **Guide to the computation of the energy spectrum and the structure function without applying Taylor's frozen turbulence hypothesis.** 1. Extract a velocity field via cross-correlation of the adjacent images, or directly tracking the particles in 3D. 2. Decompose the velocity field into the mean flow and the fluctuations (Reynolds decomposition) 3. Compute a local turbulent energy spectrum or a structure function inside the region of interest. For the former, windowing combats against undesired effects (aliasing and spectral leakage) of DFT for the Fourier analysis, and bumping accounts for the attenuation of the signal by windowing. The attenuation of the magnitude by windowing is exaggerated for this illustration.

Its Fourier transform is the velocity spectrum tensor Φ_{ij}:

$$\Phi_{ij}(\boldsymbol{\kappa}) \equiv \frac{1}{(2\pi)^3} \iiint_{-\infty}^{\infty} R_{ij}(\boldsymbol{r}) e^{-i\boldsymbol{\kappa}\cdot\boldsymbol{r}} d\boldsymbol{r}. \tag{3.24}$$

The one-dimensional energy spectra E_{ij} are considered when three-dimensional Fourier transformation is not available, and are defined as twice the one-dimensional Fourier transform of the two-point correlation tensor:

$$E_{ij}(\kappa_1) \equiv 2 \cdot \frac{1}{2\pi} \int_{-\infty}^{\infty} R_{ij}(r_1 \hat{e}_1) e^{-i\kappa_1 r_1} dr_1. \tag{3.25}$$

Eq. 3.24 and 3.25 are expressed interms of the two-point correlation function; however, they can be alternatively expressed using the Fourier transform of a turbulent velocity field, $\tilde{u}_i(\boldsymbol{\kappa}) = (1/2\pi) \int u_i(\boldsymbol{x}) \exp(-i\boldsymbol{\kappa}\cdot\boldsymbol{x}) d\boldsymbol{x}$, via the Wiener-Khinchin theorem. Eq. 3.24 becomes:

$$\Phi_{ij}(\boldsymbol{\kappa}) = \langle \tilde{u}_i(\boldsymbol{\kappa}) \tilde{u}_j^*(\boldsymbol{\kappa}) \rangle. \tag{3.26}$$

The definitions of the velocity spectrum and the one-dimensional energy spectrum functions in terms of the two-point correlation functions (Eq. 3.24 and 3.25) are well suited to theoretical considerations of random processes. This is because the process may have characteristic two-point correlation functions. Such methods have provided a means to compute the spectra from the point-wise measurements historically. A further discussion on the two equivalent representations of the energy spectrum can be found in Chapter 11 of [23](p.285-288, 3rd ed.).

With the assumption of isotropy, the energy spectrum function $E(\kappa)$ can be obtained by

stripping off the angular information from Φ_{ii}.

$$E(\kappa) = \frac{1}{2} \iiint_{-\infty}^{\infty} \Phi_{ii}(\boldsymbol{\kappa}) \delta(|\boldsymbol{\kappa}| - \kappa) d\boldsymbol{\kappa} \tag{3.27}$$

As for Eq. 3.25, let us denote the one-dimensional Fourier transform operator along the direction $\hat{x}_i$ as $\mathcal{F}_{x_i}$. The one-dimensional spectra E_{ij} are then:

$$E_{ij}(\kappa_1) = 2 \int_{-\infty}^{\infty} \left\langle \mathcal{F}_{x_1}[u_i(\mathbf{x})] \mathcal{F}_{x_1}[u_j(\mathbf{x})]^* \right\rangle_{x_2,x_3} \delta(\kappa_1' - \kappa_1) d\kappa_1' \tag{3.28}$$

$$= 2 \int_{-\infty}^{\infty} \left\langle \left[\frac{1}{2\pi} \int_{-\infty}^{\infty} u_i(\mathbf{x}) e^{-i\kappa_1' x_1} dx_1 \right] \left[\frac{1}{2\pi} \int_{-\infty}^{\infty} u_j(\mathbf{x}) e^{i\kappa_1' x_1} dx_1 \right] \right\rangle_{x_2,x_3} \delta(\kappa_1' - \kappa_1) d\kappa_1'. \tag{3.29}$$

For an isotropic fluctuating field, R_{ij} can be expressed in terms of two scalar functions:

$$R_{ij}(r) = u'^2 \left(g(r)\delta_{ij} + [f(r) - g(r)] \frac{x_i x_j}{r^2} \right). \tag{3.30}$$

Here, $f(r)$ and $g(r)$ are longitudinal and transverse two-point correlation functions respectively:

$$f(r) = \frac{\langle u_\parallel(\boldsymbol{x}) u_\parallel(\boldsymbol{x} + \boldsymbol{r}) \rangle}{\langle u_\parallel^2 \rangle} \tag{3.31}$$

$$g(r) = \frac{\langle u_\perp(\boldsymbol{x}) u_\perp(\boldsymbol{x} + \boldsymbol{r}) \rangle}{\langle u_\perp^2 \rangle} \tag{3.32}$$

where, $u_\parallel$ is the velocity component parallel to the displacement vector $\boldsymbol{r}$. With homogeneity and isotropy, the diagonal elements of E_{ij} can be expressed using $f(r)$ and $g(r)$:

$$E_{11}(\kappa_1) = \frac{2}{\pi} \langle u_1^2 \rangle \int_0^{\infty} f(r_1) \cos(\kappa_1 r_1) dr_1 \tag{3.33}$$

$$E_{22}(\kappa_1) = E_{33}(\kappa_1) = \frac{2}{\pi} \langle u_2^2 \rangle \int_0^{\infty} g(r_1) \cos(\kappa_1 r_1) dr_1. \tag{3.34}$$

The (three-dimensional) energy spectrum $E(\kappa)$ can be expressed by using the one-dimensional energy spectra as $E(\kappa) = -\frac{\kappa}{2}\frac{d}{d\kappa}E_{ii}(\kappa)$.

3.10.2 Energy spectrum computation by Fourier analysis

If presented with spatially resolved velocity field snapshots that are sampled on a uniform grid, the Fourier transform of the velocity is replaced by the discrete Fourier transform:

$$\breve{u}_i(\boldsymbol{\kappa}) = \sum_{n=0}^{N-1} u_i(\boldsymbol{x}_n) e^{-i\boldsymbol{\kappa}\cdot\boldsymbol{x}_n}$$

To derive an expression for the energy spectrum $E(k)$ in terms of $\breve{u}_i(\boldsymbol{\kappa})$, we consider the average kinetic energy:

$$k = \langle \frac{1}{2} u_i(\boldsymbol{x}) u_i(\boldsymbol{x}) \rangle = \int_0^\infty E(\kappa) d\kappa.$$

On a discretized velocity field this becomes:

$$k = \frac{1}{2N} \sum_{n=0}^{N-1} u_i(\boldsymbol{x}_n) u_i(\boldsymbol{x}_n) \tag{3.35}$$

$$= \frac{1}{2N^2} \sum_{n=0}^{N-1} \breve{u}_i(\boldsymbol{\kappa}_n) \breve{u}_i^*(\boldsymbol{\kappa}_n) \because \text{Parseval's theorem} \tag{3.36}$$

$$\approx \frac{1}{2N^2 \Delta\kappa_1 ... \Delta\kappa_d} \sum_{n=0}^{N_r-1} \langle \breve{u}_i(\boldsymbol{\kappa}_n) \breve{u}_i^*(\boldsymbol{\kappa}_n) \rangle_{\kappa_\theta, \kappa_\phi} |J(\boldsymbol{\kappa}_n)| \Delta\kappa \because \text{isotropy} \tag{3.37}$$

where $\kappa_n = 2\pi n/N$ and $|J(\boldsymbol{\kappa}_n)| = 4\pi\kappa^2$ $(d = 3)$ or $2\pi\kappa$ $(d = 2)$ where d is the dimension of the dataset. For example, $d = 2$ for a 2D slice of a velocity field embedded in 3D flow (2D PIV) or for a purely 2D flow. The approximation in Eq. 3.37 originates from the transformation of $\boldsymbol{\kappa}_n$ from the Cartesian basis to the spherical basis. The discreteness of $\boldsymbol{\kappa}_n$ and the rectangular spatial domain also contributes to this approximation. $\Delta\kappa = \sqrt{\Delta\kappa_1^2 + ... + \Delta\kappa_d^2}$ is the wavenumber spacing in the spherical coordinate system, and $N_r =$

$\lfloor \max(|\boldsymbol{\kappa}_n|)/\Delta\kappa \rfloor$.

If one has access to only two components of the 3D velocity field, which is typical for PIV experiments based on a single camera and a laser-sheet, one must further multiply Eq. 3.37 by 3/2 (appealing to isotropy).

From this we can read off:

$$E(\kappa) \approx \frac{1}{N^2 \Delta\kappa_1 ... \Delta\kappa_d} \frac{|J|}{2} \langle \breve{u}_i(\boldsymbol{\kappa}) \breve{u}_i^*(\boldsymbol{\kappa}) \rangle_{\kappa_\theta, \kappa_\phi} \tag{3.38}$$

To derive the one-dimensional energy spectrum $E_{ij}(\kappa_1)$, we consider the average of $u_i(\boldsymbol{x})u_j(\boldsymbol{x})$:

$$\langle u_i(\boldsymbol{x}) u_j(\boldsymbol{x}) \rangle = \frac{1}{2} \int_{-\infty}^{\infty} E_{ij}(\kappa_1) d\kappa_1. \tag{3.39}$$

Let us denote the one-dimensional discrete Fourier transform operator along the direction $\hat{x}_i$ as $\breve{\mathcal{F}}_{x_i}$:

$$\breve{\mathcal{F}}_{x_1}[u_j(\boldsymbol{x}_n)] = \sum_{n=0}^{N_1 - 1} u_j(\boldsymbol{x}_n) e^{-i\kappa_1 x_{1,n}}$$

where N_1 is the number of samples along the $\hat{x}_1$. Note that the exponent is $-i\kappa_1 x_{1,n}$ when $i = 1$ and not the sum $\kappa_i x_{i,n}$.

On a discretized velocity field Eq. 3.39 becomes:

$$\langle u_i(\boldsymbol{x})u_j(\boldsymbol{x})\rangle = \frac{1}{N_1...N_d}\sum_{n_1=0}^{N_1-1}...\sum_{n_d=0}^{N_d-1} u_i(\boldsymbol{x}_n)u_j(\boldsymbol{x}_n) \tag{3.40}$$

$$= \frac{1}{N_1}\frac{1}{N_1...N_d}\sum_{n_1=0}^{N_1-1}...\sum_{n_d=0}^{N_d-1} \breve{\mathcal{F}}_{x_1}[u_i(\boldsymbol{x}_n)]\breve{\mathcal{F}}^*_{x_1}[u_j(\boldsymbol{x}_n)] \because \text{Parseval's theorem} \tag{3.41}$$

$$= \sum_{n_1=0}^{N_1-1}\left[\frac{1}{N_1^2\Delta\kappa_1}\frac{1}{N_2...N_d}\sum_{n_2=0}^{N_2-1}...\sum_{n_d=0}^{N_d-1} \breve{\mathcal{F}}_{x_1}[u_i(\boldsymbol{x}_n)]\breve{\mathcal{F}}^*_{x_1}[u_j(\boldsymbol{x}_n)]\right]\Delta\kappa_1. \tag{3.42}$$

From this we can read off:

$$E_{ij}(\kappa_1) \approx \frac{2}{N_1^2\Delta\kappa_1}\frac{1}{N_2...N_d}\sum_{n_2=0}^{N_2-1}...\sum_{n_d=0}^{N_d-1} \breve{\mathcal{F}}_{x_1}[u_i(\boldsymbol{x}_n)]\breve{\mathcal{F}}^*_{x_1}[u_j(\boldsymbol{x}_n)] \tag{3.43}$$

$$= \frac{2}{N_1^2\Delta\kappa_1}\langle\breve{\mathcal{F}}_{x_1}[u_i(\boldsymbol{x}_n)]\breve{\mathcal{F}}^*_{x_1}[u_j(\boldsymbol{x}_n)]\rangle_{x_2,...,x_d}. \tag{3.44}$$

Figure 3.32a displays the three- and one-dimensional energy spectra computed by Eq. 3.38 and 3.44 for DNS data of isotropic, homogeneous turbulence obtained from Johns Hopkins Turbulence Database (JHTD) [100, 130]. In the inertial subrange, they agree with the Kolmogorov spectra ($E(\kappa) = C\epsilon^{2/3}\kappa^{-5/3}$, and $E_{11}(\kappa_1) = C_1\epsilon^{2/3}\kappa_1^{-5/3}$) using the reported dissipation rate ϵ=0.103 a.u.[d] and the Kolmogorov constants $C = 1.6$[111] and $C_1 = 0.52$[166]). For the transverse, one-dimensional energy spectra $E_{22}(\kappa_1)$ and $E_{33}(\kappa_1)$, the coefficient becomes $4C_1/3$, assuming isotropy[134].

Figure 3.32b displays the three- and one-dimensional energy spectra from a 2D slice of the same 3D HIT field as Figure 3.32a. It can be seen that the spectrum computed from the 2D slice approximates well the spectrum computed from 3D data. The slight jaggedness in Figure 3.32b can be reduced by averaging successive velocity snapshots.

d. The value can be found in the documentation of the forced isotropic turbulence data set.

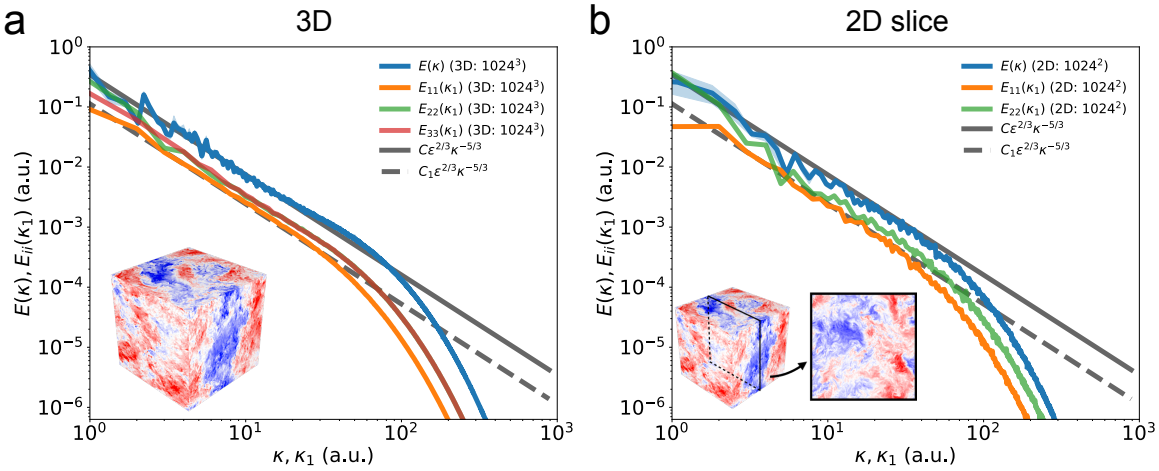

Figure 3.32: **Direct computation of three- and one-dimensional energy spectra: $E(\kappa)$ and $E_{ii}(\kappa_1)$.** (a) Three- and one-dimensional energy spectra of DNS isotropic, homogeneous turbulence with a periodic boundary condition were computed by Eq. 3.38 and 3.44. (b) Energy spectra of a 2D velocity field embedded in the 3D volume are consistent with the underlying truth if the velocity statistics on the 2D slice is a representative sample of the population. For both (a) and (b), the data are presented as mean +/-SEM where the mean is calculated as $E(\kappa) = (1/V_{\text{shell/annulus}}) \int_{\kappa}^{\kappa+\Delta\kappa} E(\vec{\kappa'}) \cdot |J| d\kappa'$ for the three-dimensional spectra. In 3D, $V_{\text{shell}}(\kappa) = (4\pi/3)[(\kappa+\Delta\kappa)^3 - \kappa^3]$ and $|J| = 4\pi\kappa'^2$. In 2D, $V_{\text{annulus}}(\kappa) = \pi[(\kappa+\Delta\kappa)^2 - \kappa^2]$ and $|J| = 2\pi\kappa'$. For $E_{11\text{or}22}(\kappa_1)$, the averaging is performed along $\hat{x}_2$.

In the case of the DNS data from a periodic box, in which all turbulent scales are well-resolved, the spectra computed using Eq. 3.38 shown in Figure 3.32 are in excellent agreement with what we expect from the continuum theory of HIT.

In the case of experimental data in which the resolution is limited on both ends (the voxel/pixel spacing at the low end and the imaging region size at the high end), a number of artifacts can affect the estimation of $E(\kappa)$. We discuss these, and simple methods to correct their effects in the following sections using $E(\kappa)$ as an example. All considerations apply equally to $E_{ij}(\kappa_1)$.

Despite these potential artifacts, obtaining spatially resolved data using PIV/PTV and computing the spectrum via the Fourier method has several advantages over canonical methods used in many classical turbulent fluctuation measurements that are based on the point-wise hot-wire anemometry and Laser Doppler velocimetry measurements:

1. One can directly compute the energy spectrum from a single velocity field snapshot.

2. This method does not require Taylor's frozen turbulence hypothesis, and can be applied to flows without a strong mean flow.

3. An instantaneous planar velocity field is sufficient to acquire the energy spectrum if the field is isotropic. (Figure 3.32b)

4. This method is more efficient than computing the two-point velocity correlation function R_{ij} thanks to Fast Fourier Transform (FFT). The temporal complexity to compute R_{ij} is $O(n^2)$, whereas FFT takes $O(n \log n)$, offering a faster turnaround.

3.10.3 Effect of domain truncation and noise

Experimentally obtained velocity fields are in general truncated, and contain noise. In this subsection we elucidate the effect of the domain truncation and noise on the energy spectrum

by truncating and adding noise to the same DNS data as used in Figure 3.32, computing spectra of the modified data and comparing the resulting spectrum to the original.

Figure 3.33 shows the 3D energy spectrum obtained by truncating the domain and computing $E(\kappa)$ using Equation 3.38. The spectrum agrees with the one computed in the full domain at low wave-numbers but differs at high wavenumbers. This can be rationalized by considering the effect of a discrete Fourier transform on a finite domain. For an instantaneous velocity field $u_i(\vec{x}_n)$, the truncated velocity field is given by $u_i^{\text{truncated}}(\vec{x}_n) = u_i(\vec{x}_n)G(\vec{x}_n)$ where $G(\vec{x}_n) = 1$ inside the (measured) domain, and 0 otherwise. Its discrete Fourier transform is then given by the convolution of $\breve{u}_i(\vec{\kappa}_n)$ with $\breve{G}(\vec{\kappa}_n)$. For example, consider $u_i(x_n) = \sin(\kappa_0 x)$ and a rectangular window with length $\ell \neq 2m\pi/\kappa_0$ ($m \in \mathbb{Z}$). The power spectrum of the DFT $\breve{u}_i(\vec{\kappa}_n)$ has a broad peak centered at $\kappa = \kappa_0$ and non-zero values in its neighborhood ('leakage'). This is a consequence of the convolution with $\breve{G}(x_n)$ that is a sinc function in the Fourier space.

The degree of the leakage in the Fourier space depends on both the signal and the window function. Hence it is important to study how the expected spectrum is affected by a rectangular window. In the case of a turbulent energy spectrum, the 'leakage' leads to overestimation at high wavenumber (Figure 3.33a). Note that in Figure 3.32a-b, the spectral leakage does not occur because the considered velocity field comes from a periodic DNS simulation and the entire domain was included.

To investigate the effect of the noise on the energy spectrum, we add Gaussian noise with its magnitude scaled by the speed at each position $u_i^{\text{noise}}(\vec{x}) = u_i(\vec{x})(1 + f(\mu = 0, \sigma))$ where $f(\mu, \sigma)$ is drawn from a Gaussin distribution. Figure 3.33b shows that the noise dominates above a certain wavenumber that depends on the signal-to-noise ratio (SNR$\equiv$Var$[u_i]$/Var$[u_i f(0, \sigma)]$). The exponent depends on the dimension of performed DFT, and the wavenumber-dependence of noise. When the latter can be ignored, the dependence becomes κ^2 for 3D DFT and κ for 2D DFT.

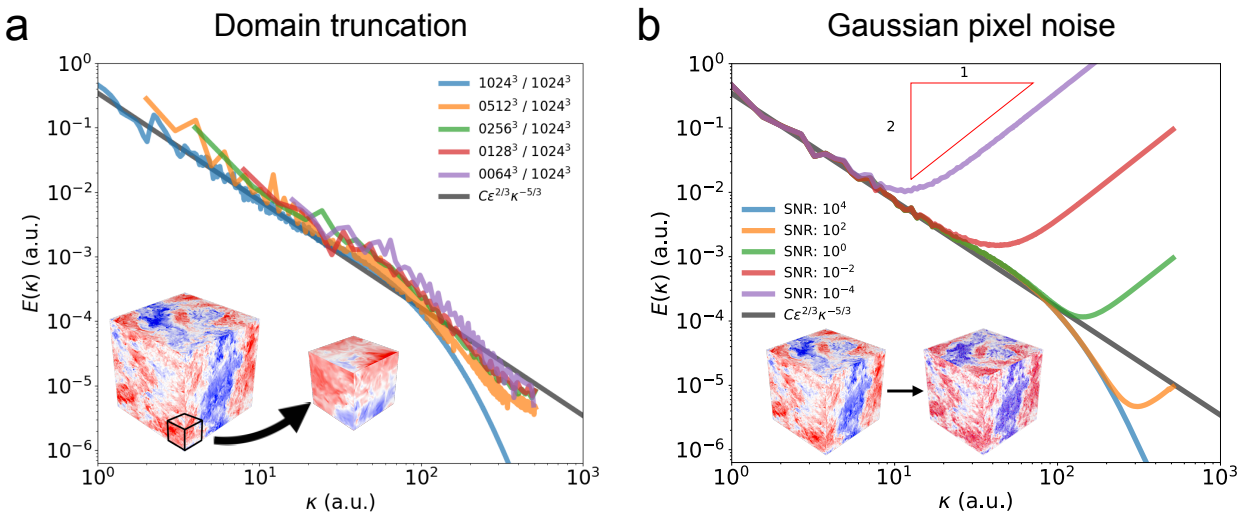

Figure 3.33: **Effects of domain truncation and gaussian noise on the energy spectrum** (a)Domain truncation- the loss of periodicity leads to overestimate the spectral contribution at high wavenumber due to aliasing and spectral leakage. (b) Gaussian noise- The noise becomes dominant at high wavenumber, depending on the signal-to-noise ratio. The power at high wavenumber depends on the Jacobian and the wavenumber dependence of noise. When the latter can be ignored, the dependence becomes κ^2 for 3D DFT and κ for 2D DFT.

In summary, the spectral leakage and noise lead to the overestimation of the spectral density at high wavenumber as shown by the light blue curve in Figure 3.31. For example, [56, 8] report an energy spectrum with this trait. Improving the image qualities and using the appropriate PIV parameters ('quarter rule'[136]) may reduce the noise[186]. In the next section, we shall see that a procedure called 'windowing' mitigates the spectral leakage.

3.10.4 Windowing and bumping

Removing the spectral leakage is not possible because the inverse of a convolution operator does not exist; however, a process called 'windowing' can mitigate the leakage by enforcing periodicity to the signal. The truncated velocity fields are first multiplied by the window function before taking the Fourier transform. The optimal choice of the window function depends on the underlying spectrum. In general, wideband windows are suited for signals with

a high dynamic range like the turbulent energy spectrum but offer less sensitivity, whereas the narrowband windows such as a rectangular window have a low dynamic range but high sensitivity. The dynamic range and sensitivity cannot both be maximized simultaneously. Therefore, it is critical to test the effect of different windows on the expected spectrum to make an informed decision. Figure 3.34a-b shows rectangular (narrowband), hamming (intermediate), flattop (wideband) windows in the real and Fourier space. The wider the main lobe becomes, the broader a peak becomes in the Fourier space. The decay rate of the side lobe peaks determines the strength of the leakage. When we compute the energy spectrum of the windowed velocity field, we multiply the spectrum computed using Eq. 3.38 by the correction factor ζ (bumping) to compensate for the loss of the signal (velocity) by windowing.

$$\zeta = \frac{\int_{\mathcal{V}} u_i(\vec{x}) u_i(\vec{x}) d\vec{x}}{\int_{\mathcal{V}} w^2(\vec{x}) u_i(\vec{x}) u_i(\vec{x}) d\vec{x}} \tag{3.45}$$

Here, $w(\vec{x})$ is a window function. Figure3.34(c-e) shows the energy spectra with no window, a flattop, and a hamming window respectively. The flattop window enables to resolve the dissipation range thanks to its high dynamic range.

3.10.5 PIV algorithm and its nature as a low-pass filter

In this section, we demonstrate that it is possible to obtain an energy spectrum that is consistent with the ground truth via a 'synthetic PIV' measurement that mimics ideal PIV conditions. The observed deviations can be explained by considering spectral leakage, and noise (Figure 3.33). We further compare the effects of the PIV interrogation window size to a low pass filter[191], and find that the effects of PIV interrogation window size are similar to those of box filtering.

To assess the spectrum of the PIV-generated velocity fields, we created synthetic images

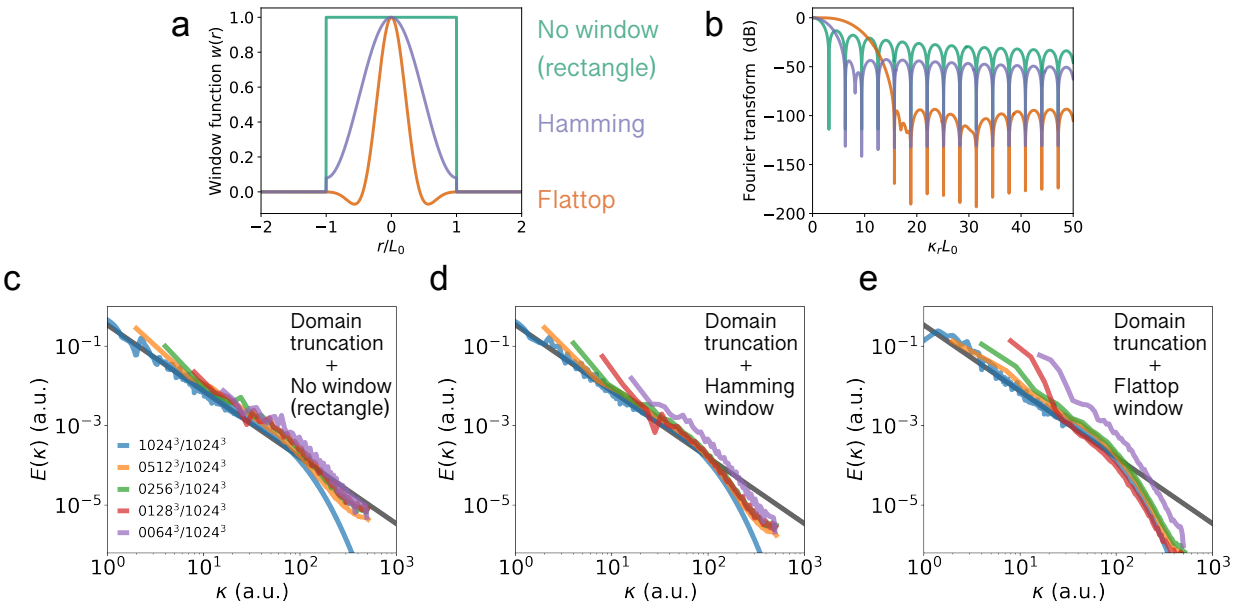

Figure 3.34: **Windowing mitigates spectral leakage originated from the domain truncation.**(a) Amplitude of the rectangle, hamming, and flattop windows are shown. Multiplying the rectangle window to the true velocity field results in a truncated velocity field with width L_0. (b) The Fourier transforms of the considered window functions reveal the degree of spectral leakage. The rectangular window has high spectral resolution but a low dynamic range (strong leakage), whereas the flattop window has the opposite character. The hamming window has an intermediate characteristics. (c) Effect of truncating a velocity field with no windowing (d) Applying the hamming window to the truncated velocity field mitigates the leakage due to the domain truncation. The shown spectral density is bumped by a correction factor ζ. (e) Same as (d) but with the flattop window.

of particles advected by a turbulent field from JHTD data. The field is resolved spatially and temporarily with a periodic boundary condition. With the optimized images and PIV settings (0.012 particle-per-pixel (ppp), L=2048px, total number of particles per image: 5×10^4, initial interrogation window size: 32px, final interrogation window size $W = 4\eta$=4px), it is indeed possible to extract the accurate three-dimensional energy spectrum from the PIV-generated field (Figure 3.35a). In terms of the image quality, we find that images with high seeding density (greater than 0.01 ppp) is critical. The temporal spacing between the adjacent frames should be less than 0.5 Kolmogorov time scales. As for the PIV settings, the smallest interrogation window in the multi-pass algorithm should be comparable to the Kolmogorov length scale. Further discussion on the required criteria to resolve a turbulent field can be found in [186, 136].

We tested two PIV algorithms (1. window deformation iterative multi-grid (WIDIM) [149] 2. Pyramid algorithm [155]), and observed that the pyramid algorithm extracts the small-scale motion better than the WIDIM; the pyramid algorithm extends the band of accurate measurement by 50% in the wavenumber space, compared to WIDIM (Figure 3.35a). The obtained spectra are in agreement with the reference up to the detection limit.

Any interrogation-based PIV acts as a low-pass filter on the true velocity field [191]. This is because the fundamental operation of PIV is peak finding of a cross-correlation map inside the interrogation windows. It assigns essentially an average displacement vector inside the interrogation window. Hence, the dimension of the interrogation window ($W_x \times W_y \text{px}^2$) sets the smallest motion PIV could detect. This effect could be modeled by a $W_x \times W_y$ box filter (Figure 3.35b). The actual PIV operation is more complex than box filtering; however, we find that the spectra of the PIV-generated fields are similar to that of the box-filtered field. If not compensated for, this effect could lead turbulence studies using PIV to report a narrower inertial subrange than the truth. Understanding this effect is therefore critical to correctly estimate the κ dependence on the energy spectrum. The same low-pass filtering

is expected for 3D PTV if the Eulerian field is reconstructed by binning the Lagrangian velocities into voxels.

Figure 3.35b suggests that the any motion smaller than the interrogation is not resolved by PIV. Based on this result, we conclude that the energy spectrum above $\kappa \approx \pi/W$ is significantly underestimated. In Figure 3f and Figure 3.31, unfilled markers indicate the underestimation due to this effect of PIV.

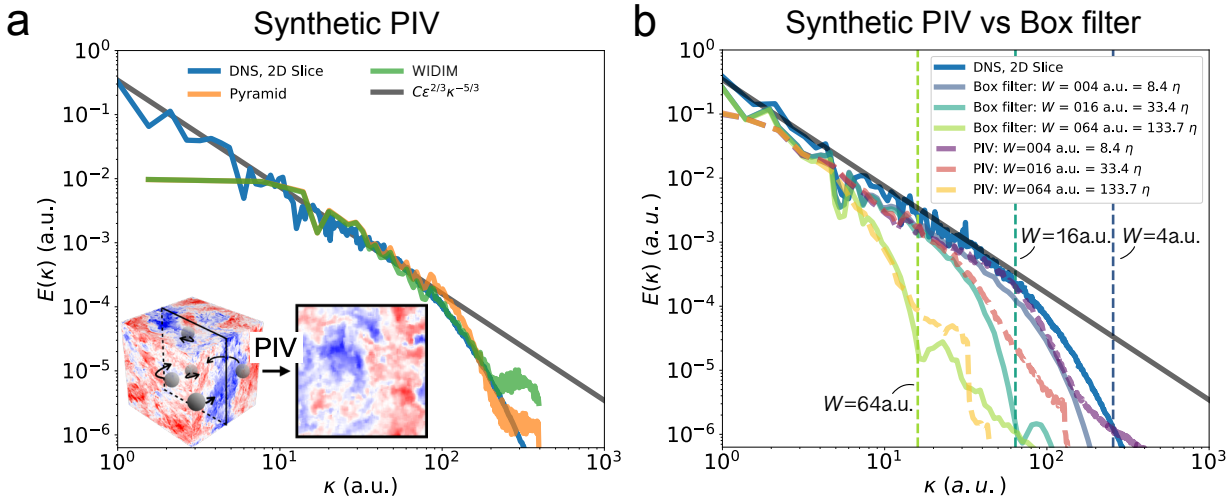

Figure 3.35: **Energy spectrum of a velocity field extracted by performing PIV on synthetic data** (a) Given images with highly seeded particles and zero noise, the pyramid algorithm (orange) [155] yields a more resolved energy spectrum than the standard cross-correlational algorithm (WIDIM, green). (b)PIV operation is comparable to box filtering with its kernel size as same as the interrogation window W. The energy spectrum of the PIV-generated field (algorithm: pyramid) deviates from the ground truth above $\kappa = \pi/W$.

3.10.6 Computation of structure function

The (second-order) structure function D_{ij} possesses equivalent information as the one-dimensional, energy spectra. With homogeneity and isotropy, it is defined as

$$D_{ij}(r) = \langle \delta u_i \delta u_j \rangle \tag{3.46}$$

with $\delta u_i(\vec{x}, \vec{r}) = u_i(\vec{x} + \vec{r}) - u_i(x)$. The longitudinal, structure function is related to the one-dimensional, longitudinal energy spectrum. For example, $D_{11}(r\hat{e_1}) = 2\int_0^\infty E_{11}(\kappa_1)[1 - \cos(\kappa_1 r)]d\kappa_1$.

We compute δu_i at every possible point on the 2D velocity field of a set of snapshots, then take an average over time and space. The number of available samples δu_i with a separation distance r depends on its position $\vec{x}$. Take a square velocity field as an example. The number of available samples with r =(diagonal distance of the square) is much more limited than small r. To ensure the same statistical weight at every r, we randomly sample m pairs for each r to compute $D_{ij}(r)$. We also make sure that each snapshot is statistically independent by only considering the snapshots that are temporally separated by integral time scale $\tau_{\mathcal{L}} = \mathcal{L}/u'$.

By definition, the structure function does not face the undesired effects in the spectral space as explained in the previous sections. It is, however, susceptible to the low-pass character of the PIV operation. Hence, we apply the same criteria as the energy spectrum, and consider that the structure function values at a scale below $r \approx 2W$ are significantly underestimated. In Figure 3g and Figure 3.31, unfilled markers indicate the underestimation due to PIV.

3.10.7 Energy spectrum over a region of interest

Eq. 3.38 and 3.44 provide means to compute the energy spectrum over a region of interest (ROI). The observable band $[\kappa_{min}, \kappa_{max}]$ is limited by the sampling frequency of the data and the size of the ROI. These *local* energy spectra do not necessarily match a part of the energy spectra of the entire flow. To match these two spectra, it is necessary for the turbulent field to be homogeneous.

In the case of inhomogeneous turbulence, the global energy spectra represent a mixture of different statistical states, and deviate from the results of HIT. In our experiments, the

flow induced by the repeated collisions of vortex rings consists of a homogeneous, isotropic turbulent core and comparatively quiescent surroundings. Therefore, we present the *local* energy spectrum over a rectangular (or cuboidal for 3D PTV) region of the homogeneous, turbulent core in Figure 3f.

3.10.8 3D energy spectrum derived from 3D PTV data

We report the energy spectrum of a fluctuating velocity field measured by 3D PTV. The extraction of all three components of velocity vectors enables the computation of the spectrum directly via Eq. 3.38. Figure 3.36 shows the energy spectrum of the central region of our turbulent blob. The temporal average of the spectrum is shown here as the turbulence inside the blob is statistically steady with weak dependence on the phase of forcing. We compare it to the corresponding spectrum from [142] by converting their 1D energy spectrum to $E(\kappa)$ via $E(\kappa) = \frac{1}{2}\kappa^3 \frac{d}{d\kappa}\left(\frac{1}{\kappa}\frac{dE_{11}(\kappa)}{d\kappa}\right)$. All energy spectra with three Re_λ exhibit the Kolmogorov scaling in the inertial subrange. Furthermore, the rescaled spectra obtained by 3D PTV and 2D PIV are consistent with the universal function reported in [142]. As discussed in the main text, both 3D PTV and 2D PIV are limited by the image resolution and the finite field of view. The size of the interrogation window determines the upper bound of the valid region of the spectrum ($\kappa\eta \leq \pi\eta/W$). If the integral scale were greater than the field of view, the spectrum could not resolve the energy containing range. This can be seen with the curve of ($Re_\lambda = 300$, 3D PTV) in Figure 3.36. The same effect is observed for ($Re_\lambda = 228$, 2D PIV) since the domain of analysis was restricted to the inner part of the energetic region($r \leq R_{\text{blob}}$).

We note that the geometry of the velocity field obtained by 3D PTV is in general a cuboid and not a cube, reflecting the differences between sensor dimensions and resolution and the maximum depth that 3D PTV accurately measures. A difference in the length of the data in each dimension affects the quality of DFT. This is because three sinc functions with different

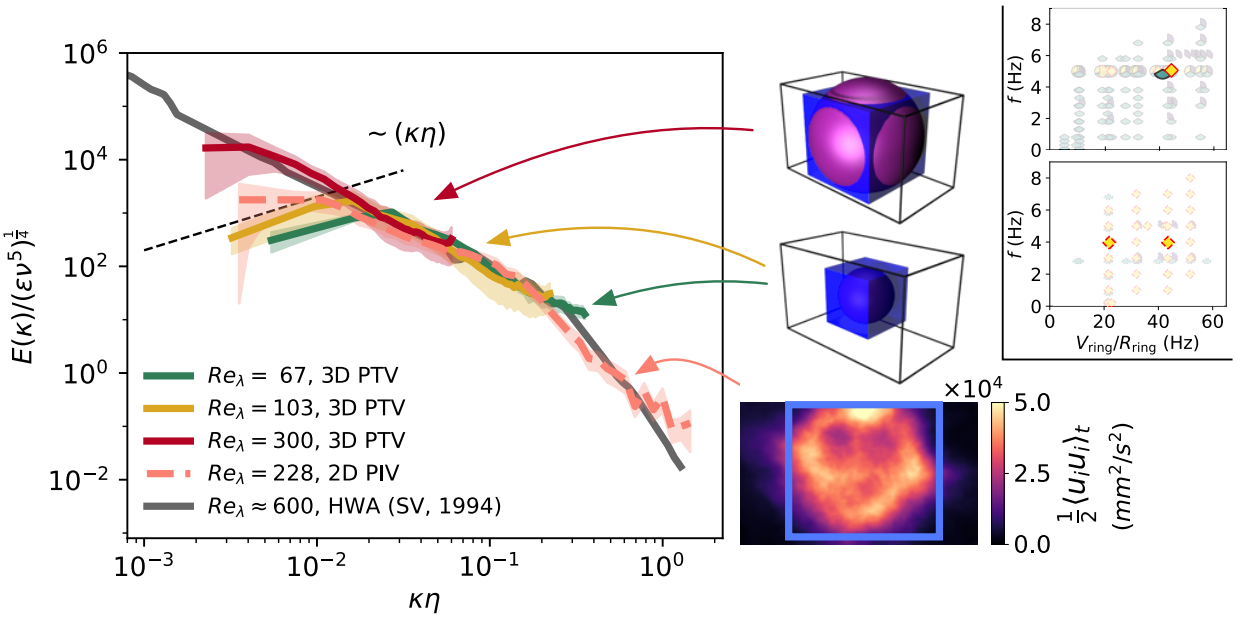

Figure 3.36: **3D energy spectra of velocity fields obtained by 3D PTV and 2D PIV.** The blue cubes or square on the right represent the domain that the DFT is conducted (Eq. 3.38). The turbulent core ($r = R_{\text{blob}}$) is represented by the purple sphere. The error bands represent the standard deviation of the shell-average of $E(\kappa) = (1/V_{\text{shell}}) \int_{\kappa}^{\kappa+\Delta\kappa} E(\vec{\kappa'}) \cdot 4\pi\kappa'^2 d\kappa'$ where $V_{\text{shell}}(\kappa) = (4\pi/3)[(\kappa+\Delta\kappa)^3 - \kappa^3]$.

frequencies are convoluted in κ space. If left uncorrected, this results in a wavy behavior of the energy spectrum at high κ. To mitigate this effect, we pad the velocity field with to make the shape of the array cubic before taking the DFT. Zero-padding simply extends the signal, and interpolates it in the wavenumber domain; however, cubing the array allows the spectral leakage to occur at the same frequencies along all the three directions, making the spectrum more readily interpretable.

3.11 Energy balance

In this section we examine the energy balance of a turbulent blob in detail. We shall quantify how much dissipation occurs inside the blob, and identify its relation with the injected power. The kinetic energy $\mathscr{E} = \frac{1}{2}U_iU_i$ of a viscous flow obeys:

$$(\partial_t + U_i\partial_i)\mathscr{E} + \partial_i T_i = 2\nu S_{ij}S_{ij} \tag{3.47}$$

where $S_{ij} = \frac{1}{2}(\partial_j U_i + \partial_i U_j)$ is the rate-of-strain tensor, and $T_i = U_i p/\rho - 2\nu U_j S_{ij}$ is the energy flux [134]. The Reynolds decomposition $U_i = \langle U_i\rangle_t + u_i$ yields

$$(\partial_t + \langle U_i\rangle_t\partial_i)\langle\mathscr{E}\rangle_t + \partial_i(u_i\mathscr{E} + \langle T_i\rangle_t) = -\overline{\epsilon} - \epsilon \tag{3.48}$$

where $\overline{\epsilon} = 2\nu\langle\overline{S}_{ij}\overline{S}_{ij}\rangle_s$ with $\overline{S}_{ij} = \frac{1}{2}(\partial_j\langle U_i\rangle_t + \partial_i\langle U_j\rangle_t)$ is the mean rate of strain. Eq. 3.48 reveals the decomposition of the energy dissipation in the mean and the fluctuating flows. In the case of a turbulent blob, the mean flow consists of eight vortex rings that repeatedly travel towards the center (See Figure 3a in the main text). On the σ_h plane, the enstrophy measurements (Figure 3.26f) indicate $\epsilon/\overline{\epsilon} = \omega^2/\overline{\Omega}^2 = O(10^2)$. Below we assume $\overline{\epsilon} \ll \epsilon$ anywhere in the system.

3.11.1 Partition of dissipation in a turbulent blob

The energy dissipation within a domain $\mathcal{V}$ that encloses a blob is

$$\mathcal{D}(r/R_{\text{blob}}) = \rho\int_{\mathcal{V}}\epsilon(\vec{r})dV \tag{3.49}$$

where $\epsilon(\vec{r}) \equiv 2\nu\langle s_{ij}s_{ij}\rangle_t$ is a spatially varying dissipation rate. The radial profile of the local dissipation rate (or enstrophy density equivalently) shows that $\epsilon(\vec{r})$ depends only on the radial distance, is constant up to a radius R_{blob}, and decays approximately as $\epsilon(r) \propto r^{-4}$

for $r \geq R_{\text{blob}}$.

$$\epsilon(r) = \begin{cases} \epsilon_0 & (r < R_{\text{blob}}) \\ \epsilon_0 (\frac{R_{\text{blob}}}{r})^4 & (r \geq R_{\text{blob}}) \end{cases} \tag{3.50}$$

It is useful to compute the dissipation within a sphere of radius r for a turbulent blob with this profile. The fraction of energy dissipation inside the sphere to the total is

$$p(r/R_{\text{blob}}) = \begin{cases} \frac{1}{4}\left(\frac{r}{R_{\text{blob}}}\right)^3 & (r < R_{\text{blob}}) \\ \\ 1 - \frac{3R_{\text{blob}}}{4r} & (r \geq R_{\text{blob}}). \end{cases} \tag{3.51}$$

If we include a cutoff in the considered integral because the chamber size is finite, the expression becomes

$$p(r/R_{\text{blob}}, (L_{box}/2)/R_{\text{blob}}) = \begin{cases} \frac{1}{4}\left(\frac{r}{R_{\text{blob}}}\right)^3 (1 - \frac{3R_{\text{blob}}}{2L_{box}})^{-1} & (r < R_{\text{blob}}) \\ \\ (1 - \frac{3R_{\text{blob}}}{4r})(1 - \frac{3R_{\text{blob}}}{2L_{box}})^{-1} & (R_{\text{blob}} \leq r \leq \frac{L_{box}}{2}). \end{cases} \tag{3.52}$$

Note that fraction of energy inside the blob to the whole depends not only the blob radius but also its respective size to the system. The same function applies to the amount of energy and enstrophy inside the sphere with radius r.

Figure 3.37(a) shows the model function (Eq. 3.50) and the scaled cummulative function p (Eq. 3.52)for $R_{\text{blob}} = \sqrt{6}R$. The value of R_{blob} with respect to the ring radius R is taken from the experimental data (Figure 3b). There is a geometrical interpretation of $R_{\text{blob}} = \sqrt{6}R_{\text{ring}}$. The symmetrical configuration of the eight vortex rings defines an

octahedron as explained in Sect3.15. Since the vortex atmosphere is ellipsoidal, the majority of the energy is housed inside a sphere as large as the circumscribed sphere of the octahedron which has a radius of $\sqrt{6}R_{\rm ring}$. One can also imagine a polyhedron such that eight spheres with radius $R_{\rm ring}$ fused together on each face of an octahedron. The radius of such a circumscribed sphere is $(1+\sqrt{2})R_{\rm ring} \approx 2.41R_{\rm ring}$, sufficiently close to $\sqrt{6}R_{\rm ring} \approx 2.45R_{\rm ring}$.

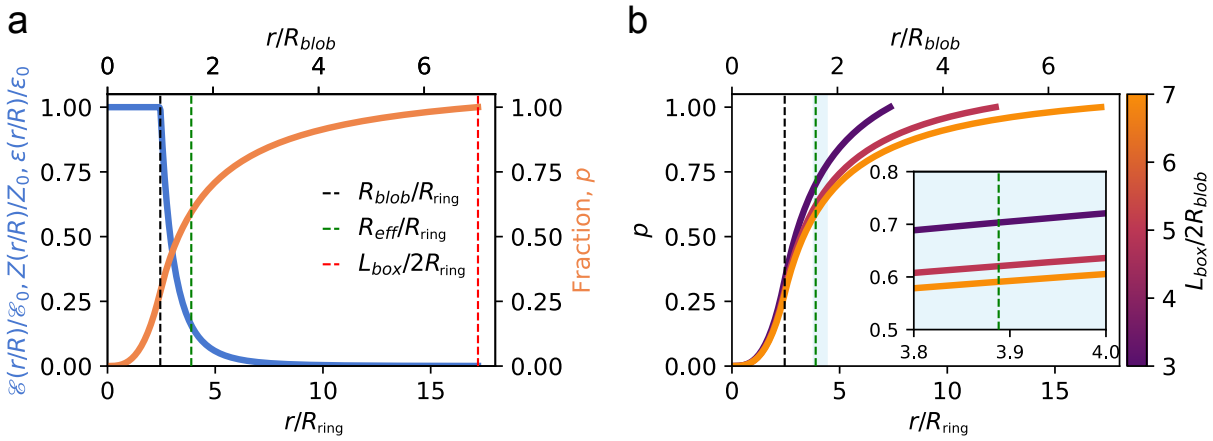

Figure 3.37: **Model radial distribution of energy $\mathscr{E}$, enstrophy Z, and dissipation rate ϵ.** (a) Radial distribution function (blue) and scaled cummulative function $p(r)$(orange) of energy/enstrophy/dissipation rate are shown for a case $R_{\rm blob} = \sqrt{6}R_{\rm ring}$ and $(L_{\rm box}/2)/R_{\rm blob} = 7$. (b)Dependence of p on the blob radius $R_{\rm blob}$ and the system size $L_{\rm box}$ is shown.

The total dissipation is

$$\mathcal{D}_{\rm tot} = \frac{16}{3}\pi\rho\epsilon_0 R_{\rm blob}^3 = \frac{4}{3}\pi\rho\epsilon_0 R_{\rm eff}^3 \tag{3.53}$$

where $R_{\rm eff} = 4^{\frac{1}{3}}R_{\rm blob} \approx 1.59R_{\rm blob}$ is the effective radius of the blob. The dissipation within a sphere of radius r is given by

$$\mathcal{D}(r/R_{\rm blob}) = p(r/R_{\rm blob})\mathcal{D}_{\rm tot}. \tag{3.54}$$

3.11.2 Estimation of dissipation rate from PIV data

Measuring the dissipation rate in turbulence robustly using PIV remains a challenging endavor [49]. Multiple methods have been proposed, including direct computation from the rate-of-strain tensor to fitting measured correlations to the structure function; all methods, however, they are often susceptible to the choice of interrogation window size and measurement noise. Ref [49] investigated five methods to estimate the dissipation rate from PIV data of zero-mean, gaseous turbulence: (1) Direct method via the rate-of-strain tensor (2) A large eddy method with subgrid scale modeling (3) A method based on the scaling $\epsilon_0 = A\frac{u'^3}{\mathcal{L}}$ (4) Fitting the energy spectrum to the Kolmogorov spectrum (5) Fitting the n-th order structure function to $(\epsilon_0 r)^{n/3}$. The conclusion reached in Ref [49] is that the method of fitting to the the second-order structure function yields the most reliable estimate.

In this section we present the results of three methods to compute the dissipation rate on our data:

1. The direct method via the rate-of-strain tensor.

2. Fitting the energy spectrum to the Kolmogorov spectrum.

3. Fitting the second order structure function to $(\epsilon_0 r)^{2/3}$.

To estimate the dissipation rate we acquired 2D PIV data with high magnification. The relevant dimensions of the experiments are shown in Figure 3.38, together with a typical snapshot of a local dissipation rate, obtained from the direct method. The data is then median-filtered (see below) and the dissipation rates estimated as follows:

1. For the direct method, we compute

$$\epsilon_{s_{ij}} = 6\nu\langle(\partial_1 u_1)^2 + (\partial_2 u_2)^2 + (\partial_2 u_1)(\partial_1 u_2)\rangle, \tag{3.55}$$

assuming the isotropy [69].

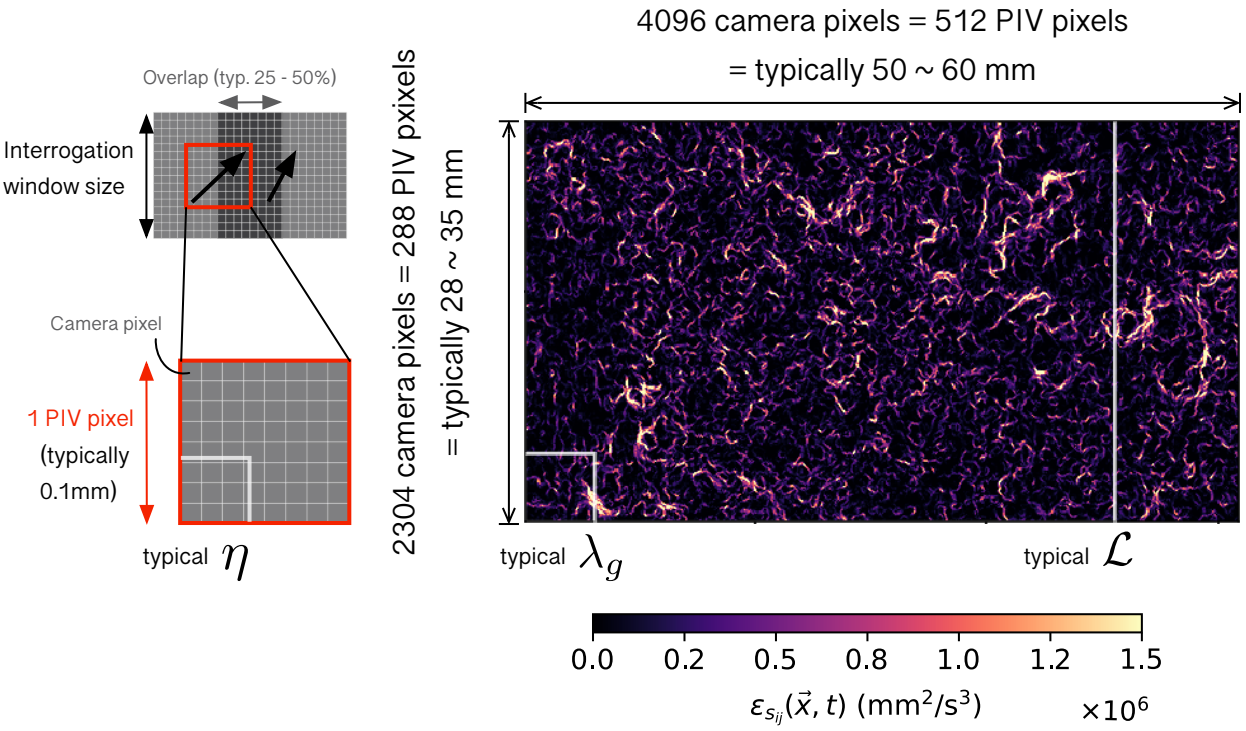

Figure 3.38: **Typical turbulent length scales (Kolmogorov, Taylor, integral length scales- $\eta, \lambda_g, \mathcal{L}$) and PIV parameters for the experiments to estimate dissipation rate.** The view spatially resolves turbulent motions at small scales where dissipation takes place. The heat map shows the local dissipation rate computed using the rate-of-strain tensor.

2. For the spectral method, we fit the one-dimensional energy spectrum $E_{11}(\kappa_1)$ to $C_1\epsilon^{2/3}\kappa_1^{-5/3}$ with $C_1 = 0.52$ [166]. We then identify numerically the plateau of the compensated energy spectrum $[E_{11}/(C_1\kappa_1^{-5/3})]^{3/2}$.

3. For the structure function method, we fit the longitudinal second-order structure function $D_{LL}(r) = \langle \delta u^2 \rangle / \langle u_i^2 \rangle$ to $C_2(\epsilon_{D_{LL}} r)^{2/3}$ where $\delta u(\vec{x}, r) = u_i(\vec{x} + r\hat{x}_i) - u_i(\vec{x})$, and $C_2 = 2.1$ [142]. We then identify numerically the plateau of the compensated structure function $1/r(D_{LL}/C_2)^{3/2}$.

Effect of median-filtering on estimation of dissipation rate

Prior to computing the dissipation rate, the PIV-extracted field is convolved with a median filter (with a kernel size of 3×3 or 5×5 px^2) to mitigate the effects of spurious velocity vectors. Median-filtering replaces a local velocity vector with a median vector in the kernel. This both removes spurious PIV vectors but also has the effect of blurring the velocity field (Figure 3.39a). Figure 3.39 shows the results of all three estimation methods as a function of the median filter window, illustrating the effects of median filtering. The data corresponds to $(V_{\text{ring}}/R_{\text{ring}}, f) = (40\text{Hz}, 7\text{Hz})$ on Figure 3.24a.

Most spurious vectors are removed after applying the smallest filter possible (3×3 PIV pixels). This effect is clearly visible in the compensated energy spectrum (See Figure 3.39b). Median-filtering with a larger kernel however, also blurs the velocity field. This in turn affects all correlations, but most strongly short-range correlations. The effect on the dissipation rate estimate obtained by each of the three methods is shown explicitly in Figure 3.39g-h. The direct method $\epsilon_{s_{ij}}$ is most susceptible out of the three because it is based on the velocity gradient. The energy function method $\epsilon_{E_{11}}$ is more robust than the direct method as long as the inertial subrange is visible (Figure 3.39b) (though median-filtering with a large kernel clips the inertial subrange). The structure function method $\epsilon_{D_{LL}}$ also has the same problem; however, the estimated value drops more slowly than $\epsilon_{E_{11}}$ as the kernel size increases (See

Figure 3.39b and d). In all methods, the estimated dissipation rate drops significantly when the kernel size is comparable to the Taylor microscale which is equal to 3 mm in Figure 3.39g-h.

Out of the three proposed methods to estimate dissipation rate, the structure function method is found to be least affected by median-filtering. As can be seen Figure 3.39g-h, applying a large kernel may remove the noise more effectively but blurs the field more, leading to underestimate dissipation rate. In the Figure 3b-c, f-g and 4a-b, we report the results based on the velocity fields that are median-filtered with the smallest kernel (3×3 px^2). Filtering with a larger kernel has the predominant effect of blurring the field. With the chosen (3×3 px^2) median filter, the three methods of energy dissipation estimation yield similar values of the dissipation rate.

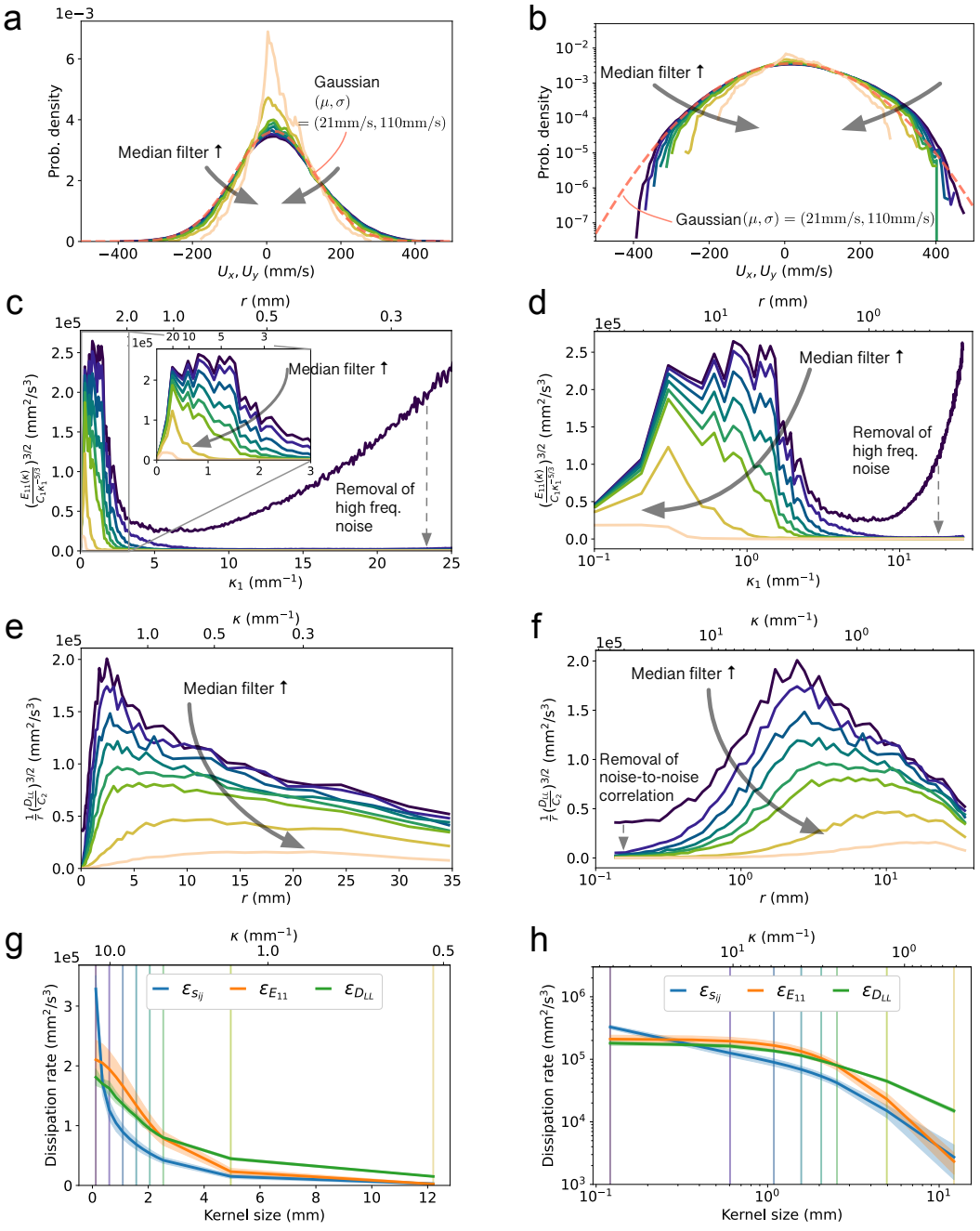

Figure 3.39: **Effect of median filtering PIV-extracted velocity fields inside a turbulent core.** (**a**, **b**) Probability distribution function of velocity components U_x and U_y (combined) on the lin-lin, and log-lin scales. (**c**, **d**) Compensated one-dimensional energy spectrum on the lin-lin, and lin-log scales. (**e**, **f**) Compensated structure functions on the lin-lin, and lin-log scales. (**g**, **h**) Effect of a median filter on the three methods used to estimate dissipation rate is shown on the lin-lin and log-log scales. The dissipation rate is estimated via the rate-of-strain tensor $\epsilon_{s_{ij}}$, energy spectrum $\epsilon_{E_{11}}$, and structure function $\epsilon_{D_{LL}}$. The error bands in (g-h) represent SD of tempo-spatial averaging (n=50 frames).

3.11.3 Partition of injected energy

The energy balance over a domain $\mathcal{V}$ that encloses a blob is

$$\mathcal{I} \approx 8K_{\text{ring}}f \tag{3.56}$$

because we expect only the energy within the vortex atmosphere is fed to sustain the blob. If there is only one vortex ring in a flow, the ratio of energy enclosed within the atmosphere to the total $c = K_{\text{ring}}/K$ is completely determined by the shape of the vortex atmosphere (see Box 3), and remains nearly the same $c \approx 77\%$ for the ellipsoidal atmosphere. For the two canonical vortex ring models, the injected power $\mathcal{I}$ is given by

$$\mathcal{I} = \begin{cases} 4c\rho\Gamma_{\text{ring}}^2 R_{\text{ring}} f \left[\ln \frac{8R_{\text{ring}}}{a} - \alpha\right] & \text{(thin-cored vortex ring)} \\ \frac{64\pi}{105} c\rho\Gamma_{\text{ring}}^2 R_{\text{ring}} f & \text{(Hill's spherical vortex).} \end{cases} \tag{3.57}$$

The coefficient represents the difference between the models. The generated vortex rings in this study has coefficients between these two models(Figure 3.17); however, it depends on the experimental conditions $(L_*, v_{\text{eff}}, D_o, D_p)$. Thus we directly measure the energy of the injected vortex rings from 2D PIV data shown in Figure 3.23.

3.11.4 Balance of energy injection and dissipation

We first turn our attention to the total energy balance ($\mathcal{D}_{\text{tot}}$ vs $\mathcal{I}_{\text{tot}} = \mathcal{I}/c$) in the chamber. Regardless of the methods to estimate the dissipation rate, the total dissipated power monotonically increases with the injected power over almost two decades (Figure 3.40e-g). The method using the rate-of-strain tensor tends to overestimate the dissipation, compared to the methods involving the energy spectrum and the structure function. This is consistent with [49] as the noise in the measured velocity field contributes to this overestimation. Removing the noise with a median filter (Figure 3.40a-c) leads the estimates by all three

methods to agree with each other(Figure 3.40d-f). This gives us more confidence that the filtered velocity field gives the more accurate estimate of the dissipation rate than the raw field. There, the dissipated power is indeed proportional to the injected power. We find $\mathcal{D}_{\rm tot}/\mathcal{I}_{\rm tot} = 1.07 \pm 0.09$ (3px $\times$ 3px(=$5.6\eta \times 5.6\eta$)), 0.64 ± 0.05(5px $\times$ 5px=$9.3\eta \times 9.3\eta$) for the median-filtered fields. The attenuation with a larger kernel is expected as it blurs the velocity field more.

As discussed in the main text, the far-field contribution in $\mathcal{I}_{\rm tot}$ should be neglected to assess the energy balance of the blob. The ratio

$$\frac{\mathcal{D}(\frac{r}{R_{\rm blob}})}{\mathcal{I}} = \frac{\mathcal{D}_{\rm tot}}{\mathcal{I}_{\rm tot}} \frac{p(\frac{r}{R_{\rm blob}})}{c} \tag{3.58}$$

represents how much injected power via vortex rings is dissipated as a function of a (scaled) radius. In a sense, this gives a conversion rate from coherent vortex motion to turbulence in terms of energy. Considering $\frac{\mathcal{D}_{\rm tot}}{\mathcal{I}_{\rm tot}} \approx 1$, the power associated to the vortex ring atmosphere is completely dissipated within a sphere of radius $r = \frac{3}{4(1-c)} R_{\rm blob} \approx 3.3 R_{\rm blob}$ with $c = 0.77$. Of which, 33% is dissipated up to $r = R_{\rm blob}$ and 68% is dissipated up to $r = R_{\rm eff} = 4^{\frac{1}{3}} R_{\rm blob}$.

3.11.5 Dissipation rate according to the energy balance

Equating the dissipation $\mathcal{D}(r/R_{\rm blob})$ (Eq. 3.54) with the injected power $\mathcal{I}$ (Eq. 3.57) gives an expression about the dissipation rate inside the turbulent blob in terms of the properties of the vortex rings: $\epsilon_0 \propto \Gamma_{\rm ring}^2 f / R_{\rm ring}^2 \propto V_{\rm ring}^2 f$ (Figure 4b). With $R_{\rm blob} = \sqrt{6} R_{\rm ring}$, ϵ_0 becomes

$$\epsilon_0 = \begin{cases} \frac{c(\log(8R_{\rm ring}/a) - \alpha)}{8\sqrt{6}\pi p} \frac{\Gamma_{\rm ring}^2 f}{R_{\rm ring}^2} & \text{(thin-cored vortex ring)} \\ \frac{2c}{105\sqrt{6}p} \frac{\Gamma_{\rm ring}^2 f}{R_{\rm ring}^2} & \text{(Hill's spherical vortex).} \end{cases} \tag{3.59}$$

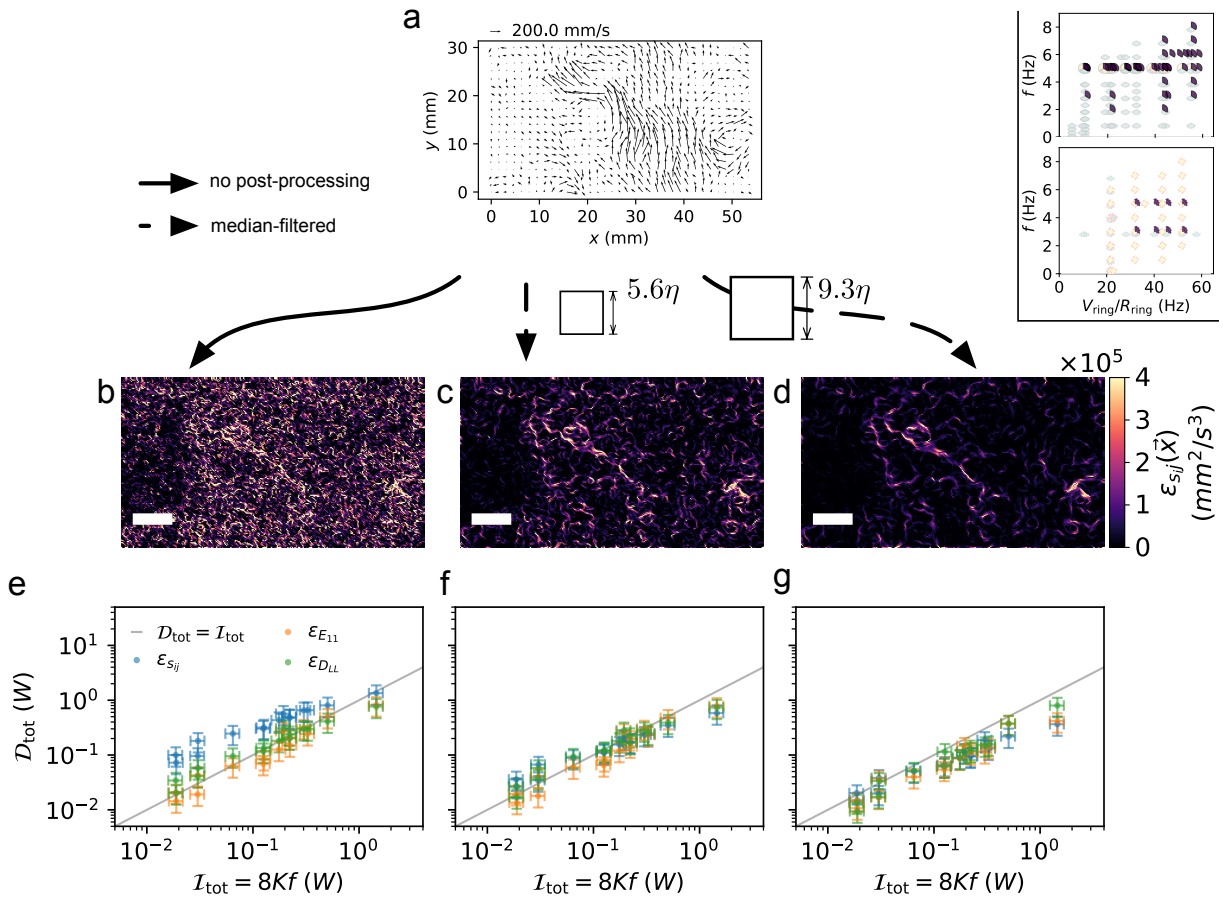

Figure 3.40: **Dissipated vs injected power inside the chamber.** (a)To compute the dissipation rate, three velocity fields are used: a raw PIV-extracted field, and two median-filtered fields. (b-d) Median-filtering the velocity fields attenuates the local dissipation rate $\epsilon_{s_{ij}}(\vec{x}) = 2\nu s_{ij}(\vec{x})s_{ij}(\vec{x})$. (e) Dissipated vs injected power inside the chamber is plotted for the three methods to estimate the dissipation rate using the raw velocity field: ϵ_{sij} uses the rate-of-strain tensor. $\epsilon_{E_{11}}$ is obtained by fitting the energy spectrum to the Kolmogorov spectrum. $\epsilon_{D_{LL}}$ is obtained by fitting the second-order structure function to Kolmogorov's 2/3 law. (f) Same as (e) but with a median-filtered velocity field (Kernel size: $5.6\eta \times 5.6\eta$). (g) Same as (e) but with another medial-filtered velocity field (Kernel size: $9.3\eta \times 9.3\eta$). Data in (e-g) are presented as mean +/-SEM (n=12).

The prefactor of Eq. 3.59 differs by the model of a vortex ring and $p(r/R_{\text{blob}})$. Here is a quick calculation of the prefactor for $r/R_{\text{blob}} = 2 \Leftrightarrow p = 5/8$ (unbounded) and $c = 0.77$. For the thin-cored model, we shall use $R_{\text{ring}}/a = 3$ as observed in the experiments, and $\alpha = 2.04$ [61] for a viscous core. The prefactors of the thin-cored model and Hill's spherical vortex model are 0.02 and 0.01 respectively. This relationship is consistent with $\epsilon_0 = \alpha_1^2 V_{\text{ring}}^2 f$ in the Figure 4b.

3.12 Tempo-spatial distribution of the local dissipation rate

The tempo-spatial variation of the energy dissipation rate is a quantity of great interest in turbulence [86, 125, 107, 108, 115, 58]. In this section, we present the tempo-spatial distribution of $\epsilon_{s_{ij}}(\vec{x},t)$ in our turbulent blob. As discussed in Section 3.11.2, the local dissipation rate $\epsilon_{s_{ij}}(\vec{x},t)$ is derived from a rate-of-strain tensor of a median-filtered velocity field (kernel size of $3\times 3\text{px}^2$, equivalent to $6\eta\times 6\eta$). The spatial average of $\epsilon_{s_{ij}}(\vec{x},t)$ yields a similar total dissipation rate as estimated by the second order structure factor and energy spectrum. The data set we present is from the experimental runs ($V_{\text{ring}}/R_{\text{ring}}$, f, method)=(42Hz, 2-7Hz, 2D PIV) on Figure 3.24a.

3.12.1 In a fully turbulent blob

We first focus on the dissipation rate inside the fully developed turbulent core ($Re_\lambda = 270$, $V_{\text{ring}}/R_{\text{ring}} = 42\text{Hz}$, $f = 7\text{Hz}$). In this regime, turbulence is very weakly dependent on the phase of forcing. As can be seen from Figure 3.41a and SI Video 13, the spatially resolved measurements reveal threads of highly dissipative regions throughout the turbulent region. The thickness of the threads is approximately 20η which coincides with a peak of the dissipation spectrum $\int_0^\infty \kappa^2 E(\kappa)d\kappa$ [134]. These filaments are dynamic. Figure 3.41b shows the value of the dissipation rate at a fixed point in space, which exhibits an intermittent behavior.

The probability distribution of the dissipation rate clearly reveals its highly uneven distribution. The average dissipation rate $\langle\epsilon(\vec{x},t)\rangle_{st}$ is overwhelmingly determined by the regions with high dissipation. Classically, Kolmogorov and Obukov predicted a lognormal distribution, which was later criticized, leading to produce the β-model [58] and multifractal models [108]; however, no consensus has been reached regarding the structure of dissipation rate and origin of intermittency. Our measurement provides a spatially resolved picture of local dissipation rate, and reveals a dynamic collection of filaments with a fractal nature.

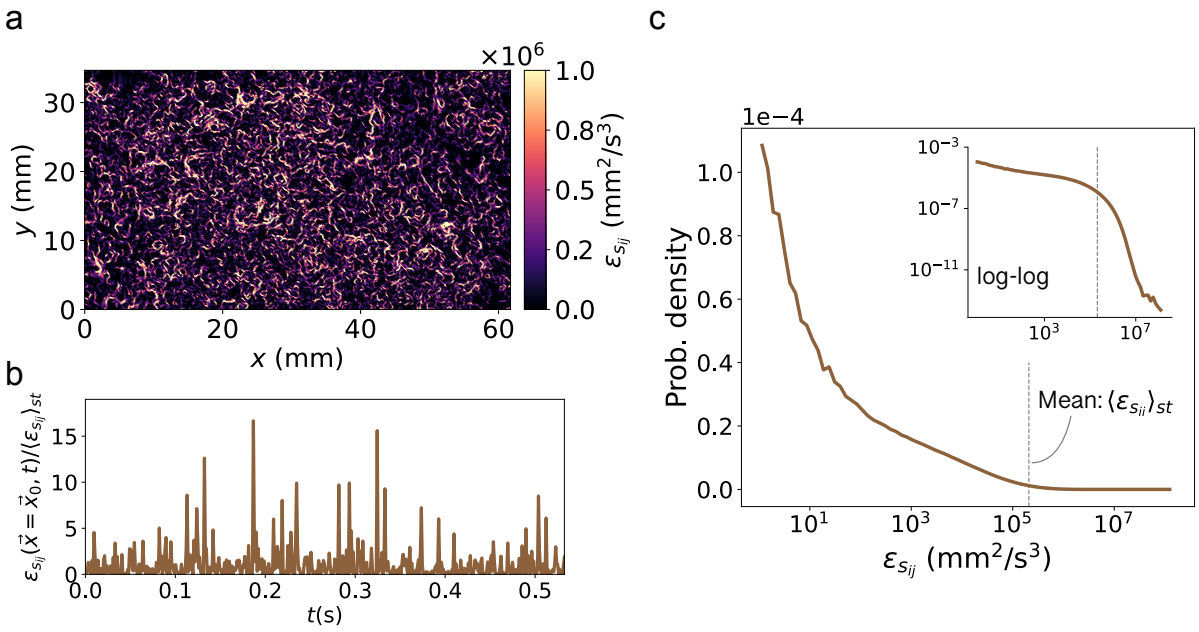

Figure 3.41: **Spatial distribution of dissipation rate inside a homogeneous, isotropic, turbulent core reveals a web-like structure of localized, dissipative region.** **($Re_\lambda = 270$, $V_{\text{ring}}/R_{\text{ring}} = 42$Hz, $f = 7$Hz)** (a) Local dissipation rate $\epsilon_{e_{ij}}(\vec{x}, t)$ (b) The dissipation rate at a fixed point exhibits an intermittent behavior. (c) Probability distribution function of $\epsilon_{e_{ij}}(\vec{x}, t)$. Kolmogorov, Taylor and integral length scales of the displayed flow are 0.047mm, 3.0mm and 25.0 mm respectively.

3.12.2 *As the forcing frequency is varied*

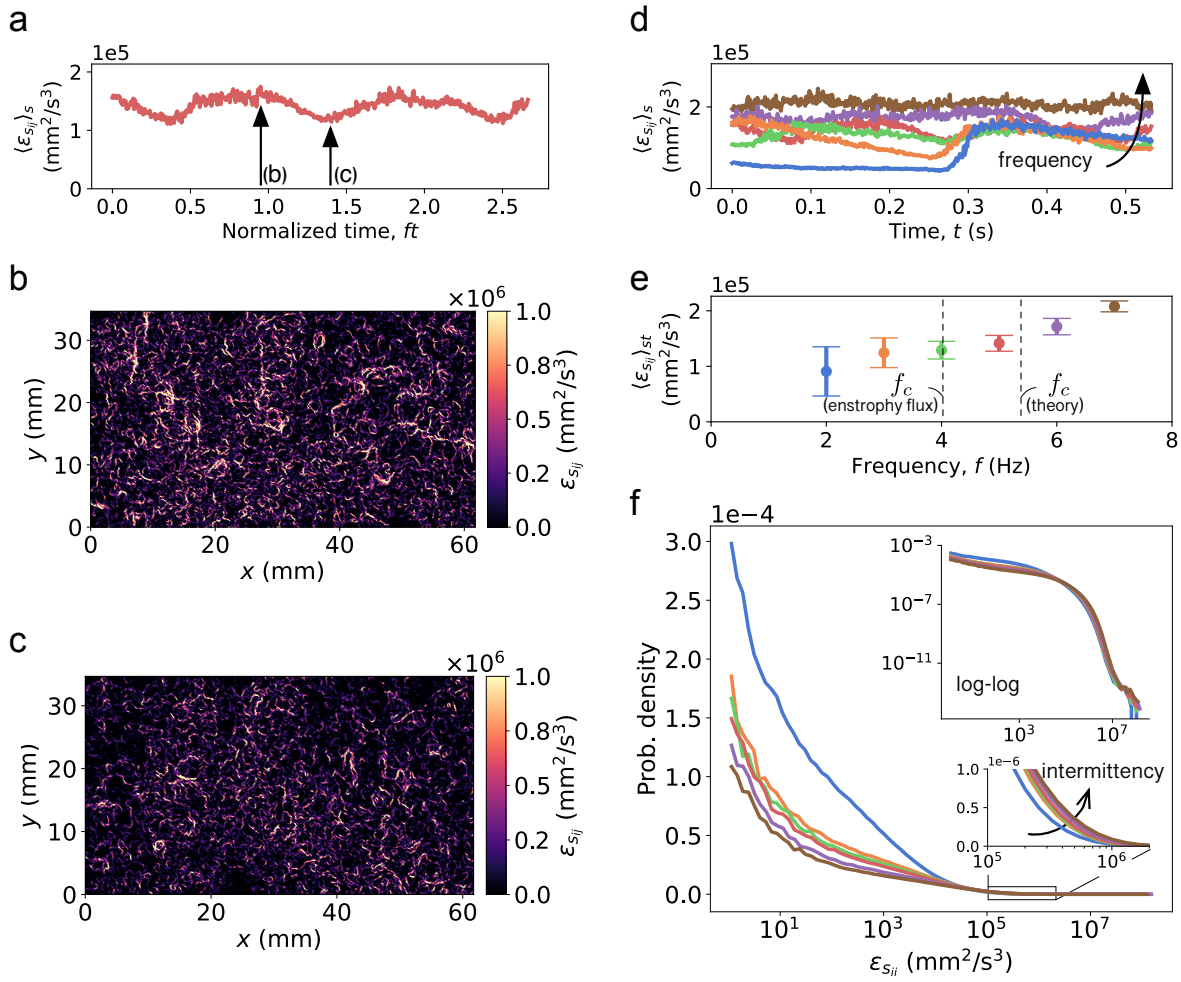

Figure 3.42: **Tempo-spatial distribution of dissipation rate inside a homogeneous, isotropic, turbulent core** (a) Spatial average of dissipation rate inside the core. (b/c)Snapshot of local dissipation rate $\epsilon_{s_{ij}}$ at the maximum/minimum. (d) Dependence on the forcing frequency. (e) Spatio-temporal average of dissipation rate against the forcing frequency is plotted. The data are presented as mean +/- SD (n=500). (f) Probability distribution function of dissipation rate inside the central region of our tank for a variety of forcing frequencies.

Figure 3.42a shows the time evolution of dissipation rate averaged over a region inside the core above the transition frequency f_c. A weak dependence on the forcing frequency can be seen. Figure 3.42b-c show spatially resolved measurements $\epsilon_{s_{ij}}(\vec{x})$ taken at a local maximum and minimum of the spatially averaged dissipation rate. SI Videow 13 shows that

the magnitude periodically varies; however, it retains a qualitatively similar structure at both moments in time.

Below the transition frequency, as localized vortex reconnections come to dominate the strain field, the phase dependence of the spatially averaged dissipation rate (Figure 3.42d) becomes more pronounced.

Above the transition frequency, on the other hand, the phase dependence of dissipation rate is washed out. In this regime, a turbulent blob is formed and the dissipation rate is proportional to the injection frequency, indicating that the viscous dissipation in turbulence matches the energy delivered by vortex rings. The same web-like structure is observed inside the turbulent blobs at different Taylor Reynolds numbers Re_λ. However, at a higher Re_λ, the flow becomes more intermittent, as reflected by the increased area fraction with a high dissipation rate (Figure 3.42f). Here, the probability distribution of the flow below the transition frequecy is also shown as a reference.

3.12.3 Note regarding periodic drives on turbulence

The response of turbulence to temporal forcing has gained significant interest in the last few decades because many turbulent flows are subject to temporal modulation. Examples include geographical flows set up by the periodical heating of the sun, and the pulsatile blood flow through arteries. Refs [30, 180, 182, 183, 90] have considered an energy injection rate of the form $\mathcal{I} = \mathcal{I}_0[1 + e\sin(2\pi f t)]$ with a small modulation amplitude ($e < 1$). They have found the enhancement of turbulent dissipation rate when the modulation frequency matches the inverse of a large eddy turnover time $\tau_\mathcal{L}$, which characterizes the energy transport time down the cascade[182].

The transition frequency, above which a turbulent blob is formed, that we predicted by either geometric arguments or matching the incoming energy to the large eddy turnover time (blue curve on the main text Figure 4) corresponds to the 'resonant frequency' at which

energy is dissipated at the maximum efficiency in a turbulent state in these studies.

A crucial difference between previous studies aimed at probing a resonant response to modulated forcing and our experiment, is the functional form of the forcing. In previous experiments a turbulent state with an intrinsic large eddy turnover time is probed at a range of modulation frequencies tuning over a dissipation 'resonance'. In our experiment, the modulation frequency is strongly coupled to the average injection rate of energy ($\mathcal{I}_0(f) = K_0 f$ where K_0 is related to the total energy delivered by vortex rings), which in turn dictates the large eddy turnover time. The temporal forcing in our experiment is therefore always near-resonant.

3.13 Enstrophy flux

As the vortex injection frequency is increased for fixed $V_{\text{ring}}/R_{\text{ring}}$ we observe a transition from a reconnection-and-escape dynamic in which most of the enstrophy leaves with the outgoing vortices to a blob state in which little to none of the injected enstrophy escapes the blob. As illustrated in Figure 4 of the main text we examined this transition by plotting the time averaged enstrophy in a cross section perpendicular to the incoming rings, as well as by integrating the enstrophy outflux.

In this section we show the enstrophy flux data in greater detail and summarize a simple image-moment approach to quantifying the visual information contained in the enstrophy cross section images (not discussed in the main text).

3.13.1 Enstrophy and mass flux through a sphere enclosing a turbulent blob

The enstrophy balance is

$$\partial_t \int_{\mathcal{V}} \Omega^2 dV = 2\int_{\mathcal{V}} \Omega_i(\partial_i U_j)\Omega_j dV - \oint_{\partial\mathcal{V}} \Omega^2 U_i n_i dS + \nu\int_{\mathcal{V}} \partial_j\partial_j\Omega^2 dV - 2\nu\int_{\mathcal{V}} (\partial_j\Omega_j)^2 dV$$

in a 3D incompressible, viscous fluid. The enstrophy is not conserved due to vortex stretching and viscous dissipation.

To examine the confinement of enstrophy, we consider its normal flux $\vec{J}_{\Omega^2}\cdot\hat{n} = \Omega^2\vec{U}\cdot\hat{n}$ through a sphere with radius $R > R_{\text{blob}}$. In the case that coherent reconnections are dominant reactions ($f < f_c$), the enstrophy flux exhibits the inflow due to the eight incoming vortex rings, followed by outflow by the six outgoing vortex rings at a later phase (Figure 3.43a and e). The mass flux also captures the inflow/outflow due to the mass transported by the incoming/outgoing vortex rings (Figure 3.43c). The crucial difference is that the mass is always balanced, whereas the enstrophy is not. Integrating the enstrophy flux over the surface and cycles gives the net amount of (escaping) enstrophy at each phase as shown by

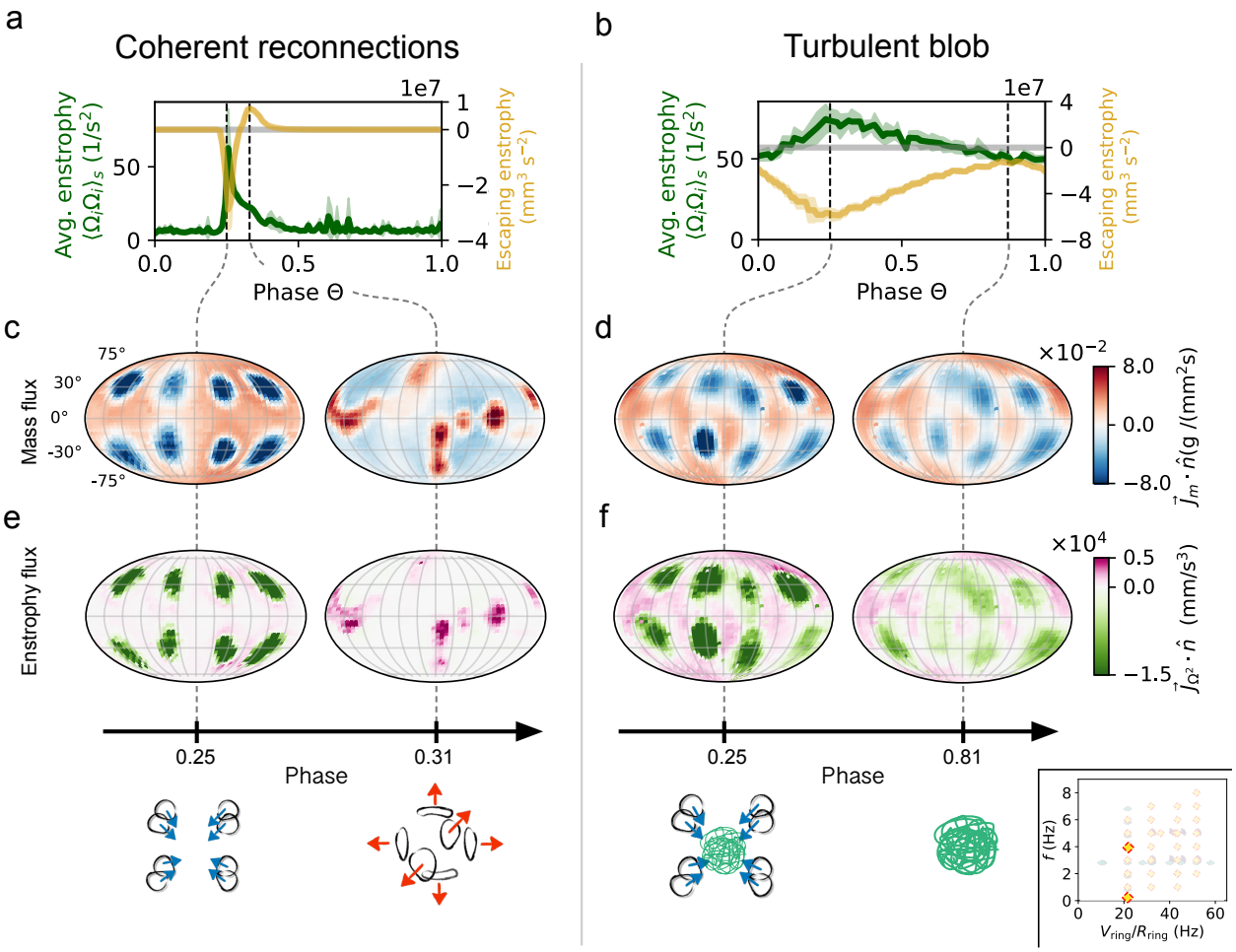

Figure 3.43: **Enstrophy flux through a sphere with radius $R = 1.2R_{\text{blob}}$ reveals the influx always outweighs the outflux throughout a cycle when a turbulent blob is formed.** (a)Enstrophy averaged over a measured volume (Green) and the (net) enstrophy flux show the arrival of the vortex rings ($\Theta = 0.25$) and the ejection event $\Theta = 0.31$. The vortex rings are fired at $f = 0.2$Hz. (b) The same as (a) but at $f = 4Hz$ at which a turbulent blob is formed. The error bands represent the standard deviation of the phase-locked average (n=2 for (a) and n=8 for (b)). (c-d) Normal mass current on the sphere is shown using the Mollweide projection. (e-f) Normal enstrophy current on the sphere is shown using the Mollweide projection.

a yellow curve in Figure 3.43(a). The positive value corresponds to the enstrophy escaping from the considered sphere. On the other hand, the integrated enstrophy flux remains always negative throughout a cycle in the state of the turbulent blob (Figure 3.43b). The enstrophy flux depicts that the inflow always outweighs the outflow, and the latter is more uniform than the case of the coherent reconnections(Figure 3.43f). Because the mass outflow cannot be zero due to incompressibility (Figure 3.43d), a small amount of enstrophy leaves the sphere. Nevertheless, the amount of enstrophy outflow remains smaller than the inflow.

3.13.2 Categorization of the flows using the time-averaged enstrophy distibution

To translate the visible transition from reconnection-and-escape to confinement dynamics, we performed a simple image moment analysis as detailed below.

For a 2D image with intensity $I_{\text{img}}(x, y)$, the (raw) moment of order (i, j) is defined as

$$m_{ij} = \sum_x \sum_y x^i y^j I_{\text{img}}(x, y). \tag{3.60}$$

The moments sequence for an image uniquely determines an image of finite size; however, they are not invariant under translation. On the other hand, the central moments

$$\mu_{ij} = \sum_x \sum_y (x^i - \overline{x})(y^j - \overline{y}) I_{\text{img}}(x, y). \tag{3.61}$$

are translationally invariant by construction. The moments of inertia is analogous to the second-order image moments ($i = j = 1$) when $I(x, y)$ is replaced by a mass distribution $\rho(x, y, z)$ of an object. Different images may have different second-order moments in the same way as the different objects may have different moments of inertia. To account for the

total intensity, the normalized central moments are also used.

$$\nu_{ij} = \frac{\mu_{ij}}{\mu_{00}^{(1+(i+j)/2)}} \tag{3.62}$$

We characterized the distribution of the time-averaged enstrophy of various collision experiments by the sum of the second-order moments $\nu_{02} + \nu_{20}$. This quantity is invariant with respect to translation, scale, and rotation, and is also known as one of Hu invariants [71]. Figure 3.44a-c shows that the cross-like pattern takes a higher value than the blob pattern. This reflects the elongated distribution of the cross-like pattern created by the secondary rings. Figure 3.44d plots our measurements on the parameter space, colored by $\nu_{02} + \nu_{20}$. Once the blob state is reached, the enstrophy distribution remains roughly the same. Hence, it tends to approach a fixed value if the blob radius were held constant. Strictly speaking, the normalized, second-order image moments take a higher value for a larger blob. As the blob size scales with the ring radius, Figure 3.44 was constructed by using only the rings with a certain radius $R_{\text{ring}} = 18 \pm 2\text{mm}$. This image analysis is consistent with the the linear trend.

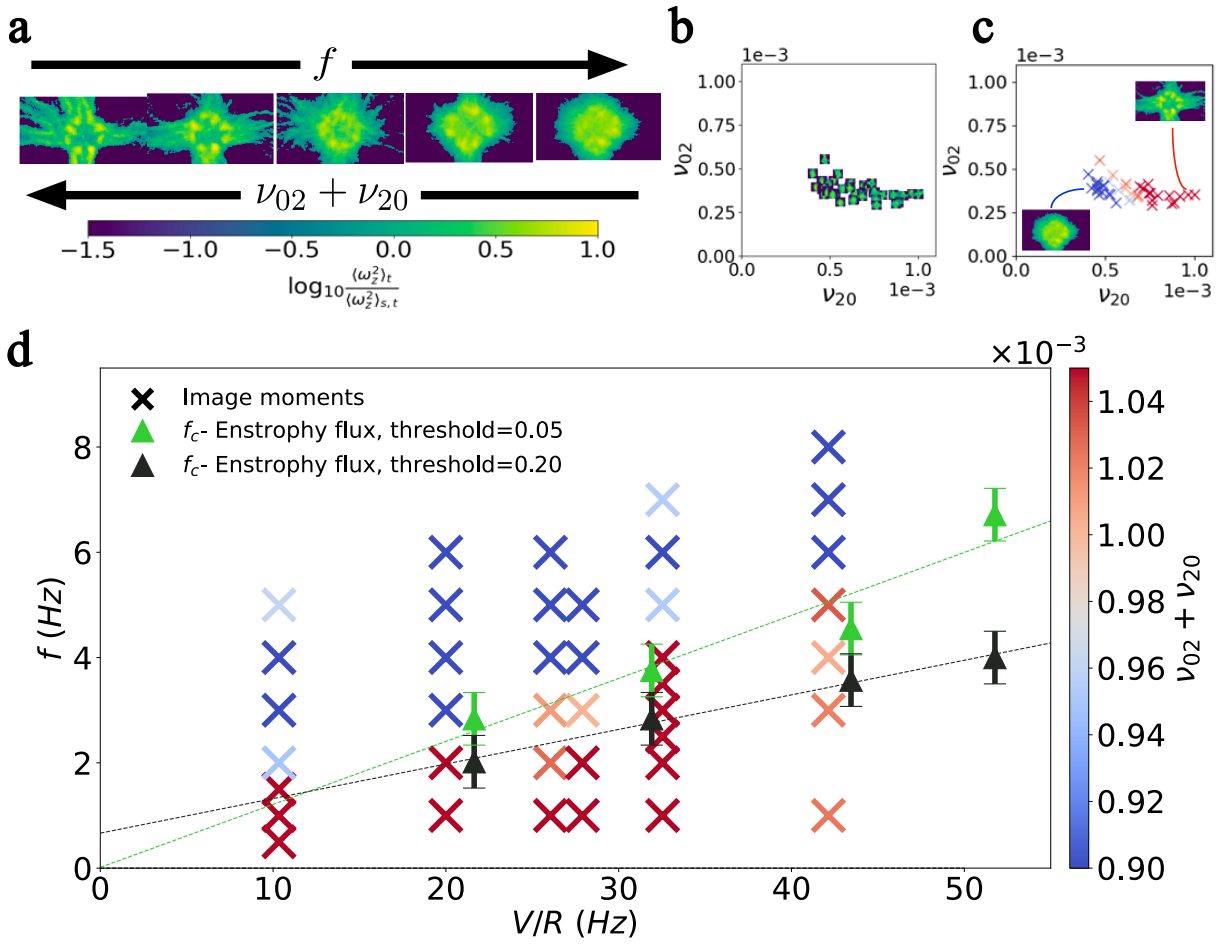

Figure 3.44: **The second-order moments of the time-averaged enstrophy distribution categorizes the flows into the non-blob and blob states.** (a)The logarithmic, time-averaged enstrophy shows the formation of a turbulent blob at high forcing frequency. The corresponding second-order moments decrease as the ejection of enstrophy via secondary vortex structures becomes weak. (b)Images of thelogarithmic, time-averaged enstrophy are plotted on the $\nu_{02} - \nu_{20}$ plane. Blob patterns are clustered in the bottom left region. (c) The same plot as (b) but colored by $\nu_{02} + \nu_{20}$. (d) $\nu_{02} + \nu_{20}$ categorizes the flows into two groups. The separation is described by a linear relation $f \sim V_{\text{ring}}/R_{\text{ring}}$, and is consistent with the transitional frequencies obtained from the enstrophy flux. The error bars represent SD (n=3).

3.14 Tuning the properties of the blob

3.14.1 Blob size

In the main text, we state that the integral scale of the turbulent is proportional to the radius of the vortex ring, and is comparable to the diameter of the blob R_{blob}. One can alter the size of the blob by using vortex rings with a different diameter. Figure 3.45 demonstrates the formation of the turbulent blobs of three different sizes using the rings of radius $R_{\text{ring}} = 11.0 - 17.7\text{mm}$.

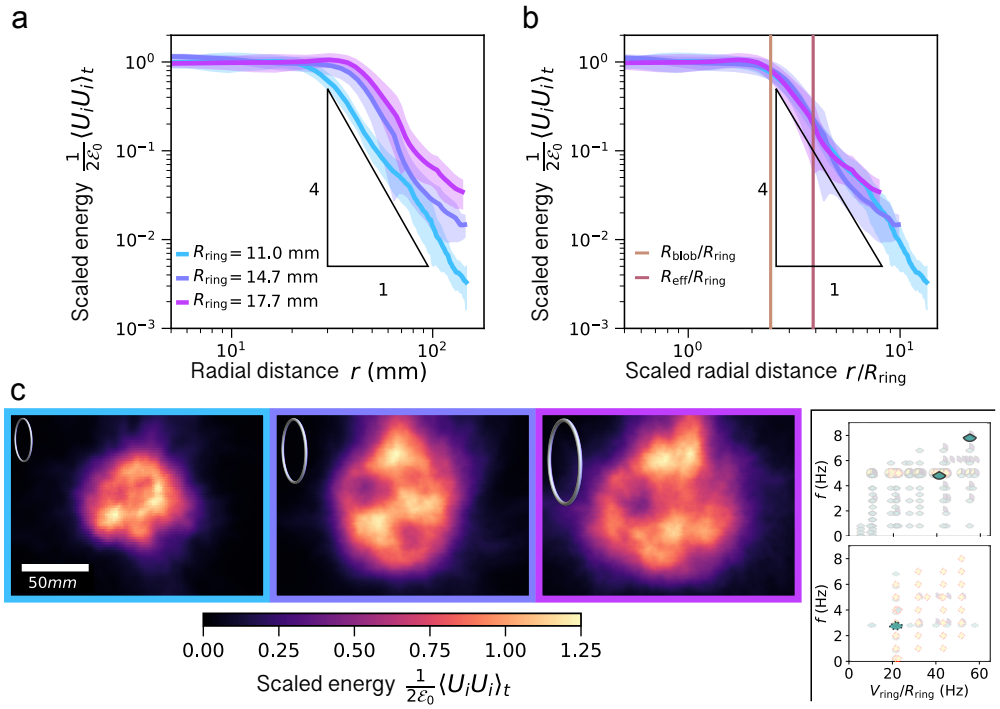

Figure 3.45: **Varying the radii of the injected vortex rings tunes the size of the turbulent blobs.** (a) Scaled radial distribution of the time-averaged energy density $(\langle U_iU_i\rangle_t/2)/\mathcal{E}_0$ for three turbulent blobs are plotted against radial distance r. R are the radii of the injected vortex rings, and $\mathcal{E}_0$ is the average energy density inside the core. (b) $(\langle U_iU_i\rangle_t/2)/\mathcal{E}_0$ vs non-dimensionalized radial distance r/R. (c) Corresponding spatial distributions of the time-averaged energy densities are shown. For (a) and (b), the error bands represent the SD of the annular average.

3.14.2 Injection of angular momentum and helicity using helical rings

The use of a helical masks instead of a circular hole mask (Figure 3.18) enables us to inject helical vortex rings with the additional non-zero inviscid invariants of angular impulse $\vec{\mathcal{A}}$ and helicity $\mathcal{H}$. There are 22 unique configurations to replace eight planar masks with either right-handed and left-handed masks at the vertices of a cube. The permutations include combinations with non-zero net helicity but zero angular impulse, zero helicity but non-zero angular impulse, non-zero angular impulse and helicity, and zero angular impulse and zero helicity.

As reported in Figure 5 of the main text we performed experiments in which we injected four distinct configurations, all with zero net angular impulse. These include:

1. Eight right-handed masks ($\mathcal{H} = 8|\mathcal{H}_{\text{ring}}|$),

2. Four right-handed and four left-handed masks I & II ($\mathcal{H} = 0$),

3. Eight left-handed masks $\mathcal{H} = -8|\mathcal{H}_{\text{ring}}|$.

We produced the vortex rings with $(L/D, v_{\text{eff}}, f)$= (2.0, 418mm/s, 5Hz) and $(D_p, D_o{}^{\text{e}})$=(160mm, 25.6mm). We found that this protocol generates turbulent blobs for all the configurations of helical masks listed above.

We compute the local helicity density by directly computing $\vec{U}(\vec{x},t)\cdot\vec{\Omega}(\vec{x},t)$. The velocity field $\vec{U}(\vec{x},t)$, measured by 3D PTV, is convoluted with a median filter (kernel size: 3px ×3px $\approx 3\eta \times 3\eta$). The vorticity field $\vec{\Omega}(\vec{x},t)$ is then calculated using the central difference method with the second order accuracy.

Figure 3.46 shows typical temporally averaged helicity, energy, and enstrophy fields on a slice that cuts through turbulent blobs generated by either planar and helical vortex rings. The turbulent blobs generated by firing together helical vortex rings are 30% larger than the blob generated by planar rings. These two blobs are created by the same driving parameters

e. D_o refers to the mean radius in the case of the helical masks.

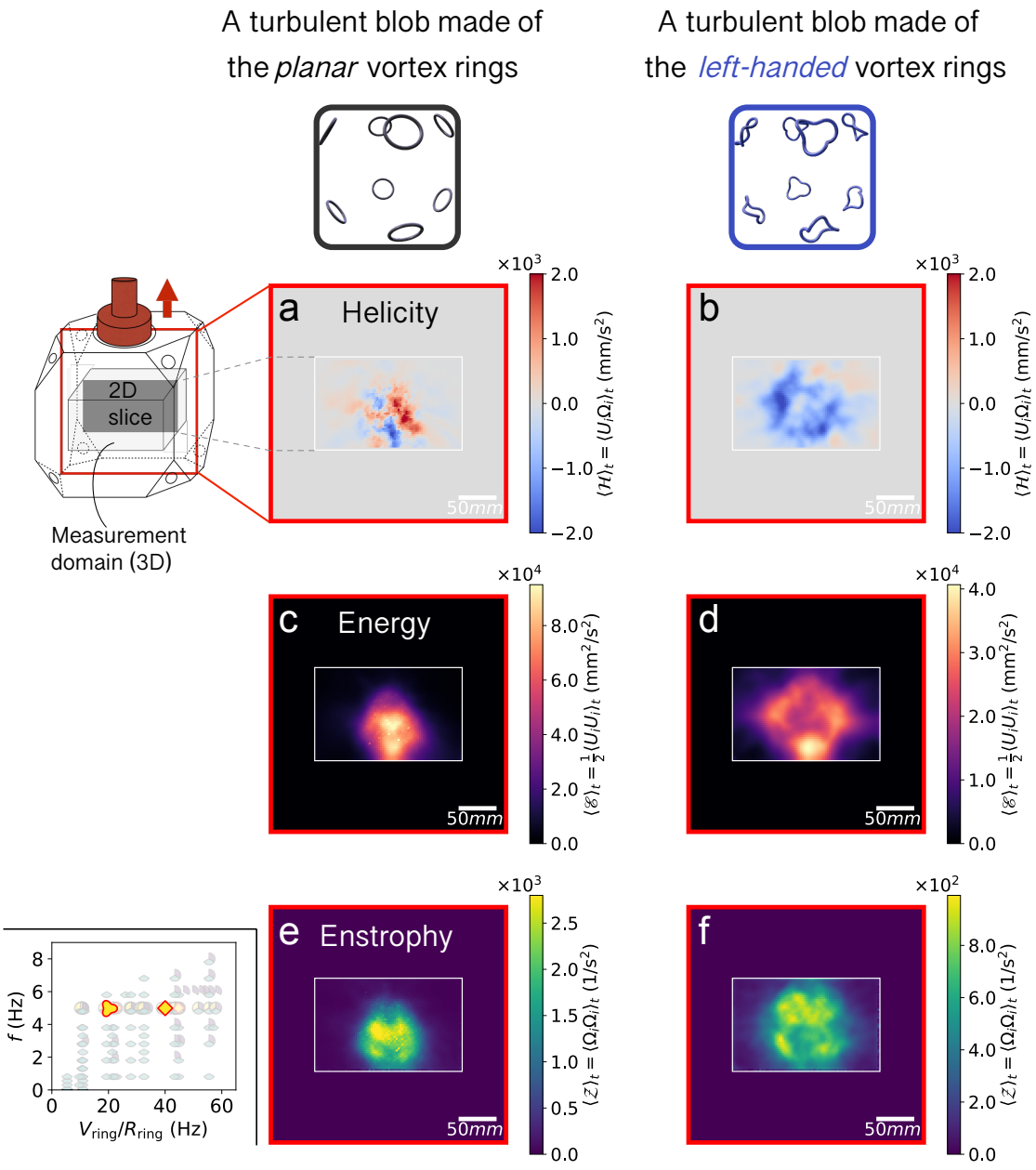

Figure 3.46: **Comparison between the turbulent blobs generated by the planar and helical vortex rings.** (a, b) Temporally averaged helicity fields of the non-helical and helical turbulent blobs respectively (c, d) Temporally averaged energy fields of the non-helical and helical turbulent blobs (e, f) Temporally averaged enstrophy fields of the non-helical and helical turbulent blobs.

$(L/D, v_{\text{eff}}, f) = (2.0, 418\text{mm/s}, 5\text{Hz})$; however, the helical rings are almost twice as slow as the planar rings. The ranges of the color bars in Figure 3.46 are different between the planar and helical blobs for this reason.

With the planar vortex rings, the generated turbulent blob contains both positive and negative helicity (Figure 3.46 a), which becomes nearly zero after integrating over the sphere. Injecting only the left-handed vortex rings result in a turbulent blob with predominantly negative helicity inside (Figure 3.46b). The use of the helical rings creates a larger blob of turbulence as shown in the temporally averaged energy (Figure 3.46 c-d) and enstrophy (Figure 3.46e-f). It also exhibits the pronounced shell-like distribution in the helicity field, depicting that helicity does not penetrate the core of the blob as effectively as the enstrophy and energy.

Integrating the 3D helicity field over a sphere of radius 60mm in the a phase-locked manner results in the results reported in Figure 5 of the main text. Figure 5 (main text) shows that the different configurations of the helical masks controllably deliver helicity to a turbulent blob. We compare the integrated helicity inside the spherical domain to the estimated value of the injected helicity $8|\mathcal{H}_{\text{ring}}|$ discussed in section 3.6.3.

The result of this comparison shows that 42-81% of the injected helicity is transferred to the spherical domain of the turbulent blob.

Estimation of the effect of corase graining on the measurement of helicity in the turbulent blob

To explore how an under-resolved velocity field and affect the measurement of helicity in the blob, we inspect a DNS dataset with helical forcing (Figure 3.47a). The dataset is 'turb-hel' on the Smart-Turb database at the University of Rome, Tor Vergata[f]. In 3D helical

f. We hereby acknowledge Professor Luca Biferale and Dr. Fabio Bonaccorso for conducting DNS simulation of helical turbulence and making it available to us through the Smart-Turb database.

turbulence, there is evidence that helicity cascades down to small scales[7], and substantial amount of helicity is stored in a large scale. This suggests an attenuation of the measured helicity of ∼10% of the original value by coarse-graining (Figure 3.47c) when the voxel pitch is 1.1 times the transverse Taylor microscale. In our experiment of a helical turbulent blob, the voxel pitch is estimated as 1-2 λ_g. Hence, we estimate 10-20% attenuation of the helicity in the Figure 5 due to our under-resolved measurements.

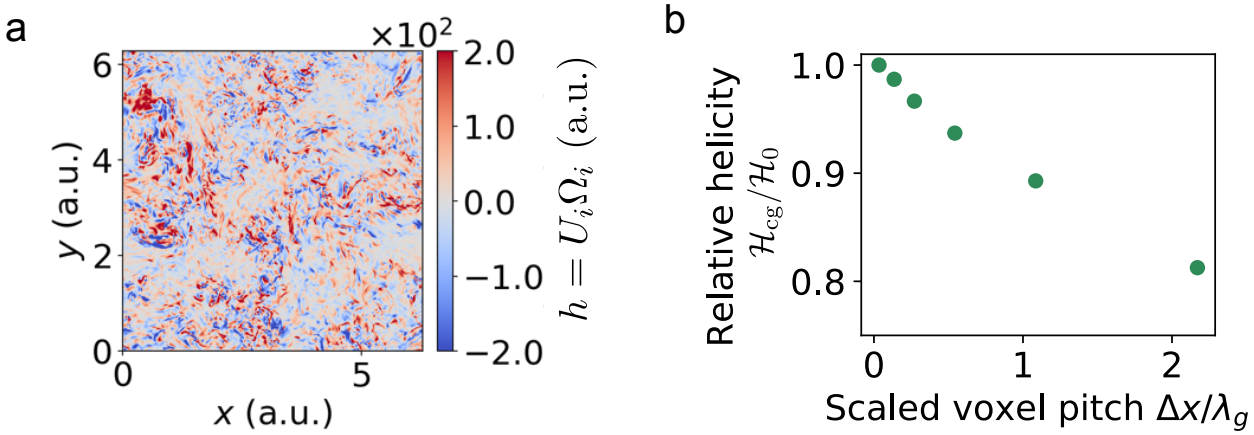

Figure 3.47: **Coarse-graining a helical, turbulent velocity field leads to underestimate total helicity.** (a) A 2D slice of a 3D helical, turbulent velocity field (b) Coarse-graining effect on helicity. $\mathcal{H}_0$ and $\mathcal{H}_{cg}$ represent total helicity in the simulation domain of the original and coarse-grained velocity fields respectively. The x-axis is the voxel pitch scaled by the transverse Taylor microscale λ_g.

3.15 Gross-Pitaevskii Simulation

In this section we report the result of our simulations of symmetric collisions of multiple quantum vortex rings using the Gross-Pitaevskii equation (GPE, Eq. 3.63). In all configurations we tested, we observe that reconnection events take place, and the secondary rings propagate away from the center of the collisions.

We simulate the dynamics of the quantum vortex rings through the Gross-Pitaevskii equation (GPE), a model equation that describes the time evolution of the superfluid wavefunction $\psi(x_i) = \sqrt{\rho(x_i)}\exp\left[i\phi(x_i)\right]$ where ρ and ϕ are the spatially varying density and phase. The GPE is given by

$$\frac{d\psi}{dt} = -\frac{i}{2}\left(\nabla^2 - |\psi|^2\right)\psi. \tag{3.63}$$

The wavefunction can be mapped to classical hydrodynamic fluid velocity and density by the Madelung transform: $\vec{u} = \nabla\phi, \rho = |\psi|^2$. The GPE is useful to study vortex dynamics as vortex reconnections occur without divergencies in physical quantities, and the topological dynamics was shown to be comparable to real viscous fluids [83].

All simulations were performed using a grid size of 0.5ξ (ξ: healing length) and time step Δt=0.02 with periodic boundary conditions unless otherwise stated.

3.15.1 Symmetric collisions of vortex rings

We study collisions between vortex rings that are configured in a symmetrical fashion. For simplicity, we restrict ourselves to use only a circular ring with a fixed circulation and a radius. We associate a configuration to a polyhedron by the following rules. 1. Consider a plane P_i that the i-th ring is embedded at an instant of time. 2. The bounded region by the n planes is the polyhedron associated to the configuration of the rings. By this construction, the initial configuration of our experiment corresponds to an octahedron.

We conducted GPE simulations of the symmetrical collisions that correspond to the platonic solids(a tetrahedron, a cube, an octahedron, a dodecahedron, and a icosahedron). They are the most symmetrical configurations for 4, 6, 8, 12, and 20 rings respectively. This is understood by counting the number of symmetry operations for the corresponding point groups. A tetrahedron belongs to T_d. A cube and an octahedron belong to O_h. A dodecahedron and an icosahedron belong to I_h in the Schönflies notation. The result is summarized in Figure 3.48.

Two observations are made: (1)The secondary rings always travel away from the center of the collision. (2)The polyhedron corresponding to the configuration of the secondary rings is dual to the initial polyhedron. All adjacent vortex lines during the collision are anti-parallel so the reconnections occur at every possible site that correspond to the vertices of the initial configuration. A symmetric collision of four rings (a tetrahedron) results in four secondary rings (a flipped tetrahedron). A symmetric collision of six rings (a cube) result in eight secondary rings (an octahedron). The propagating directions of the secondary rings are given by the normal vectors of the faces (of the dual polyhedron). The pattern extends to all platonic solid configurations. In our experiment (the octahedral configuration), we observe six secondary rings (a cube) after the reconnection events via bubbles and Lagrangian trajectories (see SI Video3).

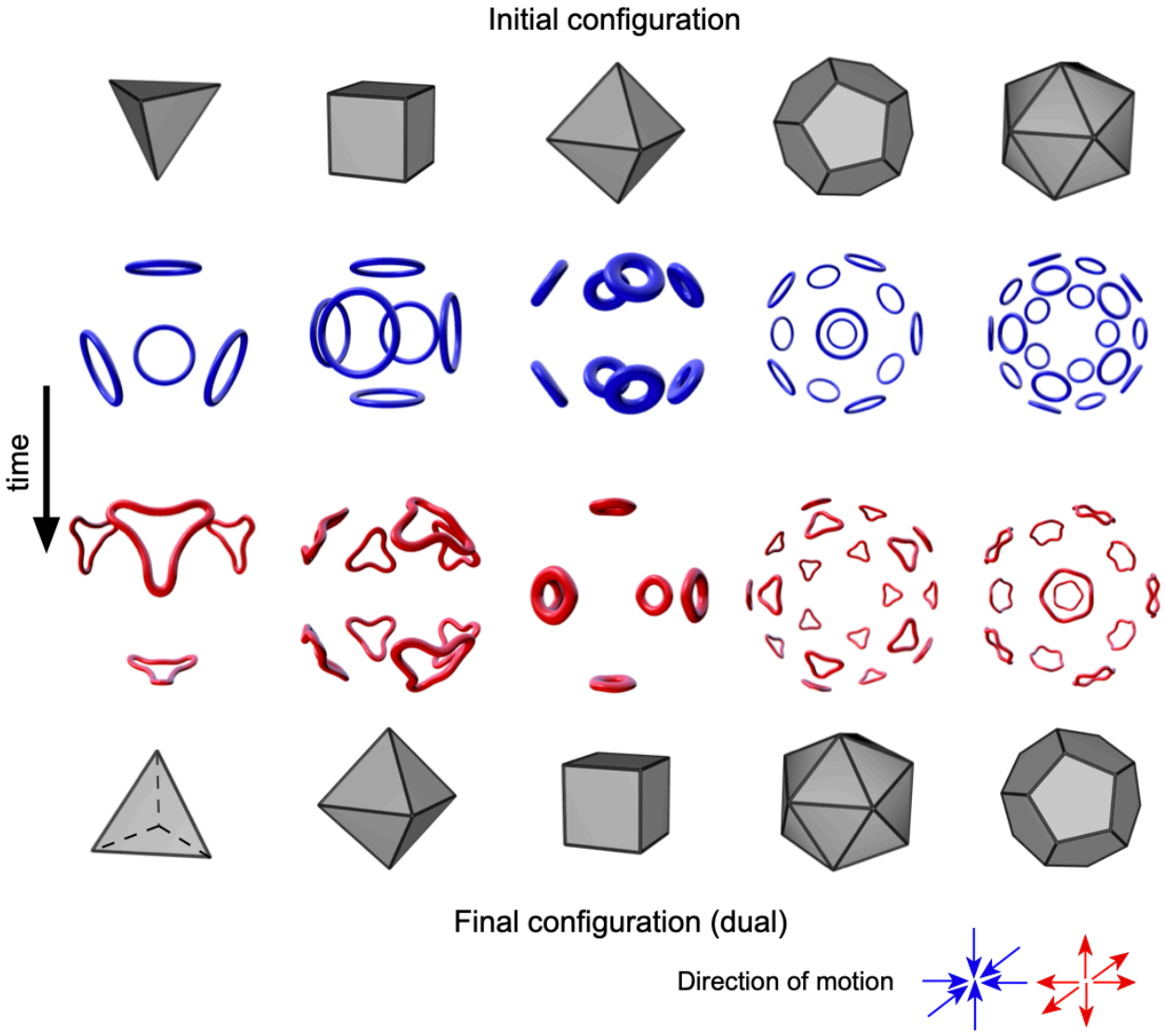

Figure 3.48: **Gross-Pitaevskii simulation demonstrates the geometric rule of the symmetric vortex ring collisions.** When vortex rings are initially set on the faces of the platonic solids, the region bounded by the planes that the secondary rings live forms the dual solids, preserving the symmetry of the vortex structures before and after the collision.

3.16 Conclusions

We have discovered that a collection of vortex rings periodically fired together leads to a self-confining turbulent blob. This bottom-up approach to turbulence provides unique design principles to position, localize and control turbulence as a state of flow. In the canonical picture of the Richardson cascade, injection and dissipation go hand in hand at dynamical equilibrium. Nevertheless, their connection often remains elusive due to the uncontrolled injection and evolution of vortical structures. The use of coherent, controllable vortex rings overcomes this issue, enabling us to inject fully controlled arbitrary ratios of inviscid conserved quantities. Enabled by the self-confinement effect we discovered, our experiment provides a unique control of injection and dissipation in turbulence. The turbulent blob, which can be measured in its entirety and is free to evolve in isolation, offers a playground for fundamental studies on inhomogeneous turbulence such as decay of turbulence without interference from boundaries, response of turbulence to a periodic drive [30, 180, 182, 183, 90, 104, 43], and the role of inviscid invariants such as helicity [87, 6] and angular impulse [144, 47] in turbulence. The steadiness of the turbulent blob makes it an interesting alternative to boundary layers [192, 20, 188, 34, 45] to assess transfer at the turbulent/non-turbulent interface. Our work demonstrates how turbulence can be treated as a state of matter that can be controlled and manipulated coherently.

CHAPTER 4

DECAY AND PROPAGATION OF TURBULENCE

When a turbulent patch is produced locally, it spreads and decays. Our isolated blob of turbulence provides an opportunity to directly investigate this process with minimal interference from mean flow. In this chapter, we first present how the turbulent blob decays. By comparing to the decay of turbulence set up in the same chamber by a different method, we experimentally demonstrate how the large-scale motion of the turbulence governs the energy decay law. Second, we characterize how turbulence spreads. We compare our findings to a transport equation of turbulent kinetic energy [36].

4.1 Decay of turbulence

4.1.1 Background

The way in which turbulence decays to a quiescent or laminar state is of fundamental importance from both scientific and industrial interests. Being able to kill turbulence enables efficient transport of fluids in a pipe, and improves aerodynamic control of an object in the air or an ocean. Nevertheless, it remains a challenge even to predict the rate of turbulence decay from the NS equations [106]. Our current understanding is based on the studies of homogeneous, isotropic turbulence (HIT) due to its theoretical simplicity. Deducing the decay rate of turbulent kinetic energy requires further assumptions [59]. In most cases, the average kinetic energy density $q(t) = (1/2)\langle u_i(\boldsymbol{x},t)u_i(\boldsymbol{x},t)\rangle_s$, or equivalently, the total energy $Q(t) = \int q(\boldsymbol{x},t)d\boldsymbol{x}$, is predicted to decay in a power law with respect to time:

$$q(t) = \frac{1}{2}\langle u_i u_i\rangle_s = C_q(t-t_0)^n \tag{4.1}$$

where t_0 is a virtual origin, and C_q is a constant. The predicted decay exponent n ranges typically from -1 to -2.5 depending on the assumptions. Is any of the proposed theory correct? The decay exponent, reported in experiments and simulations, comes with a large variation from -1 to -2 [129]. Furthermore, there is a little evidence that connects the observed decay law and the fulfillment of the corresponding theoretical assumption. This variation of the reported exponents suggest that the exponent depends on many factors such as the Reynolds number, initial conditions, boundary effects, determination of a virtual origin, ranges of data used to fit a power law, and simulation parameters.

To summarize, past experimental and numerical results strongly suggest that turbulence decay is not universal, yet what determines the decay law remains unknown.

4.1.2 Review of previous studies about the decay law

It is instructive to summarize particular theoretical predictions for energy decay exponent n before we proceed.

Case I: $n = -1$ **(Self-similar decay- high Re limit)**

The first case we review is the self-similar decay of the homogeneous, isotropic turbulence (HIT) decays in the absence of boundary effects. The result is derived from the von Kármán-Howarth equation for the time-evolution of the longitudinal velocity correlation function. The required assumption is that the velocity correlation function evolves in a self-similar manner. That is, the distribution of the eddies remains self-similar. With proper scaling in space and time, turbulence at a time t_1 becomes statistically indistinguishable at a different time t_2. This decay law is, therefore, considered applicable to turbulence in the large Reynolds number limit. The derivation can be found in [103, 15, 13, 59]. In experiments, the reported exponent at the highest available Reynolds number $O(10^6)$, using grid turbulence, is -1.18 ± 0.02 [159]. As of today, no clear $n = -1$ decay law has been observed in either experiments and simulations.

Case II: $n = -10/7 \approx 1.43$ **(Kolmogorov's decay law)**

Instead of imposing self-similarity on the correlation function, another approach is to enforce a constraint in the large-scale motion of the turbulent motions. This is motivated from Taylor-expanding the energy spectrum function near the wavenumber origin [48, 129]

$$E(\kappa, t) = \frac{I_{\mathrm{BS}}(t)}{4\pi}\kappa^2 + \frac{I_{\mathrm{L}}(t)}{24\pi}\kappa^4 + O(\kappa^6), \tag{4.2}$$

The integrals in Eq. 4.2 are

$$I_{\mathrm{BS}}(t) = \int \langle \boldsymbol{u}(\boldsymbol{x}+\boldsymbol{r}, t)\cdot\boldsymbol{u}(\boldsymbol{x}, t)\rangle d\boldsymbol{r} = 8\pi u'^2 \int_0^\infty r^2 f(r,t) dr, \tag{4.3}$$

$$I_{\mathrm{L}}(t) = \int r^2 \langle \boldsymbol{u}(\boldsymbol{x}+\boldsymbol{r}, t)\cdot\boldsymbol{u}(\boldsymbol{x}, t)\rangle d\boldsymbol{r} = 8\pi u'^2 \int_0^\infty r^4 f(r,t) dr \tag{4.4}$$

where $f(r,t)$ is a longitudinal correlation function $f(r,t) = \langle u_\parallel(\boldsymbol{x},t) u_\parallel(\boldsymbol{x}+\boldsymbol{r},t)\rangle/(u'^2)$ with $u_\parallel(\boldsymbol{x},t) = u(\boldsymbol{x},t)\cdot\boldsymbol{r}/r$. These integrals I_{BS} and I_{L} are known as the Birkhoff-Saffman [19, 144] and Loitsiansky [134, 48] integrals. Historically, Loitsiansky reached the integral I_{L} from the Kármán-Howarth equation while he considered an invariant of decay. With the assumption that $I_{\mathrm{BS}} = 0$ and $I_{\mathrm{L}} = \text{const.}$, the decay exponent becomes $n = -10/7$. Independently, Kolmogorov reached the same conclusion, thus this prediction is sometimes called Kolmogorov's decay law. The assumed constancy of the Loitsiansky integral was, however, found to be incorrect by Saffmann in 1967 [143, 144], and Chasnov showed that I_{L} diverges with a certain initial condition using large eddy simulations in 1993 [33]. Nevertheless, some modern literature [159, 190] still refer to Kolmogorov's decay law as a benchmark.

Case III: $n = -6/5 = -1.2$ **(Saffman's decay law)**

Since the constancy of Loitsiansky's integral was questioned, Saffman argued that the constancy of I_{BS} yields a decay exponent of $n = -6/5$. This decay law is in good agreement with the decay of grid turbulence [159, 89, 118, 39]. Nevertheless, it should be noted that the range in which the delay law is observed is restricted due to physical limitations of the

facilities[a]. The applicability of Saffman's decay law to general turbulence, however, remains a question. In fact, one can formulate the integral of the form

$$I_{2m}(t) \propto= u'^2 \int_0^\infty r^{2m} f(r,t) dr,$$

whose constancy results in the decay law of $n = -(4m+2)/(2m+3)$ for $m \geq 1$. Saffman's and Loitsiansky's integrals correspond to $m = 1$, and $m = 2$, respectively.

There is a wealth of literature that discusses the Kolmogorov's and Saffman's decay laws. The reason that led many to believe such *invariants of decay* exist is that the Saffman's and Loitsiansky's integrals can be written as

$$I_{\mathrm{BS}}(t) = \frac{1}{V} \langle \int_V [\boldsymbol{u} dV]^2 \rangle, \tag{4.5}$$

$$I_{\mathrm{L}}(t) = \frac{1}{V} \langle \int_V [\boldsymbol{x} \times \boldsymbol{u} dV]^2 \rangle \tag{4.6}$$

where V is some large volume embedded in turbulence. These forms suggest that I_{BS} and I_{L} are respectively, the measure of linear momentum and angular momentum[b] in a fluid. More detailed discussion on these integrals can be found in [48, 47]. Once the Loitsiansky integral was proved not to be an invariant of decay, the constancy of Saffman's integral was also downgraded to a conjecture [129]. More importantly, it fails to predict the physics behind the large variation of the observed decay laws. This formulation does not answer why some integrals are more preserved than the others.

Case IV: $n = -2$

Barenblatt *et al.* [11], and Chen & Goldenfeld [36] considered a phenomenological model of

a. In grid turbulence, (the longest distance where a measurement is taken) / (mesh size) is at most $10^{1.5}$.

b. The idea to interpret the Loitsiansky integral as a measure of angular momentum in a fluid was first coined by Landau [96]. In 2009, Davidson revised this interpretation; however, the connection between the Loitsiansky integral and the angular momentum remains valid.

the form:

$$\partial_t q(\boldsymbol{x},t) = \nabla\cdot\big(\kappa_q(\boldsymbol{x},t)\nabla q(\boldsymbol{x},t)\big) - \epsilon(\boldsymbol{x},t) \tag{4.7}$$

where κ_q is a q-dependent diffusion constant and ϵ is a local dissipation rate. We adopt the so-called zeroth law of turbulence: "the energy injection rate at large scales equals the dissipation rate at small scales" [129]. We naïvely extend the zeroth law so that a local dissipation rate takes the form of

$$\epsilon(\boldsymbol{x},t) = \epsilon_0\frac{q^{3/2}(\boldsymbol{x},t)}{\ell(t)}. \tag{4.8}$$

$\ell(t)$ is a longitudinal integral scale of turbulence, defined as

$$\ell(t) = \frac{3\pi}{4}\frac{1}{q(t)}\int_0^\infty \frac{E(\kappa)}{\kappa}d\kappa. \tag{4.9}$$

The coefficient ϵ_0 is approximately 0.5 at a high reynolds number ($Re_\lambda > 50$ [166, 179]), increases by a factor of 2.5 when Re_λ becomes 10. With dimensional analysis, Eq. 4.7 becomes

$$\partial_t q(\boldsymbol{x},t) = \ell(t)\nabla\cdot\Big(q^{1/2}(\boldsymbol{x},t)\nabla q(\boldsymbol{x},t)\Big) - \epsilon_0\frac{q^{3/2}(\boldsymbol{x},t)}{\ell(t)} \tag{4.10}$$

$$= \frac{2}{3}\ell(t)\nabla^2 q^{3/2}(\boldsymbol{x},t) - \epsilon_0\frac{q^{3/2}(\boldsymbol{x},t)}{\ell(t)}. \tag{4.11}$$

If ℓ = const., the decay law becomes $n = -2$ in the limit $t\to\infty$. This decay law is observed for turbulence generated by an oscillating grid in helium II for more than two decades [162]. Not to mention that the experimentally observed decay law is significantly different from both Kolmogorov's and Saffman's decay laws.

With all the necessary topics covered, we now describe how the isolated blob of turbulence

spreads and decays.

4.1.3 Experimental methods

We generate three kinds of turbulence by (1) oscillating a grid, (2) oscillating double grids, and (3) colliding vortex rings. We measure decaying velocity fields using 2D PIV as explained in Sect. 2.3. In doing so, we adopt a novel technique that allows the measurement spanning five orders of magnitude in time as described below.

Flow chamber and actuation

All experiments are performed in the chamber described in Sect.2. A schematic and photograph of the chamber are reproduced in Figure 4.1a and b respectively. By swapping the acrylic plates attached at the corner, we can leave the chamber either open or closed (Figure 4.1c-d).

As mentioned at the beginning of this section, we, by three distinct methods, generate turbulence in our flow chamber: *A single oscillating grid*, *double oscillating grids*, and *a turbulent blob*.

1. *A single oscillating grid (SOG)*: We oscillate an acrylic grid with a sinusoidal drive (Figure 4.2a). This method is known to create a turbulent front in a pipe for superfluid [162]. The grid is prepared by laser-cutting an acrylic plate with thickness of 1/4" =12.7mm into a circular shape with a diameter of $D_{\mathrm{grid}} = 200$ mm (Figure 4.2d). The mesh size M is 12.5 mm (Figure 4.2e). Because we drive the grid near the upper surface of the chamber, it generates a downward mean flow, making it challenging to observe fluctuations without subtracting the mean flow.

2. *Double oscillating grids (DOG)*: We oscillate double grids connected together by aluminium rods (Figure 4.2b). This method creates a region with small mean flow unlike

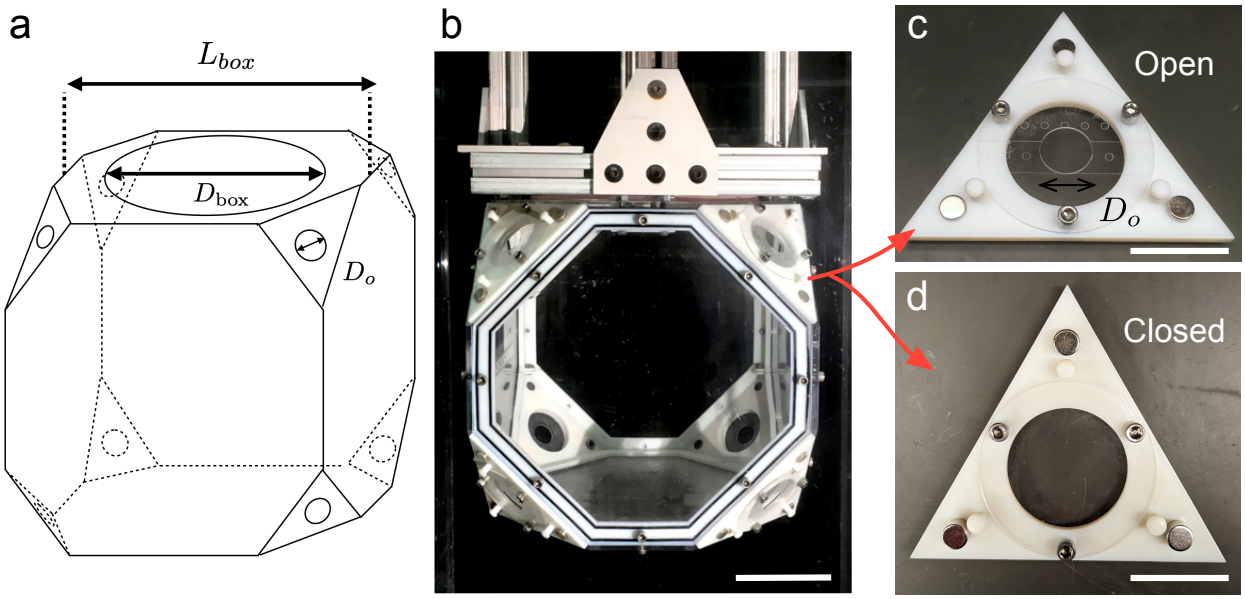

Figure 4.1: **Geometry of the flow chamber.** (**a**) Schematic of the experimental chamber is shown. (**b**) The experimental chamber consists of a 3D-printed frame and six acrylic faces. The scale bar represents 100 mm. (**c**) A 3D-printed "holster" is magnetically attached to each truncated surface of the chamber. A circular, acrylic plate with an orifice may be attached to enable generation of a vortex ring at each site. (**d**) Alternatively, a circular plate is attached to confine the flow in the chamber. The scale bars in (c) and (d) represent 50 mm.

Component	Length (mm)
Width of an experimental chamber, L_{box}	351.0
Hole diameter of a box, D_{box}	210.0
Diameter of a circular grid, D_{grid}	200.0
Mesh size, M	12.5
Thickness of a grid	9.3
Separation length between the grids, l_{sep}	210.0
Diameter of a piston, D_p	56.7
Diameter of an orifice, D_o	12.8

Table 4.1: **Dimensions of the chamber and grids used in this paper**

the SOG. These two grids are separated by 210 mm (Figure 4.2f).

3. *A turbulent blob*: We repeatedly collide vortex rings in the chamber (Figure 4.2c). When vortex rings are fired at a sufficiently high rate, this method creates a steady, isolated blob of turbulence, sitting in a quiescent environment [110]. Vortex rings are created by lifting an acrylic piston (D_p = 12.7mm, Figure 4.2h)through the upper surface of the chamber, which withdraws fluid through circular apertures, allowing boundary layers to roll up.

As in the experiments performed in Chapter 3, we use an electric linear actuator (STA2510S, Copley Controls Corp) to drive either the grid or the piston. Using the same data acquisition board (PCI-6251, National Instruments), we command either a sawtooth or a sinusoidal function. Figure 4.2g-h show an average profile of the realized output.

The physical dimensions of the grids and the chamber are described in Table 4.1.

Table 4.2 summarizes the conditions of the experiments on the decay of turbulence.

Logarithmic triggering: method of capturing decaying dynamics

Measuring the entirety of turbulence decay is challenging because temporal and spatial scales in turbulent flows drastically change during the process. To overcome this difficulty, we take images with a decreasing frame rate while turbulence decays. We design the timings of image

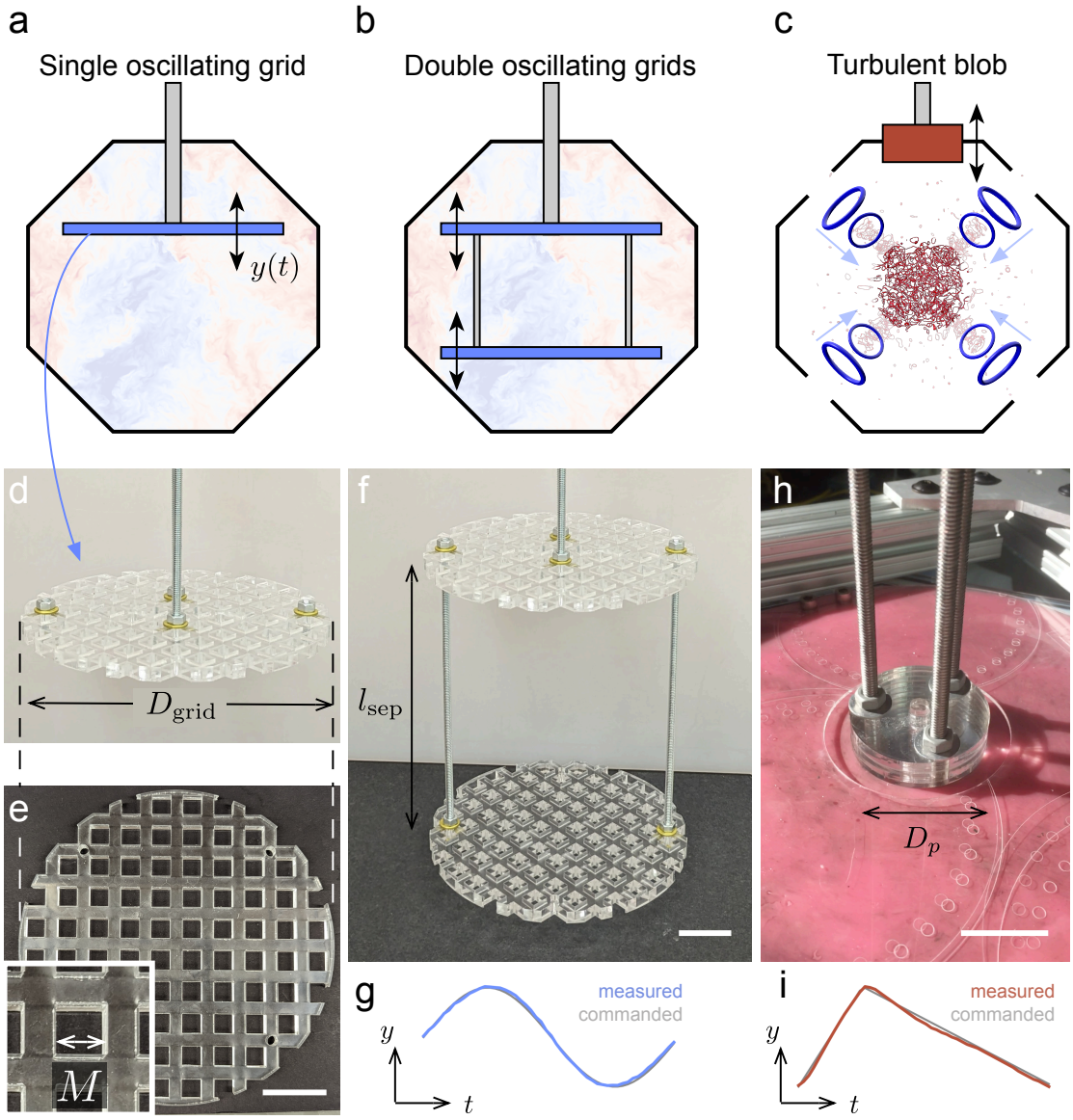

Figure 4.2: **Three methods of actuation to generate turbulence in a flow chamber:** (**a**) A single oscillating grid (**b**) Double oscillating grids (**c**) Repeated collision of vortex rings. (**d-e**) An circular, acrylic grid with square meshes is used to set up flows in the experiments. (**f**) Two identical grids are bolted together with a separation distance l_{sep} of 210 mm for the experiments involving the double oscillating grids. (**g**) Both single and double grids are driven by a sinusoidal signal in a closed chamber. The blue curve show the measured amplitude. (**h**) To create vortex rings, an acrylic, cylindrical piston used to withdraw fluid into the chamber through circular orifices. (**i**) A sawtooth profile is used to generate vortex rings repeatedly. The scale bars in (e), (f), and (h) represent 40 mm.

Method (No. of runs)	Forcing protocol	$\mathrm{Re}_L = u'\ell/\nu$	$\mathrm{Re}_\lambda = u'\lambda/\nu$
Single oscillating grid ($N = 10$)	$y(t) = A\sin(2\pi ft)$ (A, f)=(18mm, 5Hz)	5,304	95
Double oscillating grids ($N = 10$)	$y(t) = A\sin(2\pi ft)$ (A, f)=(18mm, 5Hz)	10,100	185
Repeated collision of vortex rings ($N = 21$)	Sawtooth, duty cycle of 20% (A, f)=(11.2mm, 5Hz)	15,400	203

Table 4.2: **Summary of the decay experiments**. The integral, and Taylor Reynolds numbers are the values at before we switch off forcing. See Sect. A for the definitions of the symbols.

acquisitions such that a root-mean-square displacement of tracer particles remain constant. After an initial transient period, it is widely believed that turbulent kinetic energy decays as a power law, meaning

$$q = c(t - t_0)^n$$

for $t > t_0$ with an energy decay exponent $n \leq -1$ and a virtual origin t_0[129, 59]. If the energy decays with a single power law, the interval $\Delta(t)$, required to preserve a root-mean-square displacement d, is obtained by solving

$$\int_t^{t+\Delta(t)} U_{\mathrm{rms}}(t')dt' = d.$$

This results in

$$\Delta(t) = \begin{cases} (t - t_0)\exp\left(\frac{d}{\sqrt{2c}} - 1\right) & (m = 0 \Leftrightarrow n = -2), \\ (t - t_0)\left[\left(1 + \frac{md}{\sqrt{2c}}\frac{1}{(t-t_0)^m}\right)^{\frac{1}{m}} - 1\right] & (m \neq 0 \Leftrightarrow n \neq -2), \end{cases} \tag{4.12}$$

where $m = n/2 + 1$. In the case of $n = -2$, logarithmic spacing is optimal to capture the decay as $\log \Delta(t) \sim \log t$ for $t \gg t_0$. Figure 4.3a-b illustrate the progression of the frame rate adopted to measure the entirety of decay in our experiments. The adopted scheme lasts for 1050 seconds (= 17.5 minutes) after the actuation stops, and consists of three parts. First we

trigger the camera at a constant frame rate for approximately a second. The exact duration of this part depends on the choice of a virtual origin t_0, and the initial RMS velocity. The subsequent triggering timings are determined by following Eq. 4.12 for $n = -2$. Once the frame rate reaches the minimal available value of the timing box, $f_{\min}$, as illustrated by a dashed line in Figure 4.3a, we adopt $f_{\min}$ as the frame rate.

The choice of n does not bias toward a specific decay law. The average displacement between adjacent frames may be either accelerated or decelerated, yet PIV can output accurate velocity field as long as the average displacement is in its dynamic range, specifically between the noise floor ($<$ 1px) and a half of the interrogation window size, $W/2 = 16px$. There are two ultimate cases that this logarithmic triggering fails. The first case is when the $|n|$ is too small with respect to the (magnitude of the) true decay exponent $|n_{\text{true}}|$. In this case, the displacement is simply too large for the PIV algorithm fails to find correlation between the adjacent images. The second case is when the $|n|$ is too large. In this case, the average displacement becomes lower than the noise floor. These limiting cases are easily detectable. We took a self-consistent approach in finding a reasonable choice of n and d that enables the average displacement to fit within the dynamic range of PIV throughout the decaying process. We also report that we obtained the quantitatively similar results with a different choice of n, ranging from -1 to -3 with an adequate choice of d as reported in this thesis.

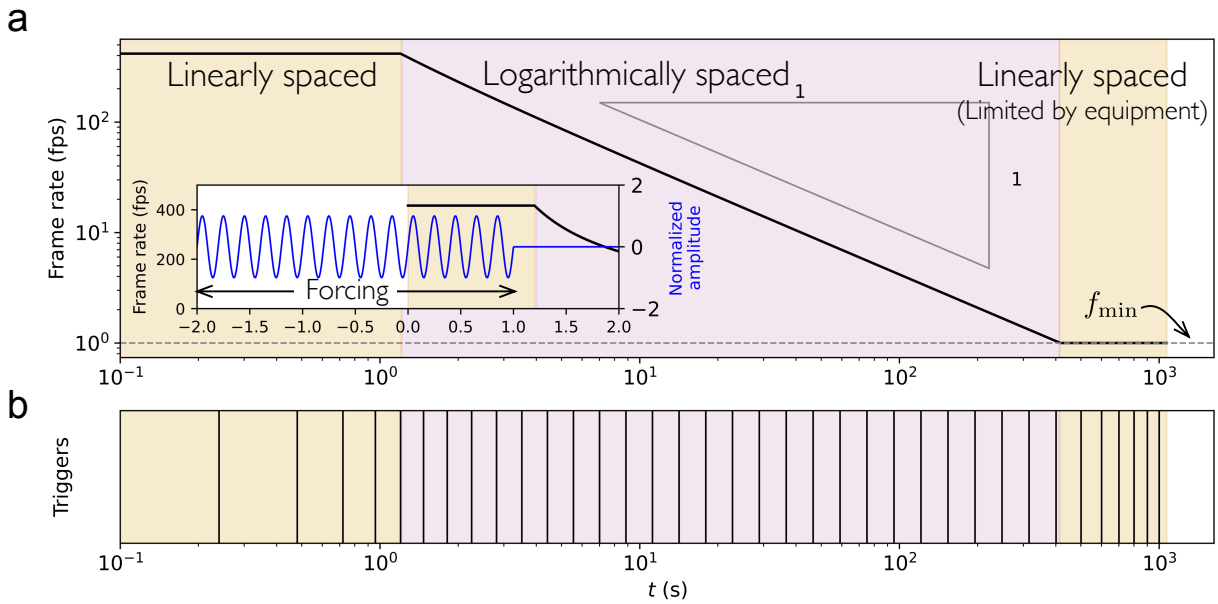

Figure 4.3: **A customized triggering scheme is applied to capture the slowing-down dynamics.** (**a**)We decrease a frame rate of a high speed camera as the dynamics slows down. (**b**) The lines indicate the timings when we trigger the camera to take an image. For clarity, we show only 1% of the triggers. Within each separation, we trigger the high speed camera a hundred times.

4.1.4 Decay of fluctuating energy

In this section, we describe the measurements of the energy decay as well as the evolution of integral scale. The turbulence generated by double oscillating grids serves as our reference to classical results. The central region between the connected grids has near zero mean flow. We first define the fluctuations, then present the results of energy and integral lengthscales. Technical aspects such as the determination of a virtual origin are discussed in Sect. C

Definition of velocity fluctuations

For steady turbulent flows, such as a pipe flow or von Kármán flow, that are forced by steady actuation, it is common to define a mean flow as a temporal average. Our experiments invite two additional definitions because (a) we force periodically and (b) we consider free evolution of turbulence. We thus define a mean flow via (a) phase average and (b) ensemble average.

1. Temporal average (for steady turbulence):
   $\langle U_i \rangle_t(x_j) = \frac{1}{T} \int_0^T U_i(x_j, t) dt$

2. Phase average (for periodic forced turbulence with a period τ):
   $\langle U_i \rangle_n(x_j, \Theta) = \frac{T}{\tau} \int_0^\tau U_i(x_j, t) \delta[(t \bmod T) - \Theta] dt$

3. Ensemble average (for evolving turbulence):
   $\langle U_i \rangle(x_j, t) = \frac{1}{N} \sum_{n=1}^{N} U_i^{(n)}(x_j, t) dt$

Here Θ is a phase with respect to periodic forcing, and $U_i^{(n)}$ refers to the velocity field of the n-th sample. To study the decay dynamics, we define fluctuating velocity using the ensemble-averaged flow.

$$u_i(x_j, t) = U_i(x_j, t) - \langle U_i \rangle(x_j, t). \tag{4.13}$$

By averaging a sufficient number of samples, the ensemble-averaged flow effectively eliminates the fluctuations observed across different runs, leading to a converged flow (Figure 4.4a-c). Figure 4.4d-f) are energy spectra of the ensemble-averaged flow, showing the convergence in the Fourier space.

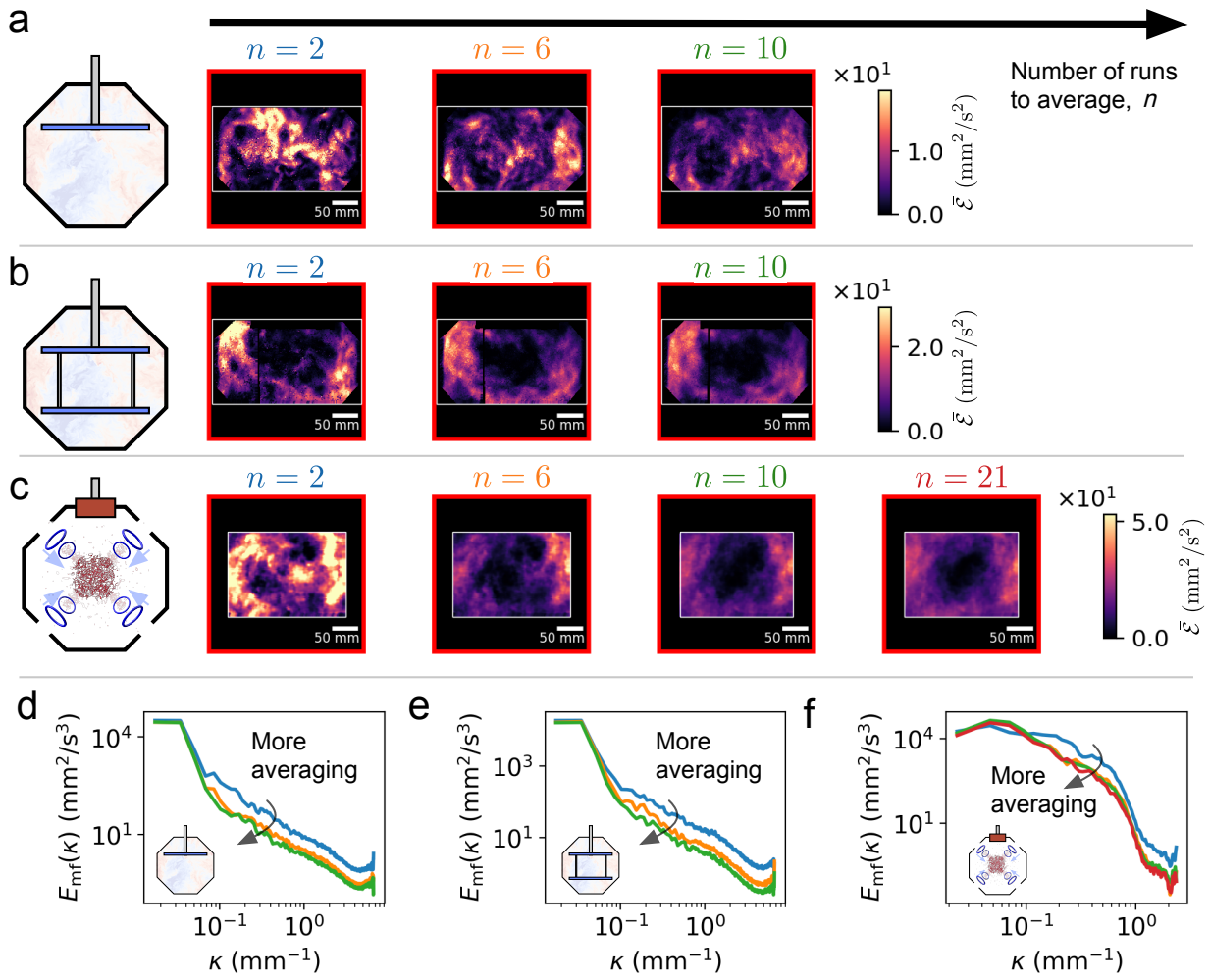

Figure 4.4: **Averaging sufficiently many samples results in a converged, time-varying mean flow for each setup.** The mean-flow energy during the decay shows the convergence as more samples are put into averaging for each seup: **(a)** a single oscillating grid, **(b)** double oscillating grids, **(c)** a turbulent blob. **(d-f)** Energy spectra of the mean flow field for each setup also display the convergence. (d) A single oscillating grid. (e) Double oscillating grids. (f) A turbulent blob.

4.1.5 Overview of turbulence decay measurements

In Figure 4.5) we show the time-evolution of the fluctuating energy for the three forcing methods (SOG, DOG, and a turbulent blob). During the recording of 1050 seconds, the energy decays over five orders of magnitudes. Figure 4.5) shows the fluctuating energy field scaled by its average value at each instant of time.

While the drive is still turned on, the flow develops into unique mean flow structure illustrated in the top row of Figure 4.5). After a few seconds of a transient period, featureless turbulence is established. In all cases, the fluctuating fields coarsen over time. A wide range of spatial scales at $t = 3$s is gone by the end ($t = 600$s) where only a few large-wavelength modes are dominant. Kolmogorov and integral length scales, respectively $\eta(t) = (\nu^5/\epsilon(t))^{1/4}$ and $\ell(t)$, describe the scale of the smallest and largest eddy. As seen in Figure 4.5), both length scales grow over time. In absence of boundaries, the separation of scales is expected to close as $\ell/\eta \propto Re^{3/4} \sim t^{(n+1)}$ if $n \neq -1$. Different growth rates of these scales manifest the coarsening behavior in Figure 4.5).

In our experiments, the integral length scale is capped by the size of the chamber. As the flow continues to decay, the motions in small scales get dissipated more, leaving only a few large vortices in the chamber. The last remaining vortex continues to decay, and the flow is eventually dominated by the convection rolls, driven by heat provided from the laser illumination.

In case of the single oscillating grid, the strong mean flow leads to require a long time for the flow to completely develop into turbulence. Thus, we first examine the results of the double oscillating grids and a turbulent blob.

4.1.6 Integral scale controls turbulence decay

Figure [**?**]a plots the decay of turbulent kinetic energy for the double oscillating grid and the turbulent blob. The measurements show the attenuation of energy over five orders of

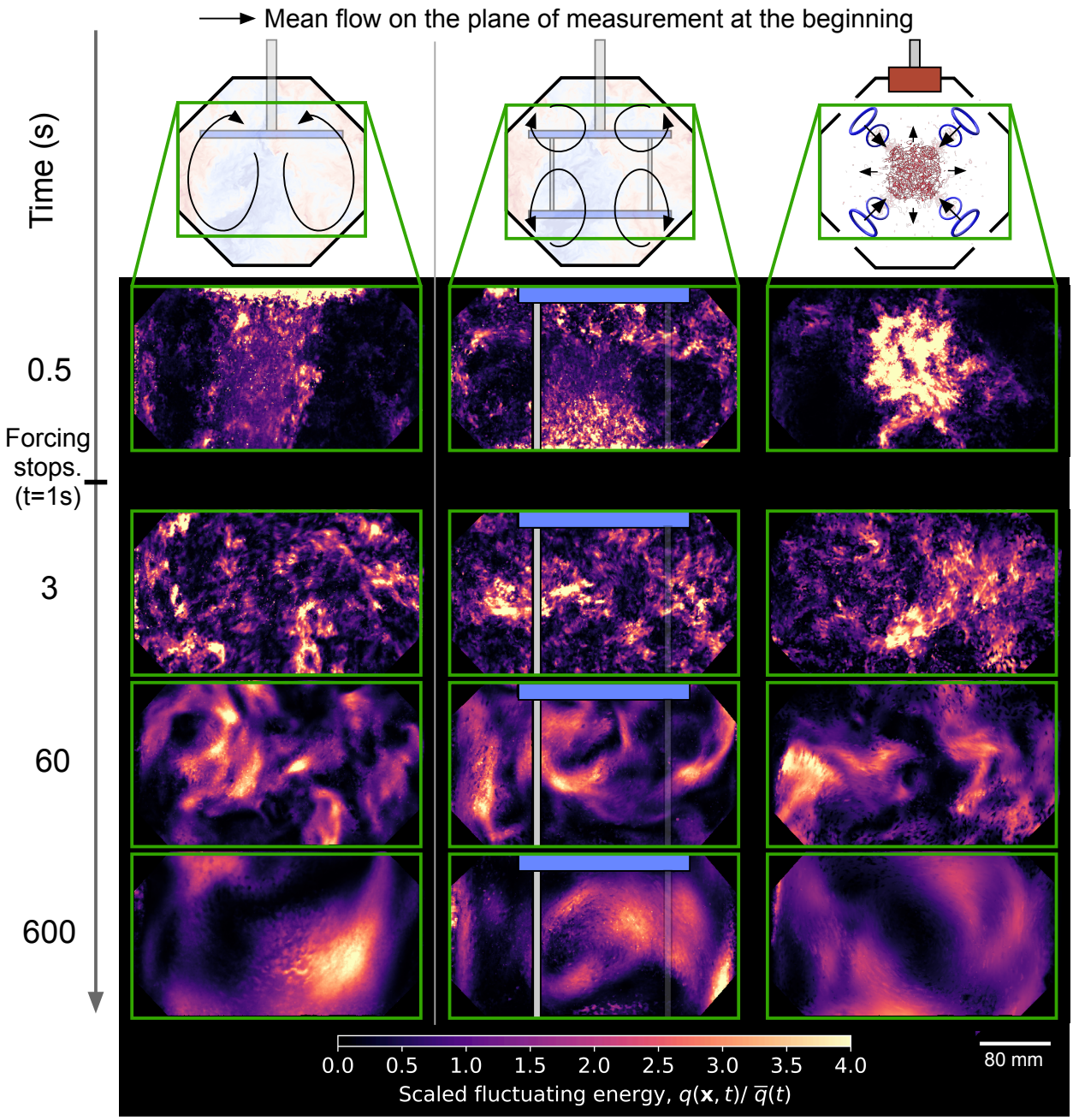

Figure 4.5: **The structure of a fluctuating energy field coarsens as it decays.** The top row shows the schematic of the mean flow structure of the three methods to initiate turbulence. The heat maps display the snapshots of the fluctuating energy field at t=0.5, 3, 60, and 600 sec. At approximately 800-1000s, the flow becomes dominated by thermal convection. The intensity is scaled by the mean value at each instant of time. **(Left)** A single oscillating grid **(Middle)** Double oscillating grids **(Right)** A turbulent blob.

magnitudes. In terms of root-mean-square velocity, it is initially around 100mm/s, dropping to 0.2 mm/s. To human eyes, it requires a patience to even notice the flow. Figure 4.6a shows highlights the two distinct decay behaviors for these methods to generate turbulence.

The double oscillating grid exhibits the decay law of $n = -2$. This is the same decay law observed in a pipe filled with He II [162]. This decay law is understood with an integral length scale ℓ being constant throughout the decay 4.1.3, and our calculation validates this assumption (Figure 4.6b, orange).

There exists two regimes of decay for a turbulent blob, which is understood via growth of the integral scale. In the early times, it decays closer to $t^{-1.3}$, and later closer to t^{-2}. It is impossible to express the measurement with a single power law by varying a virtual origin (See Sect. C for our approach to determine a virtual origin). What gives rise to two power laws? After inspecting the evolution of the integral length scale, the timing of the saturation coincides with the moment that the decay law switches. When turbulence is confined within the blob, the integral length scale is at most the radius of the blob. How does the integral length scale grow as the turbulence spreads, and fills the entire chamber? Two scenarios are possible. Eddies within the blob get stretched as the blob expands. In this case, the integral length scale is expected to be as large as the size of the box once turbulence fills the chamber at $t - t_0 = 0.5$s. The second case is that eddies are simply advected as the blob expands, keeping ℓ fixed? According to Figure 4.6b (green), we conclude that the latter takes place. The spreading of the turbulence in chamber has little effect on the growth of the integral scale. As soon as the integral scale saturates, the decay law approaches to $n = -2$.

The logarithmic recording technique reveals that the energy continues to decay over a thousand of seconds with the exponent expected with turbulent dissipation. This poses a question how flow at a low Reynolds number, Re= $O(10^1)$, exhibits a turbulent character, which we focus in the next section.

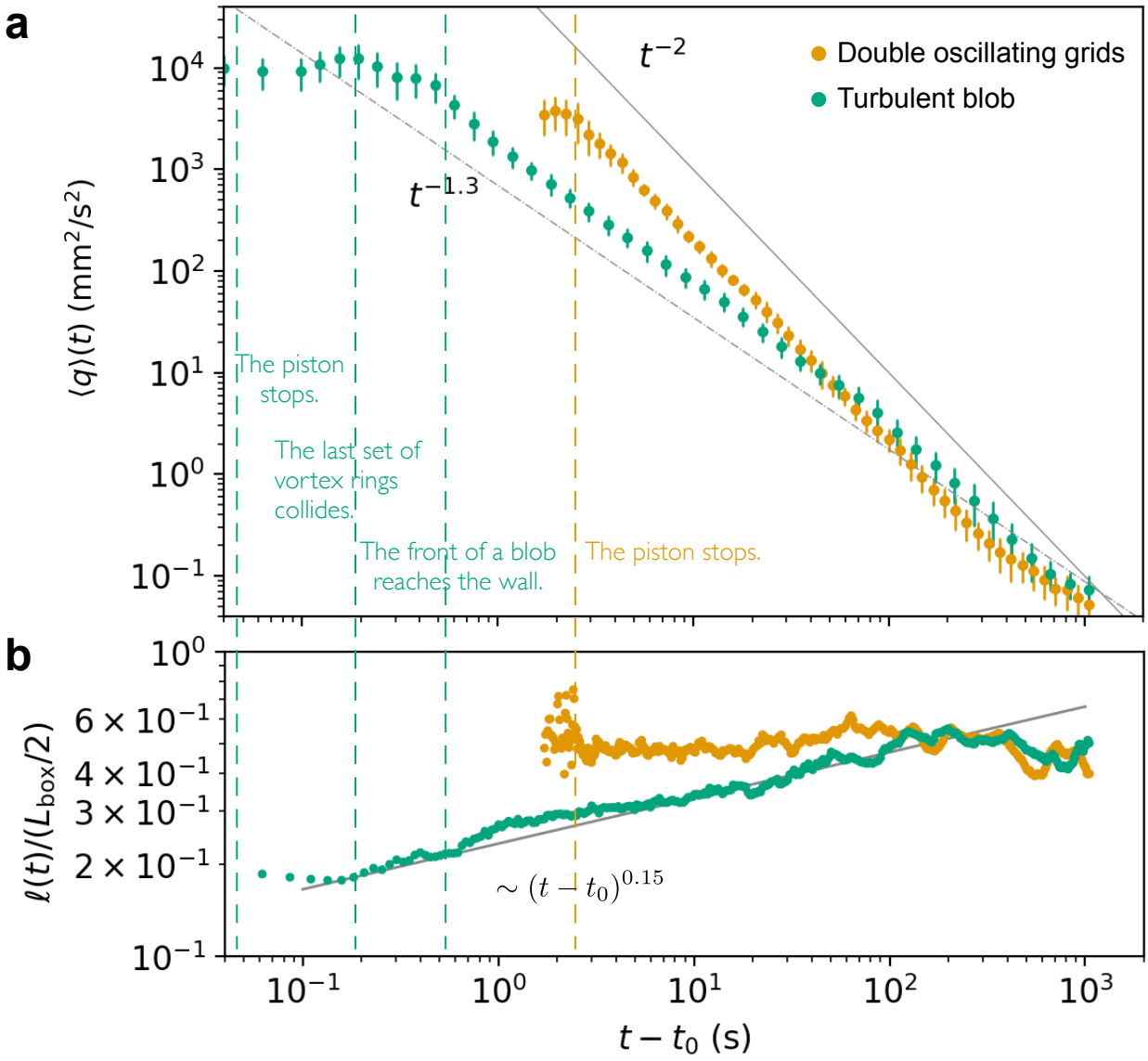

Figure 4.6: **Growth of integral lengths scale dictates the decay exponent of turbulent kinetic energy. (a)** Turbulent kinetic energy density on the measured plane for a turbulent blob and double oscillating grids. The former shows two decay regimes, while the latter follows a single power law with exponent -2. a virtual origins are -0.85 s and 1.72 s respectively. **(b)** The integral length scale $\ell(t)$ grows with a power law from approximately the blob radius ($R_{\text{blob}}/(L_{\text{box}}/2) \approx 0.3$) until saturation. Saturation coincides with the point when energy exhibits faster decay. In contrast, the integral length scale remains constant during decay of turbulence initiated by double oscillating grids.

4.1.7 The Enduring Turbulence: Evolution of spectra and dissipation rate

At the final stage of decay, observed turbulence exhibits a simplified spatial structure characterized by the presence of a large vortex occupying a chamber. During this period, one might assume that the flow is no longer turbulent. Instead, viscous dissipation $\epsilon_{\text{viscous}} \propto \nu U^2/L^2$ takes place, as opposed to turbulent dissipation $\epsilon \propto U^3/L$. Does the flow remain turbulent throughout decay?

To investigate this, we analyze the energy spectrum. Figure 4.7a illustrates the spectrum at different instants of time. Faintly plotted data points indicate regions affected by spectral leakage and attenuation caused by PIV. For detailed information on how we determine the valid spectrum region, we refer to Sect. 3.10. Initially, the spectra conform to Kolmogorov's five-thirds law, but the inertial subrange gradually diminishes over time. However, even during the final stage of decay (Figure4.7b), the spectra align with the master curve derived from a compilation of grid turbulence and boundary layer experiments [142]. The reduced inertial subrange indicates the transition into the dissipation range for the rescaled spectrum. This trend is also evident in the decay of turbulence initiated by the double oscillating grids (Figure 4.7a-b).

To rescale the spectra to the master curve, an estimation of the dissipation rate $\epsilon(t)$ is required. However, the methods outlined in Sect. 3.11.2 are not applicable for estimating $\epsilon(t)$, except for the direct method. This is because these methods rely on identifying the inertial subrange either in the energy spectrum or the structure function. In this study, we employed three alternative methods to estimate the dissipation rate, which are summarized as follows.

1. Derivative method: Compute the finite difference of the average fluctuating energy with respect to time, $d\langle q(\boldsymbol{x}, t)\rangle_s/dt$.

a. [142] plots a collection of 1D energy spectra from numerous experiments. Here we multiplied the referenced spectrum by 55/18 to compare it to our 3D spectra [134].

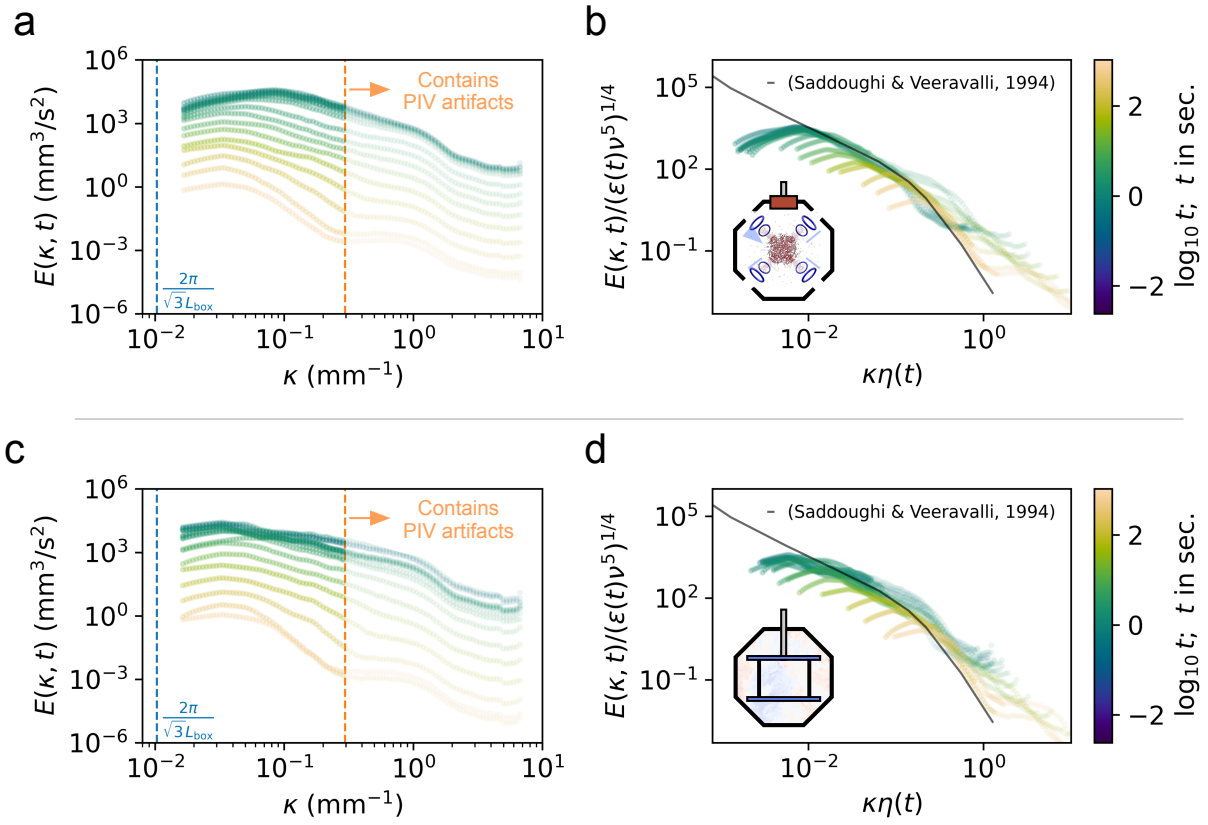

Figure 4.7: **Energy spectrum of a turbulent blob exhibits turbulent nature during the entirety of decay.** **(a)** Time evolution of 3D energy spectrum of the turbulence initiated by vortex ring collisions at different times. **(b)** Rescaled spectra of (a) are plotted along side the master curve[a] [142]. **(c)** Energy spectra of turbulence initiated by double oscillating grids. **(d)** Rescaled spectra of (c). Data points that contain artifacts from PIV are faintly shown. See Sect. 3.10.

2. Spectral method: Perform fitting to the rescaled one-dimensional energy spectrum to the master curve. We only fit the part of the spectrum that does not contain artifacts by PIV.

3. Direct method: Compute $\epsilon_{s_{ij}} = 2\nu\langle s_{ij}s_{ij}\rangle_s$ where $s_{ij} = (1/2)(\partial_j u_i + \partial_i u_j)$. This method assumes isotropy, and requires the data to be spatially resolved.

In both cases of turbulent blob and double oscillating grids, the three methods show agreement in their estimations of the dissipation rate up until the middle of the measurement period, after which the direct method starts to deviate from the other methods (see Figure 4.8a-b). This deviation suggests that the direct method underestimates the average dissipation rate. This underestimation is likely due to the fact that in the late phase of decay, dissipation predominantly occurs near the wall as a result of the presence of a large vortex. The direct method, limited in its view, fails to accurately capture the true average dissipation rate.

On the other hand, both the derivative and spectral methods consistently agree throughout the decay process. The slight deviation observed in the last few data points can be attributed to the point where turbulence ceases to exist and thermal convection becomes dominant in the flow chamber.

We are now interested in understanding how the integral scale evolves throughout the decay process. The agreement between $\epsilon_{E_{11}}$ and the measured dissipation rate, $d\langle q(\boldsymbol{x},t)\rangle_s/dt$, strongly suggests that turbulent dissipation occurs throughout the decay. By employing dimensional analysis, we define the alternative integral length scale $\mathcal{L}$ as follows:

$$\mathcal{L}(t) = \frac{\langle q(\boldsymbol{x},t)\rangle_s^{3/2}}{\epsilon_{E_{11}}(t)}. \tag{4.14}$$

While one might consider defining $\mathcal{L}(t)$ by substituting $\epsilon_{E_{11}}(t)$ with $|dq/dt|$, this approach

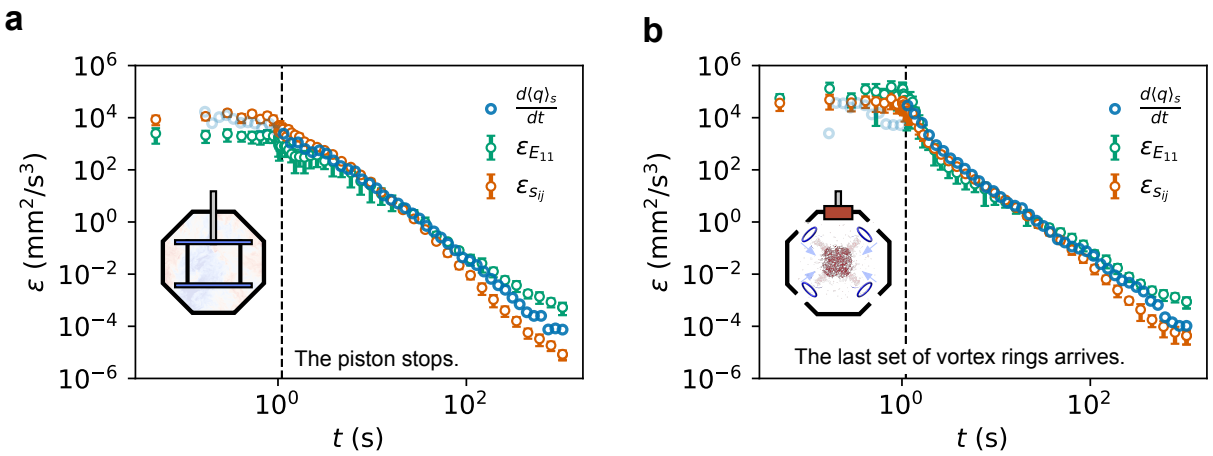

Figure 4.8: **Comparison of dissipation rate calculated by the (1) derivative (2) spectral and (3) direct methods.** **(a)** Double oscillating grids. **(b)** A turbulent blob. The faint, blue data points represent random fluctuations of turbulent energy and not dissipation.

to determining the integral scale ℓ would be circular. To avoid this circularity, we utilize the dissipation rate obtained through the spectral method. We find that the integral scale $\mathcal{L}$ exhibits a different growth exponent compared to the longitudinal integral scale $\ell(t) \propto (t - t_0)^{0.15}$ (see Figure 4.9a). This discrepancy can be attributed to the weak dependence of the non-dimensional dissipation rate ϵ_0 on the Reynolds number. It can be shown that ϵ_0 is equal to the ratio of the two integral scales, i.e., $\epsilon_0 = \ell/\mathcal{L}$. By computing the ratio of these integral scales, we observe that ϵ_0 fluctuates between 0.5 and 2.2, which is consistent with values reported in the literature ($0.5 < \epsilon_0 < 1.5$ for $50 > Re_\lambda > 5$) [165, 179].

To summarize, the rescaled energy spectrum support the view that flow is turbulent throughout decay. With the dissipation rate required to scale the spectra, the growth rate of the integral length scale is consistent with the decay exponent of turbulent energy. Figure 4.9 shows the evolution of total energy $Q(t)$ by numerically solving Eq. 4.11 in 3D with a time varying integral length scale and $\epsilon_0 = 1.0$. We employed the initial condition from a 3D PTV measurement of a turbulent blob, and chose the Neumann boundary condition. The result exhibits two decay regimes as observed in experiments.

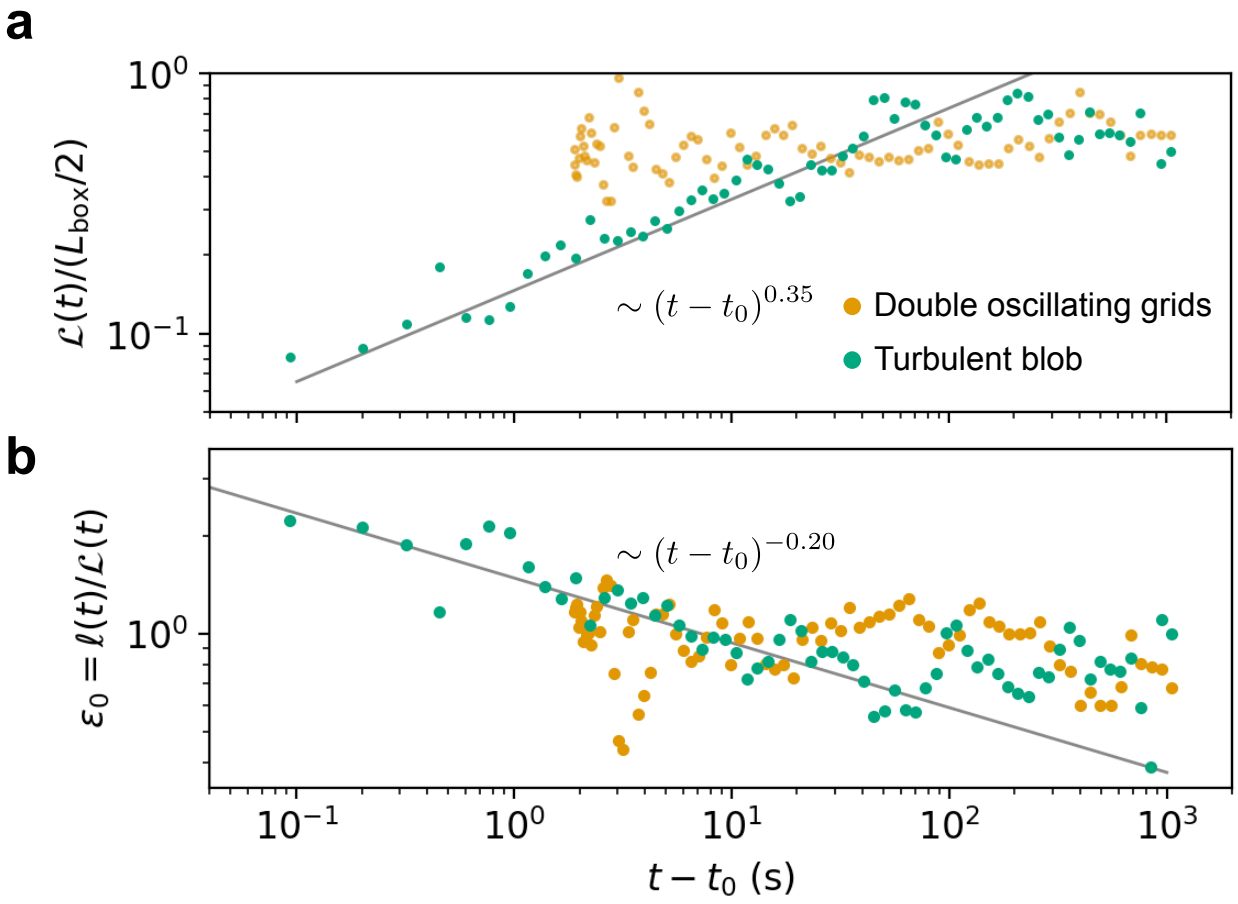

Figure 4.9: **Integral length scale, defined as $\mathcal{L}(t) = q^{3/2}(t)/\epsilon_{E_{11}}(t)$ exhibits the scaling consistent with the observed decay law: $n = 2(n_{\mathcal{L}} - 1)$. (a)** The integral length scale $\mathcal{L}$ grows and saturates for a turbulent blob. On contrary, it takes a constant value for double oscillating grids. **(b)** Non-dimensional dissipation rate ϵ_0 is plotted. The different exponents of $\ell(t) \propto (t - t_0)^{n_\ell}$ and $\mathcal{L}(t) \propto (t - t_0)^{n_\mathcal{L}}$ indicates that ϵ_0 depends on time, equivalently the Reynolds number.

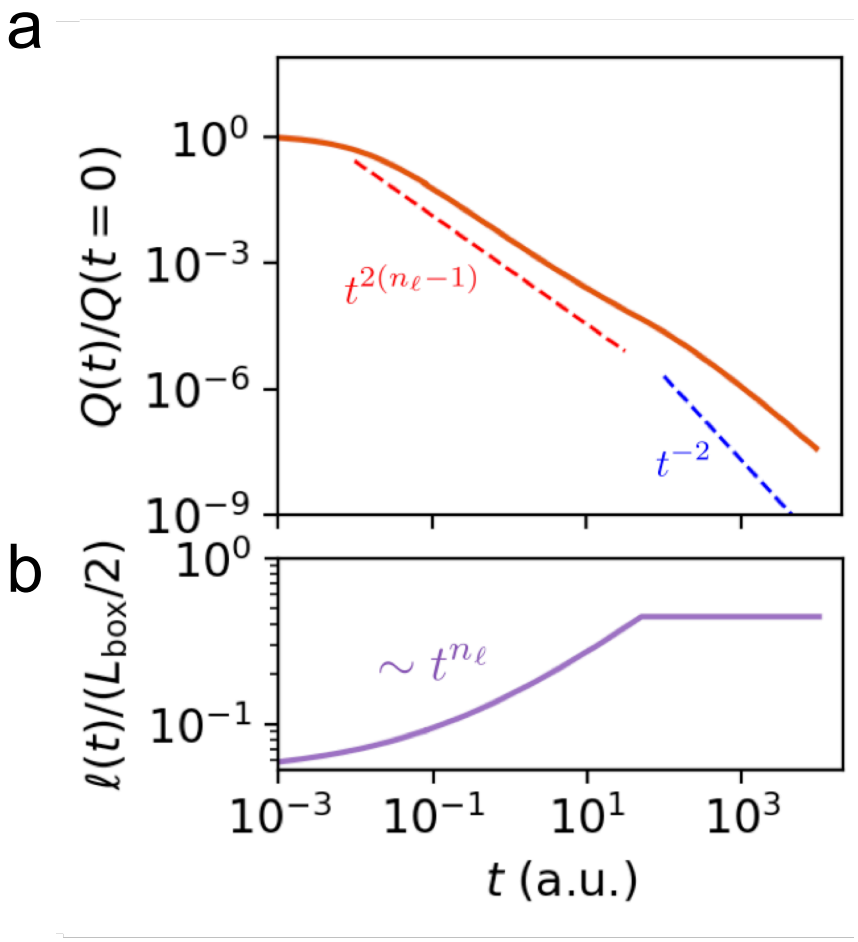

Figure 4.10: **The zeroth law with a time-varying integral length scale results in two decay regimes.** We perform a simulation of Eq. 4.11 with an experimental initial condition with a prescribed integral length scale. **(a)** Total energy in the simulation volume shows the existence of two regimes with distinct decay exponents, $2(n_\ell - 1)$ and -2. **(b)** A prescribed function of the integral length scale is plotted. n_ℓ. The simulation was performed with $\epsilon_0 = 1.0$ and $\Delta t = 0.01$.

4.1.8 Turbulence Initiated by a Single Oscillating Grid

Turbulence that is initiated by a single oscillating grid is distinct from the explored cases in two ways. First, it is dominated by a mean flow. Second, the flow is strongly anisotropic. These features lead to take a longer time for featureless turbulence to be established. This transient period is observed across the quantities we have introduced to characterize the decay (See Figure 4.11a-f). The turbulent kinetic energy is not described by a single power law but it asymptotically reaches to the t^{-2} decay. The longitudinal integral length scale $\ell(t)$ is near the saturation when the forcing stops. The presented picture still remains true: the integral length scale controls the decay of turbulent energy.

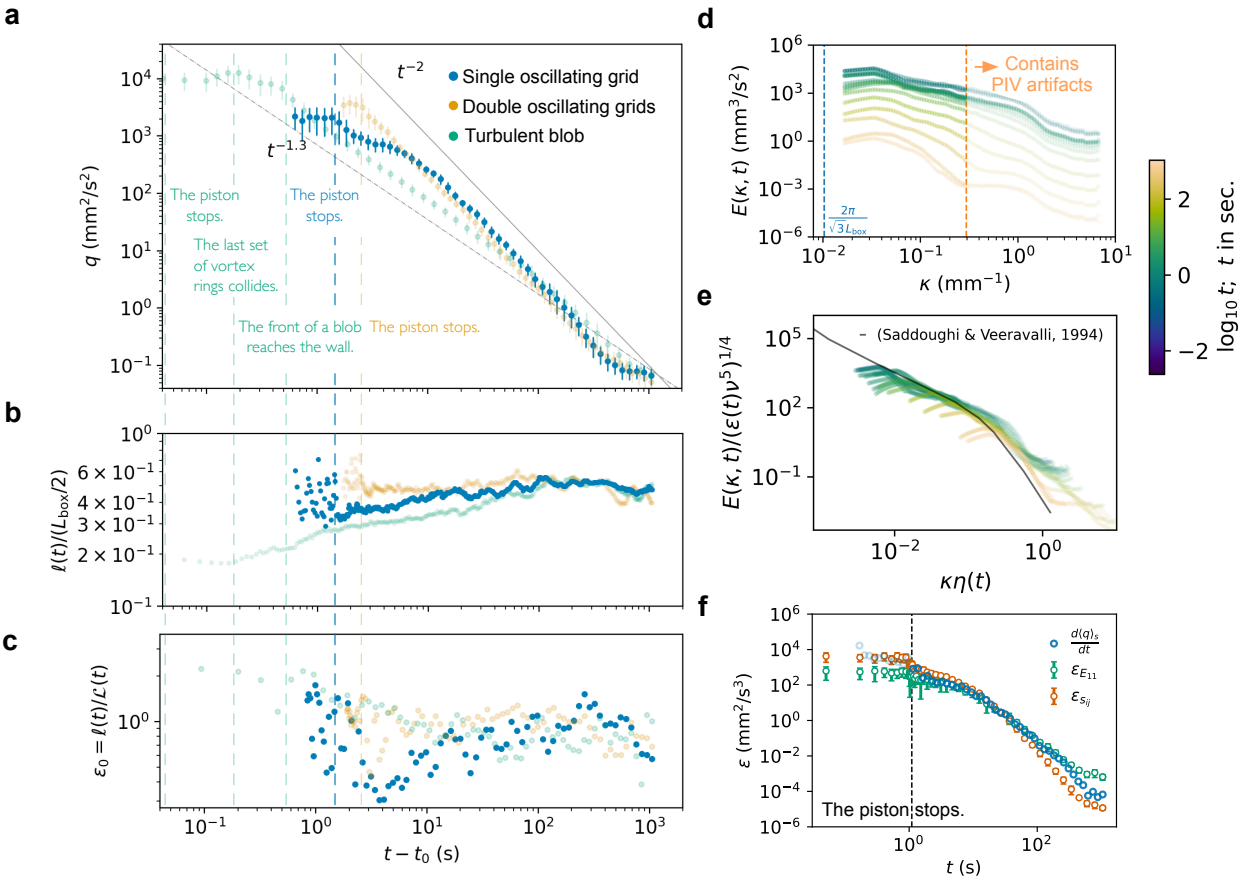

Figure 4.11: **Decay of turbulence initiated by a single oscillating grid (a)** Turbulent kinetic energy vs reduced time. ($t_0 = -0.63$ s) **(b)** Integral length scale vs time. **(c)** Dimensionless dissipation rate ϵ_0 vs time. **(d)** Time evolution of the 3D energy spectrum. **(e)** Time evolution of the rescaled 3D energy spectrum. **(f)** Dissipation rate vs time.

4.1.9 Conclusions

We investigated the decay of turbulence inside a confined box using three different turbulence generation methods: a single oscillating grid (SOG), double oscillating grids (DOG), and repeated collision of vortex rings (a turbulent blob). We observed that both SOG and DOG exhibited an energy decay characterized by a power law of t^{-2}, consistent with findings from quantum turbulence [162]. The turbulent blob showed two distinct decay regimes with power laws of $t^{-1.3}$ and t^{-2}, respectively. The transition between these regimes coincided with the saturation of the integral length scale. Numerical simulations of a model with a time-varying integral length scale supported our experimental observations. Overall, our results suggest that the integral length scale plays a crucial role in controlling the decay of turbulence inside the box.

Once turbulence becomes fully developed in a closed chamber, its length scales (integral, Taylor, and Kolmogorov scales) grow but at different rates, leading to close the separation of scales. In our experiments, it is found that the flow holds to possess turbulent character even after 800 seconds, and the energy drops close to six orders of magnitudes during this period. It is the first time when the t^{-2} decay is observed in water. Previous confirmation of this decay law took place in the closed pipe filled with He II. In both cases, this decay mode requires the saturation of integral length scale. By starting with the isolated blob of turbulence, we manage to engineer the integral length scale to be smaller than the value of saturation which is found to be about 30% of the chamber dimension. Then turbulence decays with two power laws. The first regime corresponds to the period when the integral length scale grows, and the decay law is expressed by $n = 2(n_\ell - 1)$. The second regime corresponds to the saturation of the integral scale, resulting in the t^{-2} decay. The model equation in Eq. 4.11 captures how the decay law dynamically changes as the integral length scale saturates.

Our findings confirm the validity of the zeroth law of turbulence throughout the decay

process, even at low Reynolds numbers around $O(10^1)$. This law states that, in *dynamical equilibrium*, the energy injection rate at large scales matches the dissipation rate at small scales. We observed that this law holds true even when the system is decaying, which is out of a statistical equilibrium. Our results align with previous studies where variations in the decay law were observed due to factors like limited domain size and uncontrolled growth of the integral length scale. Overall, our experiments, simulations, and theoretical analysis support the idea that manipulating the integral length scale offers control over the decay behavior of turbulence.

4.2 Propagation of turbulence

The study of turbulence blob in a quiescent fluid provides a unique opportunity to explore its spreading characteristics. In the presence of mean flow advection often hinders the intrinsic diffusivity of turbulence, making it challenging to separate transport from the mean flow. For a turbulent blob, mean flow is substantially smaller than the turbulence within the core. Although a pioneering investigation [161] using superfluids showcased the enhanced diffusivity of turbulence in a quiescent region, no experiments have been conducted to examine the intrinsic diffusivity of classical turbulence. In this section, we present findings on the spreading behavior of a spherical region of turbulence within its quiescent surroundings, marking the first investigation of its kind in classical turbulence. Our results demonstrate that the propagation of turbulence follows similar scaling laws observed in reference [161], yet with a distinctive long-tail shape instead of a sharp front.

4.2.1 Review of previous studies

The problem of turbulent mixing was initially considered by Richardson, which led to G.I. Taylor's formulation of shear-augmented diffusivity [169]. Prior to this, Kolmogorov provided a phenomenological argument in [84] for how eddies enhance diffusivity and introduced $\ell q^{1/2}$ as the effective diffusivity in turbulent flows, also known as eddy diffusivity. The key idea is that large eddies play a crucial role in turbulent transport, making the diffusivity proportional to the product of the integral scale and the characteristic velocity scale.

In our study, we consider a model (Eq. 4.11) that incorporates the concept of eddy diffusivity. Barenblatt *et al.*[11] and Chen & Goldenfeld [36] independently investigated the same model in the context of a turbulent burst in a pipe. Chen and Goldenfeld demonstrated that an initial turbulent burst develops into a sharp front, later found consistent with the experiments using superfluid [161]. In our study, we define $h(t)$ as the position of the turbulent front that separates the region with finite energy from the rest. We assume $\ell(t) =$

$\alpha h(t)$, where α is a dimensionless constant to be determined through experiments. By treating the dissipative term as small ($\epsilon_0 \ll 1$), we employ perturbation theory to derive first-order asymptotic solutions:

$$\begin{aligned}
\text{Total turbulent energy} \quad & Q(t) \sim t^{-\frac{\epsilon_0}{15\alpha^2}} \\
\text{Front position} \quad & h(t) \to \xi_0 Q^{1/5} t^{2/5} \sim t^{\frac{2}{5}-\frac{\epsilon_0}{75\alpha^2}} \\
\text{Turbulent energy density} \quad & q(r,t) \to \frac{Q}{h^3}\left(\frac{1}{10\alpha}\right)^2 \xi_0^5 \left[1-\left(\frac{r}{h}\right)^2\right]_+^2 \sim t^{-\frac{6}{5}-\frac{2\epsilon_0}{75\alpha^2}} \left[1-\left(\frac{r}{h}\right)^2\right]_+^2 \\
\text{Turbulent enstrophy density} \quad & \omega^2(r,t) \sim t^{-\frac{11}{5}-\frac{2\epsilon_0}{75\alpha^2}} \left[1-\left(\frac{r}{h}\right)^2\right]_+^3 . \qquad (4.15)
\end{aligned}$$

Here "+" is a cutoff defined as $g_+ \equiv g \cdot \Theta(g)$ where Θ is the Heaviside function. We kindly acknowledge Minhui Zhu and Nigel Goldenfeld for performing the calculations. Details of the calculation can be found in Appendix B.

4.2.2 Experimental methods

In this study, we examine the spreading behavior of a turbulent blob within a quiescent fluid. To generate an isolated turbulent blob, we repeatedly collide vortex rings, as described in [110]. Once the vortex rings are no longer fed, the turbulent blob expands naturally. By varying the size and intensity of the injected vortex rings, we manipulate the characteristics of the turbulent blob.

To capture the dynamics of the spreading process, we employ two-dimensional Particle Image Velocimetry (PIV) with two different views: a "wide" view and a "narrow" view, as illustrated in Figure 4.12a-b. Initially, we analyze the measurements obtained from the widest view to investigate how turbulence spreads in a quiescent fluid. After confirming that the qualitative results are consistent, we proceed to collect additional data using the narrow view, effectively increasing the Reynolds number of the turbulent flow. Table 4.3 provides a comprehensive summary of the experimental conditions employed in this study.

In the table, the integral length scale is estimated using the empirical relation $\alpha_0 R_{\text{ring}}$ with $\alpha_0 = 2.17 \pm 0.13$.

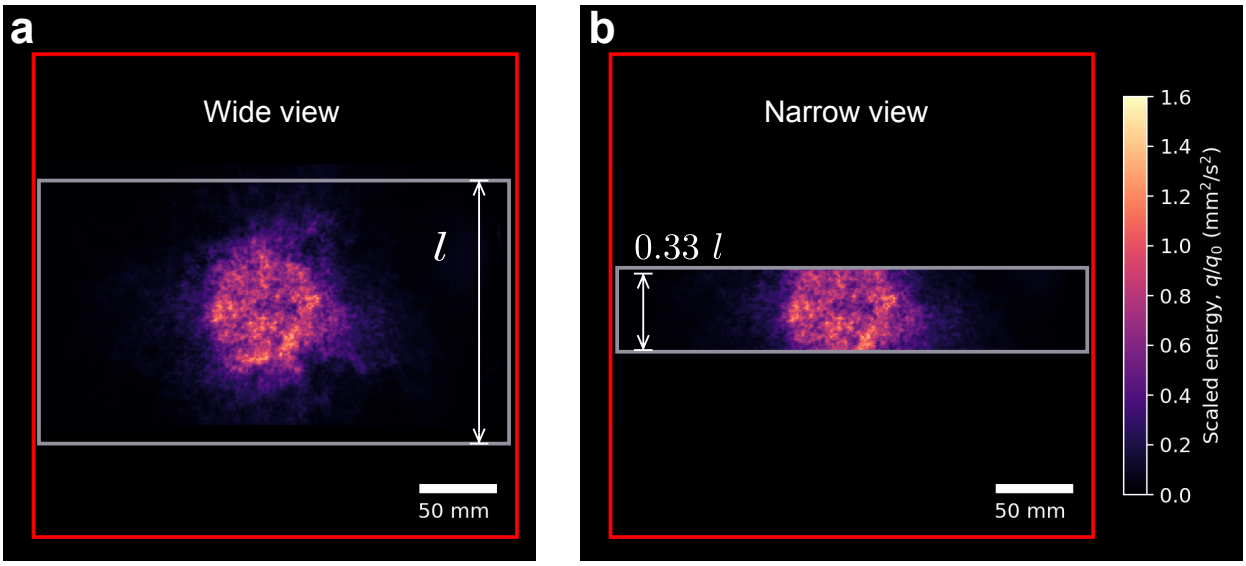

Figure 4.12: **Description of two views used for measurement of a propagating front. (a)** A wide view is used to examine the isotropy of the front. **(b)** A narrow view is used for efficient data collection to assess the effect of the Reynolds number on the front.

L_p (mm)	V_p (mm/s)	L/D	v_{eff} (mm/s)	f (Hz)	u' (mm/s)	$\mathcal{L} = \alpha_0 R_{\text{ring}}$ (mm)	Re=$u'\mathcal{L}/\nu$	Number of runs
(Wide view)								
11.2	247	2.1	213	5	288	26.3	7.6×10^3	10
(Narrow view)								
11.2	105	2.1	102	5	52	26.3	1.4×10^3	7
11.2	247	2.1	213	5	288	26.3	7.6×10^3	9
11.2	413	2.1	363	5	401	26.3	1.1×10^4	7
11.2	710	2.1	420	5	450	26.3	1.2×10^4	7
15.3	708	2.9	513	5	615	28.3	1.7×10^4	7

Table 4.3: **Experimental summary of front propagation of freely expanding turbulence**.

4.2.3 Propagation of a turbulent front

In a steady state, a turbulent blob remains confined and adjusts its dissipation rate and size to the injected vortex structure. However, once the injection of vortex rings ceases, the turbulent blob freely expands, as depicted in Figure 4.13a-c. To analyze the expansion process comprehensively, we compute the radial distribution of turbulent energy density at each frame and present it in the form of a kymograph (Figure 4.13d). Similarly, the enstrophy within the blob expands in tandem with the energy (Figure 4.14a-d). In each kymograph, we plot either energy or enstrophy that is scaled by the value at the origin. This way, the kymograph easily addresses how each quantity is spreading.

To evaluate the spreading dynamics, we examine the radial profiles of energy and enstrophy at different times (Figure 4.13a and Figure 4.16a). To track spreading, we identify the contour where the relative energy (or enstrophy) drops to a certain threshold. In Figure 4.13d and Figure 4.14d we show two contours h_p that correspond to the threshold values p of 0.5 and 0.1. Motivated from the self-similar solution of Eq. 4.11, we define the apparent front position as $h(t) = h_p/\sqrt{1-\sqrt{p}}$. This mapping translates the contour obtained by thresholding to the position of the front if shape of the front is consistent with the form in Eq. 4.15. An alternative mapping using second moment is possible but only differs by a constant.

By scaling the radial distance using the apparent front position $h(t)$ or the expected scaling law $(t-t_0)^{2/5}$ of $h(t)$, the profiles collapse. The observed front exhibits a long tail (Figure 4.15b), which resembles the mean-field solution observed in quantum turbulence. This highlights the background flow outside the blob. Similarly, the enstrophy front exhibits a shape consistent with the mean-field solution, albeit with a tail (Figure 4.16b). Because the background flow is laminar, this tail of the enstorophy front is less pronounced than the energetic front.

Furthermore, we analyze the attenuation of energy and enstrophy density at the origin

as they spread (Figure 4.13e and Figure 4.14e). Although the exact exponents are difficult to determine with a limited range, the observed evolution is consistent with the mean-field predictions. The fitted power-law exponents for the front position $h(t)$ and energy density $q(r = 0, t)$ are consistent with the mean-field expectations (See Sect 4.1.3), with $n_h = 0.38$ and $n_q = -1.3$, respectively, compared to the mean-field predictions of $n_h = 2/5$ and $n_q = -6/5$.

Finally, we investigate the dependency of the spreading behavior on Reynolds number. By controlling the injected power feeding to the blob and varying the Reynolds number at the beginning, we find that the shape of the turbulent front remains independent of Reynolds number within the range of 2600 to 174,000 (Figure 4.17).

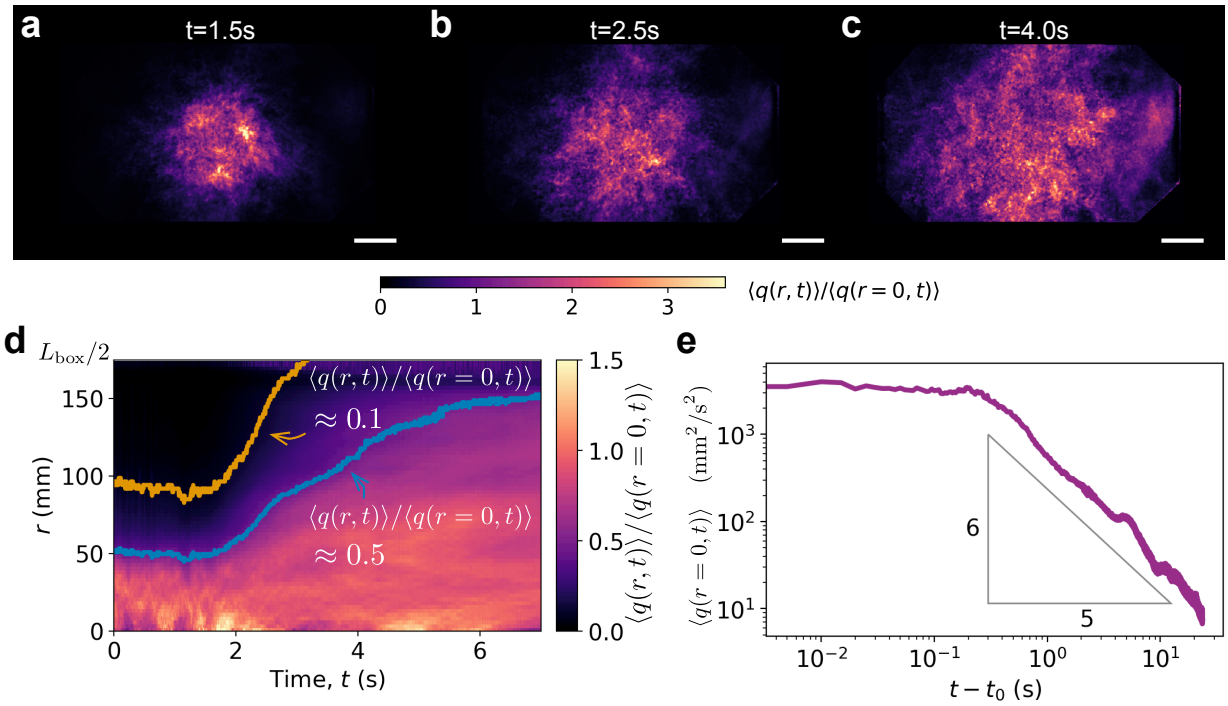

Figure 4.13: **Propagation of energy within a spherical turbulent burst.** $(L/D, v_{\text{eff}}, f)$ = (2.1, 213 mm/s, 5 Hz)**(a-c)** Snapshots of ensemble-averaged turbulent energy field at different time are shown. The last set of vortex rings arrive at $t = 1.4$s. **(d)** A kymograph of scaled turbulent energy represents the expansion of the blob. **(e)** Time-evolution of average turbulent energy on the plane of measurement is shown. Each scale bar represents 50mm.

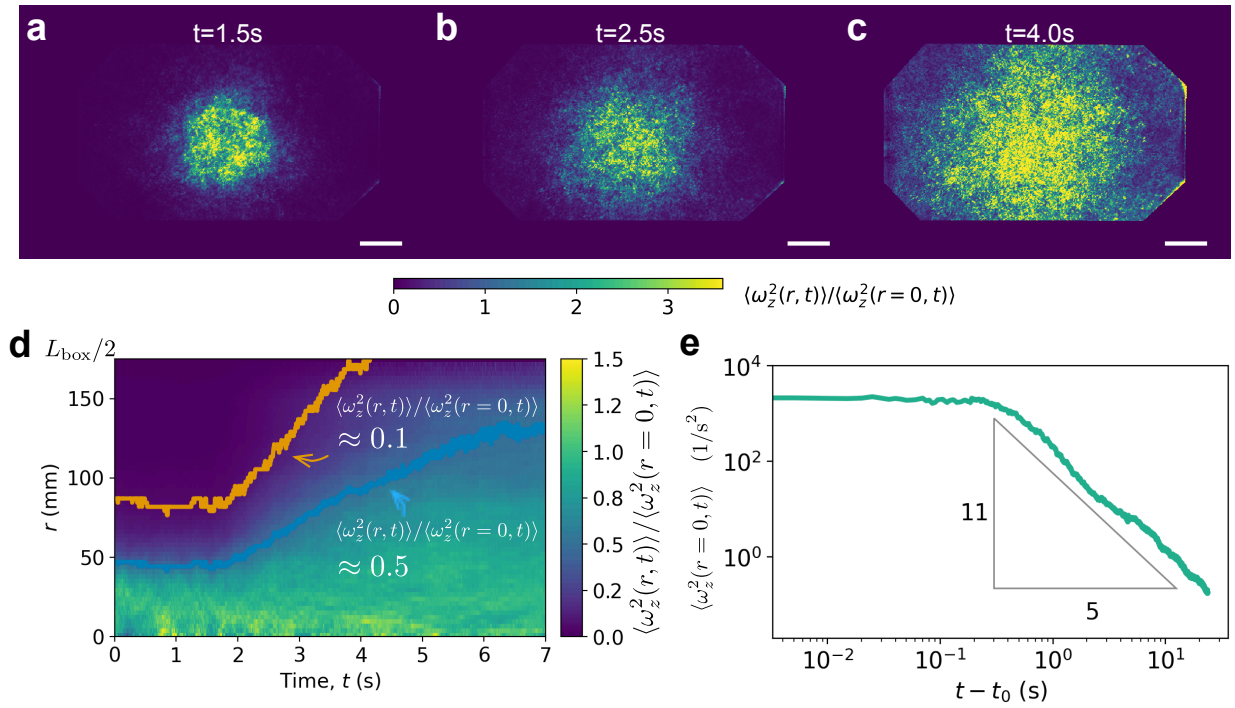

Figure 4.14: **Propagation of enstrophy within a spherical turbulent burst.** $(L/D, v_{\rm eff}, f) = (2.1,\ 213\ \text{mm/s},\ 5\ \text{Hz})$**(a-c)** Snapshots of ensemble-averaged turbulent energy field at different time are shown. The last set of vortex rings arrive at $t = 1.4$s. **(d)** A kymograph of scaled turbulent energy represents the expansion of the blob. **(e)** Time-evolution of average turbulent energy on the plane of measurement is shown. Each scale bar represents 50mm.

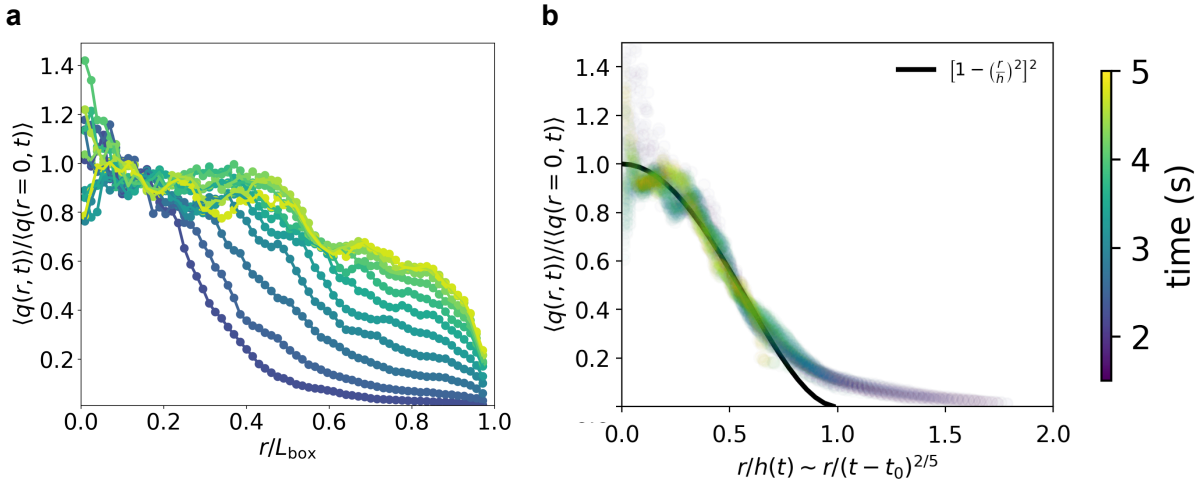

Figure 4.15: **Propagation of energy within a spherical turbulent burst.** $(L/D, v_{\text{eff}}, f)$ = (2.1, 213 mm/s, 5 Hz)**(a-c)** Snapshots of ensemble-averaged turbulent energy field at different time are shown. The last set of vortex rings arrive at $t = 1.4$s. **(d)** A kymograph of scaled turbulent energy represents the expansion of the blob. **(e)** Time-evolution of average turbulent energy on the plane of measurement is shown. Each scale bar represents 50mm.

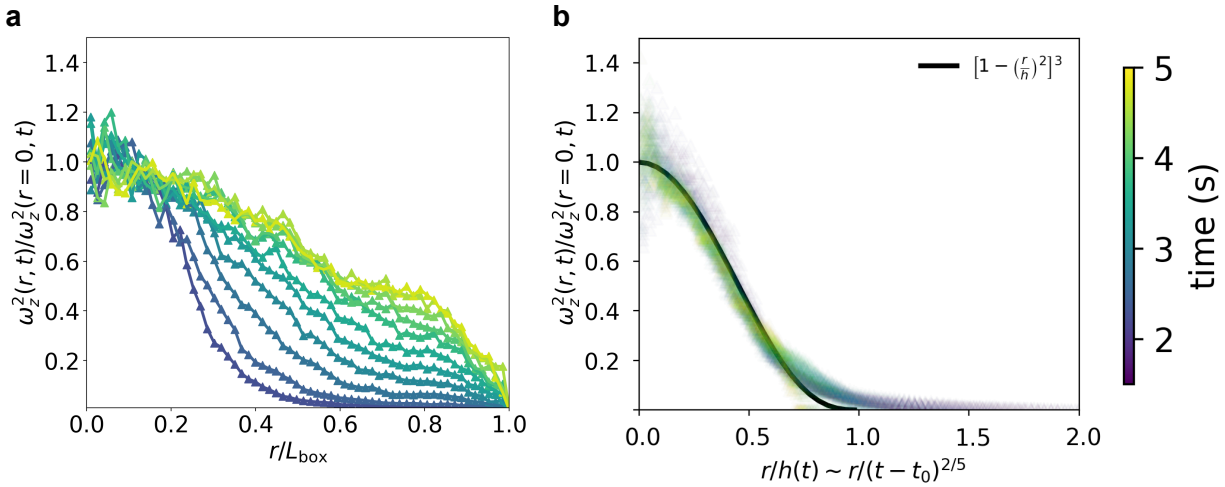

Figure 4.16: **Propagation of enstrophy within a spherical turbulent burst.** $(L/D, v_{\text{eff}}, f)$ = (2.1, 213 mm/s, 5 Hz)**(a-c)** Snapshots of ensemble-averaged turbulent energy field at different time are shown. The last set of vortex rings arrive at $t = 1.4$s. **(d)** A kymograph of scaled turbulent energy represents the expansion of the blob. **(e)** Time-evolution of average turbulent energy on the plane of measurement is shown. Each scale bar represents 50mm.

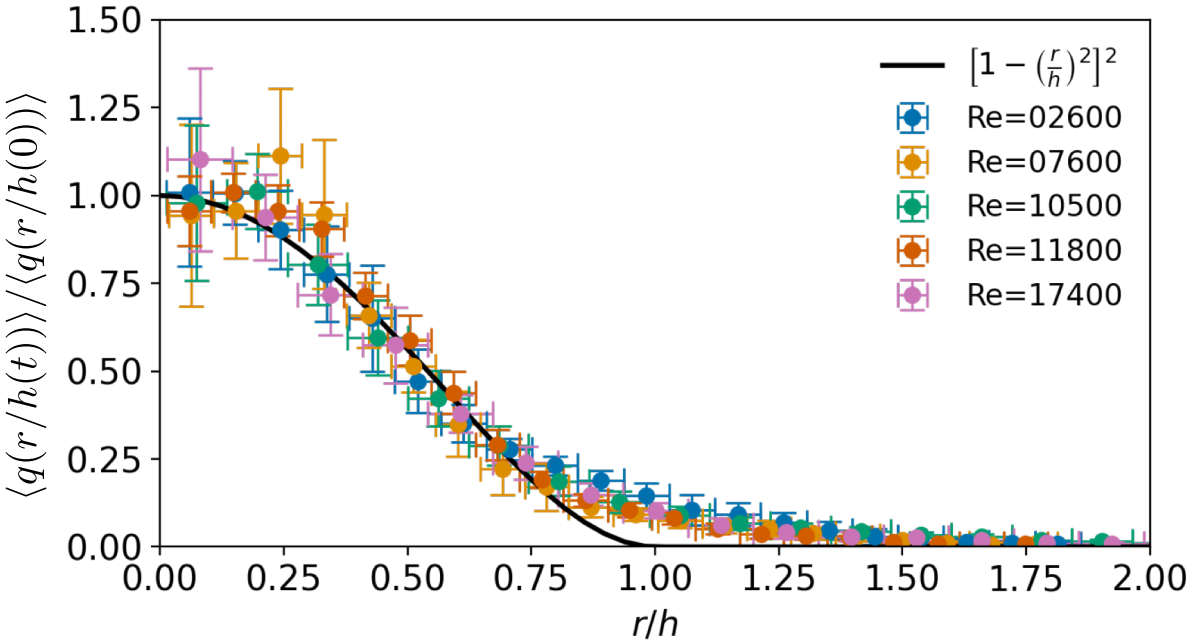

Figure 4.17: **The shape of a radially propagating turbulent front is independent of Reynolds number from 2,600-17,400.** The vertical error bars indicate the standard deviation, and the horizontal error bars represent the bin width where the mean is computed.

4.2.4 Conclusions

We have investigated how an isolated, spherical turbulent burst spreads in a quiescent fluid. We initialize the confined turbulence by repeatedly colliding vortex rings. Once the turbulence is fully established after 50 collision cycles, we let the blob freely expand while it decays simultaneously. Our findings are summarized as follows.

1. Energy and enstrophy spread with a profile with a tail unlike the observed sharp front in quantum turbulence [161]. The measured profiles in our experiment agrees with the predicted sharp profile until $r/h < 0.75$ with a tail due to the background.

2. Both turbulent energy and enstrophy spread self-similarly.

3. Fitting the $h(t)$ and the energy density at origin $q(r = 0, t)$ with same virtual origin yields $h(t) \propto (t - t_0)^{0.38}$ and $q(r = 0, t) \propto (t - t_0)^{-1.3}$. These exponents are in a closer agreement with the mean-field predictions of the eddy diffusivity model ($n_h =$

$2/5 = 0.4$, $n_{q(r=0)} = -6/5 = -1.2$) than simple diffusion ($n_h = 1/2 = 0.5$, $n_{q(r=0)} = -3/2 = -1.5$). For the latter, we refer the characteristic length such as the standard deviation or full width at half maximum (FWHM) grows as $(t - t_0)^{1/2}$.

4. No dependence on Reynolds number, in the range between 2600 and 17400, is found in how turbulence spreads.

The findings are consistent with the mean-field solution of Eq. 4.11 that incorporates eddy diffusivity. Although the dissipative term is found to be dominant, the proposed model encapsulates the diffusive dynamics as it predicts the consistent exponents of the front position $h(t)$ and the energy density at the center of the spherical turbulent burst $q(r = 0, t)$. However, the observed profile of energy and enstrophy both exhibit a tail that is not explained by the model. Preliminary simulations using observed profile as an initial condition show that the tail persists for a substantial time before it approaches the asymptotic form. Moreover, allowing the integral time scale $\ell(t)$ to vary in time, as seen in experiments, affects the stability of the solution. Future work includes unveiling (1) the source of the tail and (2) duration until the profile reaches the asymptotic form and (3) how the asymptotic form is affected by temporally varying integral scale. Overall, this experiment addresses the novelty in directly probing the transport property of turbulence. While the model with simple diffusion is possible, the formulation with the eddy diffusion is consistent with the observed dynamics of spreading with physically interpretable diffusivity of turbulence.

CHAPTER 5

CONCLUSIONS AND OUTLOOK

In this work, we have developed a novel approach to generate an isolated region of turbulence far away from the boundaries. We have thoroughly examined the behavior of turbulence within the blob and investigated its decay process. The following highlights and outlook summarize our key findings:

5.1 Key findings

Turbulence

1. Successful creation of a sustained, isolated blob of turbulence away from boundaries.
2. Controlled injection of inviscid invariants to turbulence using vortex rings.
3. Transition from coherent vortex reconnections to turbulence and development of a theory.
4. Direct measurement of a 3D turbulent energy spectrum without relying on Taylor's frozen turbulence hypothesis.
5. Observation of enduring turbulence throughout the decay process.
6. Identification of two decay laws and their relationship to the saturation of the integral length scale.
7. Direct measurement of the diffusive properties of turbulence in water.

Vortex rings

1. Creation of a helical vortex ring using a helical orifice.

2. Comprehensive characterization of inviscid invariants carried by a vortex ring using 3D PTV.

3. Data collapse of vortex ring properties (radius, circulation, and traveling speed).

4. Observation of symmetrical collision of eight identical vortex rings.

5. Discovery of duality in symmetrical collisions of identical vortex rings.

Techniques

1. Construction of a mobile 2D/3D velocimetry setup with multiple high-speed cameras, a pulsed laser, and a chiller, enabling various experimental configurations.

2. Development of an optimal triggering scheme for measuring turbulence decay over extended durations.

3. Establishment of a data infrastructure for efficient experiment management, data processing, storage, and transfer.

4. Release of a comprehensive Python library called tflow for 2D and 3D velocimetry analysis, including energy spectra, structure functions, and turbulence length scales. The library is available to the public, and is hosted at Github: https://github.com/tmatsuzawa/tflow.

5. Development of a visualization technique for Lagrangian dynamics using 3D rendering software.

6. Construction of experimental chambers and actuating mechanisms for producing the presented experimental outcomes.

5.2 Outlook

As final remarks, we offer avenues for further investigation and ask questions beyond the scope of this thesis.

Confined turbulence

1. How does energy transfer occur at the turbulent-non-turbulent interface (TNTI)?

2. How does turbulence respond to a periodic drive?

3. Can we create two blobs of turbulence with different intensities and connect them with a pipe to observe thermal-like transport?

4. Can alternative symmetrical configurations be used to confine turbulence? For example, can platonic configurations with different numbers of entrances and exits effectively confine the flow?- Icosahedral and tetrahedral configurations are next promising as they produce less number of vortex rings after collisions.

5. Can turbulence be confined with significant angular impulse? Are there optimal strategies for achieving this confinement?

6. Can the presented approach be extended to confine plasma?

Helical turbulence

1. How does helicity alter energy spectra in classical turbulence? What are the potential variations in the energy spectrum?- Our preliminary measurement yields $E(\kappa) \sim \kappa^{-5/3}$ and $\mathcal{H}(\kappa) \sim \kappa^{-8/3}$. With the ability to tune helicity in the blob, one can systematically investigate the effect of helicity on turbulence.

2. How abundant is helical turbulence in nature?

Batchelor turbulence- turbulence with significant angular impulse

1. Can one create turbulence with significant angular impulse?- Eq. 4.2 suggests that turbulence with significant angular impulse leads to alter its integral scale from $E(\kappa) \sim \kappa^2$ to $\sim \kappa^4$ near origin. Answering this question has a potential to control the integral length scale at will.

2. How does turbulence with significant angular impulse decay?

3. Does turbulence possess a memory?- In the concluding stage of our decay experiments, the majority of recorded footage reveals the presence of a prominent clockwise-rotating vortex. Interestingly, when we introduce the opposite angular impulse, the chirality of the final vortex is influenced. This observation challenges Kolmogorov's hypothesis, which suggests the loss of such memory as eddies cascade down. By leveraging a turbulent blob, we have the opportunity to investigate the point at which turbulence relinquishes information by tracking the behavior of inviscid invariants.

Helical vortex rings

1. How do inviscid invariants of a helical vortex ring evolve?

2. What is the stability of a helical ring? How does it maintain its structure over time?

Techniques

1. Can we develop a physically consistent deconvolution operator, using a data-driven and self-consistent approach, to address artifacts in PIV-extracted flows such as blurring and spectral leakage?

APPENDIX A

SYMBOLS AND CONVENTIONS

Here we summarize the symbols and conventions used in this thesis.

For a vector field $U_i(x_j, t)$,

$$\langle U_i \rangle (x_j, t) = \int f(x_j, t) U_i(x_j, t) dx_j dt \tag{A.1}$$

refers to an ensemble average with the probability function $f(x_j, t)$. In experiments, $f(x_j, t)$ is unknown a priori. Instead of ensemble averaging, we frequently perform temporal averaging of $U_i(x_j, t)$:

$$\langle U_i \rangle_t (x_j) = \frac{1}{\tau} \int_0^\tau U_i(x_j, t) dt. \tag{A.2}$$

The ensemble averaging and the temporal averaging are said to be identical for a statistically stationary system (ergodicity).

The spatial average is denoted by a subscript s.

$$\langle U_i \rangle_s (t) = \frac{1}{\mathcal{V}} \int_{\mathcal{V}} U_i(x_j, t) dV \tag{A.3}$$

Similarly, the average over a polar angle is denoted by θ.

$$\langle U_i \rangle_\theta (r, \phi, t) = \frac{1}{2\pi} \int_0^{2\pi} U_i(r, \theta, \phi, t) r d\theta \tag{A.4}$$

To study the phase dependence of the flow, we use the following notion to denote the phase $\Theta \in [0, 1)$ throughout the paper.

$$t = nT + \Theta \tag{A.5}$$

Here, $n \in \mathbb{Z}$ is a number of cycles, and T is a forcing period. The phase-locked (or phase-averaged) quantity is denoted by a subscript n, and is given by

$$\langle U_i \rangle_n(x_j, \Theta) = \frac{T}{\tau} \int_0^\tau U_i(x_j, t) \delta[(t \bmod T) - \Theta] dt \tag{A.6}$$

for $\tau \bmod T = 0$. These averaging procedures can be combined. For example, we presented the energy averaged over space and cycles (Eq. A.3 and A.6) in Figure 3.2d.

$$\frac{1}{2}\langle U_i U_i \rangle_{sn}(\Theta) = \frac{T}{\tau}\frac{1}{\mathcal{V}} \int_0^\tau \int_\mathcal{V} \frac{1}{2} U_i(x_j, t) U_i(x_j, t) \delta[(t \bmod T) - \Theta] dV dt \tag{A.7}$$

Table A.1: **Nomenclature**

	Basics
p	Pressure
Re	Reynolds number, $Re = (u'\mathcal{L})/\nu$
t	Time, $t = (n + \Theta)T; n \in \mathbb{Z}$
U_i	The i-th component of a velocity field
u_i	The i-th component of a fluctuating velocity field
	or a velocity field in a general context
u'	Strewamwise, root-mean square fluctuating velocity, $u' = (1/d)\sqrt{\sum_{i=0}^{d} u_i^2}$
Ω_i	The i-th component of a vorticity field $\vec{\Omega} = \nabla \times \vec{U}$
ω_i	The i-th component of a vorticity of a fluctuating velocity field
	or vorticity in a generic context, $\vec{\omega} = \nabla \times \vec{u}$
Θ	Phase with respect to a forcing period, $\Theta \in [0, 1)$
ρ	Density of a fluid
ν	Kinematic viscosity
x, y, z	Cartesian coordinates

Table A.1: **Nomenclature (cont'd)**

σ, φ, z	Cylindrical coordinates
r, θ, ϕ	Spherical coordinates
$\vec{\kappa}, \kappa_i$	Wavenumber
δ	Kronecker delta

	Symbols
$\langle A \rangle$	Ensemble average of A
$\langle A \rangle_n$	Phase-locked average of $A(t)$ (Average over cycles with frequency f), $\langle A \rangle_n(\Theta) = \frac{1}{fT} \int_0^T A(t)\delta((ft - \Theta) \bmod 1))dt$
$\langle A \rangle_s$	Spatial average of $A(x_i)$, $\langle A \rangle_s = \frac{1}{V} \int_{\mathcal{V}} A(x_i)dV$
$\langle A \rangle_t$	Temporal average of $A(t)$, $\langle A \rangle_t = \frac{1}{T} \int_0^T A(t)dT$
$\langle A \rangle_\phi$	Azimuthal average of $A(r, \theta, \phi)$ in spherical coordinates, $\langle A \rangle_\phi = \frac{1}{2\pi} \int_0^{2\pi} A(r, \theta, \phi) r^2 \sin\theta d\phi$
$\langle A \rangle_\theta$	Polar average of $A(r, \theta, \phi)$ in spherical coordinates, $\langle A \rangle_\theta = \frac{1}{\pi} \int_0^{\pi} A(r, \theta, \phi) r^2 \sin\theta d\theta$
$\breve{u}_i$	Discrete Fourier transform of a fluctuating velocity field u_i
$\tilde{u}_i$	Continuous Fourier transform of a fluctuating velocity field u_i

	Chapter 2: Apparatus and Methods
f	Forcing frequency
v_{eff}	Effective velocity of a piston, $v_{\text{eff}} = P\langle V_p \rangle$
D_o	Diameter of an orifice in the experimental setup
D_p	Diameter of a piston in the experimental setup
L_p	Stroke length

Table A.1: **Nomenclature (cont'd)**

L_{box}	Length of the experimental chamber
N	Number of orifices in the experiments
R_p	Radius of a piston; $R_p = D_p/2$
T	Forcing period, $T = 1/f$
V_{p}	Velocity of a piston
	Chapter 3: Creation of an isolated blob of turbulence
	Section 3.6: Vortex rings (Inviscid invariants)
$\vec{A}$ or A_i	Angular impulse over an entire space
H	Helicity over an entire space
$\vec{I}$ or I_i	Hydrodynamic impulse over an entire space
K	Kinetic energy over an entire space
$\vec{L}$	Angular momentum
$\vec{P}, P_i$	Linear momentum
Γ	Circulation
	Section 3.6: Vortex rings and
	(Canonical modelsNorbury's family of vortex rings)
a	Radius of a vortex core
c	Proportionality constant related to energy partition of a vortex ring, $K_{\text{atmosphere}} = cK_{\text{ring}}$
c_1	Parameter related to vorticity distribution of experimental vortex rings Eq. 3.21
A_{sph}	Radius of Hill's spherical vortex

Table A.1: **Nomenclature (cont'd)**

H_{ring}	Helicity of a vortex ring/loop
I_{ring}	Hydrodynamic impulse of a vortex ring
K_{ring}	Kinetic energy inside the vortex atmosphere with a presence of a vortex ring: $K_{\text{ring}} = cK$
R_{ring}	Radius of a vortex ring (radial distance to the first moment of vorticity)
V_{ring}	Self-induced velocity of a vortex ring
Γ_{ring}	Circulation of a vortex ring
Ω_{ring}	Volume of a vortex atmosphere
α	Constant in a vortex ring model
β	Constant in a vortex ring model
ψ	Streamfunction
K_1	The first kind of the elliptic integrals
K_2	The second kind of the elliptic integrals
α_{Norbury}	Shape parameter of a vortex family in [124]
K_{added}	Kinetic energy outside the vortex atmosphere with a presence of a vortex ring
K_{rect}	Kinetic energy associated to a rectilinear motion of a vortex ring
K_{int}	Kinetic energy associated to a internal motion of a vortex ring
K_ψ	Kinetic energy inside a volume bounded by an isocontour of a streamfunction ψ
M_{ij}	Added mass tensor
	Section 3.6: Vortex rings (Production and measurement)
$\vec{d}$	Unit vector of propagation of a vortex ring

Table A.1: **Nomenclature (cont'd)**

h	Semi-major radius of a vortex ring
l	Semi-minor radius of a vortex ring
$L_*, L/D$	Formation number
K_{exp}	Kinetic energy inside the vortex atmosphere, measured by the PIV experiments
P	Velocity program factor, $P = \langle V_p^2 \rangle_t / \langle V_p \rangle_t^2$
R_{slug}	Reynolds number of a slug of fluid
V_{slug}	Velocity of a slug of fluid
Γ_{c}	Circulation of a vortex ring within a core
	Section 3.6: Vortex rings (Helicity attenuation)
a'	Clipping length
R_{major}	Semi-major length of a twisted vortex loop
R_{minor}	Semi-minor length of a twisted vortex loop
Tw	Twist of a vortex loop
Wr	Writhe of a vortex loop
ψ	Complex scalar function to construct a twisted vortex loop
χ	Parameter associated to a core size of a vortex loop
	Section 3.8-3.9: Turbulent blob and Turbulent statistics
k	Turbulent kinetic energy, $k = \frac{1}{2}\langle u_i u_i \rangle$
u'	Characteristic fluctuating speed, $u' = \sqrt{u_i u_i}/N; i = 1 - N$
C	Kolmogorov constant related to $E(\kappa)$, $E(\kappa) = C\epsilon_0^{2/3}\kappa^{-5/3}$ in the inertial subrange

Table A.1: **Nomenclature (cont'd)**

C_1	Kolmogorov constant related to $E_{11}(\kappa)$, $E_{11}(r) = C_1\epsilon_0^{2/3}\kappa_1^{-5/3}$ in the inertial subrange
C_2	Kolmogorov constant related to $D_{LL}(r)$, $D_{LL}(r) = C_2(\epsilon_0 r)^{2/3}$ in the inertial subrange
$\mathcal{E}_0$	Average kinetic energy inside a turbulent blob
$\mathscr{E}$	Kinetic energy per unit mass $\mathscr{E} = U_i U_i/2$
$\mathcal{L}$	Large eddy turnover time, $\mathcal{L} = u'^3/\epsilon_0$
R_{blob}	Radius of a turbulent blob
R_{eff}	Effective radius of a turbulent blob, $R_{\text{eff}} = 4^{1/3}R_{\text{blob}}$
δu	Difference of fluctuating velocity between two positions, $\delta u_i = u_i(\vec{x} + \vec{r}) - u_i(\vec{x})$
ϵ	Dissipation rate
ϵ_0	Dissipation rate inside a homogeneous turbulent blob
η	Kolmogorov length scale $\eta = (\frac{\nu^3}{\epsilon_0})^{\frac{1}{4}}$
λ	Transverse Taylor microscale
$\overline{\Omega}_i$	The i-th component of vorticity of a temporally averaged flow $\langle U_j \rangle_t$

Section 3.10: Energy spectrum and structure function

$f(r)$	longitudinal velocity correlation function
$g(r)$	transverse velocity correlation function
k	Average fluctuating kinetic energy
k_{local}	Average fluctuating kinetic energy in the measurement domain
$w(x_i)$	Window function
D_{ij}	Second-order structure function

Table A.1: **Nomenclature (cont'd)**

D_{LL}	Second-order longitudinal structure function
$E_{ij}(\kappa_1)$	One-dimensional turbulent energy spectrum along x_1
$E(\kappa)$	Turbulent energy spectrum
$\mathcal{F}_{x_i}$	Fourier operator along the direction $\hat{x}_i$
J	Jacobian
R_{ij}	Velocity two-point correlation function
W_x	Interrogation window size along the x direction
W_y	Interrogation window size along the y direction
ζ	Correction factor due to windowing
κ_θ	Polar component of a wavenumber vector
κ_ϕ	Azimuthal component of a wavenumber vector
κ_{Ny}	Nyquist wavenumber
κ_r	Radial component of a wavenumber vector, $\kappa_r = \sqrt{\kappa_i \kappa_i}$
Φ_{ij}	Velocity spectrum tensor

Section 3.11-12: Energy balance of a blob and dissipation rate

$p(r/R_{\text{blob}})$	Fraction of dissipation (energy, or enstrophy) inside a sphere of radius r to the total Eq. 3.51
s_{ij}	Rate-of-strain tensor of a fluctuating velocity, $s_{ij} = \frac{1}{2}(\partial_j \langle u_i \rangle + \partial_i \langle u_j \rangle)$
$\mathcal{D}$	Dissipated power, $\mathcal{D} = \rho \int_{\mathcal{V}} \epsilon(\vec{r}) dV$
$\mathcal{D}_{\text{tot}}$	Total dissipated power inside the experimental chamber
$\mathcal{I}$	Injected power, $\mathcal{I} = 8 K_{\text{ring}} f$
$\mathcal{I}_{\text{tot}}$	Total injected power inside the experimental chamber
S_{ij}	Rate-of-strain tensor, $S_{ij} = \frac{1}{2}(\partial_j U_i + \partial_i U_j)$

Table A.1: **Nomenclature (cont'd)**

$\overline{S_{ij}}$	Rate-of-strain tensor of mean flow, $S_{ij} = \frac{1}{2}(\partial_j \langle U_i \rangle + \partial_i \langle U_j \rangle)$
$\epsilon_{s_{ij}}$	Dissipation rate that is computed via a rate-of-strain tensor s_{ij}
$\epsilon_{D_{LL}}$	Dissipation rate that is computed via a second-order structure function
$\epsilon_{E_{11}}$	Dissipation rate that is computed via a one-dimensional energy spectrum
$\tau_{\mathcal{L}}$	Large eddy turnover time, $\tau_{\mathcal{L}} = \mathcal{L}/u'$
	Section 3.13: Enstrophy flux and confinement transition
f_c	Transitional forcing frequency from coherent vortex reconnections to formation of a turbulent blob
m_{ij}	Image moment of order (i, j) (Eq. 3.60)
$\vec{J}_m$	Mass current $\vec{J}_m = \rho\vec{U}$
$\vec{J}_{\Omega^2}$	Enstrophy current, $\vec{J}_{\Omega^2} = \Omega^2\vec{U}$
α_0	Parameter 0 in Figure 3.4; $\mathcal{L} = \alpha_0 R_{\text{ring}}$
α_1	Parameter 1 in Figure 3.4; $\epsilon_0 = \alpha_1 V_{\text{ring}}^2 f$
ν_{ij}	Second-order image moments
I_{img}	Intensity distribution of an image
Φ_m	Integrated mass flux
Φ_Z	Integrated enstrophy flux
	Section 3.14: Tuning the properties of the blob
$\mathcal{E}_0$	Average energy density inside the blob ($r < R_{\text{blob}}$
h	Helicity density, $h = U_i\Omega_i$
$\mathcal{H}_0$	Total helicity
$\mathcal{H}_{\text{cg}}$	Helicity of a coarse-grained velocity field

Table A.1: **Nomenclature (cont'd)**

$\mathcal{H}_{\text{ring}}$	Helicity that is endowed within a helical vortex ring
	Section 3.15: Gross-Pitaevskii simulation
Ψ	Wavefunction
Φ	Phase
ρ	Density
ξ	Healing length
	Chapter 4: Decay and propagation
ℓ	longitudinal integral length scale (Eq. 4.9)
$\mathcal{L}$	integral length scale;
n	Exponent of turbulent kinetic energy
n_ℓ	Exponent of a longitudinal integral length scale
$n_\mathcal{L}$	Exponent of an integral length scale
q	Turbulent kinetic energy; $q = u_i u_i/2 \propto (t - t_0)^n$
t_0	Virtual origin
Δ	Temporal interval of customized triggering
ϵ_0	Dimensionless dissipation rate; $\epsilon = \epsilon_0 q^{3/2}/\ell$
κ_q	Coefficient of diffusion for turbulent kinetic energy

APPENDIX B

LONG-TIME ASYMPTOTICS OF A SPHERICAL TURBULENT BURST

Here we derive the asymptotic solutions of a propagating spherical turbulent front in d dimensions. We hereby acknowledge Minhui Zhu and Nigel Goldenfeld for performing the calculations. In the Section 4.2.3, we compare our experimental measurements with their predictions.

We begin with the model equation about turbulent energy density $q(\boldsymbol{x},t) = u_i u_i/2$.

$$\partial_t q(\boldsymbol{x},t) = \nabla \cdot \ell(t) q^{1/2}(\boldsymbol{x},t) \nabla q(\boldsymbol{x},t) - \epsilon_0 \frac{q^{3/2}}{\ell}. \tag{B.1}$$

Define $h(t)$ as the location of turbulence propagation front from the original. The turbulence is contained in the region specifed by $r \leq h(t)$. Assume $\ell(t) = \alpha h(t)$ where α is a dimensionless constant to be determined by experiment. Now Eq. B.1 is reduced to

$$\partial_t q = \alpha h(t) \nabla \cdot q^{1/2} \nabla q - \epsilon_0 \frac{q^{3/2}}{\alpha h(t)}. \tag{B.2}$$

Assuming spherical symmetry in d-dimensional space, Eq. B.2 is further reduced to

$$\partial_t q = \alpha h(t) \left[\frac{d-1}{r} \sqrt{q}\, \partial_r q + \frac{(\partial_r q)^2}{2\sqrt{q}} + \sqrt{q}\, \partial_r^2 q \right] - \epsilon_0 \frac{q^{3/2}}{\alpha h(t)} \tag{B.3}$$

In addition, we define the total energy of turbulence $Q(t)$ as

$$Q(t) \equiv \int d^d \vec{r}\, q(\vec{r},t) = \int_0^{h(t)} S_d\, q(r,t)\, r^{d-1} dr, \quad \text{where } S_d = \frac{2\pi^{d/2}}{\Gamma(d/2)} \tag{B.4}$$

At $t = 0$, we adopt the initial conditions $h(0) = a$ and $Q(0) = Q_a$. The dimensional analysis

yields

$$q(r,t) = \frac{Q_a^\theta}{t^{\theta d}} f\left(\frac{r}{Q_a^{\theta/2} t^\theta}, \frac{a}{Q_a^{\theta/2} t^\theta}, \alpha, \epsilon_0\right) \tag{B.5}$$

$$h(t) = Q_a^{\theta/2} t^\theta f_h\left(\frac{a}{Q_a^{\theta/2} t^\theta}, \alpha, \epsilon_0\right) \tag{B.6}$$

where $\theta \equiv 2/(d+2)$.

To find the long-time asymptotics of the equation, we consider Eq. B.2 as a perturbation theory, and assume $\epsilon_0 \ll 1$.

In the unperturbed case, where $\epsilon_0 = 0$, the total energy is conserved:

$$\frac{dQ}{dt} = 0, \quad Q(t) = Q_a \tag{B.7}$$

The unperturbed equation is

$$\partial_t q_0 = \alpha h_0(t) \left[\frac{d-1}{r}\sqrt{q_0}\,\partial_r q_0 + \frac{(\partial_r q_0)^2}{2\sqrt{q_0}} + \sqrt{q_0}\,\partial_r^2 q_0\right]. \tag{B.8}$$

Consider a following initial profile:

$$q_0(r,0) \propto \left[1 - \left(\frac{r}{a}\right)^2\right]_+^2 \tag{B.9}$$

where "+" is a cutoff defined as we find the zeroth order solution as $g_+ \equiv g \cdot \Theta(g)$. Θ is the Heaviside function. The solution is

$$q_0(r,t) = \frac{Q_a}{h_0^d}\left(\frac{\theta}{4\alpha}\right)^2 \xi_0^{2/\theta}\left[1 - \left(\frac{r}{h_0}\right)^2\right]_+^2 = \frac{Q_a}{S_d I_d h_0^d}\left[1 - \left(\frac{r}{h_0}\right)^2\right]_+^2$$

$$h_0(t) = \left(\xi_0^{1/\theta} Q_a^{1/2} t + a^{1/\theta}\right)^\theta \tag{B.10}$$

where ξ_0 is a dimensionless coefficient defined such that $h_0(t) \to \xi_0 Q_a^{\theta/2} t^\theta$ as $t \to +\infty$:

$$\xi_0 = \left[4\theta^{-1} (S_d I_d)^{-1/2} \alpha \right]^\theta \tag{B.11}$$

where $I_d = \frac{8}{d(d+2)(d+4)}$.

Now we turn our attention to the dissipative case ($\epsilon_0 > 0$). Assume that the system evolves adiabatically. That is, the solutions remain in the same functional forms except the constant Q_a. With this assumption, Q_a is replaced with a time-dependent function $Q(t)$, leading to

$$\begin{aligned} q(r,t) &= \frac{Q(t)}{h^d} \left(\frac{\theta}{4\alpha} \right)^2 \xi_0^{2/\theta} \left[1 - \left(\frac{r}{h(t)} \right)^2 \right]_+^2 \\ h(t) &= \left[\xi_0^{1/\theta} \left(Q(t) \right)^{1/2} t + a^{1/\theta} \right]^\theta . \end{aligned} \tag{B.12}$$

Integrating both sides of Eq. B.2 over the space yields

$$\begin{aligned} \frac{dQ}{dt} &= -\frac{\epsilon_0}{\alpha h} \int q^{3/2} d^d \mathbf{r} \\ &= -\frac{3\theta}{2(d+6)} \frac{\epsilon_0}{\alpha^2} \frac{\xi_0^{1/\theta} Q^{3/2}}{\xi_0^{1/\theta} Q^{1/2} t + a^{1/\theta}} \end{aligned} \tag{B.13}$$

where we plug in the adiabatic forms Eq. B.12 for $h(t)$ and $q(t)$. As $t \to +\infty$, Eq. B.13 takes the asymptotic form of

$$\frac{dQ}{dt} = -\frac{3\theta}{2(d+6)} \frac{\epsilon_0}{\alpha^2} \frac{Q}{t} \quad \Rightarrow \quad Q \to Q_0 \left(\frac{t}{t_0} \right)^{-\frac{3\theta}{2(d+6)} \frac{\epsilon_0}{\alpha^2}} \sim t^{-\frac{3\theta}{2(d+6)} \frac{\epsilon_0}{\alpha^2}} \tag{B.14}$$

Subsequently, the front position $h(t)$ and energy density function $q(r,t)$ are given by

$$
\begin{aligned}
h(t) &\to \xi_0 Q^{\theta/2} t^{\theta} \sim t^{\theta - \frac{3\theta^2}{4(d+6)}\frac{\epsilon_0}{\alpha^2}} \\
q(r,t) &\to \frac{Q}{h^d}\left(\frac{\theta}{4\alpha}\right)^2 \xi_0^{2/\theta}\left[1-\left(\frac{r}{h}\right)^2\right]_+^2 \sim t^{-d\theta - \frac{3\theta^2}{2(d+6)}\frac{\epsilon_0}{\alpha^2}}\left[1-\left(\frac{r}{h}\right)^2\right]_+^2 .
\end{aligned}
\tag{B.15}
$$

The predictions for the $d = 3$ are explicitly shown in Sect. 4.2.1.

APPENDIX C

DETERMINATION OF VIRTUAL ORIGIN

In this section we address how we determine a virtual origin of a function that decays with a power law. Consider a quantity $x = A(t - t_0)^n$. The inaccurate estimation of virtual origin t_0 underestimates or overestimates the exponent n. To remove any subjective bias, we determine t_0 with the following procedure.

1. Guess n.
2. Perform weighted linear regression on $x^{1/n}(t)$ in the domain $[t_a, t_b]$ where the power law is expected. The weight is proportional to $\log t/t_a$.
3. Read off the x-intercept t_0^{est}.
4. Compute a cost function. The cost function is the coefficient of variance $\frac{\text{RSS}}{N-1} \cdot \frac{1}{\text{Mean of the sample, } x^{1/n}}$ over the first half of the measurement after the quantity starts decaying.
5. Repeat 2-5 for a different set of the exponent n and the fitting domain $[t_a, t_b]$.
6. Determine t_0 and n by finding the minimum of the cost function.

To assess the robustness of the algorithm, we test with synthetic data sets. Each data set consists of 50 samples of a signal with a single power law ($n = -2$) and the Gaussian noise scaled by the signal. That is, the noise is equal to $x_{\text{scale}} \times \mathcal{N}(\mu = 0, \sigma)$. Figure C.1a-b display the two samples with different noise levels ($\sigma = 0.1$ and 0.4). With the proposed algorithm, Figure C.1c displays that the proposed algorithm accurately extracts the correct power law as long as the noise level is low. The experimental data is estimated to have the noise level of $\sigma = 0.1 - 0.2$.

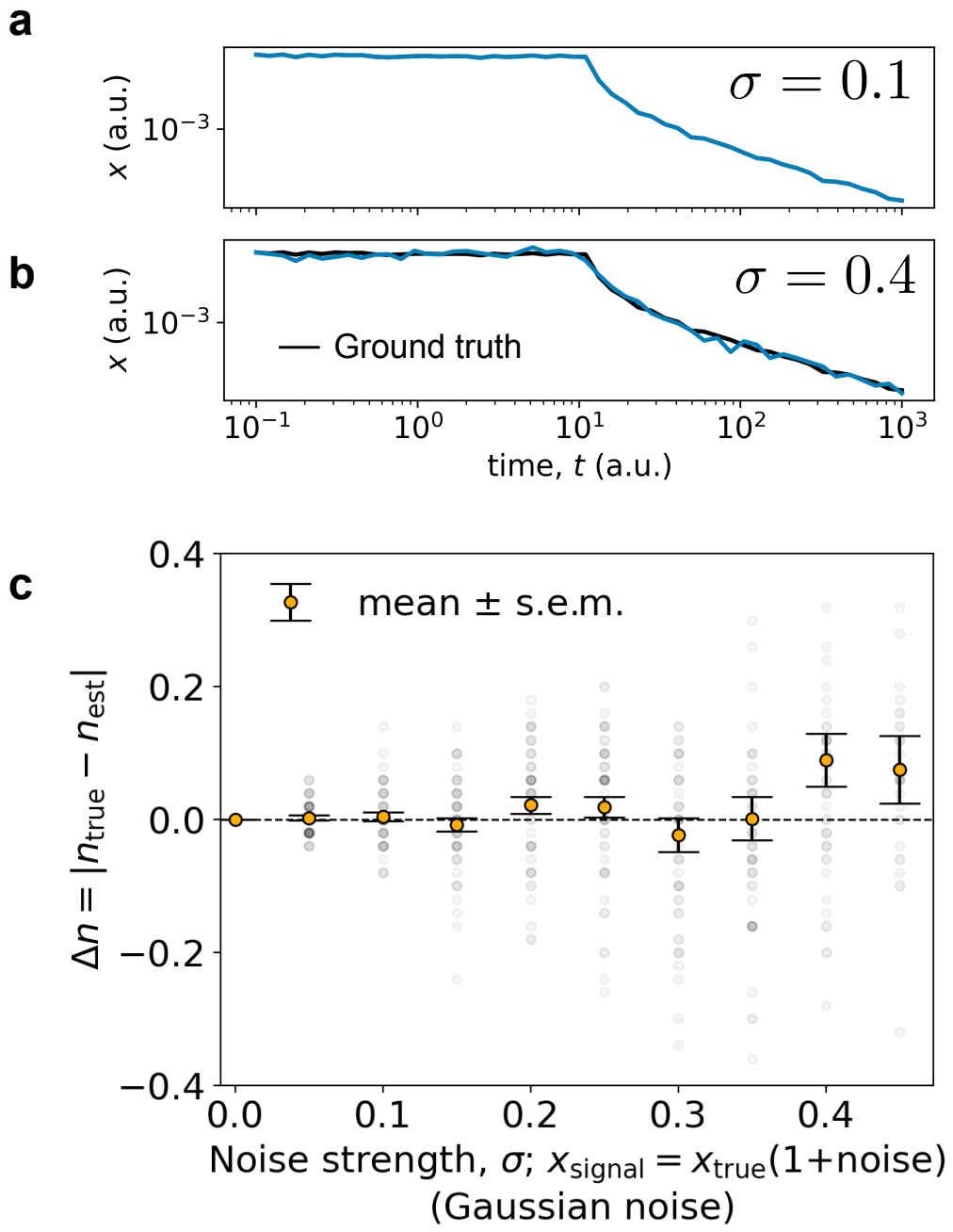

Figure C.1: **Our proposed algorithm to extract virtual origin robustly measures the true exponents.** We generate samples that obey a power law ($n = -2$) with Gaussian noise scaled by its magnitude. $x_{\text{signal}} = x_{\text{true}}(1 + \text{noise})$. The noise level is characterized by a standard deviation of the normal distribution. **(a)** A sample with a low noise level. **(b)** A sample with a high noise level. **(c)** Deviation of the estimated decay law from the ground truth shows that the robustness of the algorithm even at a high noise level. For each noise level, 50 samples were studied.

REFERENCES

[1] M. Acarlar and C. Smith. A study of hairpin vortices in a laminar boundary layer. part 1. hairpin vortices generated by a hemisphere protuberance. *Journal of Fluid Mechanics*, 175:1–41, 1987.

[2] M. Acarlar and C. Smith. A study of hairpin vortices in a laminar boundary layer. part 2. hairpin vortices generated by fluid injection. *Journal of Fluid Mechanics*, 175:43–83, 1987.

[3] R. J. Adrian. Hairpin vortex organization in wall turbulence. *Physics of Fluids*, 19(4):041301, Apr. 2007.

[4] D. G. Akhmetov. Formation and basic parameters of vortex rings. *Journal of Applied Mechanics and Technical Physics*, 42(5):794–805, Sept. 2001.

[5] D. G. Akhmetov. *Vortex Rings*. Springer-Verlag, Berlin Heidelberg, 2009.

[6] A. Alexakis. Helically decomposed turbulence. *Journal of Fluid Mechanics*, 812:752–770, Feb. 2017. Publisher: Cambridge University Press.

[7] A. Alexakis and L. Biferale. Cascades and transitions in turbulent flows. *Physics Reports*, 767:1–101, 2018.

[8] C. Atkinson, N. A. Buchmann, O. Amili, and J. Soria. On the appropriate filtering of PIV measurements of turbulent shear flows. *Experiments in Fluids*, 55(1):1654, Dec. 2013.

[9] K. Avila, D. Moxey, A. De Lozar, M. Avila, D. Barkley, and B. Hof. The onset of turbulence in pipe flow. *Science*, 333(6039):192–196, 2011.

[10] M. Avila, D. Barkley, and B. Hof. Transition to turbulence in pipe flow. *Annual Review of Fluid Mechanics*, 55:575–602, 2023.

[11] G. Barenblatt, N. Galerkina, and M. Luneva. Evolution of a turbulent burst. *Journal of engineering physics*, 53(5):1246–1252, 1987.

[12] G. I. Barenblatt. *Scaling, self-similarity, and intermediate asymptotics*. Cambridge University Press, 1996.

[13] G. K. Batchelor. *The theory of homogeneous turbulence*. Cambridge university press, 1953.

[14] G. K. Batchelor and I. Proudman. The large-scale structure of homogenous turbulence. *Philosophical Transactions of the Royal Society of London. Series A, Mathematical and Physical Sciences*, 248(949):369–405, 1956.

[15] G. K. Batchelor and A. A. Townsend. Decay of isotropic turbulence in the initial period. *Proceedings of the Royal Society of London. Series A. Mathematical and Physical Sciences*, 193(1035):539–558, 1948.

[16] G. K. Batchelor and A. A. Townsend. Decay of turbulence in the final period. *Proceedings of the Royal Society of London. Series A. Mathematical and Physical Sciences*, 194(1039):527–543, 1948.

[17] G. Bellani and E. A. Variano. Homogeneity and isotropy in a laboratory turbulent flow. *Experiments in Fluids*, 55(1):1646, Jan. 2014.

[18] L. H. Benedict, H. Nobach, and C. Tropea. Estimation of turbulent velocity spectra from laser Doppler data. *Measurement Science and Technology*, 11(8):1089–1104, July 2000.

[19] G. Birkhoff. Fourier synthesis of homogeneous turbulence. *Communications on Pure and Applied Mathematics*, 7(1):19–44, 1954.

[20] D. K. Bisset, J. C. Hunt, and M. M. Rogers. The turbulent/non-turbulent interface bounding a far wake. *Journal of Fluid Mechanics*, 451:383–410, 2002.

[21] E. Bodenschatz, G. P. Bewley, H. Nobach, M. Sinhuber, and H. Xu. Variable density turbulence tunnel facility. *Review of Scientific Instruments*, 85(9):093908, 2014.

[22] J. Bosbach, D. Schanz, P. Godbersen, and A. Schröder. Spatially and temporally resolved measurements of turbulent rayleigh-bénard convection by lagrangian particle tracking of long-lived helium-filled soap bubbles. In *Proceedings of 14th International Symposium on Particle Image Velocimetry*, volume 1, pages 1–12. ILLINOIS Tech/Paul V. Galvin Library, 2021.

[23] R. N. Bracewell. *Fourier Transform and Its Applications*. McGraw-Hill electrical and electronic engineering series. McGraw-Hill, New York, NY, Aug. 1978.

[24] M. P. Brenner, S. Hormoz, and A. Pumir. Potential singularity mechanism for the euler equations. *Physical Review Fluids*, 1(8):084503, 2016.

[25] S. L. Brunton, B. R. Noack, and P. Koumoutsakos. Machine learning for fluid mechanics. *Annual review of fluid mechanics*, 52:477–508, 2020.

[26] P. Buchhave, W. K. George, and J. L. Lumley. The Measurement of Turbulence with the Laser-Doppler Anemometer. *Annual Review of Fluid Mechanics*, 11(1):443–503, 1979.

[27] O. Cadot, J. H. Titon, and D. Bonn. Experimental observation of resonances in modulated turbulence. *Journal of Fluid Mechanics*, 485:161–170, 2003.

[28] G. Călugăreanu. Sur les classes d'isotopie des noeuds tridimensionnels et leurs invariants. *Czechoslovak Mathematical Journal*, 11(4):588–625, 1961.

[29] D. Carter, A. Petersen, O. Amili, and F. Coletti. Generating and controlling homogeneous air turbulence using random jet arrays. *Experiments in Fluids*, 57(12):189, Nov. 2016.

[30] H. E. Cekli, C. Tipton, and W. van de Water. Resonant enhancement of turbulent energy dissipation. *Physical review letters*, 105(4):044503, 2010.

[31] K. Chang, G. P. Bewley, and E. Bodenschatz. Experimental study of the influence of anisotropy on the inertial scales of turbulence. *Journal of fluid mechanics*, 692:464–481, 2012.

[32] G. T. Chapman and M. Tobak. *Observations, theoretical ideas, and modeling of turbulent flows—past, present, and future*. Springer, 1985.

[33] J. Chasnov. Computation of the loitsianski integral in decaying isotropic turbulence. *Physics of Fluids A: Fluid Dynamics*, 5(11):2579–2581, 1993.

[34] K. Chauhan, J. Philip, C. M. De Silva, N. Hutchins, and I. Marusic. The turbulent/non-turbulent interface and entrainment in a boundary layer. *Journal of Fluid Mechanics*, 742:119–151, 2014.

[35] C. Chen and G. Cheng. Anomalous dimension in the solution of the barenblatt's equation. *Journal of Mathematical Physics*, 39(3):1589–1600, 1998.

[36] L.-Y. Chen and N. Goldenfeld. Renormalization-group theory for the propagation of a turbulent burst. *Physical Review A*, 45(8):5572, 1992.

[37] M. Cheng, J. Lou, and T. T. Lim. Collision and reconnection of viscous elliptic vortex rings. *Physics of Fluids*, 31(6):067107, June 2019. Publisher: American Institute of Physics.

[38] K. T. Christensen and R. J. Adrian. Statistical evidence of hairpin vortex packets in wall turbulence. *Journal of Fluid Mechanics*, 431:433–443, Mar. 2001.

[39] G. Comte-Bellot and S. Corrsin. The use of a contraction to improve the isotropy of grid-generated turbulence. *Journal of fluid mechanics*, 25(4):657–682, 1966.

[40] G. Comte-Bellot and S. Corrsin. Simple eulerian time correlation of full-and narrow-band velocity signals in grid-generated,'isotropic'turbulence. *Journal of Fluid Mechanics*, 48(2):273–337, 1971.

[41] T. J. Cornwell. Multiscale CLEAN Deconvolution of Radio Synthesis Images. *IEEE Journal of Selected Topics in Signal Processing*, 2(5):793–801, Oct. 2008. Conference Name: IEEE Journal of Selected Topics in Signal Processing.

[42] S. C. Crow. Stability theory for a pair of trailing vortices. *AIAA journal*, 8(12):2172–2179, 1970.

[43] S. C. Crow and F. Champagne. Orderly structure in jet turbulence. *Journal of fluid mechanics*, 48(3):547–591, 1971.

[44] W. Cui, L. Liu, X. Yang, Y. Wang, L. Feng, and V. Springel. An ideal mass assignment scheme for measuring the Power Spectrum with FFTs. *The Astrophysical Journal*, 687(2):738–744, Nov. 2008. arXiv: 0804.0070.

[45] C. B. da Silva, R. J. Dos Reis, and J. C. Pereira. The intense vorticity structures near the turbulent/non-turbulent interface in a jet. *Journal of Fluid Mechanics*, 685:165–190, 2011.

[46] J. O. Dabiri and M. Gharib. Fluid entrainment by isolated vortex rings. *Journal of Fluid Mechanics*, 511:311–331, 2004.

[47] P. Davidson. The role of angular momentum conservation in homogeneous turbulence. *Journal of fluid mechanics*, 632:329–358, 2009.

[48] P. Davidson. *Turbulence: an introduction for scientists and engineers*. Oxford university press, 2015.

[49] J. de Jong, L. Cao, S. H. Woodward, J. P. L. C. Salazar, L. R. Collins, and H. Meng. Dissipation rate estimation from PIV in zero-mean isotropic turbulence. *Experiments in Fluids*, 46(3):499, Oct. 2008.

[50] A. de la Torre and J. Burguete. Slow dynamics in a turbulent von kármán swirling flow. *Physical review letters*, 99(5):054101, 2007.

[51] Z. Dou, Z. K. Pecenak, L. Cao, S. H. Woodward, Z. Liang, and H. Meng. Piv measurement of high-reynolds-number homogeneous and isotropic turbulence in an enclosed flow apparatus with fan agitation. *Measurement Science and Technology*, 27(3):035305, 2016.

[52] Y. Dubief and F. Delcayre. On coherent-vortex identification in turbulence. *Journal of turbulence*, 1(1):011, 2000.

[53] K. Duraisamy, G. Iaccarino, and H. Xiao. Turbulence modeling in the age of data. *Annual review of fluid mechanics*, 51:357–377, 2019.

[54] B. Eckhardt, T. M. Schneider, B. Hof, and J. Westerweel. Turbulence transition in pipe flow. *Annu. Rev. Fluid Mech.*, 39:447–468, 2007.

[55] J. Finnigan. Turbulence in plant canopies. *Annual review of fluid mechanics*, 32(1):519–571, 2000.

[56] J. M. Foucaut, J. Carlier, and M. Stanislas. PIV optimization for the study of turbulent flow using spectral analysis. *Measurement Science and Technology*, 15(6):1046–1058, May 2004. Publisher: IOP Publishing.

[57] L. E. Fraenkel. Examples of steady vortex rings of small cross-section in an ideal fluid. *Journal of Fluid Mechanics*, 51(1):119–135, 1972.

[58] U. Frisch, P.-L. Sulem, and M. Nelkin. A simple dynamical model of intermittent fully developed turbulence. *Journal of Fluid Mechanics*, 87(4):719–736, 1978.

[59] W. K. George. The decay of homogeneous isotropic turbulence. *Physics of Fluids A: Fluid Dynamics*, 4(7):1492–1509, 1992.

[60] W. K. George and J. L. Lumley. The laser-doppler velocimeter and its application to the measurement of turbulence. *Journal of Fluid Mechanics*, 60(2):321–362, Sept. 1973.

[61] M. Gharib, E. Rambod, and K. Shariff. A universal time scale for vortex ring formation. *Journal of Fluid Mechanics*, 360:121–140, 1998.

[62] A. Glezer. The formation of vortex rings. *The Physics of Fluids*, 31(12):3532–3542, Dec. 1988.

[63] C. Goepfert, J.-L. Marié, D. Chareyron, and M. Lance. Characterization of a system generating a homogeneous isotropic turbulence field by free synthetic jets. *Experiments in fluids*, 48(5):809–822, 2010.

[64] N. Goldenfeld. *Lectures on phase transitions and the renormalization group*. CRC Press, 2018.

[65] N. Goldenfeld, O. Martin, Y. Oono, and F. Liu. Anomalous dimensions and the renormalization group in a nonlinear diffusion process. *Physical Review Letters*, 64(12):1361–1364, 1990.

[66] P. R. Griffiths and G. L. Pariente. Introduction to spectral deconvolution. *TrAC Trends in Analytical Chemistry*, 5(8):209–215, Sept. 1986.

[67] S. Grossmann, D. Lohse, and C. Sun. High–reynolds number taylor-couette turbulence. *Annual review of fluid mechanics*, 48:53–80, 2016.

[68] R. Gurka, A. Liberzon, and G. Hetsroni. Pod of vorticity fields: A method for spatial characterization of coherent structures. *International Journal of Heat and Fluid Flow*, 27(3):416–423, 2006.

[69] J. O. Hinze. Turbulence. *(No Title)*, 1975.

[70] B. Hof, A. Juel, and T. Mullin. Scaling of the turbulence transition threshold in a pipe. *Physical review letters*, 91(24):244502, 2003.

[71] M.-K. Hu. Visual pattern recognition by moment invariants. *IRE Transactions on Information Theory*, 8(2):179–187, Feb. 1962. Conference Name: IRE Transactions on Information Theory.

[72] D. Hurst and J. Vassilicos. Scalings and decay of fractal-generated turbulence. *Physics of Fluids*, 19(3):035103, 2007.

[73] W. Hwang and J. Eaton. Creating homogeneous and isotropic turbulence without a mean flow. *Experiments in Fluids*, 36(3):444–454, 2004.

[74] T. Ishihara, T. Gotoh, and Y. Kaneda. Study of High–Reynolds Number Isotropic Turbulence by Direct Numerical Simulation. *Annual Review of Fluid Mechanics*, 41(1):165–180, 2009.

[75] Y. J. Jeon, G. Gomit, T. Earl, L. Chatellier, and L. David. Sequential least-square reconstruction of instantaneous pressure field around a body from tr-piv. *Experiments in Fluids*, 59:27, Feb. 2018. ADS Bibcode: 2018ExFl...59...27J.

[76] J. Jeong and F. Hussain. On the identification of a vortex. *Journal of fluid mechanics*, 285:69–94, 1995.

[77] T. Kambe. *Elementary fluid mechanics*. World Scientific, 2007.

[78] H. Kellay, T. Tran, W. Goldburg, N. Goldenfeld, G. Gioia, and P. Chakraborty. Testing a missing spectral link in turbulence. *Physical review letters*, 109(25):254502, 2012.

[79] S. Kida and M. Takaoka. Bridging in vortex reconnection. *The Physics of fluids*, 30(10):2911–2914, 1987.

[80] S. Kida and M. Takaoka. Vortex reconnection. *Annual Review of Fluid Mechanics*, 26(1):169–177, 1994.

[81] S. Kida and M. Takaoka. Vortex reconnection. *Annual Review of Fluid Mechanics*, 26(1):169–177, Jan. 1994. Publisher: Annual Reviews.

[82] A. Kistler and T. Vrebalovich. Grid turbulence at large reynolds numbers. *Journal of Fluid Mechanics*, 26(1):37–47, 1966.

[83] D. Kleckner and W. T. M. Irvine. Creation and dynamics of knotted vortices. *Nature Physics*, 9(4):253–258, Apr. 2013.

[84] A. N. Kolmogorov. The local structure of turbulence in incompressible viscous fluid for very large Reynolds numbers. *C. R. Acad. Sci. URSS*, 30:301–305, 1941.

[85] A. N. Kolmogorov. A refinement of previous hypotheses concerning the local structure of turbulence in a viscous incompressible fluid at high reynolds number. *Journal of Fluid Mechanics*, 13(1):82–85, 1962.

[86] A. N. Kolmogorov. A refinement of previous hypotheses concerning the local structure of turbulence in a viscous incompressible fluid at high reynolds number. *Journal of Fluid Mechanics*, 13(1):82–85, 1962.

[87] R. H. Kraichnan. Helical turbulence and absolute equilibrium. *Journal of Fluid Mechanics*, 59(4):745–752, 1973.

[88] R. H. Kraichnan and D. Montgomery. Two-dimensional turbulence. *Reports on Progress in Physics*, 43(5):547, 1980.

[89] P.-Å. Krogstad and P. Davidson. Is grid turbulence saffman turbulence? *Journal of Fluid Mechanics*, 642:373–394, 2010.

[90] A. K. Kuczaj, B. J. Geurts, and D. Lohse. Response maxima in time-modulated turbulence: Direct numerical simulations. *EPL (Europhysics Letters)*, 73(6):851, 2006.

[91] A. Y.-S. Kuo and S. Corrsin. Experiment on the geometry of the fine-structure regions in fully turbulent fluid. *Journal of Fluid Mechanics*, 56(3):447–479, 1972.

[92] T. Kurian and J. H. M. Fransson. Grid-generated turbulence revisited. *Fluid Dynamics Research*, 41(2):021403, 2009.

[93] D. Küchemann and J. Weber. Vortex Motions. *ZAMM - Journal of Applied Mathematics and Mechanics / Zeitschrift für Angewandte Mathematik und Mechanik*, 45(7-8):457–474, 1965.

[94] R. Labbé, J.-F. Pinton, and S. Fauve. Study of the von kármán flow between coaxial corotating disks. *Physics Of Fluids*, 8(4):914–922, 1996.

[95] H. Lamb. *Hydrodynamics*. University Press, 1924.

[96] L. D. Landau and E. M. Lifshitz. *Fluid Mechanics: Landau and Lifshitz: Course of Theoretical Physics, Volume 6*, volume 6. Elsevier, 2013.

[97] R. B. Larson. Turbulence and star formation in molecular clouds. *Monthly Notices of the Royal Astronomical Society*, 194(4):809–826, 1981.

[98] S. Le Dizes and F. Laporte. Theoretical predictions for the elliptical instability in a two-vortex flow. *Journal of Fluid Mechanics*, 471:169–201, 2002.

[99] G. Lemoult, L. Shi, K. Avila, S. V. Jalikop, M. Avila, and B. Hof. Directed percolation phase transition to sustained turbulence in couette flow. *Nature Physics*, 12(3):254–258, 2016.

[100] Y. Li, E. Perlman, M. Wan, Y. Yang, C. Meneveau, R. Burns, S. Chen, A. Szalay, and G. Eyink. A public turbulence database cluster and applications to study lagrangian evolution of velocity increments in turbulence. *Journal of Turbulence*, (9):N31, 2008.

[101] Y. Li, E. Perlman, M. Wan, Y. Yang, C. Meneveau, R. Burns, S. Chen, A. Szalay, and G. Eyink. A public turbulence database cluster and applications to study Lagrangian evolution of velocity increments in turbulence. *Journal of Turbulence*, 9:N31, Jan. 2008.

[102] T. T. Lim and T. B. Nickels. Instability and reconnection in the head-on collision of two vortex rings. *Nature*, 357(6375):225–227, May 1992. Number: 6375 Publisher: Nature Publishing Group.

[103] C. Lin. Note on the law of decay of isotropic turbulence. *Proceedings of the National Academy of Sciences*, 34(11):540–543, 1948.

[104] D. Lohse. Periodically kicked turbulence. *Physical Review E*, 62(4):4946, 2000.

[105] E. N. Lorenz. Deterministic nonperiodic flow. *Journal of atmospheric sciences*, 20(2):130–141, 1963.

[106] V. L'vov and I. Procaccia. Turbulence: a universal problem. *Physics World*, 9(8):35, 1996.

[107] B. B. Mandelbrot. Possible refinement of the lognormal hypothesis concerning the distribution of energy dissipation in intermittent turbulence. In *Statistical models and turbulence*, pages 333–351. Springer, 1972.

[108] B. B. Mandelbrot. Intermittent turbulence in self-similar cascades: divergence of high moments and dimension of the carrier. *Journal of fluid Mechanics*, 62(2):331–358, 1974.

[109] T. Matsuzawa, N. P. Mitchell, S. Perrard, and W. Irvine. Creation of an isolated turbulent blob fed by vortex rings. *arXiv preprint arXiv:2211.00771*, 2022.

[110] T. Matsuzawa, N. P. Mitchell, S. Perrard, and W. T. Irvine. Creation of an isolated turbulent blob fed by vortex rings. *Nature Physics*, pages 1–8, 2023.

[111] W. D. McComb. The physics of fluid turbulence. *Oxford*, 1990.

[112] R. McKeown, R. Ostilla-Mónico, A. Pumir, M. P. Brenner, and S. M. Rubinstein. Cascade leading to the emergence of small structures in vortex ring collisions. *Physical Review Fluids*, 3(12):124702, 2018.

[113] R. McKeown, R. Ostilla-Mónico, A. Pumir, M. P. Brenner, and S. M. Rubinstein. Turbulence generation through an iterative cascade of the elliptical instability. *Science Advances*, 6(9):2717, Feb. 2020. Publisher: American Association for the Advancement of Science Section: Research Article.

[114] M. V. Melander and F. Hussain. Cut-and-connect of two antiparallel vortex tubes. *CTR. Rep.*, (S-21):257, 1988.

[115] C. Meneveau and K. Sreenivasan. The multifractal nature of turbulent energy dissipation. *Journal of Fluid Mechanics*, 224:429–484, 1991.

[116] H. Moffatt. Generalised vortex rings with and without swirl. *Fluid Dynamics Research*, 3(1-4):22, 1988.

[117] H. K. Moffatt. The degree of knottedness of tangled vortex lines. *Journal of Fluid Mechanics*, 35(1):117–129, 1969.

[118] M. S. Mohamed and J. C. LaRue. The decay power law in grid-generated turbulence. *Journal of Fluid Mechanics*, 219:195–214, 1990.

[119] P. Moin. Revisiting Taylor's hypothesis. *Journal of Fluid Mechanics*, 640:1–4, Dec. 2009. Publisher: Cambridge University Press.

[120] P. Moin. Revisiting taylor's hypothesis. *Journal of Fluid Mechanics*, 640:1–4, 2009.

[121] P. Moin and K. Mahesh. Direct numerical simulation: a tool in turbulence research. *Annual review of fluid mechanics*, 30(1):539–578, 1998.

[122] D. Moxey and D. Barkley. Distinct large-scale turbulent-laminar states in transitional pipe flow. *Proceedings of the National Academy of Sciences*, 107(18):8091–8096, 2010.

[123] T. Mullin. Experimental studies of transition to turbulence in a pipe. *Annual Review of Fluid Mechanics*, 43:1–24, 2011.

[124] J. Norbury. A family of steady vortex rings. *Journal of Fluid Mechanics*, 57(3):417–431, Feb. 1973. Publisher: Cambridge University Press.

[125] A. M. Oboukhov. Some specific features of atmospheric tubulence. *Journal of Fluid Mechanics*, 13(1):77–81, 1962.

[126] Y. Oshima. Head-on Collision of Two Vortex Rings. *Journal of the Physical Society of Japan*, 44(1):328–331, Jan. 1978.

[127] Y. Oshima. Head-on collision of two vortex rings. *Journal of the Physical Society of Japan*, 44(1):328–331, 1978.

[128] R. Ostilla-Mónico, R. McKeown, M. P. Brenner, S. M. Rubinstein, and A. Pumir. Cascades and reconnection in interacting vortex filaments. *Physical Review Fluids*, 6(7):074701, 2021.

[129] J. Panickacheril John, D. A. Donzis, and K. R. Sreenivasan. Laws of turbulence decay from direct numerical simulations. *Philosophical Transactions of the Royal Society A*, 380(2218):20210089, 2022.

[130] E. Perlman, R. Burns, Y. Li, and C. Meneveau. Data exploration of turbulence simulations using a database cluster. In *Proceedings of the 2007 ACM/IEEE Conference on Supercomputing*, pages 1–11, 2007.

[131] E. Perlman, R. Burns, Y. Li, and C. Meneveau. Data exploration of turbulence simulations using a database cluster. In *SC '07: Proceedings of the 2007 ACM/IEEE Conference on Supercomputing*, pages 1–11, Nov. 2007.

[132] H. Poincaré. Sur les courbes définies par les équations différentielles. *CR Acad. Sci., Paris*, 90:673–675, 1880.

[133] Y. Pomeau. Front motion, metastability and subcritical bifurcations in hydrodynamics. *Physica D: Nonlinear Phenomena*, 23(1-3):3–11, 1986.

[134] S. B. Pope. *Turbulent flows*. Cambridge University Press, Cambridge ; New York, 2000.

[135] A. Praskovsky and S. Oncley. Measurements of the kolmogorov constant and intermittency exponent at very high reynolds numbers. *Physics of Fluids*, 6(9):2886–2888, 1994.

[136] M. Raffel, C. E. Willert, F. Scarano, C. J. Kähler, S. T. Wereley, and J. Kompenhans. *Particle Image Velocimetry: A Practical Guide*. Springer International Publishing, 2018. OCLC: 1035110003.

[137] G. W. Rayfield and F. Reif. Quantized vortex rings in superfluid helium. *Physical Review*, 136(5A):A1194, 1964.

[138] D. Rempfer and H. F. Fasel. Evolution of three-dimensional coherent structures in a flat-plate boundary layer. *Journal of Fluid Mechanics*, 260:351–375, 1994.

[139] O. Reynolds. Xxix. an experimental investigation of the circumstances which determine whether the motion of water shall be direct or sinuous, and of the law of resistance in parallel channels. *Philosophical Transactions of the Royal society of London*, (174):935–982, 1883.

[140] R. S. Rogallo and P. Moin. Numerical simulation of turbulent flows. *Annual review of fluid mechanics*, 16(1):99–137, 1984.

[141] D. Ruelle and F. Takens. On the nature of turbulence, commum. math, 1971.

[142] S. G. Saddoughi and S. V. Veeravalli. Local isotropy in turbulent boundary layers at high reynolds number. *Journal of Fluid Mechanics*, 268:333–372, 1994.

[143] P. Saffman. The large-scale structure of homogeneous turbulence. *Journal of Fluid Mechanics*, 27(3):581–593, 1967.

[144] P. Saffman. Note on decay of homogeneous turbulence. *The Physics of Fluids*, 10(6):1349–1349, 1967.

[145] P. G. Saffman. *Vortex dynamics*. Cambridge university press, 1995.

[146] T. Sato, G. Huetsi, and K. Yamamoto. Deconvolution of window effect in galaxy power spectrum analysis. *Progress of Theoretical Physics*, 125(1):187–197, Jan. 2011. arXiv: 1010.0289.

[147] F. Scarano. Iterative image deformation methods in piv. *Measurement science and technology*, 13(1):R1, 2001.

[148] F. Scarano, L. David, M. Bsibsi, and D. Calluaud. S-piv comparative assessment: image dewarping+ misalignment correction and pinhole+ geometric back projection. *Experiments in fluids*, 39(2):257–266, 2005.

[149] F. Scarano and M. L. Riethmuller. Advances in iterative multigrid piv image processing. *Experiments in fluids*, 29(Suppl 1):S051–S060, 2000.

[150] D. Schanz, S. Gesemann, and A. Schröder. Shake-The-Box: Lagrangian particle tracking at high particle image densities. *Experiments in Fluids*, 57(5):70, Apr. 2016.

[151] M. W. Scheeler, W. M. van Rees, H. Kedia, D. Kleckner, and W. T. Irvine. Complete measurement of helicity and its dynamics in vortex tubes. *Science*, 357(6350):487–491, 2017.

[152] M. W. Scheeler, W. M. van Rees, H. Kedia, D. Kleckner, and W. T. M. Irvine. Complete measurement of helicity and its dynamics in vortex tubes. *Science*, 357(6350):487–491, Aug. 2017.

[153] W. Schoppa and F. Hussain. Coherent structure generation in near-wall turbulence. *Journal of fluid Mechanics*, 453:57–108, 2002.

[154] G. B. Schubauer and H. K. Skramstad. Laminar boundary-layer oscillations and stability of laminar flow. *Journal of the Aeronautical Sciences*, 14(2):69–78, 1947.

[155] A. Sciacchitano, F. Scarano, and B. Wieneke. Multi-frame pyramid correlation for time-resolved PIV. *Experiments in Fluids*, 53(4):1087–1105, Oct. 2012.

[156] R. Seoud and J. Vassilicos. Dissipation and decay of fractal-generated turbulence. *Physics of fluids*, 19(10):105108, 2007.

[157] H.-Y. Shih, T.-L. Hsieh, and N. Goldenfeld. Ecological collapse and the emergence of travelling waves at the onset of shear turbulence. *Nature Physics*, 12(3):245–248, 2016.

[158] B. A. Singer and R. D. Joslin. Metamorphosis of a hairpin vortex into a young turbulent spot. *Physics of Fluids*, 6(11):3724–3736, Nov. 1994.

[159] M. Sinhuber, E. Bodenschatz, and G. P. Bewley. Decay of turbulence at high reynolds numbers. *Physical review letters*, 114(3):034501, 2015.

[160] M. Sipos and N. Goldenfeld. Directed percolation describes lifetime and growth of turbulent puffs and slugs. *Physical Review E*, 84(3):035304, 2011.

[161] M. R. Smith. A study of homogeneous turbulence using superfluid helium. *Physica B: Condensed Matter*, 197(1-4):297–305, 1994.

[162] M. R. Smith, R. J. Donnelly, N. Goldenfeld, and W. Vinen. Decay of vorticity in homogeneous turbulence. *Physical review letters*, 71(16):2583, 1993.

[163] A. J. Smits, B. J. McKeon, and I. Marusic. High–reynolds number wall turbulence. *Annual Review of Fluid Mechanics*, 43:353–375, 2011.

[164] K. Sreenivasan. Fractals and multifractals in fluid turbulence. *Annual review of fluid mechanics*, 23(1):539–604, 1991.

[165] K. R. Sreenivasan. On the scaling of the turbulence energy dissipation rate. *The Physics of fluids*, 27(5):1048–1051, 1984.

[166] K. R. Sreenivasan. On the universality of the kolmogorov constant. *Physics of Fluids*, 7(11):2778–2784, 1995.

[167] K. R. Sreenivasan, S. Tavoularis, R. Henry, and S. Corrsin. Temperature fluctuations and scales in grid-generated turbulence. *Journal of Fluid Mechanics*, 100(3):597–621, 1980.

[168] I. S. Sullivan, J. J. Niemela, R. E. Hersheberger, D. Bolster, and R. J. Donnelly. Dynamics of thin vortex rings. *Journal of Fluid Mechanics*, 609:319–347, 2008.

[169] G. I. Taylor. The dispersion of matter in turbulent flow through a pipe. *Proceedings of the Royal Society of London. Series A. Mathematical and Physical Sciences*, 223(1155):446–468, 1954.

[170] T. Theodorsen. Mechanism of turbulence. In *Proceedings of the Second Midwestern Conference on Fluid Mechanics*, pages 1–19, 1952.

[171] W. Thielicke and E. Stamhuis. PIVlab – Towards User-friendly, Affordable and Accurate Digital Particle Image Velocimetry in MATLAB. *Journal of Open Research Software*, 2(1):e30, Oct. 2014.

[172] A. Tinaikar, S. Advaith, and S. Basu. Understanding evolution of vortex rings in viscous fluids. *Journal of Fluid Mechanics*, 836:873–909, 2018.

[173] T. Tran, P. Chakraborty, N. Guttenberg, A. Prescott, H. Kellay, W. Goldburg, N. Goldenfeld, and G. Gioia. Macroscopic effects of the spectral structure in turbulent flows. *Nature Physics*, 6(6):438–441, 2010.

[174] C.-Y. Tsai and S. E. Widnall. The stability of short waves on a straight vortex filament in a weak externally imposed strain field. *Journal of Fluid Mechanics*, 73(4):721–733, 1976.

[175] M. Van Dyke. *An album of fluid motion*, volume 176. Parabolic Press Stanford, 1982.

[176] P. L. van Gent, D. Michaelis, B. W. van Oudheusden, P. E. Weiss, R. de Kat, A. Laskari, Y. J. Jeon, L. David, D. Schanz, F. Huhn, S. Gesemann, M. Novara, C. McPhaden, N. J. Neeteson, D. E. Rival, J. F. G. Schneiders, and F. F. J. Schrijer. Comparative assessment of pressure field reconstructions from particle image velocimetry measurements and lagrangian particle tracking. *Experiments in Fluids*, 58(4):33, Apr. 2017.

[177] B. W. van Oudheusden. Piv-based pressure measurement. *Measurement Science and Technology*, 24(3):032001, Mar. 2013.

[178] W. M. van Rees, F. Hussain, and P. Koumoutsakos. Vortex tube reconnection at re= 104. *Physics of fluids*, 24(7):075105, 2012.

[179] J. C. Vassilicos. Dissipation in turbulent flows. *Annual review of fluid mechanics*, 47:95–114, 2015.

[180] R. A. Verschoof, A. K. te Nijenhuis, S. G. Huisman, C. Sun, and D. Lohse. Periodically driven taylor–couette turbulence. *Journal of fluid mechanics*, 846:834–845, 2018.

[181] R. Volk, E. Calzavarini, E. Leveque, and J.-F. Pinton. Dynamics of inertial particles in a turbulent von kármán flow. *Journal of Fluid Mechanics*, 668:223–235, 2011.

[182] A. von der Heydt, S. Grossmann, and D. Lohse. Response maxima in modulated turbulence. ii. numerical simulations. *Physical Review E*, 68(6):066302, 2003.

[183] A. von der Heydt, S. Grossmann, and D. Lohse. Response maxima in modulated turbulence. ii. numerical simulations. *Physical Review E*, 68(6):066302, 2003.

[184] T. Von Kármán. *Aerodynamics*, volume 9. McGraw-Hill New York, 1963.

[185] A. Weigand and M. Gharib. On the evolution of laminar vortex rings. *Experiments in Fluids*, 22(6):447, Apr. 1997.

[186] J. Westerweel, G. E. Elsinga, and R. J. Adrian. Particle image velocimetry for complex and turbulent flows. *Annual Review of Fluid Mechanics*, 45:409–436, 2013.

[187] J. Westerweel, G. E. Elsinga, and R. J. Adrian. Particle image velocimetry for complex and turbulent flows. *Annual Review of Fluid Mechanics*, 45(1):409–436, 2013.

[188] J. Westerweel, C. Fukushima, J. M. Pedersen, and J. Hunt. Momentum and scalar transport at the turbulent/non-turbulent interface of a jet. *Journal of Fluid Mechanics*, 631:199–230, 2009.

[189] B. Wieneke. Piv uncertainty quantification from correlation statistics. *Measurement Science and Technology*, 26(7):074002, 2015.

[190] M. Wilczek, A. Daitche, and R. Friedrich. On the velocity distribution in homogeneous isotropic turbulence: correlations and deviations from gaussianity. *Journal of Fluid Mechanics*, 676:191–217, 2011.

[191] C. E. Willert and M. Gharib. Digital particle image velocimetry. *Experiments in Fluids*, page 13, 1991.

[192] R. P. Xavier, M. A. Teixeira, and C. B. da Silva. Asymptotic scaling laws for the irrotational motions bordering a turbulent region. *Journal of Fluid Mechanics*, 918, 2021.

[193] D. Xu and J. Chen. Accurate estimate of turbulent dissipation rate using piv data. *Experimental Thermal and Fluid Science*, 44:662–672, 2013.

[194] J. Yao and F. Hussain. Vortex reconnection and turbulence cascade. *Annual Review of Fluid Mechanics*, 54:317–347, 2022.

[195] J. Zhou, R. J. Adrian, S. Balachandar, and T. Kendall. Mechanisms for generating coherent packets of hairpin vortices in channel flow. *Journal of fluid mechanics*, 387:353–396, 1999.

[196] R. Zimmermann, H. Xu, Y. Gasteuil, M. Bourgoin, R. Volk, J.-F. Pinton, E. Bodenschatz, and I. C. for Turbulence Research. The lagrangian exploration module: An apparatus for the study of statistically homogeneous and isotropic turbulence. *Review of Scientific Instruments*, 81(5):055112, 2010.